INVESTIGATION AND CONTROL OF WATER TREATMENT PLANT WITH CONSIDERATION OF MICRO-GRID CONCEPT

A THESIS SUBMITTED IN PARTIAL FULFILLMENT OF THE REQUIREMENTS FOR THE DEGREE OF DOCTOR OF PHILOSOPHY

C ROHMINGTLUANGA

MZU REGN. NO. 1800052

Ph.D. Reg No. MZU/Ph.D./1299 of 10.08.2018

DEPARTMENT OF ELECTRICAL ENGINEERING

SCHOOL OF ENGINEERING AND TECHNOLOGY

MAY 2023

INVESTIGATION AND CONTROL OF WATER TREATMENT PLANT WITH CONSIDERATION OF MICRO-GRID CONCEPT

BY

C Rohmingtluanga

Department of Electrical Engineering

Name of Supervisor: Dr Subir Datta

Joint- Supervisor: Prof. Nidul Sinha

Submitted

In partial fulfillment of the requirement of the Degree of Doctor of Philosophy in Electrical Engineering of Mizoram university, Aizawl.

CERTIFICATE

This is to certify that the work contained in the thesis entitled "**Investigation and control of water treatment plant with consideration of microgrid concept**", submitted by C Rohmingtluanga, Ph.D Registration No. MZU/Ph.D/1299 of 10.08.2018, for the award of the degree of Doctor of Philosophy to the department of Electrical engineering, School of engineering and technology, Mizoram University: Aizawl, India is a record of bonafide research works carried out by him under my direct supervision and guidance.

I considered that the thesis has reached the standards and fulfilling the requirements of the rules and regulations relating to the nature of the degree. The contents embodied in the thesis have not been submitted for the award of any other degree in any other university.

Prof. Nidul Sinha   Dr Subir Datta

Joint-Supervisor   Supervisor
Department of Electrical Engineering   Department of Electrical Engineering
National Institute of Technology,   School of Engineering & Technology
Silchar   Mizoram University
Silchar, Assam   Aizawl: Mizoram

Date: 10.05.2023

Place: Aizawl

DECLARATION

MIZORAM UNIVERSITY

MAY 2023

I, C Rohmingtluanga, hereby declare that the subject matter of this thesis is the record of work done by me, that the contents of this thesis did not form basis of the award of any previous degree to me or to the best of my knowledge to anybody else, and that the thesis has not been submitted by me for any research degree in any other University/Institute.

This is being submitted to the Mizoram University for the degree of Doctor of Philosophy in Electrical Engineering.

Date: 10.05.2023

Place: Aizawl

C Rohmingtluanga

Reg No. MZU/Ph.D/1299 of 10.08.2018

Candidate

HOD   **Supervisor**

Department of Electrical   Department of Electrical
Engineering   Engineering

iii

ACKNOWLEDGEMENT

(C ROHMINGTLUANGA)

DEDICATION

I dedicate my work to my late Grandfather, late Grandmother and my Parents

TABLE OF CONTENTS

LIST OF FIGURES

LIST OF TABLES

LIST OF ABBREVIATIONS

SDGs	Sustainable Development Goals
GDP	Gross Domestic Product
SCADA	Supervisory control and data acquisition
DG	Distributed generation
PV	Photovoltaic
UV	Ultraviolet
LOH	Loss of Head
WWTPs	Waste Water Treatment Plants
DWTPs	Drinking water treatment plants
DEA	Data envelopment analysis
BOD	Biochemical oxygen demand
COD	Chemical oxygen demand
GPS-X	wastewater modelling simulation software
NH4+	Ammonium Ion
WDS	water distribution systems
W-DSO	water distribution system operator
EPA	Environmental Protection Agency
ABB-DOC	ABB software for Exercising single-line diagrams of low and medium voltage electrical plants
MILP	mixed-integer linear programming model
GAMS	General Algebraic Modeling Systems
BESS	battery energy storage systems
IT	Information Technology
MOSCAD	MOTOROLA SCADA
RTU	Remote terminal unit
VRLA	Valve regulated lead acid
SPSS	statistical program for social sciences
HMIs	human-machine interfaces

ETAP	Electrical Transient Analyzer Program
OCTC	Off Circuit Tap Changer
SVC	Static Var Compensator
EPRI	Electrical Power Research Institute
EMS	Energy Management Systems
DMS	Distribution Management Systems
FACTS	Flexible AC Transmission Systems
SSSC	static synchronous series compensator
TCR	thyristor controlled reactor
CSC	Thyristor-Controlled Series Capacitor
TSR	Thyristor Switched Reactors
UPFC	unified power flow controller
UPGD	United Power Generation & Distribution Co. ltd.
CCPP	combined cycle power plant
MEC	Microbial Electrolysis Cell
HIL	Hardware-In-The-Loop
VSI	voltage source inverter
UPS	Uninterruptable Power Supply (UPS
SOGIFLL	second order generalized integrator (SOGIFLL)
PCC.	point of common coupling
PI	proportional-integral
PLL	phase-locked loop
PCI	proportional complex integral
VSC	voltage source converter
CMS	Centralised Monitoring system
CCT	critical clearing time
MCC	motor control center
HVDC	high-voltage DC transmission
MGCC	microgrid central controller
CMGs	coupled microgrids
GWO	grey wolf optimization

PID	Proportional Integral Derivative
PSO-PID	particle swarm optimization PID
TLBO-PID	Teaching Learning Based Optimization PID
ImGS	Interconnected Microgrid system
ST	solar tower
AWEC	Archimedes wave energy conversion
GEC	geothermal energy conversion
BDDG	biodiesel driven generator
ES	energy storage units,
DC	direct current
PFOID	proportional–fractional-order integral derivative
BOA	butterfly optimization algorithm
LFC	load frequency control
I-SSO	improved-salp swarm optimization
PSO	particle swarm optimization
GA	genetic algorithm
HHO	Harris Hawks Optimizer
RESs	renewable energy sources
ITAE	integral time absolute error
SCA	Sine Cosine Algorithm
MVO	Multi-verse optimizer
ALO	Ant lion Optimizer
ANFIS	Adaptive Neuro-Fuzzy Inference System
WTPs	Water Treatment Plants
P-f	power-frequency
Q-V	reactive power-voltage
AI	Artificial Intellegence
IPS	intermediate Pumping station
3DOF-FOPIDN	Three degree of freedom fractional order PID with filter
3DOF-TIDN	Three degree of freedom tilt integral derivative with filter
GAWSS p-I&II	Greater Aizawl Water Supply Scheme Phase-I and II

PHED	Public Health Engineering Department
MLD	Million Liter per Day
P&E	Power and Electricity Department
lpcd	Litres per person (capita) per day
NRW	non-revenue water
GAWSS P-III	Greater Aizawl Water Supply Scheme Phase-III
VT pump	Vertical Turbine Pumps
LT	Law Tension
HT	High Tension
NREL	National Renewable Energy Laboratory
ZEDA	Zoram Energy Development Agency
MISTIC	Mizoram Science, Technology & Innovation Council
DHI	Diffuse horizontal irradiance
DNI	Direct normal irradiance
GHI	Global horizontal irradiance
SCCC	Mizoram state climate change cell
HP	horse power
SLD	single line diagram
APFC	Automatic Power Factor Corrector
CT	Current Transformer
PT	Potential Transformer
NO	Normally Open
NC	Normally Closed
NI	Normally Inactive
NA	Normally Active
PAC	poly-aluminum chloride
Alum	aluminum sulphate
NTU	Nephelometric turbidity units
TDS	total dissolved solids
L-BWT	Level of Backwash Tank
L-FTB	Filter Bed Level

FM -Rate	Flow Meter rate
BWP	Backwash Pump
SP	Set Points
BWT	Backwash Tank
FB-OFR	Filter Bed Open channel flow rate
N-R	Newton-Raphson
G-S	Gauss-Seidel
IDMT	Inverse time relays with definite minimum time
IEC	International Electrotechnical Commission
TCCs	time-current characteristics
OT	relay tripping time
LI	long inverse
EI	extremely inverse
VI	very inverse
NI	normally inverse
OF	objective function
LA	lightning arresters
MCCB	Moulded Case Circuit Breakers
CWPH-I	Clear Water Pump House I
CWPH-II	Clear Water Pump House II
RWPH	Raw Water Pump House
MV	medium voltage
ANN	artificial neural network
ANFIS	adaptive neuro fuzzy inference system
FLC	fuzzy logic controller
GDC	generalized droop control
IPM	interior (or buried) permanent magnet machine
MPPT	maximum power point tracking
SPM	surface-mounted permanent magnet machines
MSC	machine-side converter
GSC	grid-side converter

PLL	phase lock loop
PCC	point of common coupling
NN	Neural Networks
FL	Fuzzy Logic
MFs	membership functions
P	active power
Q	and reactive power
F	frequency
V	voltage
psigmf	sigmoidal membership functions
trimf	triangular membership function
MISO	Multi Input Single Output
RMSE	Root Mean Square Error
SHG	small hydro Generator
ESSs	energy storage systems
MMG	multi-microgrid
IAE	Integrated Absolute Error
ITAE	Integrated Time Absolute Error
ISE	Integrated Square Error
ATSE	Integrated Time-weighted Square Error
SPV	Solar photo voltaic
EHHO	Enhanced harris Hawks Optimization
LCP	Local Control Panel
OT	Operating time of relay
LFA	Load flow analysis

LIST OF SYMBOLS

S	Minimum pump inlet belt submergence
D	Inlet belt design outside diameter
H	Minimum Liquid depth
V	Velocity in m/s
g	Acceleration due to gravity 9.81 m/s^2
A	Distance of the pump inlet belt center line to the intake structure entrance,
B	Distance from the back wall to the pump inlet belt center line
Q	Discharge of pump, m^3/s
H_s	Suction head
H_d	Delivery head,
H_f	friction loss
E	Efficiency of the pump
U	Velocity, m/s
r_H	hydraulic radius, m
S	Slope
C	Hazen-William's coefficient
n	Manning's coefficient
P(kW-motor)	Pump power in kilowatts,
q(m3/hr)	Rate of flow in cubic meter per hour,
ρ(kg/m^3)	Fluid density in kilogram per cubic meter,
h(m)	Pump differential head in meter
P(Pa)	Differential pressure in Pascal or N/m2
P_G	Generated Active Power
Q_G	Generated Reactive Power
|V|	Voltage Magnitude of the bus
δ	Phase angle of the bus
a	% tap change in tap-changing transformer

P_D	Active power demand
Q_D	Reactive power demand
i	Bus number in Load flow analysis
$G_{sh} + jB_{sh}$	Shunt admittance
τ	The instant of time when fault occurs
I_F	Fault current
T_D	Time delay
TD	Time dial settings
I_P	Pick up current settings
I_L	Load current
I_{pv}	represents the output current of the solar PV system,
I_{rs}	Reverse saturation current,
Θ	Temperature of the p-n junction,
A	ideality factor,
I_{scr}	Short-circuit current of a single PV cell
S	solar irradiation level,
N_s and n_p	Series and parallel number of PV cells in a string,
q (1.602e-19C)	the unit electric charge
k (1.38e-23 J/K)	Boltzmann's constant
T	Operating temperature of the solar PV system,
T_{ref}	Cell temperature reference
$k\Theta$	Solar temperature coefficient
G_s	PV cell conductance
V_{pv}	Output voltage of the SPV
C_{pv}	Capacitance of the SPV output
R_1	Output resistance of the SPV
L_1	Output inductance of the SPV
D_1	Output diode of the SPV
S_1	Boost converter switching value of the SPV
S_2 & S_3	Buck boost converter switching value of the BESS
V_b	Output voltage of the battery

C_b	Output capacitance of the battery
I_b	Output current of the battery
I_2	Output line current of the battery
L_2	Output inductance value of the battery
V_{dc}	DC link voltage of the converter
C_{dc}	DC link capacitance of the converter
R_s	Line resistance
L_s	Line Inductance
V_m	Voltage at Point of common coupling load side
C_d	Load capacitance value
I_o	Output current at Load
R_L	Series Load resistance
I_L	Series load current
V_{sa}, I_{sa}	Phase a output voltage and current of PMSG
V_{sb}, I_{sb}	Phase b output voltage and current of PMSG
V_{sc}, I_{sc}	Phase c output voltage and current of PMSG
V_{pv}^*	Voltage Reference value
S_1^*	Average duty ratio of the converter
ρ (kg/m)	Air density
$A \ (= \pi r^2)$	Blade swept area of the PMSG
r	Wind turbine radius
V_ω (m/s)	The wind velocity
C_P	The power coefficient;
λ and β	Represent the tip ratio and blade pitch angle
P_T	The mechanical power generated by a wind turbine
V_{sd} and V_{sq}	The stator voltages are identified
I_{sd} and I_{sq}	The stator currents
L_d and L_q	The inductances of the dq axis
R_s	The resistance of the stator
$\omega_e = np$	The angular frequency, where np corresponds to the number of poles

ψ_{fl}	The permanent flux linkage
T_m	The mechanical torque
T_e	The electrical torque
J	Moment of inertia
B	The friction coefficient
ψ_d	Flux aligning with the d-axis,
ψ_q	Flux aligning with the q-axis
V_d	The voltage phasor along the d-axis
V_q	The stator voltage phasor along the q-axis
I_d	Stator current along the d axis
I_q	Stator current along the q axis
I_{L1abc}	The phase currents of linear load (L1) derived from DG1
Z_L	The line impedance
Q_A	The reactive power at point A
P_A	Real power at point A
V_1	is the inverter output voltage at point A
V_2	is the voltage at the point of common coupling (PCC)
δ	is the power angle
Θ	The phase angle of the line impedance ZL
X_L	The reactance of the line
R_L	Represent inductance of the line
Q_{vir} , P_{vir}	the virtual reactive power and real power
f	Frequency of the microgrid system
V	Voltage of the microgrid system
P and Q	The two active and reactive power inputs of ANFIS
A1 and A2	The membership functions of input P in ANFIS
B1 and B2	Represent the membership functions of input Q in ANFIS
i	Represents node in ANFIS structure
B_i (or A_i)	is the linguistic label
α_i, β_i, c_i	are known as the parameter set
$\overline{w_i}$	is the output of the fourth layer

P_m	represents mechanical power derived from the rotor shaft
P_w	is the power of wind content in the virtual stream tube
T_{ct}	Cell temperature °C
T_{at}	Ambient temperature °C
$s(t)$	Random irradiance,
NOCT	Nominal cell operating temperature °C
I_{sc}	Short-circuit current A
K_{ct}	Current temperature coefficient mA/°C
V_{oc}	Open-circuit voltage V
K_{vt}	Voltage temperature coefficient mV/°C
V_{mp}	Voltage at maximum power V
I_{mp}	Current at maximum power A
FF	Fill factor
η_{cells}	Number of PV cells,
V	Terminal voltage of PV
I	Current of PV and is denoted in (A)
$P_{pv}(s(t))$	PV power output (W).
F_0	Fuel curve intercept coefficient (units/h/kW),
F_1	Fuel curve slope (units/h/kW),
P_{dg}	Electrical output of the generator (kW)
Y_{dg}	Rated capacity of the generator (kW).
SOC (t) and SOC (t-1)	The current and previous energy capacity of the BESS over one time step
S_{bess}	Self-discharge rate.
P_{bess}^{ch} and P_{bess}^{dis}	Charging and discharging power to and from the BESS which are functions of the energy surplus and deficits from the energy supply system
η_{bess}^{c} and η_{bess}^{d}	Charging and discharging efficiencies of the BESS.
K_P	Proportional gains
K_I	Integral gains

K_D	Derivative gains
$P(s+1)$	The position vector of hawks in the next iteration s
$P_{rabbit}(s)$	The position of rabbit
$P(s)$	The current position vectors of hawks
x_1, x_2, x_3, x_4 and j	Random numbers inside (0,1), which are updated in each iteration
u_b and l_b	show the upper and lower bounds of variables
$P_{rand}(s)$	Randomly selected hawk from the current population
P_m	The average position of the current population of hawks
E	The energy of a prey
E_o	The initial energy
S	The maximum number of iterations
t	The current iteration
M	Random vector of the size of 1xd
V_{id}	The particle (hawk) velocity
X_{id}	The current particle (hawk) (solution)
P_{id} and P_{gd}	pbest and gbest.
rand ()	Random number between (0,1)
cl, c2	Learning factors.
K_{Ts}	Gain of the time constant
K_{Is}	Gain of integral part
K_{Ds}	Gain of the derivative part
K_{ps}	Gain of the proportional part
K_{WTG}	Gain of Wind turbine generator
T_{WTG}	Time constant of wind turbine generator
K_{PV}	Gain of Solar photo voltaic
T_{PV}	Time constant of Solar photo voltaic
K_{BES}	Gain of Battery energy storage system
T_{BES}	Time constant of Battery energy storage system
T_N	Time constant of area N

CHAPTER

1

Introduction

In this chapter the background and motivation behind the research are explained and introduced. The main goals of the thesis as well as its contributions are emphasized and summarized. Lastly, literature including summarization of each chapter has been introduced.

1.1. Background

Water is an essential resource that impacts numerous facets of development and is linked to almost all Sustainable Development Goals (SDGs). It supports healthy ecosystems, encourages economic progress, and is fundamental to life itself. However, more than two billion people lack access to safe drinking water services, while 3.6 billion people do not have access to proper sanitation facilities, and 2.3 billion people lack basic handwashing facilities. This lack of access to water and sanitation facilities poses significant challenges to economic growth, poverty eradication, and sustainable development, resulting from gaps in access to water and sanitation, population growth, increased water-intensive expansion patterns, pollution, and increased rainfall variability. Climate change is also expressed through water, with water being a factor in nine out of ten natural disasters. This means that water-related threats to the climate have an impact on food, energy, urban, and environmental systems simultaneously. Thus, if we want to meet our climate and development goals, water must be a central component of adaptation measures. Economic growth is reliant on water, and a decline in water supplies has a negative impact on manufacturing and can result in slower economic growth. Moreover, water-related losses in agriculture, health, income, and prosperity can significantly reduce Gross Domestic Product (GDP) growth rates by up

to 6% by 2050. Consequently, achieving global poverty alleviation targets requires ensuring a sustainable and reliable supply of water in the face of growing scarcity.

Improving water supply is crucial for both rural and urban areas, as all life on earth depends on it and pollution continues to rise. Municipalities prioritize sustainable water supply, aiming to lead in this area. Additionally, the increasing consumption of fossil fuels like coal, natural gas, and oil is leading to higher energy costs, which must be considered in managing industries and public water treatment facilities. A water supply system consists of several components, including a raw water pumping station, water treatment facility, intermediate pumping stations (also called booster stations), and a main reservoir. Each pumping station draws power from the grid through distribution firms or the power and electricity agency, and the plant design and pump capacity affect their power requirements.

In light of the effects of climate change and increasing environmental pollution, it has become increasingly important to preserve water resources and enhance pumping and treatment plants. Public drinking water systems rely on a range of water treatment techniques. Common processes employed by these systems include coagulation, flocculation, sedimentation, filtration, and disinfection. Typically, the first step in water treatment is coagulation, in which positively charged chemicals are introduced to the water. These chemicals balance out the negative charge of dirt and other dissolved particles in the water, causing them to bond together and form larger particles. Salts, aluminium, or iron are often used for this purpose. Following coagulation is the flocculation process, which involves gently mixing the water to create larger, heavier particles known as flocs. During this phase, water treatment facilities may add additional chemicals to aid in the formation of these flocs.

Many organizations and companies worldwide use supervisory control and data acquisition (SCADA) systems to monitor and manage water treatment processes in industries and plants. These systems can be centralized computer systems that are safe, efficient, and accessible both locally and remotely. SCADA-based WTPs help identify ongoing or new issues with water quality, quantity, and losses. Implementing a SCADA system for WTPs and supply systems generally aims to optimize plant processes, maintain good water quality, and reduce water losses. However, most existing WTPs are still manually operated and maintained by field staff, with manual

laboratory procedures used to process and monitor water quality and quantity. This manual approach can result in inaccurate readings and slow processing in WTPs.

Unlike other industries, public water treatment facilities require a medium to high tension power supply, which is then stepped down to a low tension for auxiliary loads. These facilities are typically considered bulk consumers, and their operating and energy costs are usually covered by the government or municipal in most countries. To ensure uninterrupted power supply, many facilities also have high Tension (HT) diesel generators and diesel engine driven pumps as backup. However, the use of diesel generators can result in high operating costs and environmental pollution due to the emission of CO_2 gas. Therefore, sustainable treatment and power supply are becoming important to reduce the load and ensure a reliable public water supply.

Renewable energy sources have become increasingly popular in recent years due to their environmental benefits and cost-effectiveness when compared to traditional centralized power plants. Fossil fuels used in power plants release harmful greenhouse gases, and with limited supplies and increasing energy consumption, their impact on the environment is a major concern. Many power plants are located remotely, far from cities, and require extensive transmission and distribution lines to provide electricity to customers. However, a significant amount of power is lost during transmission, which necessitates power substations to increase the voltage level during transmission and decrease it during consumption to minimize these losses.

In today's world, there are various challenges associated with centralized power plants, such as environmental concerns and limited availability of fossil fuels. Therefore, the use of distributed generation (DG) has become more important due to its convenience, loss reduction, and technical solutions. Renewable energy sources, such as solar and wind power, are commonly used as the primary power sources for DG units due to their practically limitless supply and minimal environmental impact.

However, renewable energy sources are unpredictable and uncontrollable, which requires the use of power electronic devices for efficient control. For example, wind turbines generate AC voltage with the aid of several generator types and an AC-DC-AC back-to-back converter, which involves converting the input AC voltage to a DC voltage and then back to an AC voltage with a desired voltage magnitude and frequency. Similarly, Solar photovoltaic (SPV) systems can be connected to the grid

through either single stage or double stage connections to loads, using a three-phase or single-phase inverter to directly transform the input DC to AC, the input source voltage can be boosted using a DC/DC converter, and another inverter can transform the DC voltage to AC voltage due to the nonlinear characteristics of the SPV system.

A microgrid refers to a compact system that links several Distributed Generators (DGs) based on renewable energy sources to distributed loads, energy storage, and electronic converters. It can operate with centralized, semi-centralized, or decentralized control methods and can have two modes of operation, i.e., grid-connected and autonomous operation modes (islanded). A microgrid system can be designed to operate in a decentralized control scheme and autonomous mode to reduce costs by minimizing the need for communication technologies and allowing for the integration of a significant number of renewable sources in areas where a utility grid is not feasible or cost-effective, such as edge-of-grid or remote/regional areas. In such a system, one or more DGs often utilize droop control to achieve power-sharing and manage frequency and voltage. The active and reactive powers are controlled at each DG's output while it is in droop control, and the microgrid's voltage and frequency are maintained within allowed ranges to ensure system stability.

Autonomous/independent microgrids have emerged as a cost-effective solution for powering rural and remote areas without the need for extensive transmission and distribution networks. However, the seasonal variations and unpredictability of fuel transportation costs create additional challenges for operating autonomous microgrids. To mitigate these challenges, microgrid operators are increasingly looking to harness renewable energy resources where they are abundant, such as wind or solar power, and reduce dependence on diesel or gas-based sources. This trend has led to a growing interest in microgrid projects for remote areas. Various studies have shown that implementing isolated/autonomous microgrids can significantly lower the high cost of electricity, making it more affordable to electrify isolated off-grid villages. These microgrids typically rely on diesel or gas-driven synchronous generators, as well as renewable energy sources that are interfaced with power electronic converters.

1.2. Literature

1.2.1 Water Treatment Plant

WTPs commonly use sedimentation to separate particles from water. During the sedimentation process, heavier flocs sink to the bottom of the tank as they are denser than water. The clear water above is then filtered to remove any remaining solids. Various filter materials with different pore sizes, such as sand, gravel, and charcoal, are used in the filtration process to eliminate germs, dissolved contaminants, and odors from the water. Chemical disinfectants like chlorine, chloramine, or chlorine dioxide may also be added by the WTP after filtration to eliminate any remaining parasites, bacteria, or viruses. To ensure safe drinking water, WTPs ensure that the chemical disinfectant concentration in the water leaving the facility is low. The remaining disinfectant also helps eliminate bacteria present in the pipes that transport water from the treatment facility to homes and businesses [1-3].

WTPs are facilities that purify water to make it safe for human consumption or for industrial use by removing harmful substances and improving water quality. The purification process involves several methods, including physical, chemical, and biological treatment processes. Physical treatment processes involve the removal of large debris and particles from the water through screening. Smaller particles are then removed through sedimentation, where they settle out of the water by gravity. The next step is filtration, which removes any remaining particles that were not eliminated during sedimentation [4-6]. Chemical treatment is used to remove contaminants such as pathogens, chemicals, and minerals. Chlorination is a widely used chemical treatment process where chlorine is added to the water to kill bacteria and other pathogens. Biological treatment involves introducing microorganisms to the water to break down organic pollutants. This process is commonly used to treat wastewater in sewage treatment plants [7-8].

In recent years, there has been an increasing interest in alternative water treatment technologies such as membrane filtration, reverse osmosis, and ultraviolet disinfection. Membrane filtration uses membranes to remove impurities from the water, while reverse osmosis applies pressure to eliminate impurities. Ultraviolet disinfection uses UV radiation to kill bacteria and other pathogens [9-10]. The effectiveness of water treatment processes depends on various factors such as the type and level of contaminants, the design of the treatment plant, and the quality of the water source.

Therefore, WTPs require regular monitoring and maintenance to ensure proper functioning and compliance with regulatory standards for safe drinking water [11].

A Conventional Treatment Plant such as rapid sand treatment process and slow sand treatment process follows a typical flow pattern to achieve this objective, as shown in Figure 1.1. The safety and suitability of drinking water for public use depends on its chemical, physical, and biological properties. It is preferable to obtain drinking water from a source that is not contaminated. However, raw water from surface water sources is typically unsuitable for drinking purposes. developing a remote-control system suitable for rural water treatment projects is crucial to ensure safe drinking water and represents an important step towards realizing a safe water supply. The primary goal of water treatment is to produce potable and safe drinking water [12-14].

The quality of raw water input often varies with the seasons, necessitating frequent filter bed cleaning. However, the timing for this process is often determined manually, leading to inadequate filtration and plant process breakdowns. Mechanical monitoring equipment used for filter bed Loss of Head (LOH) monitoring also has a limited lifespan and requires regular maintenance to function effectively [15-16]. Additionally, the large motor pumps used in many WTPs consume a significant amount of energy, impacting the treatment process and causing financial strain. Transmission and distribution losses also have a considerable cost impact, making it crucial to decrease losses in the transmission and distribution system while improving plant efficiency. Responsibility for optimization, quality monitoring, and loss minimization falls on the water supply department or companies. Despite this, the majority of current WTPs lack a SCADA system for tracking and managing the water supply and distribution networks [17].

In recent studies, it has been shown that the energy efficiency of Waste water treatment plant (WWTPs) is often unsatisfactory. Efficient management of pump energy in this area can bring both economic and environmental benefits. However, despite the availability of on-line sensors that provide high-frequency information about pump systems, energy assessment is typically only carried out a few times a year using aggregated data. This means that pump inefficiencies are often detected late, and understanding the dynamics of pump systems is often insufficient [18-19].
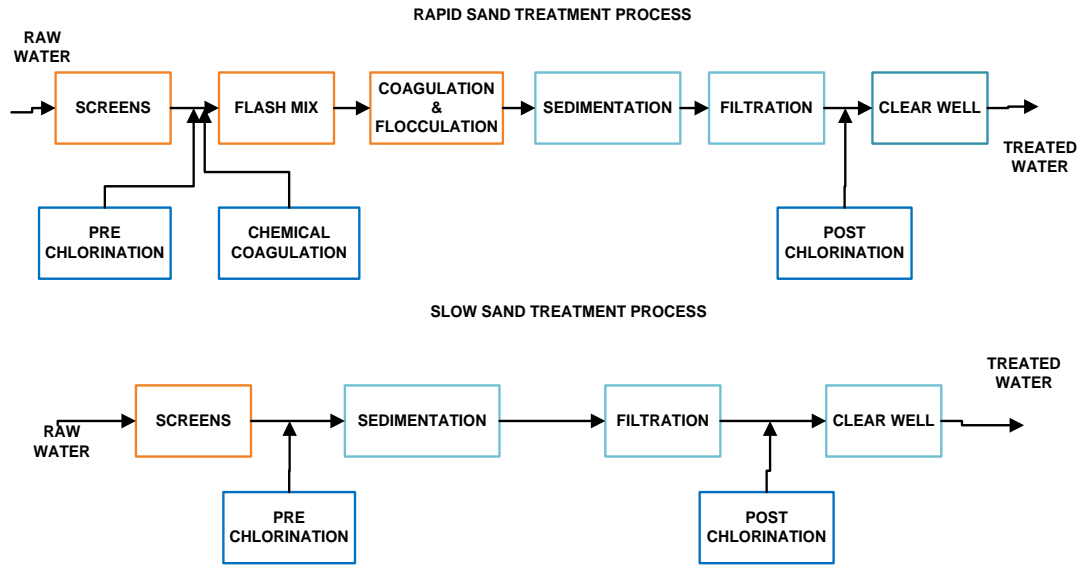
Figure 1.1 Conventional WTP.

To address this issue, a data-driven methodology based on fuzzy logic that can support daily energy decision making is proposed. This approach provides plant managers with detailed information about pump performance and offers case-based suggestions for reducing pump system energy consumption and extending pump lifespans. The methodology was tested in a case study at a WWTP in Germany, where it was able to identify energy inefficiencies and provide case-based solutions that led to a reduction in pump energy consumption by 18.5% [20].

1.2.2 Power System in WTP

In [21], evaluation of the energy efficiency of a sample of drinking WTPs (DWTPs) is discussed using data envelopment analysis (DEA) tolerance method. The results of the study showed that data variability had a significant impact on the energy efficiency scores of approximately one-third of the DWTPs evaluated. Even in the best-case scenario, most of the DWTPs were deemed inefficient, indicating that there is potential for them to reduce the energy used to treat raw water. The study highlights the importance of considering data variability in benchmarking for policymakers. Failure to do so can lead to biased conclusions, and in this study, the inclusion of this information altered the rankings of some energy-efficient DWTPs. The findings emphasize the need to account for data uncertainty in regulatory decision-making, especially when using efficiency scores to set water tariffs.

WWTPs are expected to conserve energy and materials to meet the growing demand for sustainability. To achieve this goal, efficient management and decision-making mechanisms are necessary to optimize resource allocation. In recent years, advanced computational techniques, such as neural networks and genetic algorithms, have been applied to industrial problems to mine latent rules from massive data using statistical learning. In [22], a deep learning-based approach is proposed for energy and materials-saving management in WWTPs using real-world data from a treatment plant in Chongqing, China. The treatment processes are modelled through neural networks, which estimate the materials cost that meets single indexes. The genetic algorithm is then used to compute the overall cost that simultaneously satisfies all indexes. Empirical results show that the proposed management method can reduce the total energy and materials cost by 10%-15%.

In WWTPs, energy consumption is a crucial factor, with aeration systems being major contributors to energy usage. However, some newer plants, such as the Tao-bay plants in northern Taiwan, have yet to introduce automated control on their aeration systems. To address this, numerical methods were utilized in [23] to predict the optimized airflow rate and energy consumption, providing references for the first-phase plant operation. The effluent concentrations for these parameters were compared to the numerically calculated values for calibration purposes. Additionally, an empirical correlation was proposed for alternative airflow and relative electricity consumption calculations. A SCADA system consisting of current and water quality sensors with an online interface was developed to monitor the aeration system of the case-study plant. Selected real-time data for dissolved oxygen (DO) and electricity usage related to the biological treatment were recorded in the cloud server and used for verifying and compensating existing data measured in the plant. The GPS-X model predicted an energy-saving rate of approximately 20% for the Tao-bay plant in 2018, based on monthly energy consumption data, 18-21% for plants operating in the 50,000-10,000 CMD range. When adjusting DO every 1 mg/L to fit a sewage-discharge criterion, the energy-saving rate was approximately 5-7%.

In [24], decreasing the electricity consumption of pump groups in water distribution systems (WDS) is discussed, specifically the parallel water-intake pump group that consists of fixed-frequency and variable-frequency pumps. The study

proposes an optimal regulation method by designing a regulation strategy for the water level of the clean water tank and calculating the intake water flow of the parallel pump group. The optimization problem, with constraints such as limited pressure fluctuations of WDS and required flow of water supply, is solved by using dynamic programming algorithm and particle swarm optimization algorithm to minimize electricity consumption. Experiment was conducted, and the results indicate that the proposed optimal regulation method can achieve electricity savings of up to 4.20%.

In [25], the development and implementation of a new control system for the colbun/machicura hydro-generation complex located in Chile is discussed. The system is equipped with advanced production planning functions such as Reservoir Inflow Forecasting and Generation Scheduling, generation control functions such as Regulation Adjustment and Generator Setpoint Control, and hydraulic monitoring and control functions, along with a complete set of SCADA functions. The optimization algorithms used in the system are based on a unified methodology that employs Linear Programming. This approach ensures high effectiveness and cohesiveness among all the application functions, making the system one of the most advanced control systems for hydro-generation facilities currently in operation. The paper provides a general overview of the real-time control system and detailed descriptions of the software applications. After rigorous tuning and testing, the system has demonstrated high efficiency and effectiveness in the field.

In [26], the energy generation using non-conventional sources and their application in water supply and treatment systems for potable, commercial, and industrial water, as well as water recycling is discussed. The study prioritized the development and implementation of cost-effective systems that utilize non-conventional energies, such as wind and solar, to provide water supply from deep wells and water treatment using natural sources like ozone and UV systems. factors such as electric power generation, computerized controls, power transformer design, electric grid integration, water treatment systems using ozone and UV, filtration, and electrical safety were considered for energy generation/transmission and water treatment systems.

In [27], an optimization framework that integrates the energy flexibility of water treatment, desalination, and distribution systems into power distribution systems operation is proposed. The framework involves a water distribution system operator

(W-DSO) co-optimizing the operation of variable speed pumps and water storage tanks in water treatment, desalination, and distribution systems to minimize daily energy costs, given expected water demand and energy tariffs. The optimized energy flexibility of W-DSO is then incorporated into the operation of power distribution systems, considering operational constraints of both power and water distribution networks, ensuring reliable supply to customers. Simulation results demonstrate the effectiveness of the proposed model in enhancing the economic efficiency of a 15-node water network test supplied by a 33-bus power distribution system.

In [28], the important aspects of plant-wide electrical reliability assessments and design for water and waste WTPs is explored. The identification of key issues is based on several case studies that involve system configurations, power quality, standby emergency power, utility service arrangements, and other relevant considerations. The case studies also take into account the requirements of the Environmental Protection Agency (EPA) and California. Regarding the reliable design of electrical systems.

In rural areas of the Midwestern United States, agricultural and irrigation loads are a significant part of the daily electrical demand faced by rural electric cooperatives, particularly during the Spring and Summer growing seasons. Effective load monitoring and control are crucial for efficient management of electrical energy supply and demand. To address this issue. In [29], the implementation of a SCADA system as a load management solution to monitor and control agricultural and irrigation loads, especially during peak electrical energy demand hours is discussed. Furthermore, distributed generation (such as solar, wind, and CHP) can be integrated to help meet peak demand. DCG can help bridge the gap between demand and supply. The combination of a SCADA system and DCG is expected to result in a 20% to 43% recovery in lost energy sales during load control days.

Computer-based control systems such as SCADA/DCS systems have become increasingly popular in the field of industrial energy management. Therefore, in [30], it is aimed to explore the various issues related to industrial energy management through online control and provide an overview of the status of DCS-based energy management systems in industrial complexes. Specifically, the role of DCS systems in industrial energy management were emphasized.

With the increasing demand for electrical energy and the need to reduce carbon emissions, energy management systems are facing new challenges. Governments are encouraging sustainable energy generation, leading to a rapid increase in the installation of SPV plants. Due to the variable nature of renewable energy sources, it is becoming essential to install battery energy storage systems (BESS) for both residential and industrial customers to manage energy. In [31], a new way to use a SCADA system to enable direct communication between the monitored system and a data server, where the data is analyzed to optimize the system design is presented. A mathematical model is presented to optimize the BESS size, minimizing energy exchange with the utility grid. A case study is conducted on a residential customer to demonstrate the effectiveness of the proposed approach in BESS design.

Water companies provide an essential service to society and ensuring their sustainability is crucial. To achieve this goal, it's important for these organizations to operate effectively and efficiently. Information Technology (IT) solutions, such as SCADA systems for operation and maintenance and Smart Metering systems for sales and customer relationship management, play a critical role in improving performance. However, the analysis of the benefits of these technologies has typically focused on technical characteristics and functionalities, rather than the impact on organizational processes and the value created. In [32], an analysis of the benefits of these technologies is proposed based on the processes and activities they enable, taking into account the resources they consume and the costs associated with them. The optimization of these costs can lead to efficiency gains and the generation of useful information, which can create value for the water company.

1.2.3 SCADA System in WTP

Drinking water is a finite natural resource that is being rapidly depleted due to the pollution caused by rapid social development. This pollution is affecting both surface and underground water reserves. One of the biggest challenges in managing modern city water supply systems is to maintain a consistent supply of chemically and biologically safe drinking water.

In [33], real-time monitoring systems for water quality and quantity parameters provide timely alerts and more time for reaction is discussed. One possible solution to

this challenge is to use a real-time measuring station equipped with an industrial SCADA system that can be optimized for efficient performance. The SCADA system provides continuous monitoring of various physical, chemical, and biological parameters, enabling fast and reliable detection of any deviations in the system. The saved data provides the opportunity for further analysis of the measured parameters and dependencies between them. One possible methodology for controlling, reducing, and optimizing water loss in the communal water supply system is to efficiently utilize modern SCADA systems that can be implemented into existing water supply systems and become an integral part of the new optimized operational management and control.

In [34] a three-tier structure SCADA system was developed to protect the water environment of Tuojiang River. The system consisted of a monitoring station, central station, and control & management centre. Survey data was transmitted to the computer system through RS-232 at the monitoring station. A classic plan was based on the Motorola SCADA (MOSCAD), which included MOSCAD-M RTU, MOSCAD FIU, and MDLC. The central station and control & management centre were usually connected through the internet. Factor analysis method was used to process the original data by statistical program for social sciences (SPSS) to draw concise and accurate conclusions of water pollution. According to the results, the accumulative contribution rate of 6 common factors accounted for 94.053%, which included most information of 14 original indexes. It proved that industrial pollution, agricultural irrigation, and domestic sewage were the main causes of water pollution in Tuojiang River.

In [35], it is proposed that a rule-based supervisory system that uses fuzzy logic to predict turbidity sensor failures in the water intake stage zone. Experts' knowledge and historical data were used to create the rules. The study includes a practical example of a turbidity sensor located in the water intake stage of Puerto Mallarino DWTP from Public Service Company of Cali (EMCALI EICE ESP) in Colombia.

The implementation, upgrading, and optimization of higher-level SCADA control centres is a continuous process. IGSS is one of the most popular SCADA software options in the market, particularly in the water sector, due to its favourable characteristics. To address this, [36] proposes a solution for optimizing IGSS SCADA resources by integrating water and wastewater pumping stations into a higher-level

SCADA system. It is based on a comprehensive analysis of the locally implemented solutions and the OPC interface, including both OPC UA and classic OPC.

A completely independent real-time measuring station using an industrial SCADA system was implemented in [37] to protect natural water resources that can independently measure water quality parameters. Real-time monitoring of water quality and quantity parameters provides an on-time alert and reaction time. This SCADA system offers 24/7 monitoring of various physical, chemical, and biological parameters, facilitating fast and reliable pollutant detection. Saved data also enables additional off-site analysis of measured parameters and their connections. The system comprises a Central Monitoring Station, a Local Monitoring Station located near Demir Kapija, and several mobile monitoring stations. The Local Monitoring Station is equipped with industrial Programmable Logic Controllers (PLCs) to integrate the work of diverse instruments, real-time measuring devices, analytical measuring devices, and station functionality equipment. Data from remote real-time stations is continually transmitted to the CMS for further analysis.

The integration of automation and optimization systems using SCADA technology can significantly improve the flexibility and reliability of power control systems. To expand this, in [38], design of a SCADA system that enables communication between devices using different protocols is done. The system comprises a Remote Terminal Unit (RTU), a Master station, and their corresponding human-machine interfaces (HMIs). To build the RTU prototype, a Raspberry Pi was used to communicate with the master station using the IEC 60870-5-104 protocol. The master station will be created using C# language and will include an HMI and front-end communication that can communicate with both the Modbus and IEC 60870-5-104 protocols. This system is expected to be used for microgrid systems or for laboratory-scale training.

1.2.4. Analysis of Treatment Plant

The demand for electricity has increased significantly in recent years, especially during summer when consumption peaks. This is due to changing consumer habits, improving quality of life, and growth in the economic and industrial sectors. Conducting a load flow analysis (LFA) is a basic requirement for power system analysis. The LFA provides information about voltages, real and reactive power

generated and absorbed, and line losses across the entire system. Short circuit analysis provides information to determine if the interrupting capacities of the power system components are adequate enough to protect the power system. This data is also used to evaluate the appropriate sizing of protective relays and sensing equipment.

In [39], a power supply model for a 220/63/30 kV substation is presented. A power flow analysis based on the Newton-Raphson method using Electrical Transient Analyzer Program (ETAP) software version 16.0.0 was conducted. Additionally, a short circuit analysis was simulated to verify the protection devices under fault conditions and at different voltage levels for various operating scenarios of the substation, including three-phase fault, two-phase earth fault or isolated, and earth faults. All faults simulated in the analysis comply with IEC 60909.

In [40], an explanation of performing LFA for IEC projects using ETAP, as well as the selection of electrical equipment parameters based on ETAP results is proposed. LFA is a fundamental analysis for electrical power system design and planning. It covers the required inputs for modeling an electrical system, including standard/typical values and assumptions to be made when input data is not available. It also discusses acceptable limits of LFA results and methods for achieving correct results. The power system equipment is designed to withstand worst-case conditions, and this paper also highlights the importance of analysing certain worst-case scenarios using LFA.

Also, in [40], selection of a transformer is proposed for a project, such as the primary voltage, secondary voltage, rated apparent power, impedance, X/R ratio, impedance tolerance value, and tap position are important inputs. The rated apparent power is chosen based on the expected load, and it should be verified through LFA and motor starting analyses. The transformer's impedance should be in accordance with industry standards. The X/R ratio can be calculated using the transformer's copper loss based on established methods. If copper loss data is not available, the typical X/R ratio provided in ETAP can be used. The Off Circuit Tap Changer (OCTC) tap position is selected based on the ETAP result. The transformer impedance tolerance value should be determined based on established guidelines, with ETAP considering a positive tolerance for LFA.

Moreover, in [41] the ETAP software provides the percentage loading of a bus, which is used to determine the maximum allowable loading of the bus during the

FEED and detail engineering stages. Typically, buses are allowed to load up to 80% during the FEED stage and up to 90% in the detail engineering stage. The bus rating is determined based on the current flowing through it. To calculate the current, the total apparent power of the load connected to the bus is determined, assuming 100% voltage across the switchgear bus. A standard bus rating is chosen, which is higher than the calculated current flowing through the switchgear. Sometimes, the ETAP results show a higher current than the calculated value because ETAP considers the actual voltage at different operating conditions, which may vary from 95% to 100%.

In [42], the effects of load variation on power systems is discussed, which can result in voltage fluctuations and negatively impact the performance of loads, as well as other parameters like power loss and power factor. The focus of the article is on the simulation of a 132/11 kV Distribution Sub Station using SVC (Static Var Compensator) technology to enhance voltage levels. The main objective is to improve voltage levels during peak load conditions, while also reducing power loss and improving power factor. The simulation is conducted using the ETAP software and the recorded parameters are compared with the simulation results.

Voltage sag is a common issue in heavily loaded power distribution systems, where permissible voltage variation levels are low. Due to heavy loading, voltage levels are not maintained up to the mark, resulting in voltage sag. The main cause of voltage sag is an imbalance in reactive power generated by the load. There are several methods for voltage improvement at the distribution side, with the most common being tap setting of the transformer. However, this method has limitations related to insulation and dielectric strength. Another method to enhance voltage is to improve the power factor by inserting a switched capacitor. Reactive power support at the weakest bus also helps to improve voltage levels, and various compensating devices like switched condensers, synchronous motors, etc., can provide reactive power support. [43], is one of the advanced compensating devices for reactive power support. SVC, a widely used member of the FACTS family, helps to maintain the voltage profile when connected at the weakest bus by inserting current. The LFA is useful in identifying the bus where the SVC needs to be installed.

LFA is a numerical algorithm that provides essential information about the parameters of a power system. The Newton-based Load Flow solution method was

first developed in 1967 by Tinney and Hart, and later the conventional Newton method was introduced by Stott, which uses the Jacobian matrix to calculate the incremental correction of the state variables. LFA is a crucial component of Energy Management Systems (EMS) and Distribution Management Systems (DMS). LFA provides critical information about power generation, power delivery, system losses, current flow through each branch, active and reactive power, and voltages at each bus [44].

Transient stability analysis is a critical component in power systems, particularly for smaller power plants. This analysis seeks to determine if a system will maintain synchronism with other generating plants after disturbances. In [45] the transient stability of an 80MW power plant owned by United Power Generation & Distribution Co. ltd. (UPGD) was analyzed using ETAP software. The plant, operating as an Independent Power Producer (IPP), includes a total of 12 generators operating in parallel, sometimes in islanding mode and sometimes in grid mode. Stability was studied for both modes of operation under various abnormal conditions to predict the behavior of the generators. Specifically, the study examined the impact of generator parameters such as fault clearing time and inertia on transient stability. The goal was to vary the parameters and observe their impact on transient stability using the ETAP software to simulate symmetrical and unsymmetrical faults in the system.

The success of a power system operation relies heavily on an engineer's ability to provide a continuous and dependable power supply to loads. Power system stability refers to the condition where synchronous machines in the system maintain synchronization. Stability issues in power systems are generally categorized into two types: steady-state stability and transient stability [46]. Steady-state stability relates to the system's ability to restore synchronization after minor and gradual disturbances. On the other hand, transient stability pertains to the power system's ability to withstand the transition that follows a significant disturbance and achieve a suitable operational state. The primary objective of transient stability analysis is to determine if the system returns to a steady-state condition after a disturbance has been cleared.

Whereas, in [47] Power systems are facing increasing stress, making transient stability analysis a major issue in their operation. Transient stability analysis is a highly nonlinear problem, especially for large power system networks. In this study, the impact of different faults, such as 3-phase faults, LG faults, and sudden generator

removal, were analyzed at various bus levels in power plant. The critical clearing time required for stable operation of the system was calculated using the ETAP software.

In [48], modelling a combined cycle power plant is discussed in ETAP software for transient stability studies. ETAP is a useful tool for reducing network malfunction and increasing system efficiency by ensuring proper relay coordination within a shorter time frame. The transient stability studies determine the system's electrical frequency, speed deviations, real and reactive power flows of the machines, the machine power angles, as well as the voltage levels of the buses and power flows of lines and transformers in the system. ETAP software was used to perform transient stability analysis. The critical clearing time (CCT) was calculated for a given fault. The system's frequency and voltage were analysed for different loading conditions.

The use of non-conventional energy sources and distributed generation has introduced significant changes to the electrical infrastructure, which has led to an increased need for automation and monitoring systems. The constant improvement of SCADA systems has allowed for remote operation of power networks and the implementation of state estimation. Engineers require real-time simulation to test new automation and control solutions. To address this [49] highlights the importance of real-time simulation and its role in validating new automation schemes. The use of ETAP real-Time in a SCADA system facilitates the implementation of state estimation which describes the development of an equivalent model for network emulation.

In [50], an electrical model of a 1240 MW combined cycle power plant (CCPP) is discussed using ETAP and performed LFA, voltage stability, and short circuit analyses. The effect of power grid voltage instability on the power plant's system buses were evaluated. Also, LFA with the Newton Raphson algorithm was performed to identify buses operating at under voltage due to power grid voltage instability and improved their voltages based on given voltage constraints that depend on buses' criticality with respect to loads. To improve steady-state voltage stability, on-load tap changers and reactive power compensation was used. Comparison of the results of the short circuit analysis with the short circuit current values experienced by the power plant sources was done. Overall, favourable results was achieved through ETAP for all power system analyses.

Also, in [51] Under-voltage caused by power grid instability is discussed, this can negatively impact the distribution system of the plant, leading to tripping of loads, transmission lines, and other system elements, which can cause a series of outages. Reactive power correction is a commonly used technique to improve voltage stability. The optimal location for reactive power installation is essential in determining the improvement in voltage stability. Reactive compensation installation at "weak" buses can improve overall voltage stability. Also, the goal of short circuit analysis is to determine the magnitude of fault currents at different points in the plant. Electrical equipment in the plant should be capable of handling mechanical, thermal, and heating stresses generated by this fault current. The results of short circuit analysis can be used to determine the short circuit ratings of electrical equipment in the plant.

In [52], importance of SCV is discussed. Where, SVC offers several advantages, including being cheaper, faster in operation, more reliable, and having a higher capacity compared to synchronous condensers. When slow-acting voltage regulators are used with SVC for voltage control, it responds faster than other devices. SVC is widely used in reactive power control, enabling voltage enhancement, improvement in overall efficiency, and voltage stability improvement by varying the firing delay angle of the thyristor. Additionally, SVC can improve power factor simultaneously.

In [53], voltage stability of a CCPP's electrical system under LFA is studied on an ETAP simulation. The power flow and voltage values of all buses in the system are obtained, which can aid in the plant's normal operation. An under-voltage was introduced on the power grid side, and its impact on the system buses is assessed. On-load tap changers and optimal capacitor placement techniques are employed to enhance the voltages of the buses identified as under-voltage buses. Other reactive compensation methods, as well as FACTS devices, can also be incorporated in future research. Symmetrical fault current magnitudes with phase angles are analyzed during the short circuit analysis, and the results are encouraging, as they are comparable to those obtained from the plant resources. These values can be used to design the plant's phases and protective schemes settings. This research work can be beneficial in implementing design modifications in the plant or in situations where buses are overloaded due to poor system maintenance.

One significant application of ETAP analysis is its ability to simulate various types of electrical networks. For example, a methodology for modeling and simulating a power system under normal and faulted conditions using ETAP is presented in [54]. The study demonstrates that ETAP is a powerful tool for simulating various types of power systems, including distribution and transmission networks. One of the key applications of ETAP in industrial plants is its use in modeling and simulating electrical systems. In [54], the authors present an ETAP-based study on the modeling and simulation of an electrical power system in an industrial plant. The study demonstrates that ETAP can accurately model and simulate various electrical systems in industrial plants.

Another application of ETAP analysis is its use in optimizing the performance of power systems. Therefore, in [55] it is presented that an optimization algorithm that uses ETAP to minimize power loss and improve voltage profiles in a power system. The results of the study show that the optimization algorithm is an effective tool for enhancing power system performance. In [55], an optimization algorithm using ETAP is presented for improving the power factor of an industrial plant. The study shows that ETAP can be used to optimize electrical systems in industrial plants to improve the performance.

ETAP analysis is also used in the design and evaluation of renewable energy systems. For example, an ETAP-based study is presented in [56] for evaluating the performance of a SPV system connected to a distribution network. The study shows that ETAP analysis can be used to evaluate the impact of renewable energy sources on power systems. an ETAP-based study is presented for evaluating the performance of a motor control center (MCC) in an industrial plant. The study shows that ETAP analysis can be used to evaluate the impact of electrical systems on the overall performance of industrial plants.

One of the advantages of ETAP analysis is its ability to simulate transient phenomena in power systems. An ETAP-based study presented in [57] demonstrates the effectiveness of the software for simulating voltage sag and swell events in a distribution network, an ETAP-based study is presented for simulating the voltage transients in an industrial plant caused by lightning strikes. The study shows that ETAP

can accurately simulate transient events and can be used to develop effective protection strategies for electrical systems in industrial plants.

However, the limitations of ETAP analysis in industrial plants should also be considered. One of the main limitations is the complexity of the software, which can make it difficult for novice users to operate. Additionally, the accuracy of the simulation results depends on the quality of the input data and assumptions made during the simulation [58]. In conclusion, ETAP analysis is a powerful tool for the design, analysis, and optimization of electrical systems in industrial plants. It has numerous applications and benefits, including its ability to simulate transient events. However, the limitations of the software should be considered, and the accuracy of the simulation results should be verified with real-world data.

1.2.5 Microgrid Concept in Treatment Plants

In [59], the smart grid initiative was discussed, focusing on the integration of SCADA systems to improve the electric utility power infrastructure. The smart grid initiative offers numerous opportunities to enhance efficiency and performance. However, it also presents challenges in ensuring safety, security, and reliability for microgrids, utilities, and consumers. One critical aspect of designing the capabilities of the smart grid is the integration of SCADA systems, which allow utilities to remotely monitor and control network devices to achieve reliability and demand efficiencies. The paper also explores the communication technologies used in smart grids with renewable energy sources.

In [60], a SCADA tool designed for an intelligent microgrid is proposed. This tool provides control over a microgrid that incorporates inverters, batteries, and generators with power meters. The microgrid generates energy through solar panels, a geothermal generator, and a biomass generator, and stores it in batteries. The data collected from these components is displayed on a PC interface. The communication between the components and the application is established using various protocols and standards. The application detects connected devices, reads inverter and power meter values such as power and voltage, and allows for modification of these values, as well as generator speed, through the interface.

In Indonesia, microgrid systems have been increasingly installed in remote and underdeveloped areas to provide electricity. However, most microgrid systems lack remote control and monitoring capabilities, leading to manual and local operation that can result in system unresponsiveness, maintenance difficulties, and shortened asset lifetimes [61]. It aims to improve microgrid systems by implementing remote control and monitoring capabilities through cross-protocol communication and an energy balance control based on automatic frequency reading. To achieve this objective, a SCADA master Station equipped with a HMI was designed to control microgrid system equipment using the Modbus and IEC 60850-5-104 protocols. The experiment results show that the proposed SCADA Master station program successfully carried out telecontrol, tele-information, and telemetering through the two communication protocols. Additionally, the proposed energy balance control interface was successfully implemented through the SCADA system automatically.

Microgrids can be an effective way to provide electricity to remote communities where connecting to the main power grid is not economically feasible. Indigenous towns in La Guajira, Colombia, called Rancherias, are a prime example of such communities. The participation of these communities in microgrid solutions is crucial because the system should be designed to function with minimal external intervention. In [62], an educational tool to introduce the key concepts of microgrids is proposed and also discusses recent advancements in social SCADA systems, which are used to transmit security and operational information to the community.

In [63], a novel AC/DC microgrid configuration that focuses on the electricity-water nexus is discussed. The standalone system consists of a photovoltaic generator, a hybrid fuel cell system, a storage system, and both DC and AC loads. The microgrid's unique feature is its ability to treat waste water, providing an additional source of purified water and cheap hydrogen fuel for the Proton Exchange Membrane Fuel Cell (PEM fuel cell). The Microbial Electrolysis Cell (MEC) generates hydrogen and purified water, enhancing the microgrid's resilience during natural/climate disasters or in remote areas. A dynamic control strategy is proposed for optimal power management during microgrid stand-alone operation. To validate the proposed configuration and control strategy, the AC/DC microgrid is modelled and simulated in MATLAB/Simulink. The system's power balance behaviour is evaluated during

different scenarios. Additionally, a real-time Hardware-In-The-Loop (HIL) based experimental setup with physical power components and a LabVIEW-based control system is designed and tested to confirm the simulation results. Given the natural/climate disasters in recent decades and the availability of abundant waste water supplies in Southeast Texas, the proposed AC/DC microgrid is a feasible solution to increase the power system's resilience.

Investigation of the feasibility of a microgrid powered mainly by renewable energy sources is discussed in [64] to provide electricity for an industrial-scale drinking WTP located in the Netherlands. The study considered both grid-connected and standalone microgrid scenarios, using actual data on wind speed and solar radiation, manufacturer data on technology components, and a flexible demand model based on demand response. The results show that the site has a high potential for renewable energy, which can provide between 70% and 96% of the plant's electricity demand through a combination of SPV and wind power generation. The study also found that onsite wind power potential is particularly high and can meet 82% of the plant's electricity demand without the need for SPV. However, SPV can provide a more balanced supply and can supply electricity when wind production is insufficient. Furthermore, adding SPV also increases the benefits of the demand response strategy. Therefore, the study recommends a solar-wind system combination rather than a wind-only system. A 100% renewable system would require very large battery storage, which is not currently economically feasible.

1.2.6 DG Unit Control in Microgrids

In [65], distributed energy resources (DERs) are discussed, viz. solar and wind power, are typically connected to the load or main grid through a power electronic inverter that helps manage the output voltage and power. These inverters can operate in either grid-connected or autonomous modes. When in grid-connected mode, DERs act as current sources and use a voltage source inverter (VSI) to maintain voltage and frequency stability, ride-through capabilities, and islanding operation. To ensure optimal performance, distributed sources require fast islanding detection to switch between control structures in the two operating modes, which have distinct and

possibly incompatible steady-state dynamics and features [65]. Due to these constraints, the control of distributed generation is a critical aspect of its installation.

The control of output power and load sharing among Distributed Generation (DG) units is commonly accomplished through the use of conventional droop control. This method involves drooping the frequency versus active power and drooping the voltage magnitude versus reactive power. In [66], droop control is applied to the parallel connection of Uninterruptable Power Supply (UPS) systems in both autonomous and grid-connected modes, the real and reactive power management strategies of electronically interfaced DG units using droop control are investigated in the context of a multiple-DG microgrid system. The study employs eigenvalue analysis to examine the microgrid's dynamic behaviuor and select control parameters.

In [67], a droop control strategy is proposed for a single-phase SPV system connected to the grid. This approach eliminates the need for communication between multiple distributed generation (DG) units. The droop coefficient for active power control is designed as a proportional-integral (PI) controller, while the droop coefficient for reactive power control is a proportional gain related to the voltage sag percentage. This helps to regulate the voltage magnitude, particularly in predominantly inductive grids. Therefore, it presents a controller that utilizes supervisory control and communication between DGs in a single-phase inverter-based microgrid system. The controller ensures smooth mode transfer between islanding and grid-tie modes while taking advantage of the fast inverter operation and avoiding large transients.

Moreover, the power-sharing assumption in the traditional droop method is mostly based on an inductive line assumption. However, in low voltage microgrids, the DG units may have different output impedances, and the high line impedance ratio may lead to various impedances, such as resistive or inductive. These differences result in more severe real and reactive power control coupling, leading to reduced system stability. The stability margin of a microgrid can decrease as the droop controller gains are increased, eventually resulting in instability for high values of active power or frequency droop gain [68]. However, it has been observed that stability results depend heavily on microgrid loading conditions and network parameters. Therefore, it considers the effects of droop control gains and microgrid topology while simplifying certain assumptions to reduce computational complexity.

Apart from controlling output power and voltage, microgrid control strategies can also address power quality issues such as voltage unbalance [70]. Voltage unbalance is primarily caused by the utility grid (under grid-connection mode) and the presence of unbalanced loads such as unevenly distributed single-phase loads within the microgrid network. Voltage unbalance can negatively impact equipment like induction motors, power electronic converters, and adjustable speed drives. Accurate power flow analysis is crucial for power system control, protection, and management. However, most of the current research on this topic focuses on large power systems using a positive-sequence representation.

In certain investigations, constant current control mode is employed to manage the output power of distributed generators (DGs) in a grid-connected Microgrid system, ensuring a steady power supply to both the grid and the loads [69]. However, when intentional islanding is needed, the control mode switches to constant voltage mode, and load shedding was done to maintain power balance between the source and the load. Islanding detection is achieved by monitoring the voltage and frequency ranges.

In [70], power synchronization control is used to control a voltage source converter (VSC) connected to a weak grid. This method controls power transfer to the grid directly and does not require current controllers or limitations, and also avoids the use of a phase-locked loop (PLL). The author added a current limitation controller and a PLL for synchronization in case of emergencies. To reduce complexity and prevent cascading outages from spreading from one system to another, high-voltage DC (HVDC) transmission is introduced in [71] as a viable solution for connecting renewable energy sources to the grid. It is shown that increasing the load angle causes the system's zeros to move closer to the origin, limiting the bandwidth, and requiring a higher DC capacitance value. Power synchronization control uses AC voltage and active power control loops to make the VSC operate like a synchronous machine, which supports weak AC systems.

Some experts have expressed scepticism towards the use of adaptive control for power electronics and systems applications as the estimation of unknown parameters can be unreliable [72]. In [72], current controllers in grid connected mode and voltage controllers in autonomous mode are designed based on the transfer function of the dynamic model of Microgrid. Reference [73] presents a conventional qd-axis current

control strategy for DG units in grid connected mode, while in autonomous mode, the control system switches to voltage control with an internal oscillator to determine the voltage magnitude and frequency of the system. Furthermore, [74] aims to ensure seamless transfer of the Microgrid between grid connected mode and autonomous mode. The current controller forces the current to zero with a short transient, while the voltage controller maintains the voltage after the transition.

1.2.7 Autonomous Microgrid System Operation

In islanded or autonomous mode, microgrids are typically operated using droop control to ensure power is shared appropriately among DERs while maintaining regulation of voltage and frequency by one or more DERs. This requires continuous control of active and reactive power output for each droop-controlled DER to keep the microgrid's frequency and voltage within acceptable limits, ensuring system stability [75]. Additionally, each microgrid is connected to a common power exchange link through its interlinking converter, enabling power exchange with other microgrids in the event of power deficiency or over-generation. Each microgrid can operate independently at any predetermined frequency and voltage level without disrupting the operation of neighbouring microgrids.

A microgrid can be supervised and monitored by a microgrid central controller (MGCC), which responds to voltage and frequency deviations [76]. The MGCC has slower dynamics compared to the local controllers. Some authors propose analytical approaches to determine the set-points for droop parameters to regulate the voltage and frequency of the microgrid within acceptable limits. In other approaches, the droop coefficients of the DERs are optimized by the MGCC based on the load demand to minimize fuel cost and power loss [77]. Other solutions to address voltage and frequency problems in microgrids include charging and discharging BESs, load-shedding, demand response, curtailment of renewable sources, and provisional coupling of neighbouring microgrids or a utility feeder, if available.

Overloading occurs when the microgrid's generation capability is temporarily insufficient compared to its total demand, and load-shedding is typically used to address this issue and restore voltage and frequency to acceptable levels. On the other hand, over-generation occurs when the microgrid experiences excessive generation

and an excess of power through one or more of its non-dispatchable DERs [78]. Curtailing renewable energy resources is a possible solution to address over-generation conditions. However, both load-shedding and curtailing renewable sources are considered uneconomical, as they can reduce the system's reliability and resiliency.

Proper planning based on risk assessment can prevent overloading and over-generation scenarios in microgrids. One approach is to overdesign and oversize the distributed generators (DGs) or use large-scale energy storage systems to mitigate voltage and frequency issues. However, this can result in high installation and operational costs. Another proposed approach is to interconnect neighbouring autonomous microgrids during such situations to support each other and ensure system stability. This system of interconnected autonomous microgrids is called coupled microgrids (CMGs) [79]. Connecting microgrids through a physical link can be an effective operational strategy during power deficiencies or surpluses, and forming CMGs can improve system reliability.

1.2.8 Autonomous Microgrids Coupling

The CMG model, which is based on the availability of communication infrastructure and the concept of the power market, has been discussed in reference [80-81]. According to this model, a common power exchange link, such as distribution lines, can be introduced to physically connect the microgrids. The interconnecting link can either be AC or DC. While a direct AC-AC connection between a microgrid and the power exchange line can be easily established through a conventional circuit breaker or interconnecting static switch, it may lead to reduced autonomy in the operations of neighbouring microgrids [82]. This is because each microgrid may have a unique structure and control mechanism. Therefore, a power electronic converter-based interlinking structure is preferred. This allows every microgrid to function independently and autonomously while also facilitating power exchange with neighbouring microgrids [83].

The sharing of power between two islanded microgrids during mutual contingency is the subject of a study conducted in [84]. Meanwhile, an autonomous control approach to power sharing with neighbouring microgrids through a back-to-back converter in the presence of a utility grid is proposed in [85]. Interconnecting

neighbouring microgrids can support each other in case of faults leading to a section outage or during normal conditions to minimize the levelized cost of electricity.

An approach based on optimization is developed in [86] to enable efficient power exchange between microgrids. Another approach proposed in [87] utilizes decision-making to determine the most appropriate microgrid(s) to connect to an overloaded microgrid, based on various factors such as surplus power availability, electricity cost, reliability, and proximity of neighbouring microgrids, as well as voltage/frequency deviation in the Coupled Microgrids. The goal is to allow a microgrid to connect to any other microgrid, even if it is not adjacent, via a power exchange highway [88]. The main purpose of this connection is to enable power exchange while maintaining isolation between microgrids, allowing microgrids with different operational regulations to exchange power through dc-links in back-to-back converters [89]. A single-phase ac power line can be used to establish such an interconnecting link, reducing costs while still meeting power transfer requirements during overloading and/or overgeneration. Coordination between converters and control techniques will be complex to couple multiple microgrids, requiring 2N converters to interconnect N microgrids and a common interlinking link that operates at a predefined frequency and voltage [90]. A communication network is also necessary to synchronize microgrids for power exchange, which requires a suitable data communication link.

As a result, it has been found that deploying a dc-link for interconnecting microgrids is a more efficient and practical approach. In this topology, only one converter is required to connect each microgrid to the dc power exchange link, which makes it more cost-effective than the two previous ac topologies that require more power electronic converters. Although the power loss in dc interconnecting lines is lower, most of the commercial power line infrastructure, equipment, and accessories are based on ac systems. Efficient coordination and management of power transactions between microgrids using VSCs and transmission lines present significant challenges. To realize such operations, three different structures for CMG formation and control principles for converters are discussed [91]. It is essential to ensure the stability of the CMG network since interconnections between microgrid networks may result in system oscillations that could cause the entire network to shut down due to instability.

1.2.9 Coupled Microgrid Stability

Before forming a coupled microgrid network, it is crucial to ensure the stability of the system. One approach is eigenvalue-based small signal stability analysis, as proposed in [92]. In addition, [93] recommends evaluating the number of inertial and non-inertial DGs, their ratings, and loads to ensure stability. Reference [94] investigates the influence of the number of microgrids and the length and X/R ratio of lines on stability. Prior to any transformation in the architecture of the CMG, [95] suggests a decision-making function and small signal stability evaluation.

If properly designed, it is shown that the eigenvalue loci of the new CMG network are approximately within the same operating point eigenvalues of each microgrid when operating independently [96]. Moreover, [97] has performed a sensitivity analysis along with stability analysis and has revealed that microgrids with smaller stability margins may cause a drop in the overall system stability margins of other microgrids after they are coupled.

The stability of a coupled microgrid can be significantly affected by the nominal power of DERs, but not by the load demand or power factor. The length and X/R ratio of microgrid lines can also impact stability, while loop or radial configuration does not seem to have any effect. Developing a general stability guideline for CMGs is challenging since its operation depends on various system conditions. Monte Carlo simulations have been employed in some studies to evaluate the network characteristics and topology that affect the small-signal stability of converter-dominated microgrids [98]. It was found that simple radial topologies are more stable, but they reduce network reliability and resilience to faults. As the network becomes more meshed, the stability decreases.

Therefore, it is advisable to keep the topology simple and operate the CMG in a ring configuration with a tie-open point. The research suggests that connecting two adjacent converters with a low-impedance line can negatively impact the stability margin of the system. Therefore, it is advisable to establish enough electrical decoupling or isolation between adjacent converters to prevent unstable interactions. Moreover, the length of lines connecting adjacent microgrids can affect the stability margins of the CMG, according to [99]. The optimal and most resilient topology for forming the CMG can be selected based on stability studies.

In situations where the distance between microgrids is significant, a dc interconnecting link is a more suitable option due to its lower cost and less complex protection scheme. However, as the distance between microgrids increases, the power-sharing based on droop control can deteriorate and eventually disappear, and the performance of the microgrid network can become sluggish due to the increased line resistance. Additionally, unequal line resistances can result in circulating current within the microgrid network. While some techniques have been proposed to address these issues, such as those discussed in [100], they may not perform as well as the ac droop control technique.

To address these research gaps, [101] proposed a fully decentralized approach to address over-generation and overload problems by coupling neighboring microgrids using one of the three topologies mentioned above. This approach does not require any data communication between the microgrids or their controllers, operating solely on local measurements at the point of common coupling, which eliminates the need and cost of communication infrastructure. This enhances the resilience and self-healing capability of each microgrid while ensuring individual autonomy and the ability to operate at any frequency and voltage level. Furthermore, this approach is fully scalable, allowing it to couple any number of autonomous microgrids.

1.2.10. Optimization and Control of Microgrid

In [102], a study proposing a grey wolf optimization (GWO) approach-based proportional Integral derivative (PID) controller is proposed for load frequency control (LFC) of stand-alone microgrid and multi-microgrids with renewable energy sources connected via tie-line systems. The GWO was utilized to generate optimal gains of the PID controller for dynamic stability of the system under various disturbances, including step load perturbations, sporadic RES integration such as wind and solar power, and parametric uncertainty of the system. Simulation results demonstrated the efficacy and robustness of the proposed GWO controller in stabilizing system frequency and tie-line flow under various perturbations. The performance of the proposed controller was compared with conventional PID, particle swarm optimization (PSO)-PID, and TLBO-PID controllers in terms of settling time, peak

overshoot/undershoot, and other metrics. The results validated the potential benefits of the proposed controller.

In [103], a novel approach for coordinated frequency control of an Interconnected microgrid system (ImGS) is proposed which comprises solar tower (ST), Archimedes wave energy conversion (AWEC), geothermal energy conversion (GEC), biodiesel driven generator (BDDG), energy storage (ES) units, and direct current (DC) links. The approach employs independent three-area interconnected systems, and proportional–fractional-order integral derivative (PFOID) controllers with optimal gains obtained using a butterfly optimization algorithm (BOA) and system participation factors. The results demonstrated the superiority of the BOA-based PFOID controllers. Furthermore, rigorous sensitivity analysis was conducted to evaluate the superiority of the BOA-optimized PFOID controller in preserving system stability of the ImGS under different loading conditions and synchronizing tie-line coefficients with ±25% change and bias values with +20% change without resetting nominal condition gain values.

In [104], the effects of tie-line power between conventional power sources and renewable energy systems on frequency deviations is discussed. They proposed an optimal control method for minimizing tie-line power in a way that reduces frequency and tie-line power errors while maintaining a balance between generation and load. This active power and frequency control approach, which included energy storage as an integral part of the renewable energy system, is commonly referred to as LFC. The researchers implemented the proposed system using Matlab Simulink and conducted simulations to evaluate its performance under changing load conditions. The results showed that the energy storage system applied to optimal control had a quick response to frequency deviation, achieving a response rate of nearly 80%.

Also, in [105], a robust type-II fuzzy PID controller for secondary frequency control in an islanded AC microgrid system is proposed, which maintains the nominal values of both frequency and tie-line power under different uncertainties. The performance of the proposed controller was compared with type-I fuzzy controller, a PID controller, and a PI controller. meta-heuristic improved-salp swarm optimization (I-SSO) algorithm was adapted and compared its performance with those of the original SSO, particle swarm optimization (PSO), and genetic algorithm (GA)

techniques. The analysis showed that the proposed I-SSO tuned type-II fuzzy controller exhibited superior performance for LFC in a multi-area islanded AC microgrid system under different uncertainty conditions.

A new method based on Harris Hawks Optimizer (HHO) to optimize the parameters of the Proportional-Integral (PI) controller used for LFC in a multi-interconnected system with renewable energy sources (RESs) is discussed in [106]. They used the integral time absolute error (ITAE) of the frequency and tie-line power as the objective function during the optimization process. The effectiveness of the proposed approach was evaluated under different load disturbance scenarios, and the results were compared with those obtained using other optimization algorithms as well as the traditional controller. Sensitivity analysis was also conducted by changing the system parameters within a range of 10%, and the performance of the HHO-LFC was evaluated. The authors concluded that their proposed approach based on HHO is reliable and superior in designing LFC for multi-interconnected systems with renewable energy sources.

In [107] an ANFIS-based control system for a microgrid is proposed with renewable energy sources such as solar and wind power. The system is designed to optimize the microgrid operation and improve its power quality. The authors utilized a fuzzy logic controller to generate control signals, and ANFIS was used to tune the controller parameters. Simulation results showed that the proposed system can effectively regulate the power flow and enhance the stability of the microgrid.

Also, in [108] an ANFIS-based control system for a microgrid that integrates renewable energy sources and energy storage devices. The system aims to minimize the energy cost and improve the microgrid's stability. The authors used an ANFIS-based controller to regulate the power flow and optimize the energy management of the microgrid. Simulation results demonstrated that the proposed system can reduce the energy cost and enhance the reliability of the microgrid. Also, [109] proposed an ANFIS-based energy management system for a microgrid with renewable energy sources like solar and wind power. The system is designed to optimize energy consumption and reduce the carbon footprint. The authors used an ANFIS-based controller to regulate the power flow and manage energy storage devices. The

simulation results showed that the proposed system can effectively reduce energy consumption and improve the microgrid's environmental sustainability.

In [110], an ANFIS-based energy management system for a microgrid is discussed that integrates renewable energy sources and energy storage devices. The system is designed to minimize the energy cost and improve the microgrid's reliability. The authors used an ANFIS-based controller to regulate the power flow and manage the energy storage devices. Simulation results demonstrated that the proposed system can effectively reduce the energy cost and enhance the microgrid's reliability.

To mitigate the adverse effects of unpredictable variations in renewable energy sources (RES), several control concepts have been proposed in the literature. In [111], the autonomous mode of AC-microgrid is focused and proposes an ANFIS scheduled PID controller to handle sudden changes in load and wind speed variation. The study also presents a comparative performance analysis of the proposed controller. The simulations were conducted using MATLAB and the results demonstrate that the ANFIS-PID controller exhibits less oscillatory behaviour. In [112], an ANFIS-based power control system for a microgrid is proposed with renewable energy sources such as solar and wind power. The system aims to regulate the power flow and improve the microgrid's power quality. The authors used an ANFIS-based controller to generate the control signals, and the simulation results showed that the proposed system can effectively regulate the power flow and enhance the power quality of the microgrid.

1.3. Summary and Motivation

In this section, we have reviewed several control techniques proposed in the literature to address WTP related topics, ETAP analysis, multi area microgrid system including operation of ANFIS based microgrid system has been studied. Various issues such as Stability including overloading and excessive generation in autonomous microgrids were also the focus of the literature. Moreover, gap in consideration of microgrid based WTP and gaps in the topic related research can be seen in most of the literature as shown in the above topics. Furthermore, several proposed techniques to address these gaps were also highlighted.

Based on the above literature review, WTP of Aizawl, India has been selected as a suitable site for consideration of the study system and based on the findings appropriate

control mechanisms has been developed in Simulink environment that are introduced and discussed in the remaining chapters. These methods aim to alleviate the stability, control and excessive generation in multi area microgrid system with the consideration of the proposed WTP, leading to improved voltage and frequency quality through droop control and various optimization method, Also, coordination of power-sharing within various DERs such as Solar, Wind, Small hydro, Diesel engine generator and local battery energy storage system (BES). The proposed techniques overcome the limitations of existing similar techniques in the literature and are more generalized, allowing for consideration of self-sufficient WTP based microgrid system in future.

1.4 Scope of the Study

1.   Most of the existing literature and studies in the field of WTPs primarily concentrate on WWTPs and improvements related to water quality and quantity in the treatment process. However, research specifically addressing conventional WTPs, particularly those employing SCADA-based systems with a focus on self-energy sufficiency, is scarce. As a result, the concept of microgrid-based WTP has emerged as a potential game changer in the current scenario, with the potential for significant improvements in the efficiency and sustainability of water treatment processes.

2.   Several studies have highlighted the potential of SCADA systems in the field of supervisory monitoring and control for various treatment plants and industries. These studies suggest that SCADA can be effectively utilized to enhance system efficiency. Hence, conducting research on the implementation of SCADA systems in existing WTPs could be valuable in improving the quality and quantity of treatment parameters. Furthermore, such research could also provide insights and opportunities for future advancements in this area.

3.   Various literature shows that, there is ample opportunity to integrate various renewable energy sources, such as solar, wind, and hydro, into existing WTPs to optimize power flow, improve efficiency, and minimize energy consumption costs. However, a thorough feasibility analysis is crucial to accurately assess the cost constraints and technical barriers associated with implementing renewable energy sources in WTPs. Therefore, conducting a comprehensive feasibility study of the

existing system is essential to determine the viability of such initiatives, considering both cost implications and technical considerations.

4. Several analyses and studies conducted using ETAP, a widely used Electrical Transient and Analysis Program, have shown its potential in evaluating and forecasting the performance of existing treatment plants. Such analyses can be instrumental in identifying areas for improvement in the existing system, as well as in the proposed microgrid system for WTPs. By leveraging the capabilities of ETAP, valuable insights can be gained to optimize system performance and enhance the efficiency of water treatment processes.

5. Although there is a significant body of research exploring the potential of microgrid systems to improve system performance by incorporating various renewable energy sources (RES), there is a noticeable gap in analyzing existing systems using the microgrid concept. Therefore, conducting an analysis that considers existing WTPs as multi-area microgrid systems has the potential to bring about significant improvements in the treatment industry. Such an analysis could provide valuable insights on how microgrid technologies can be applied to optimize the energy management and overall performance of water treatment processes.

6. Many research studies have highlighted the positive outcomes of utilizing droop control with state-of-the-art optimization techniques and AI-based systems to enhance system parameters, such as active power-frequency (P-f) and reactive power-voltage (Q-V). Therefore, conducting real-time tests of implementing droop control using AI, such as ANFIS, specifically in the intake process of a WTP, can provide valuable insights into the performance of such advanced control schemes compared to conventional control approaches. This analysis could shed light on the potential benefits of using AI-based droop control in WTPs.

7. Several studies in the literature highlight the critical importance of LFC in regulating multi-area/interconnected power systems to mitigate undesirable oscillations. While various optimization techniques and controllers, such as conventional controllers, fractional order controllers, and cascaded controllers, are commonly employed in LFC, there remains a significant gap in addressing the challenges of LFC in conventional systems, particularly when considering existing plants, such as WTPs, that may require cascaded and higher degree controllers for

effective control. Therefore, consideration of higher degree controller in the existing system is important.

8. In the context of LFC, different algorithms are commonly employed for optimizing the gains and other associated parameters of controllers. However, the potential of utilizing the Enhanced Harris Hawks optimization technique in the context of multi-area Microgrid systems is yet to be explored to determine its effectiveness in comparison with conventional optimization techniques.

1.5. Research Objectives

The primary goal of the research is to investigate the existing WTP and propose a microgrid concept as well as develop operational and control techniques for power exchange among interconnected microgrids, accounting for the uncertainties associated with renewable energy sources and loads. Several control structures and optimization techniques have been proposed to ensure efficient operation of the microgrid cluster under any unexpected changes in these uncertain quantities.

The key objectives of the research work are as follows:

1. To investigate the nature, system and functioning of existing WTP in Aizawl, India. And to analyse existing SCADA operations and its schemes for water monitoring as well as optimum operational control.

2. To explore the feasibility and upgrade the power system of the existing WTP by integrating a microgrid system based on renewable energy sources (RESs).

3. To investigate and analyse the existing WTP through various scenarios, including with and without a microgrid system, and implementing relay coordination and discrimination, LFA, short circuit analysis.

4. To design and implement a microgrid system consisting of wind, solar, and battery-based sources for the study WTP system and develop control schemes to enhance its dynamic performance under different operating conditions.

5. To perform LFC of the multi-area microgrid system incorporated with SPV, wind, small hydro power plant, biodiesel, etc., serving the WTP.

1.6 Organization of Thesis

The organization of the thesis is outlined as follows:

Chapter 1. This chapter gives a brief introduction to the body of the thesis, it includes

the relevant literature survey such as relating to WTP, SCADA system and various analysis using ETAP and optimization as well as control schemes considering microgrid system. The key outline and objectives of the thesis are also discussed in this chapter.

Chapter 2. this chapter focuses on the study of existing WTP in Aizawl, India, tackling the whole operation and process flow as well as operation and functions of SCADA system, feasibility study of various renewable energy sources and analysis of operation cost etc. concluded and focussing on implementation of Microgrid system considering on water treatment based multi area system.

Chapter 3. In this chapter, monitoring using SCADA system study of Intake, as well as improvement of basic treatment operations using implementation of ladder logic is done in the study existing system. This brings improvement in filtration process by implementing logic for monitoring and automation algorithm as well as pump operation schedule. Showing that SCADA brings improvement in treatment process.

Chapter 4. This chapter presents analysis of existing WTP with and without consideration of Microgrid concepts by implementing various RES's. ETAP analysis focuses on LFA, Relay coordination and discrimination settings as well as Short Circuit Analysis.

Chapter 5. In this chapter, implementation of real time analysis is seen focusing on droop control enhancement by ANFIS. The main focus is consideration of Intake WTP as a model microgrid system by implementing real time data set. The analysis shows comparison of ANFIS with conventional controller claiming that ANFIS shows better performance compare to conventional controllers.

Chapter 6. This chapter deals with multiarea microgrid concept while considering intake, WTP and intermediate Pumping station (IPS) as a model-based multi area microgrid system. The analysis shows LFC based performance comparison of enhanced Harris Hawks optimization vs conventional optimization technique. Moreover, implementation of higher degree Fractional order controller such as 3DOF-FOPIDN and 3DOF-TIDN controllers is seen, the analysis shows the superiority of 3DOF-FOPIDN controller in terms of LFC analysis.

Chapter 7. This chapter concludes the research work and highlights the scope of future works relating to the current scenario.

CHAPTER

2

Study and Analysis of SCADA based Water Treatment Plant

2.1. Introduction

Mizoram is the 23rd state of the Indian Union, located in Northeast India, with Aizawl as its seat of government and capital city. Even though officially established on 25th February 1890, provision of adequate water supply remains an enormous challenge for Aizawl, as the city is located on the top of a hill at 1132m from mean sea level. Being situated on top of a hill, pumping of water is inevitable. The first organized water supply project namely, Greater Aizawl Water Supply Scheme Phase-I (GAWSS p-I) was started in the year 1983 under the initiatives of Public Health Engineering Department (PHED). The project aimed at production of 10.8 Million Liter per Day (MLD) of treated water from River Tlawng located at 12 km and pumping to a height of 1080m in the city. The scheme was commissioned in 1988 [113], This water supply scheme of phase I consists of four major components :(1) Intake Pump House near Tlawng river, (2) WTP with clear water pump house, (3) IPS at Lawipu & (4) Clear Water Reservoir at Tuikhuahtlang. As the population of the city had already exceeded the designed capacity as the original designed population of 1,60,000 souls was trimmed down to 80,000 souls when it was sanctioned. The GAWSS P-II was started in 2007 to provide additional 24 MLD of treated water to bridge the demand and also to cover the fringe areas left out in Phase-I. The scheme was commissioned in 2012 [114]. The water supply scheme of phase II consists of the following components (1) Phase II raw I with pre settling tank at Tlawng, (2) Phase II raw II at Tlawng, (3) WTP at Dihmunzawl with clear water pump house and (4) main reservoir at Tuikhuahtlang.

SCADA system was implemented in the existing WTP (GAWSS p-I&II) in 2019 generally for monitoring and improving the plant efficiency. Data such as Water quality (using pH, turbidity and chlorine analyser) and water quantity at each pumping stations (using electromagnetic flowmeter and ultrasonic level and pressure analyser) are collected continuously through PLC and continuous monitoring of energy consumption using digital energy meter is done online from the central SCADA station. The required Power Supply for GAWSS P-I&II is tapped from Power and Electricity (P&E) Department under 132 kV level and further stepped down to 33/11/0.415 kV by using Power Transformers at various locations. The power supply network consists 4.3 km span of 132 kV Single circuit Tower type Transmission line from sending end i.e. P&E department and 2.8 km span of 33 kV pole type distribution span from receiving end to various pumping stations.

As the population rapidly expanded in Aizawl area, the water supply level from GAWSS P - I & II became 75 Litres per person (capita) per day (lpcd) only. Therefore, Greater Aizawl water supply schemes phase III (GAWSS P-III) was implemented in the year 2018 with a capacity of 37 MLD to overcome water supply issues in Aizawl area. GAWSS P-III consists the following components (1) Intake at Tlawng, Setlak (2) WTP at Mualkhang, Tanhril (3) Intermediate Pumping Station at Industrial Growth Center (IGC), Tanhril and (4) Main reservoir at Laipuitlang. GAWSS P- III is equipped with SCADA and similar to phase I&II, the required power supply is provided under P&Ed consisting 5.2 km span of 33 kV Double circuit Tower type transmission line and two numbers of 33/11 kV Substation for further distribution of power supply to various pumping stations within the whole treatment system.

Based on the literature and as per the above data. The objectives of tis chapter are as follows.

1. Study and analysis of the whole utility process of WTP in Aizawl.

2. SCADA based study for realizing the monitoring process through various field instrument.

3. Study of various electrical loads, characteristics and operational cost of the treatment plant.

4. To study various challenges including installation feasibility of renewable energy sources i.e. DERs within WTP.

5. To focus on implementation feasibility of an important concept called as Microgrid based WTP system so as to overcome and minimize various challenges.

2.2. Overview of Greater Aizawl Water Supply System Phase-I and -II

The geographical map of Greater Aizawl Water Supply scheme phase I&II is shown in Figure 2.1. As mentioned earlier Raw water is collected from Tlawng River through intake and further pumped to WTP for filtration and treatment. After cycles of treatment and filtration, the treated water is further pumped to the main reservoir at Tuikhuahtlang for further distribution to the Aizawl city.
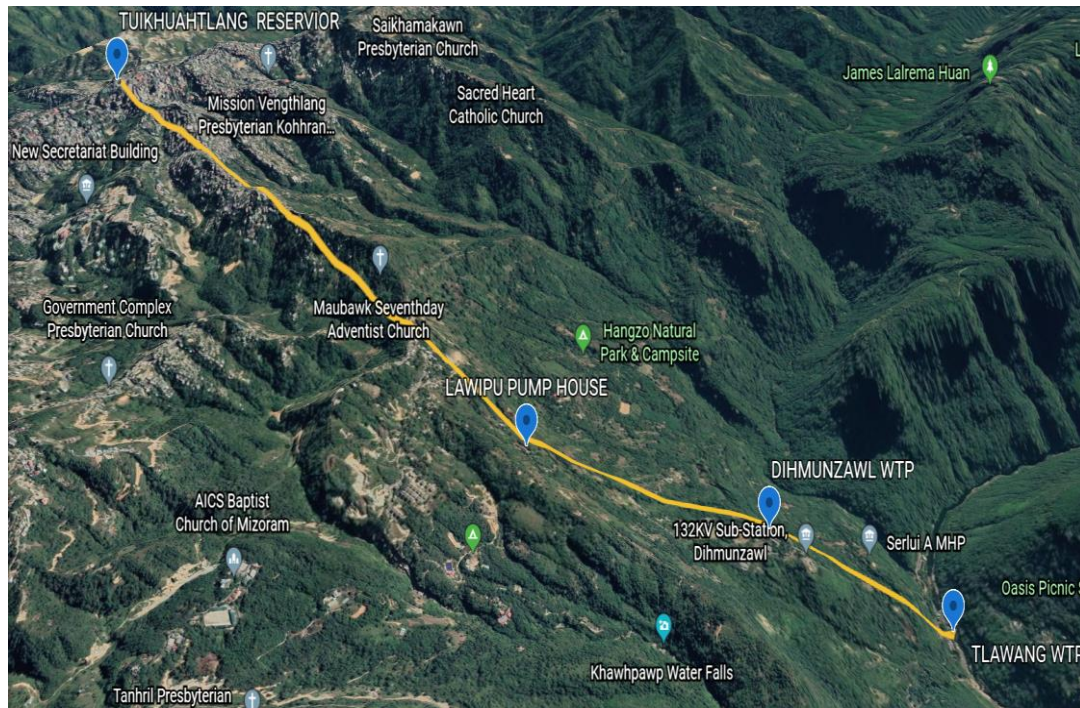
Figure 2.1 Geographical map of GAWSS P-I&II

Based on Figure 2.1, it can be observed that the primary water source for both Phase I and Phase II of the GAWSS is the Tlawng river. Phase I consists of an intake with three Vertical Turbine (VT) pump sets and a Clariflocculator with a capacity of 10.8 MLD. This is followed by the main WTP with a pump house located after the Clear Water sump, which includes Electrical Motor pump sets and Diesel Engine Pump sets. The IPS located at Lawipu, 2.4 km from the pump house, serves as a booster for pumping the water to the main reservoir located at Tuikhuahtlang, which is 4.82 km from IPS at Lawipu. On the other hand, GAWSS P -II includes an intake (phase 2 raw 1) consisting of five submersible pumps located at Tlawng, followed by

a pre-settling tank that serves as the first stage of sludge removal. The raw water pump house no. 2 (phase 2 raw 2) consists of three vertical pump sets, and the main WTP with pump house is located at Dihmunzawl, around 290.42 meters high from the intake (phase 2 raw 1) at Tlawng. The main reservoir is located at Tuikhuahtlang, around 745 meters high from the WTP. In case of power failure, Diesel Generator sets are used as the main source of backup power for each pumping station.

2.3. Different Methodologies Applied for Study of GAWSS Phase I and II

In order to understand the complete nature and working principle of the existing system of GAWSS P-I&II. Different methodologies and approach were applied in the study of GAWSS phase I &II as shown in the following Table 2.1.

Table 2.1. Methodology for study of GAWSS P-I&II

Sl. No.	Methodology/ Approach	Descriptions
1	Site survey:	One of the most important tasks is to physically survey the whole WTP system. A site survey of GAWSS P- I and II involved a series of visits to the sites to understand each of the treatment unit and pumping unit including functioning and role of SCADA monitoring system.
2	Item Inspection/ Verification at site	To know the current situation of each site, an item inspection was carried out to understand the status of the existing equipment, which further helped in understanding individual roles of SCADA monitoring system.
3	Internet Based Research:	A thorough Internet based study was carried out for better understanding of the equipment used and to have an in-depth knowledge of the evolving technology. This study enables us in rationalizing the best practice and methods of the whole system
4	Consultation with experts and PHED officials	Several discussions was made in consultation with experts, field staffs and PHED officials. This enables us to collect history, common practice, existing data and challenges in complete relating to the study system, it is important that the concerned Department is consulted, in each and every approach of the study.

2.4. Necessity of SCADA System

The implementation of SCADA systems for WTPs and Water Supply systems aims to optimize plant processes, maintain water quality, and reduce water losses. With the use of modern technologies like SCADA or IoT, many WTPs are now operated and

maintained automatically, resulting in improved efficiency and productivity. In the past, most of the WTPs in Mizoram, India did not have SCADA systems for monitoring and controlling water supply systems. Therefore, the PHE department undertook improvement and upgradation efforts by implementing real-time control and monitoring through SCADA systems. Based on earlier observations, the need for SCADA systems in existing WTP systems was affirmed.

1.   GAWSS P- I, located at Lawipu and Tlawng, has shown signs of wear and tear over the years, with pipes and pumps that are outdated and equipment that is no longer functional.

2.   The equipment in GAWSS P-I requires replacement or upgrading, as some of it has become non-operational.

3.   GAWSS P-II, located at Dihmunzawl and Tlawng, although commissioned more recently than GAWSS P-I, has been in operation for 10 years. However, similar to GAWSS P-I, most of its pipes, pumps, and equipment are outdated and operated manually.

4.   The data collected from both these systems may be inaccurate or missing.

5.   Many of the pressure gauges are non-functional and malfunctioning.

6.   Water levels in all pumps are manually measured using a thread, which is highly inaccurate.

7.   Flow meters are not installed in any of the pipelines, and it has been observed that certain lines lack adequate space for the installation of the latest electromagnetic flow meters.

8.   Energy consumption for most of the pumps in GAWSS P-I and GAWSS P-II is not measured, making it impossible to assess the efficiency of the pumps.

9.   pH, level, turbidity, and chlorine level are regularly and manually measured by field staff, but the data collected is imprecise and inconsistent.

10. Most of the data collection is done manually by field staff, with measurements taken at an average interval of every 10 minutes, 24/7, depending on water conditions. The measuring instruments are inaccurate, and the process is time-consuming, posing a challenge for the department due to the significant manpower required.

Therefore, from the above observations SCADA system was implemented in various locations of GAWSS P-I&II as shown in Figure 2.2. The figure shows

complete map of the WTP and various SCADA instrumentation installed at various locations. i.e. from Intake at Tlawng river to main reservoir at Tuilhuahtlang. The central SCADA station located at Dihmunzawl receives all data from various field instruments through PLC and the main purpose of SCADA system is to monitor the quality as well as quantity of various water parameters so as to acquire water management facilities and analysis. Also, Table 2.2 and Table 2.3 show various duties and important monitoring strategies of GAWSS P-I&II SCADA system.
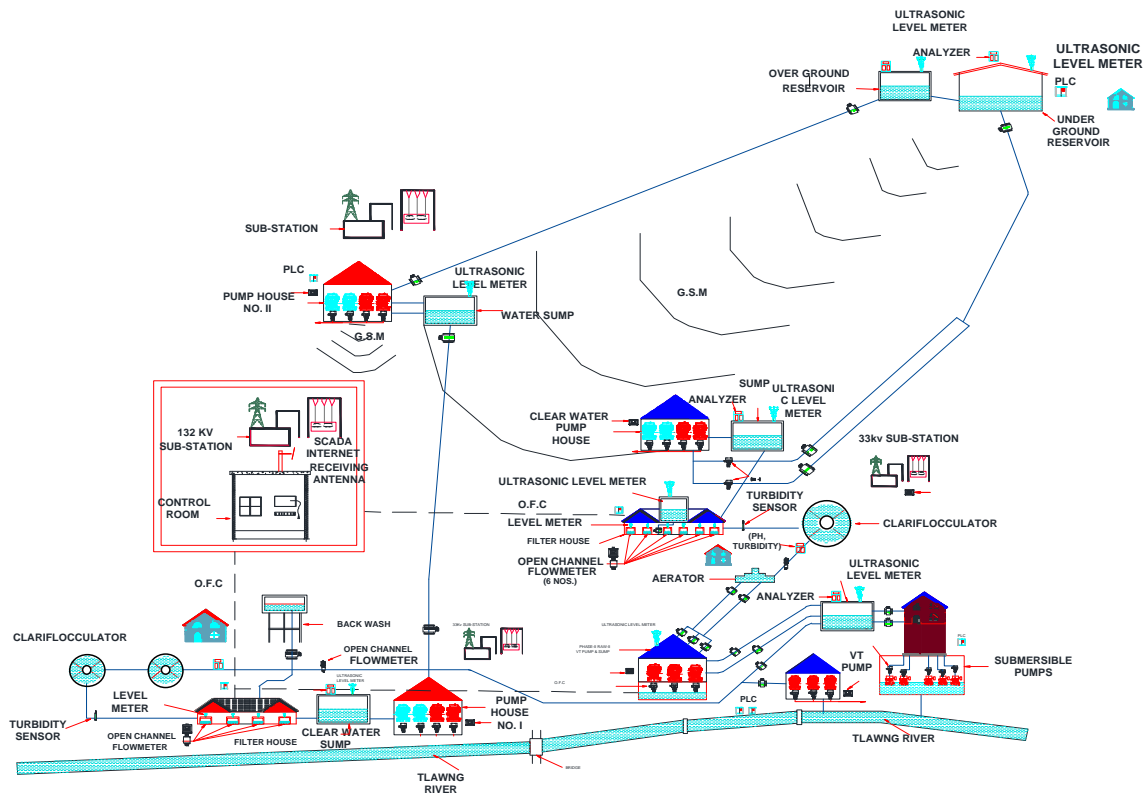
Figure 2.2 Complete map of GAWSS P-I&II

Table 2.2 Important duties of SCADA in various locations of GAWSS P- I

Sl No.	At GAWSS P- I	Monitoring
1	Vertical Turbine at Tlawng for flow	pressure and energy monitoring
2	WTP at Tlawng	pH Analyser, Chlorine Analyser, Turbidity Analyser and Flow Meter
3	Backwash Tank at Tlawng	Flow Meter
4	Clear Water Sump Tank at Tlawng	level monitoring
5	Clear Water Pump at Tlawng	flow, pressure and energy monitoring
6	Pumps at Pump House-II, Lawipu	flow, pressure and energy monitoring
7	Clear Water Sump Tank at Lawipu	level monitoring

Table 2.3 Important duties of SCADA in various locations of GAWSS P- II

Sl. No	At GAWSS P- II	Monitoring / Purpose
1	Pumps at Raw-I at Tlawng	flow, pressure and energy monitoring
2	Pre-settling Tank at Tlawng	Level, Flow monitoring
3	Pumps at Raw-II at Tlawng	flow, pressure and energy monitoring
4	Areator at Dihmunzawl	installation of pH Analyser, Chlorine Analyser and Turbidity Analyser
5	WTP at Dihmunzawl	Flow Meter
6	Backwash Tank at Dihmunzawl	Flow Meter
7	Clear Water Sump Tank at Dihmunzawl	level monitoring, pH Analyser, Chlorine Analyser and Turbidity Analyser
8	Clear water Pump at Dihmunzawl	flow, pressure and energy monitoring
9	Main Reservoir at Tuikhuahtlang	Chlorine, Turbidity, Flow and Level Monitoring
10	PHE Site Office	Monitoring Unit and Central SCADA station/Monitoring Unit

2.5. SCADA System Architecture for GAWSS Phase I and II

The architecture of the SCADA system for the GAWSS P-I and P- II is illustrated in Figure 2.3. The SCADA system comprises of seven stations, each equipped with a PLC, HMI, RTU, Analyzer panel, sensors, and UPS battery backup with an isolation transformer. The central SCADA system, located at Dihmunzawl, serves as the master control and monitoring station, with each location of the SCADA unit interconnected using optical fiber and Global System for Mobile communication (GSM)/General Packet Radio Service (GPRS) devices, as depicted in Figure 2.3.

Various types of sensors, such as Electromagnetic flow meters, Open channel flow meters, and Pressure Transmitters, have been installed at the pipelines and channels to monitor the quantity, pressure, and flow of water. These sensors serve three purposes: monitoring the flow rate, assessing the health of the pipes, and identifying water losses between the outlet of the pump house and delivery at the reservoir. Additionally, Analyzer panels consisting of pH, Turbidity, and Chlorine sensors have been installed at the intake, WTP, and reservoirs to monitor the quality of raw water and treated water. Energy meters have also been installed at each pump house to monitor power consumption and optimize pump scheduling. Furthermore, level detectors have been installed at each reservoir, filter house, including the backwash tank, for effective monitoring.
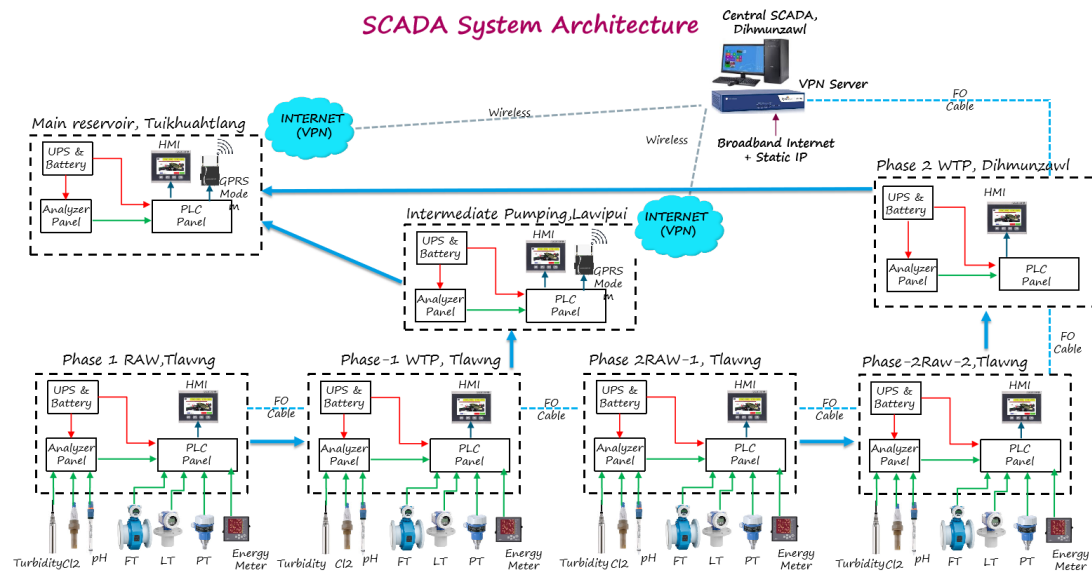
Figure 2.3 SCADA system architecture for GAWSS P- I and P- II.

The following components are installed in SCADA system of GAWSS P-I&II

1. Electromagnetic flow meter -32
2. Open channel flow meter – 20
3. Pressure transmitter - 12
4. pH sensor – 7
5. Level meter - 7
6. Turbidity sensor – 7
7. Chlorine sensor - 4
8. Energy meter – 17
9. Pressure Transmitter - 25
10. PLC with HMI & GSM modem-7
11. SCADA station with PC system -1
12. Optical fibre cable- 3.5 km
13. Online UPS with stabilizer system - 8
14. Internet facilities- 1

The flow meter plays a crucial role in monitoring the flow rate and quantity of water in the pipelines. It serves three key purposes: Flow rate monitoring: The flow meter accurately measures the rate at which water is flowing through the pipelines, providing real-time data on the water flow rate. Health of pipe lines: The flow meter helps in assessing the health of the pipelines by monitoring the flow characteristics. Any abnormalities in the flow rate or pattern can indicate potential issues such as leaks, blockages, or pipe damage, allowing for prompt action to address them. Water loss monitoring: The flow meter helps in tracking water losses between the outlet of the pump house and the delivery point at the reservoir. By measuring the water flow quantity, it enables the identification of any discrepancies or losses in the water supply system, aiding in efficient water management and conservation efforts.

In addition to the flow meter, other essential components of the SCADA system for WTPs and water supply systems include pressure transmitters, pH, turbidity, and chlorine sensors, energy meters, level detectors, PLCs with HMIs and GSM modems for data transfer, UPS with isolation transformers to protect against surges and voltage fluctuations, a main SCADA station with a personal computer and a big screen acting as a master station, optical fiber and GSM modem for communication between PLCs, and internet connectivity for online remote monitoring, troubleshooting, and remote access to the SCADA system.

2.5.1. SCADA System and Display

SCADA system and display of various sites at GAWSS P-I&II is discussed and observed in this section.

2.5.1.1 GAWSS P- I

A. Intake

The intake for Phase I of the GAWSS is situated at Tlawng river. It includes three Vertical Turbine Pumps, each with a power rating of 90 kW. The SCADA system at the intake site is equipped with an Energy meter, Pressure Transmitter, Electromagnetic flow meter, and a PLC panel with HMI for data acquisition and transmission to the main SCADA center located at Dihmunzawl. Optical fiber is used for communication of data between the PLC and the main SCADA center. The SCADA system allows for monitoring of pump scheduling, overall readings, and sensor data, as depicted in Figure 2.4.

B. Water Treatment Plant

WTP of GAWSS is depicted in Figure 2.5. Raw water from the intake is pumped to the WTP for treatment and filtration. The WTP is equipped with an analyzer panel for monitoring raw and treated water quality, open channel flow meter, level meter, electromagnetic flow meter, energy meter, and pressure transmitter. Data communication is facilitated through optical fiber connected to the PLC panel and HMI. Additionally, the SCADA system monitors pump scheduling, backwash scheduling, and overall readings for GAWSS P-I&II
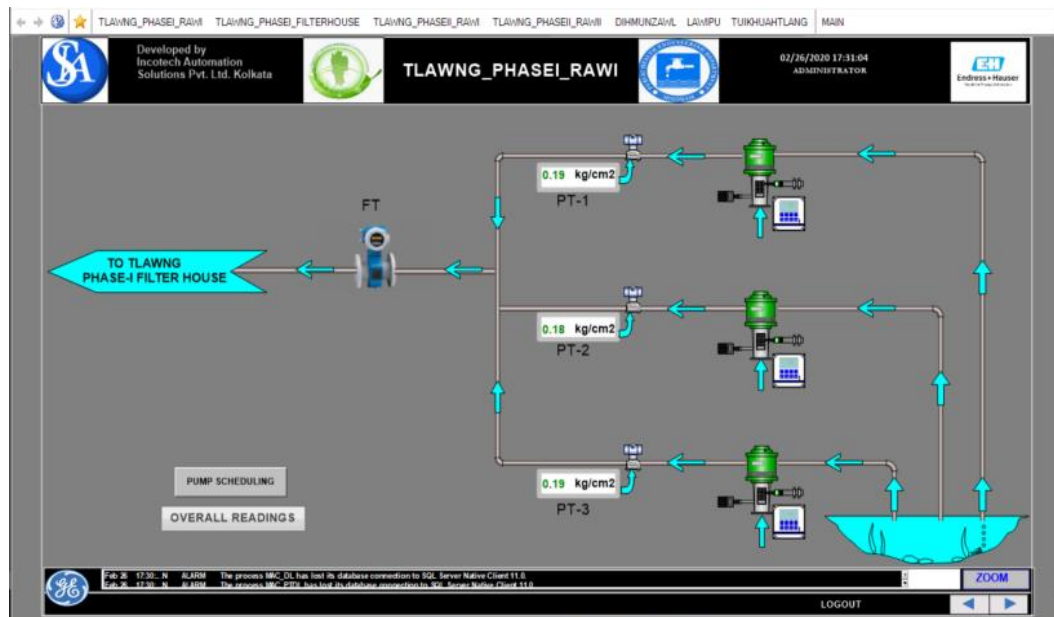
Figure 2.4. SCADA screen of Intake, GAWSS P- I.
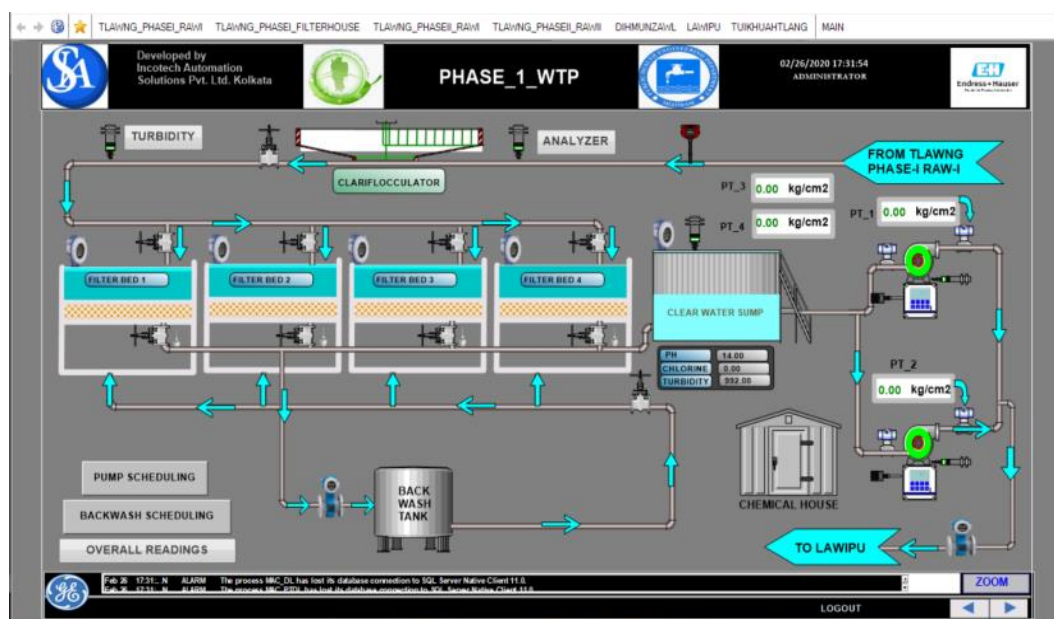
Figure 2.5 SCADA screen WTP, GAWSS P- I

C. Intermediate Pumping Station (IPS)

The IPS located at Lawipu acts as a booster for Phase I of the GAWSS. It receives treated water from the WTP and is equipped with level meters, energy meters, electromagnetic flow meters, and pressure transmitters, as depicted in Figure 2.6. All the data, including pump scheduling, from the IPS is transmitted to the main SCADA center through GPS/GPRS communication. The IPS then pumps the treated water to the main reservoir located at Tuikhuahtlang.
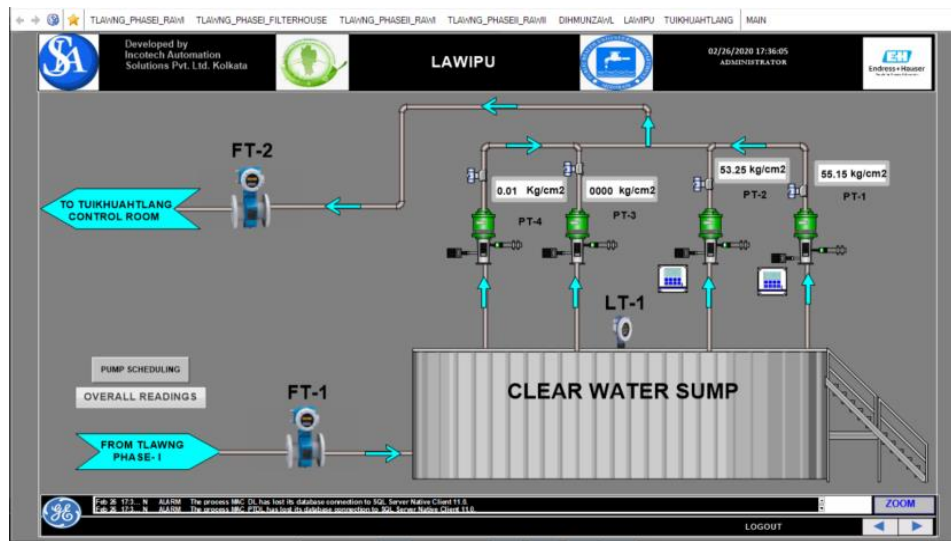
Figure 2.6. SCADA screen IPS, GAWSS P- I

2.5.1.2 GAWSS P- II

SCADA screen and display of various sites at GAWSS P-II is discussed and observed in this section.

A. Intake

The Phase II intake at Tlawng comprises of two pumping stages, referred to as Phase II Raw I and Phase II Raw II.

A.1 Phase II raw I

Phase II Raw I comprise of a set of five submersible pumps that are situated inside a Jack well, as illustrated in Figure 2.7. The raw water sourced from Tlawng river is collected and stored in a pre-settling tank for further analysis of its quality.

Apart from the PLC and HMI, various other instruments have been installed at Phase II raw I, including an energy meter, electromagnetic flow meter, pH analyzer, turbidity analyzer, and level meter. These instruments are used for measuring pump energy consumption and water parameters in the pre-settling tank, which is located just after the pump house. Optical fiber is used as the communication media for transferring data to the main SCADA center. Overall readings and pump scheduling can also be monitored through the screen.

A.2. Phase II raw II

GAWSS P- II raw II consists of a raw water sump and three VT (Vertical Turbine) Pumps. Installed at this station are an energy meter, level meter, flow meter, and PLC

with HMI for collecting pump data and monitoring water parameters. Pump scheduling and overall readings can be viewed on the SCADA screen, similar to other pumping stations. Optical fiber is used for data transfer to the main SCADA center. Figure 2.8 illustrates the SCADA screen of GAWSS P- II raw II. The treated water from Dihmunzawl is then pumped to the main reservoir at Tuikhuahtlang, with optical fiber used as a communication media for data transfer to the main SCADA center through the PLC. Pump scheduling, backwash scheduling, and overall readings can be viewed through the SCADA system, as depicted in figure 2.9.
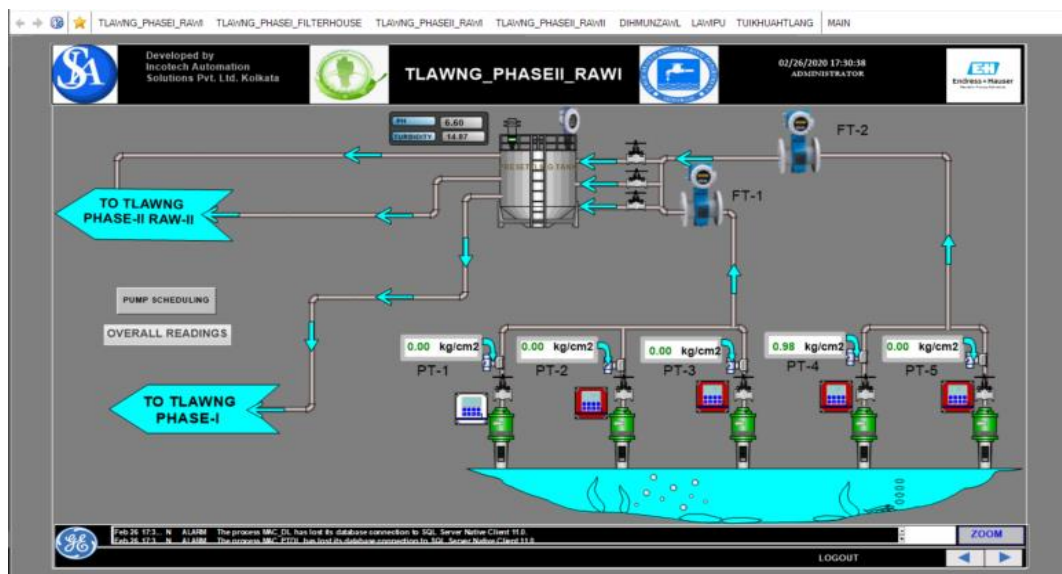
Figure 2.7. SCADA screen, GAWSS P- II raw I
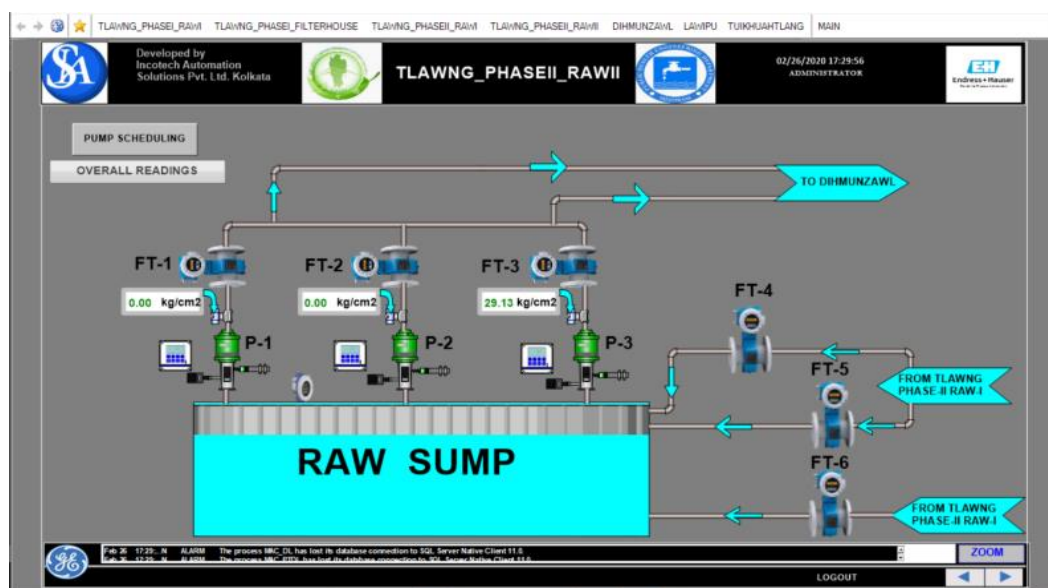
Figure 2.8. SCADA screen, GAWSS P- II raw II

B. Water Treatment Plant

The primary WTP of GAWSS P- II, situated in Dihmunzawl, receives water from the Phase II raw II pumping station, as depicted in Figure 2.9. The raw water undergoes processing through various units, including Aerator, Clariflocculator, Filter House, and Chemical House, before being pumped to the main reservoir at Tuikhuahtlang through the Pump House.
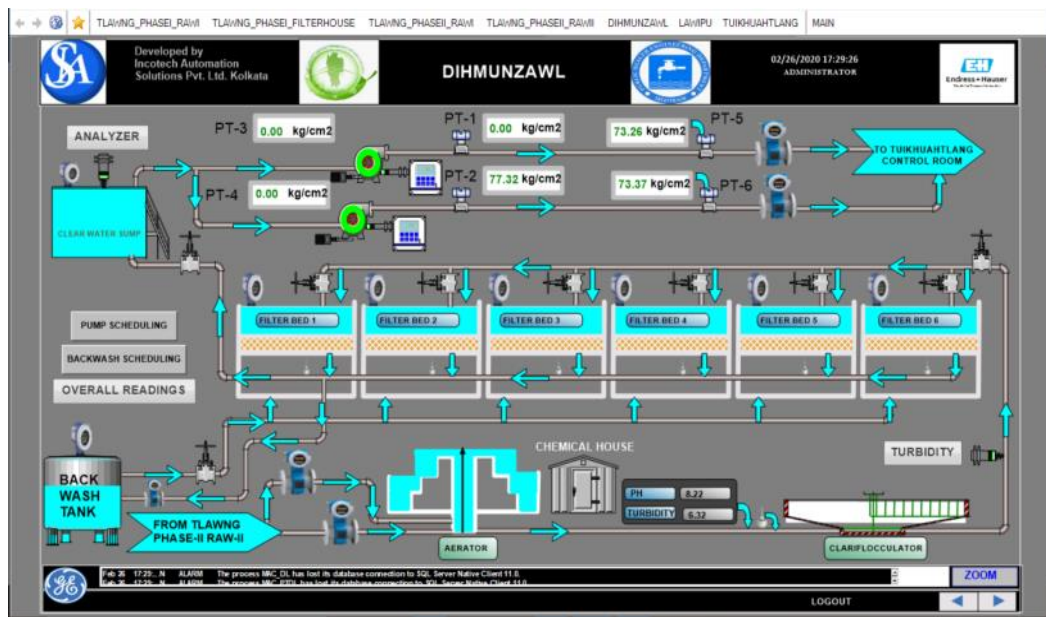
Figure 2.9. SCADA screen, GAWSS P- II WTP

The water parameters, such as Turbidity and pH, are closely monitored at various points in the water treatment process. After the raw water passes through the aerator, a turbidity analyzer is used to measure the quality of the water just after the Clariflocculator. Level meter and open channel flow meter are installed at the filter bed to assess its health and determine optimal backwash scheduling. Energy meter, pressure meter, and electromagnetic flow meter are also installed to monitor pump parameters and flow rate of water from the clear water sump. Additionally, an analyzer device is installed to monitor pH, Turbidity, and chlorine content of the treated water.

C. Reservoir

The main water reservoir at Tuikhuahtlang, which has a static head of 1037.03 meters, comprises two main reservoirs for phase I and phase II. Electromagnetic flow meter, Level meter, and Analyzer panel were installed to measure water quantity, flow rate, and quality. All data are collected and processed through PLC and HMI and

transferred to the main SCADA center at Dihmunzawl through GSM/GPRS, as shown in the figure 2.10.
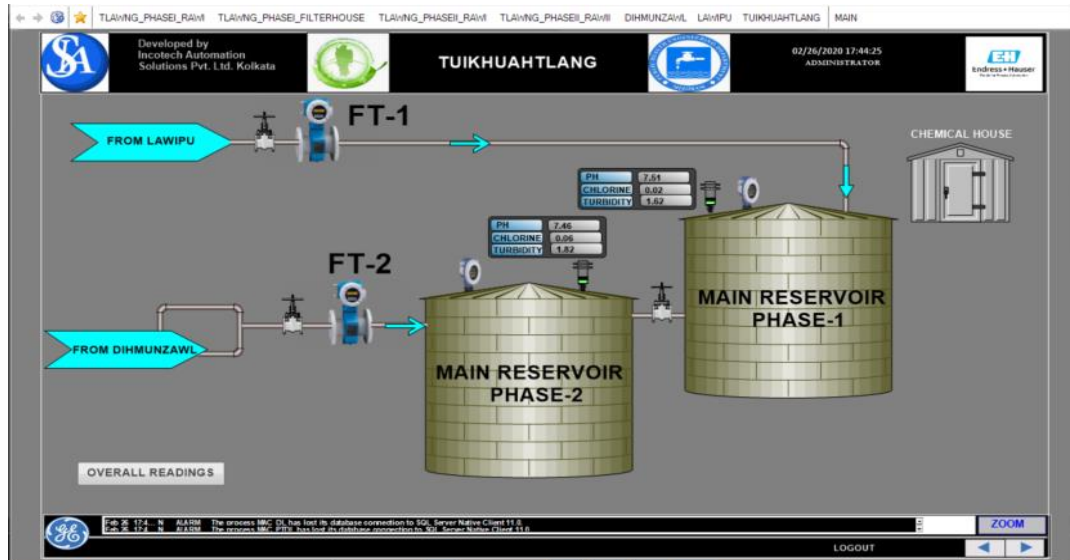
Figure 2.10. SCADA screen, GAWSS P- I & II reservoir

2.6 Power Supply of GAWSS P –I and -II

The power supply for GAWSS P-I&II is sourced from the P&Ed under the government of Mizoram. A dedicated power supply is tapped from the 132 kV Substation at Luangmual (P&E department), which continuously feeds the pumping station through the 132/33 kV Substation at Dihmunzawl operated by the PHE department. The stepped-down power is then distributed through various 33/11 kV or 33/3.3 kV Substations at different pump houses to feed various loads within the WTP.

Table 2.4 Phase-I electrical load details

Sl. No.	Description	Load/Pump Type	Quantity	kW	Operating Voltage
1	Intake	VT pump	3	90	3.3 kV
2	Filter House	Electric motor	2	635	3.3 kV
3	IPS at Lawipu	Electric motor	2	635	3.3 kV
4	LT loads	Light/ fan etc.	-	40	0.415

Details of HT and Law Tension (LT) electrical loads for Phase I&II are provided in Table 2.4 and 2.5, respectively. Additionally, Table 2.6 showcases the details of the installed energy meters for monitoring HT and LT energy consumption. Furthermore, Table 2.7 presents the energy consumption bill for one year (2021-2022) of GAWSS

P-I&II, excluding the diesel generator set filling and operation costs. The table reflects an average energy consumption bill of approximately 55 Crore, excluding arrear and diesel costs.

Table 2.5 Phase-II electrical load details

Sl. No.	Description	Load/Pump Type	Quantity	kW	Operating Voltage
1	Raw I	Submersible pump	5	713	11 kV
2	Raw II	Submersible pumps	3	713	11 kV
3	Filter House, Dihmunzawl	Electrical motor	2	1700	11 kV
4	LT loads	Light/ Fan etc	-	60	0.415 V

Table 2.6 Energy meter details of HT and LT metering

SN	Description	Energy Meter (HT)	Energy Meter (LT)
1	Operating Voltage	11,3.3 and 33 kV	0.415 kV
2	Class	0.2 s	0.2 s
3	Phase	3 p, 3 Wire	3 P, 4 wire
4	Load Survey	kWh, kVA ,pf, V, I, kVAR	kWh, kVA, pf, V, I, kVAR
5	Power Consumption	As per IS 14697 for CT/PT operated	As per IS 14697 for CT/PT operated
6	Watt hour meter	As per IS 13779 for whole current	As per IS 13779 for whole current
7	Communication	RS485, Optical	RS485, Optical

Table 2.7. Approximate energy bill (2021-22) of GAWSS P-I&II

Sl. No.	Month	Average Energy bill (Lakhs)
1	January	477
2	February	475
3	March	463
4	April	552
5	May	541
6	June	554
7	July	487
8	August	519
9	September	404
10	October	472
11	November	476

12	December	54054676
13	Total	549363957.8
14	Approximate	55 crore per year

2.7 Greater Aizawl Water Supply Schemes Phase III

The Greater Aizawl Water Supply Scheme phase III was discussed in the introduction and as per the data presented in Table 2.8, it is projected that the demand for water supply in Aizawl city will face a shortage of 36.43 MLD during the intermediate period of 2033.

Table 2.8. Population & water demand forecast

Year	Population	Water Availability	Water Demand	Deficits
2011	2,93,416	34.8 MLD		
2018(Base Year)	3,39,000	34.8 MLD	54.64 MLD	19.84 MLD
2033 (Intermediate Year)	4,45,000	34.8 MLD	71.22 MLD	36.43 MLD
2048 (Ultimate Year)	5,57,000	71.8 MLD	88.92 MLD	17.12 MLD

The following figure 2.11. shows the complete map of Greater Aizawl Water Supply chemes phase III, Similar to phase I&II. The raw water from Tlawng river is being tapped by a submerged weir and pumped through pump house at intake to the WTP with a capacity to treat 37 million litres per day. The treated water is then lifted to the Main Reservoir at Laipuitlang, located at a static height of 1192m from river Tlawng (RL 49.5m) at a distance of 15.00 kms through 2-pumping stations. The source of water is Tlawng River at about 12 km away from the city. The treatment plant was designed and constructed based on the standard specifications prescribed in "Manual on Water Supply and Treatment Third edition" published by Central Public Health and Environmental Engineering Organization, Ministry of urban Development, New Delhi, May 1999. Components and functions of each of the pumping stations is shown in table 2.9.

Table 2.9. Components and function of P- III at various stages

SN	Components
1	Submersible weir & Intake JackWell at River Tlawng, Raw Water Pumping Plants- 3 Nos Vertical Turbine Pumps each of 887 cum/hr discharge capacity at an operating head of 144 mtr. Prime mover = 11 kV, 550 KW 4 pole Vertical Electric Motor.

2	Conventional treatment Plant consisting of Cascade Aerator, Clarifloculator, Parshall Flume, Rapid Sand Filtration, Flash Mixer, Disinfection by chlorination, bypass arrangement between Clariflocculator and Filter House. And Sludge pit.
3	Chemical House with dosing arrangements and laboratory facilities, Laboratory with necessary instruments and chemicals for water quality test and monitoring.
4	Pre-chlorination and Post-chlorination arrangement with chlorination building and supply and installation of Electro-chlorinator for generating chlorine from common salt
5	Clear water Reservoir of suitable capacity at WTP & IPS (Each 1.58 ML)
6	Pump houses for accommodating Raw & Clear Water Pumps along with all accessories and Electrical system and for Back Wash Water Arrangement, Clear Water Pumping Plants: 4Nos.Horizontal Centrifugal Pumps at WTP & IPS with discharge capacity 802 cum/hr driven by Electric Motor and 4-Nos pumps of 402 cum/hr discharge driven by Diesel Engine at WTP & IPS and operating head of 499 m & 519 m respectively. At WTP & Intermediate Pumping Station Prime mover =11 kV, 1750kW & 1850kW 4 pole motor and 1200 HP diesel engine respectively.
7	Supply and installation of Ultrasonic Flow Transmitter in each delivery main.
8	33/11 kV Power Sub Stations: 3.5 MVA transformers with accessories and with substation equipment at head works, 7.5 MVA transformers with accessories and with substation equipment at WTP and 7.5 MVA transformers at IPS in the city area.
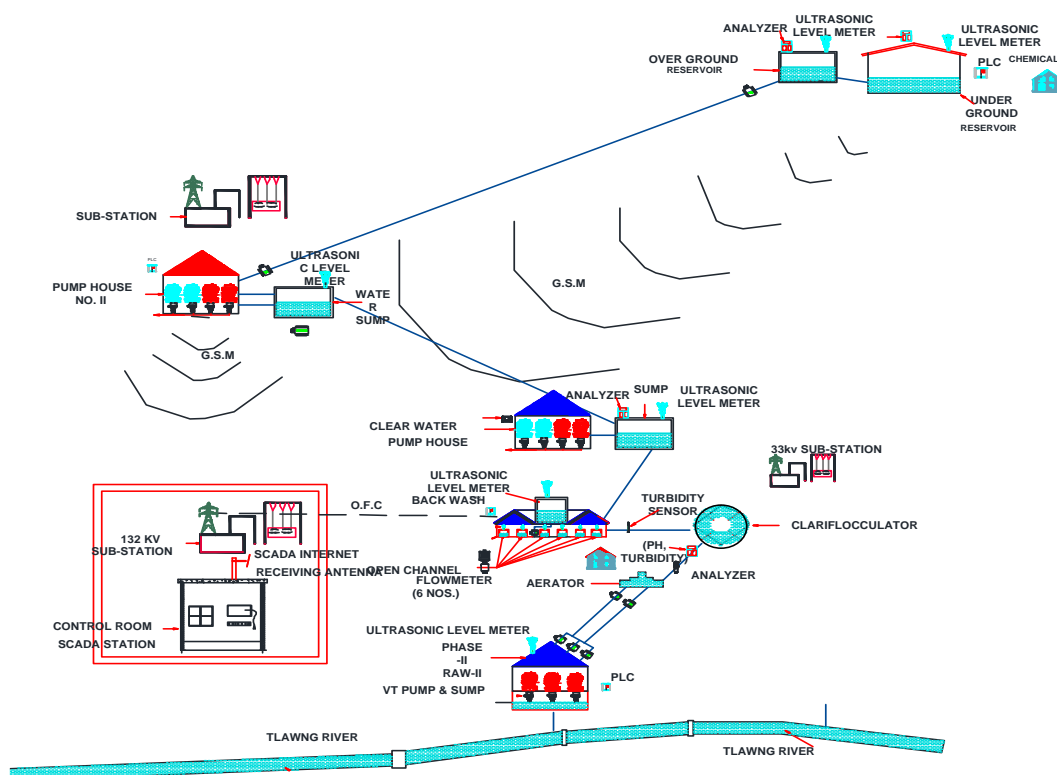
Figure 2.11. Complete map of GAWSS P- III

2.7.1 Process Flow

As shown in the figure 2.11 and 2.12, the raw water is pumped from intake well to cascade aerator for removal of dissolved gases and heavy metals such as iron. After the cascade aerator, PAC (Polly aluminium chlorite) with lime will be dosed at the upstream of the Parshallflume for coagulation purpose. Raw water mixed with lime and PAC will enter into the flash mixers, where coagulation will be achieved with help of flash mixer blades. From flash mixer, the raw water enters clarifloculator, where flocs developed in the central flocculation chamber and gets settled at the bottom of the clarification chamber. Weir plat is installed in the peripheral of launder of the Clarifloculator to collect the overflow i.e the clarified water. The clarified water from Clariflocculator flows through gravity to the filter beds for the removal of remaining suspended solids. The treated water from filter bed is collected in clear water reservoirs for distribution to the users. The Backwash water from filter beds is collected in the back wash recycling sump and is periodically pumped back into raw water channel. The treatment plant comprises of following process units:

Cascade Aerator - 1 No, Parshall Flume channel - 1 No, Chemical House with dosing facilities - 1 No, Flash Mixers - 1 No, Distribution chamber - 1 No, Clarifloculator - 1 No, Rapid Gravity Sand Filters - 10 Nos, Overhead tank - 1 No, Electro Chlorination room - 1 No, Sludge sump - 1 No, Backwash water recycling sump - 1 No, Clear water Reservoir - 1 No, Clear water pump House - 1 No, Substation and DG room - 1 No.
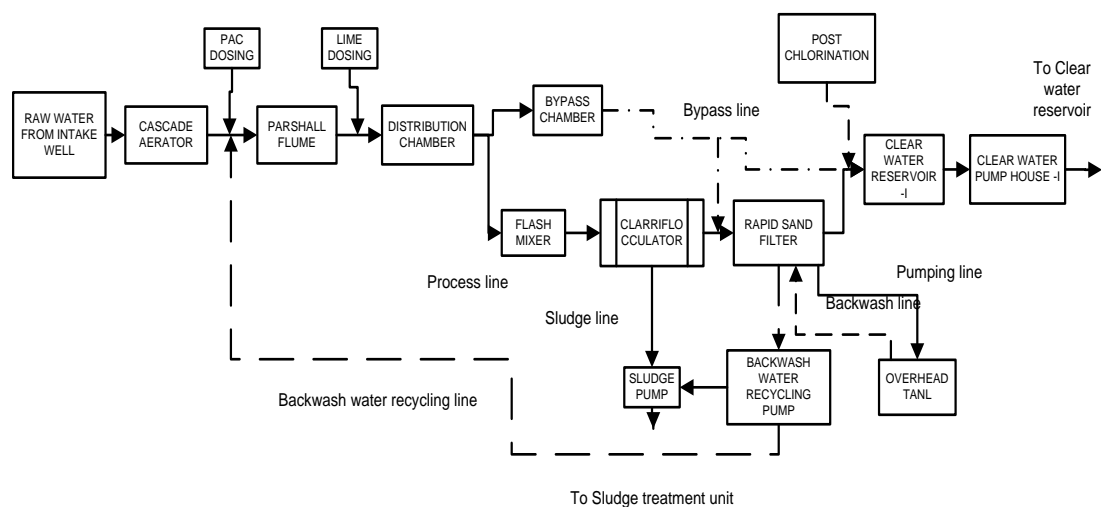
Figure 2.12 Process flow of SCADA in GAWSS P-III

2.7.2 SCADA System of GAWSS P- III

As the monitoring and functions of the overall SCADA system in phase III is almost similar with GAWSS P-I&II, the complete details and process description of SCADA function of GAWSS P-III is not described in this section. However, SCADA screens of phase III is attached in Appendix -A. Moreover, complete SCADA details of Intake as well as power supply details and its basic automation description is discussed in this section. Figure 2.13 shows the salient features of the geographical representation of phase III WTP SCADA system at Aizawl.
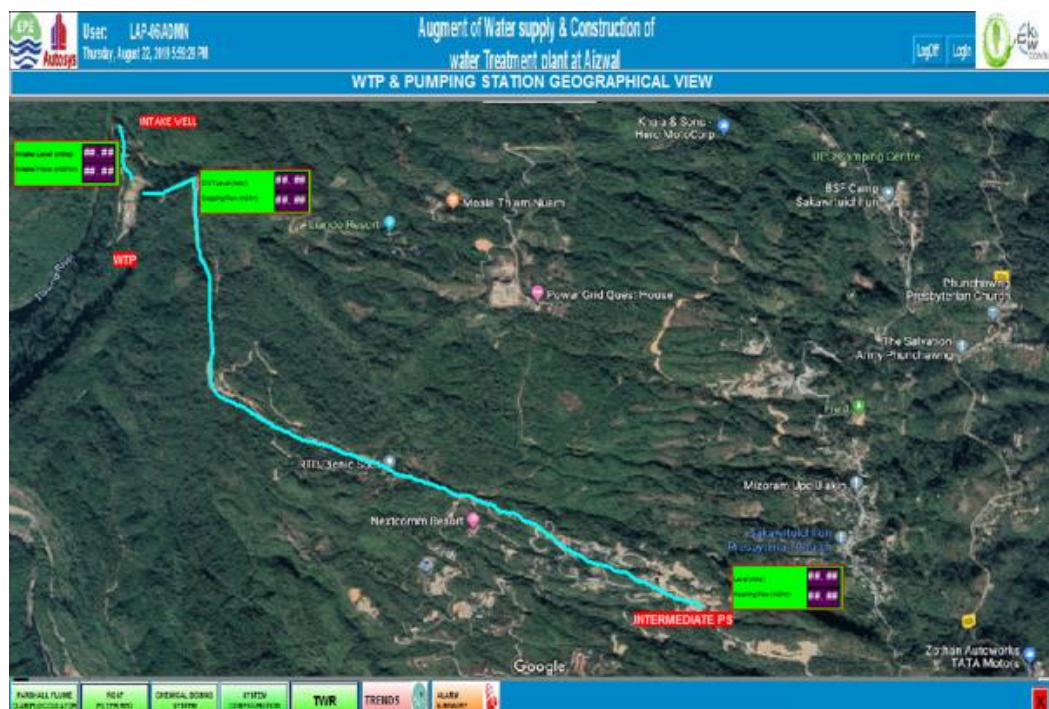
Figure 2.13. Geographical map of GAWSS P- III

2.7.3 Intake SCADA System

SCADA Operation of intake well as well as description of various functions is shown in table 2.10. where various equipment such as Intake well Pump-A/B/C, 11KV DG SET, 180KVA, 415V DG SET, 11 kV Soft Start, 150 kVA LT Transformer, HT panels, LT motors, electrical actuators, Level meter and flow meter are monitored and controlled through SCADA system, periodic data reports as well as interlocking system of the panels and monitored and controlled as per requirement at the SCADA screen. As the Process envisaged in the WTP is only for pH, Turbidity, removal of iron and disinfection, we have considered provision of on line Transmitters for pH (PH - 101) and Turbidity (TUB -101) in the Raw Water Channel to monitor the quality of

water prior to Treatment. This data is fed real time to the PLC. In case of lower /higher than the set limit, alarm will alert the operator to correct the respective dosing system.

Figure 2.14 shows the SCADA screen of Intake system, where pump energy consumptions, raw water level, pressure and flow are measured. The SCADA platform offers manual and auto mode of operations for valve operations and motor operations. Most of the data such as energy meter, flow meter and pressure etc. are stored in the server as per the format given in the SCADA system. Alarm system for pressure, level and flow etc. are incorporated for safety and operation purposes.

Table 2.10. Raw water intake well SCADA description

Operation of Intake SCADA equipment					
Sl. No	Equipment Description	Live Value	Remote monitoring	Report	Interlock
1	Intake well Pump-A/B/C	Current	Start	Motor Operating Hours will recorded in SCADA	Intake well Pump Interlock with Intake well level & Pressure Transmitter & Motor winding & bearing Temperature.
		Voltage	Stop		
		Frequency	ON		
		Bearing Temperature	OFF		
		Winding Temperature	Trip		
		Running Hours			
2	11kV DG SET	Current	Start	Fuel Consumption & Operating Hours will recorded in SCADA	No Interlock. Monitoring Only
		Voltage	Stop		
		kW	ON		
		kWH	OFF		
		PF	Trip		
		kVA			
		Battery Voltage			
		Lube Oil Temperature & Pressure	3		
		Engine RPM			
		Operating Hours			
3	180kVA,415V DG SET	Current	Start	Fuel Consumption & Operating Hours will be recorded in SCADA	LV DG Set Interlock with LT EB Incoming Power
		Voltage	Stop		
		kW	ON		
		kWH	OFF		
		PF	Trip		
		kVA			
		Battery Voltage			
		Lube Oil Temperature & Pressure			
		Engine RPM			
		Operating Hours			
4	11kV Soft Start	-	Start	-	Soft Starter Interlock with HT Panel
			Stop		
			ON		

		OFF			
		Trip			
5	150kVA LT Transformer	Winding Temperature	-	-	No Interlock. Monitoring Only
		Oil Temperature			
6	HT Panel	Current	Start	-	HT Panel Interlock with Motor Bearing & Winding Temperature.
		Voltage	Stop		
		kW	ON		
		kWH	OFF		
		PF	Trip		
		kVA			
7	LT Motors	-	Start	-	LT Motors Interlock with Level & Pressure Transmitter.
			Stop		
			ON		
			OFF		
			Trip		
8	Electrical Actuators	-	Start	-	Electrical Actuators Interlock with HT Motor & Engine
			Stop		
			OPEN		
			CLOSE		
			Trip		
9	Level Transmitter	Current Level Height	-	-	Level Transmitter Interlock with Motor.
10	Flow Meter	Current Flow	-	Cumulative flow will recorded in SCADA	No Interlock. Monitoring Only
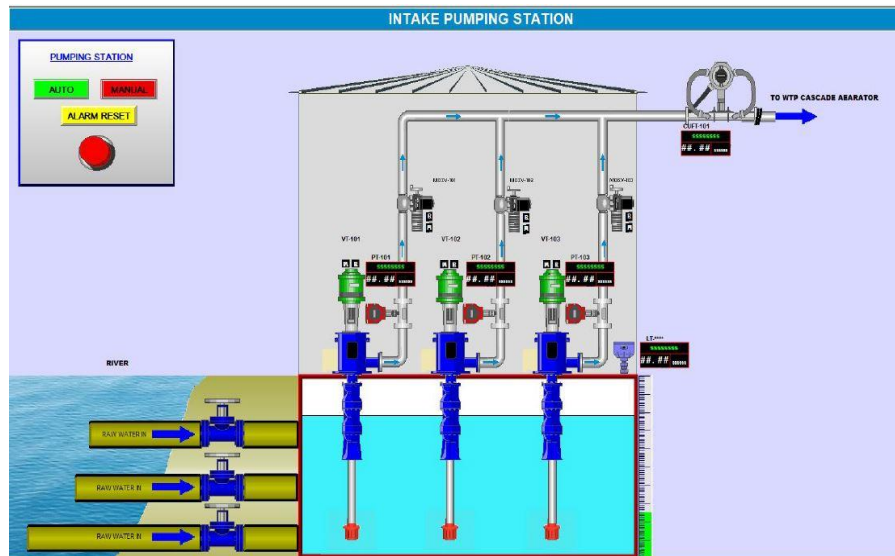
Figure 2.14 Intake SCADA Screen of Phase III

2.8 Power Supply and Electrical Description of GAWSS P-III

The power supply for GAWSS P-III is sourced from the Power and Electricity Department, which utilizes a 33 kV double circuit transmission line spanning 4.3 km.

The power is transmitted to the 33/11 kV Substation at WTP, where it is stepped down and distributed for pumping raw water to the intake. Additionally, the same power is transmitted at 33 kV to the IPS, located approximately 4.5 km away from WTP. The 33/11 kV Substation at IPS further steps down the power to feed 0.415 kV compatible loads for the pumps and auxiliary loads. The electrical load details at various locations within GAWSS P-III are provided in Table 2.11.

Table 2.11 electrical load details of GAWSS P-III

Sl. No	Description	Total kW	No of Motors Working	Total Running Load In kW	Running Load In kVA (assuming 0.83 pf)	Transformer Capacity in kVA
1.	Intake (RWPS)					
a.	HT Motors	550	2	1100	1325	2000.00
b.	LT Motors(Aux)	60		60	73	150.00
2.	WTP (CWPS-1)					
a.	HT Motors	1750	2	3500	4216	5000.00
b.	LT Motors(Aux)	204		204	245.78	500.00
3.	IPS (CWPS-2)					
a.	HT Motors	1850	2	3700	4457	5000.00
b.	LT Motors(Aux)	59		59	71	150.00
	Total			8623	10387.78	12800.00
	Total in MW/MVA			8.6	10.4	12.8
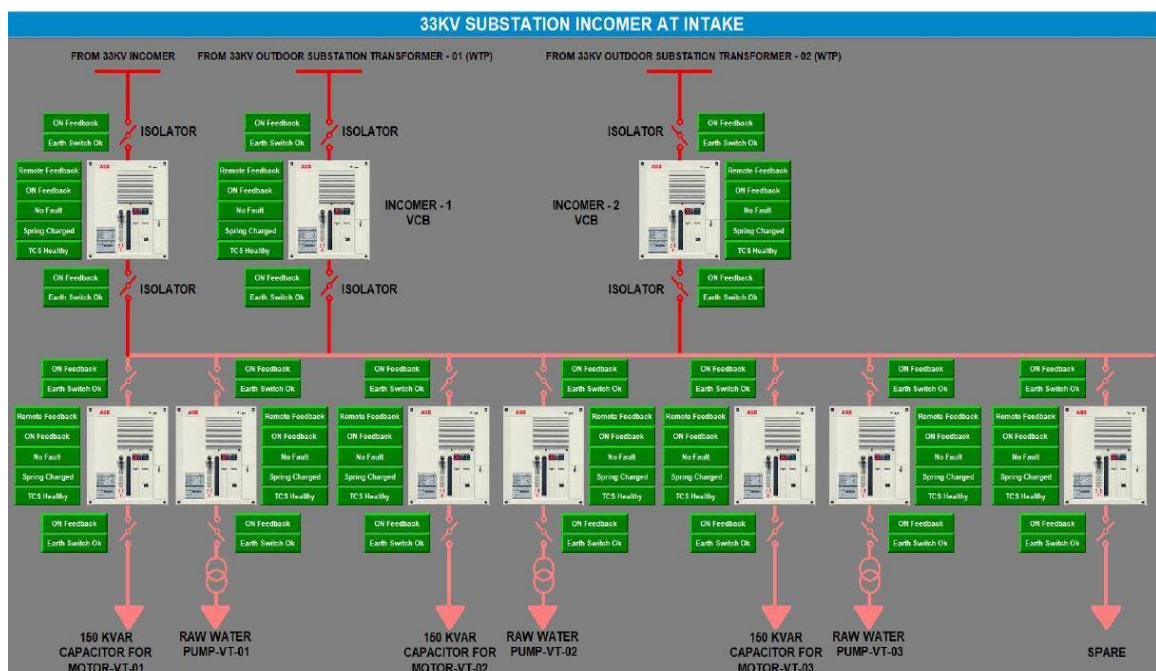
Figure 2.15. SCADA screen for Intake electrical panel.
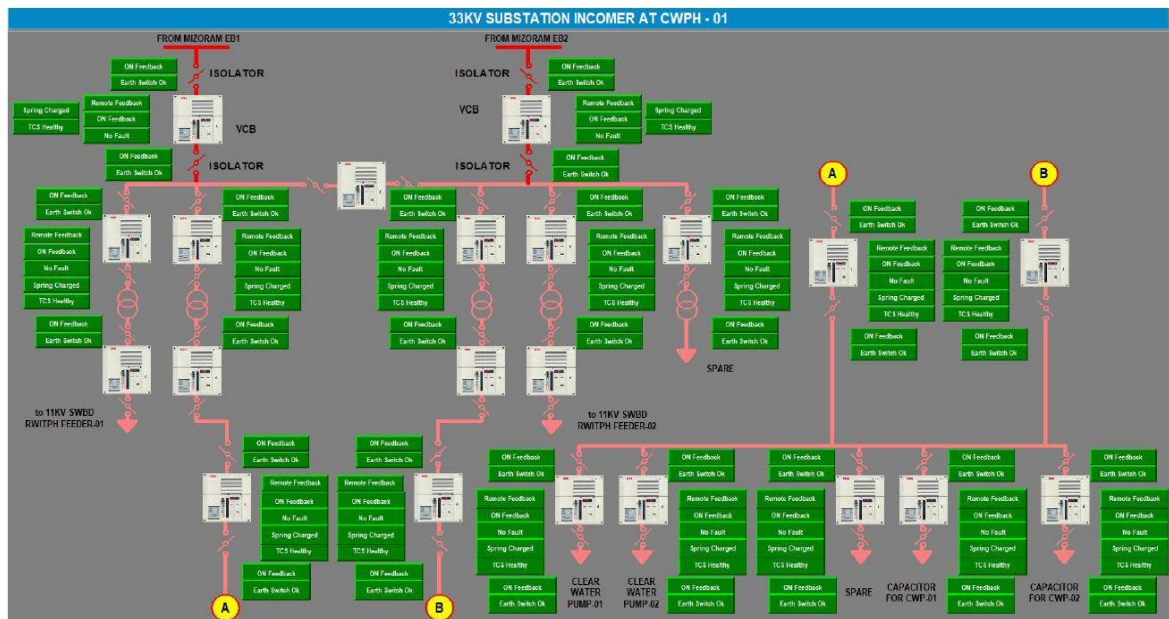
Figure 2.16. SCADA screen for Incomer/WTP electrical panel
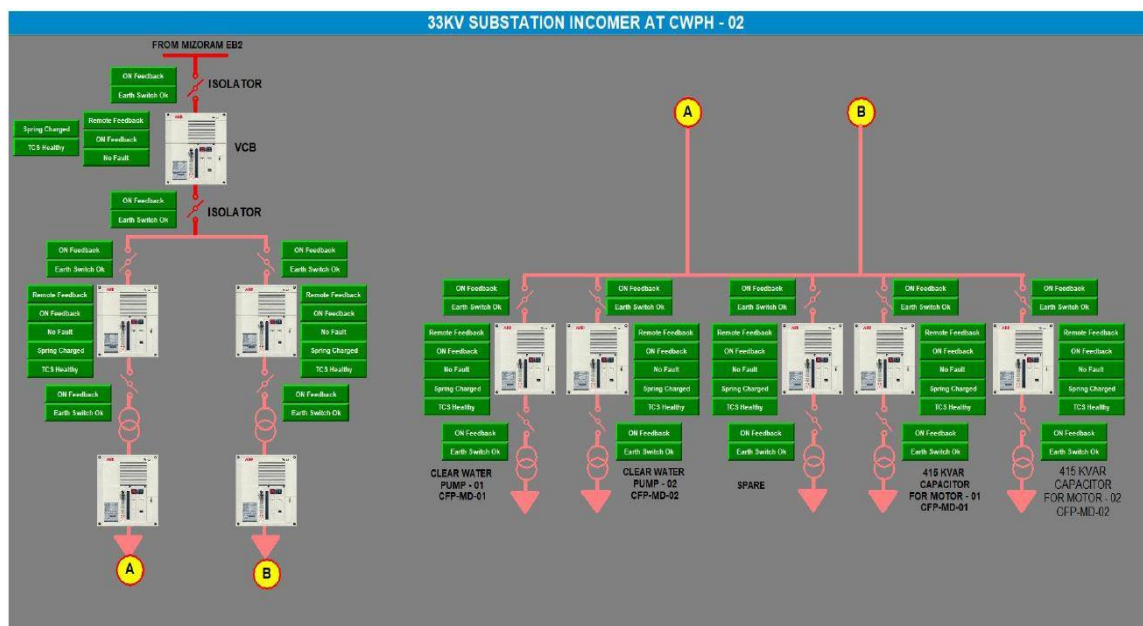
Figure 2.17. SCADA screen for IPS Pump house II electrical panel

Furthermore, SCADA screens for all electrical equipment and instrumentation at locations such as Intake, WTP, and Intermediate Pumping Stations are illustrated in Figure 2.15, Figure 2.16, and Figure 2.17, respectively. The corresponding control panels for each electrical equipment are detailed in the previous tables. Table 2.12 shows details of pump stages, discharge and heads related including motor load for Raw water, clear water 1A, Clear water 1 B and IPS and Table 2.13. Shows the

approximate calculated total monthly energy bill for one year at GAWSS P-III excluding diesel engine operation cost

Table 2.12. Details of each of the pumping station in phase III

Pumping stations	Pump	Motor	Discharge	Head
Raw Water	3 nos, 4 Stages (1 Standby)	550 kW	887 m^3/hr	183 m
Clear Water 1 A	2 nos, 6 Stages	1750 kW (Electric Motor)	803 m^3/hr	507 m
Clear Water 1 B	2 nos, 7 Stages	1475 HP (Diesel Engine	402 m^3/hr	507 m
IPS	2 nos, 6 Stages	1850 kW (Electric motor)	803 m^3/hr	536 m
IPS	2 nos, 7 Stages	1475 HP (Diesel Engine)	803 m^3/hr	536 m

Table 2.13. Energy consumption cost of GAWW P-III for the year 2022-2023

Sl. No.	Month	Energy Bill in Lakhs (Approximate)
1	January	610
2	February	610
3	March	611
4	April	611
5	May	611
6	June	610
7	July	601
8	August	610
9	September	609
10	October	610
11	November	610
12	December	618
13	Total	7322

2.9 Feasibility Study of RES Implementation in the Study System

Feasibility study of Various Energy Resources such as SPV, wind turbine generator (WTG) and Hydro energy generation availability including cost analysis is done in this section in the WTP considering Aizawl area so as to improve the energy efficiency and to minimize the energy cost. It aims to improve the system by focusing on feasibility of Microgrid concept in the WTP.

2.9.1 Solar Feasibility

According to the 17th Electric Power survey, Mizoram has a power requirement of 107 MW, but the state's own generating stations have a total installed capacity of only 29.35 MW. Mizoram heavily relies on outside sources like Central sector generating stations (CGS) of North Eastern Power Corporation Ltd (NEEPCO) and

NHPC Ltd. to meet its energy demand. However, power generation from CGS is significantly reduced during the dry season as most of the generating stations are hydel, resulting in frequent interruptions and load shedding throughout the state [115]. This situation is particularly challenging in rural areas, where some villages still lack access to electricity. The topographical nature of Mizoram makes transmission of power between stations challenging, requiring uninterrupted power sources for the smooth operation of offices. Solar on-grid and off-grid power plants have been identified as suitable solutions to address these power supply issues in the state.

Table 2.14. One-year solar report of NREL during 2018

Unit	W/m^2	W/m^2	W/m^2	Degree	mbar
Month	Solar Zenith Angle	DHI	DNI	GHI	Surface Albedo
Feb	97.51448	87.3631	200.7143	211.1429	0.130714
Mar	91.02474	107.9301	193.4059	241.2191	0.132513
Apr	84.12251	116.2528	158.6625	232.7333	0.146931
May	79.07738	125.2487	118.4368	211.9315	0.143871
June	76.97268	134.0125	90.07639	198.8111	0.168458
Jul	77.91246	136.4341	90.01478	202.414	0.162715
Aug	81.9805	137.4825	91.64247	201.7796	0.159032
Sept	88.31817	110.2792	156.8944	215.0667	0.153931
Oct	95.23364	77.91935	167.9503	182.1747	0.150134
Nov	100.5935	56.69167	250.0556	194.0069	0.137472
Dec	102.8992	41.4207	252.5793	169.2984	0.120712

Here, in this study various data report from 2018 to 2020 obtained by plotting the geocoordinates of the GAWSS P-I&II and III from National Renewable Energy Laboratory (NREL) [116] is shown in the following tables and figures viz. Table 2.14, 2.15, 2.16 also figure 2.18, 2.19 and 2.20 shows the respective graphs of the data.

Table 2.15. One-year solar report of NREL during 2019

Unit	w/m2	w/m2	w/m2	Degree	mbar
Month	Solar Zenith Angle	DHI	DNI	GHI	Surface Albedo
Feb	97.56057	68.97619	221.8661	199.9375	0.130714
Mar	91.08042	98.95699	193.7151	231.4987	0.132513
Apr	84.17111	115.6583	186.1889	251.7653	0.146931
May	79.10574	120.5161	176.9368	253.3414	0.143871
June	76.97697	134.0639	119.5778	221.6708	0.168458
July	77.89258	129.8763	91.32124	194.6183	0.162715
Aug	81.9381	133.4772	114.7352	210.7003	0.159032
Sept	88.26226	115.3569	123.5972	198.6514	0.153931
Oct	95.18177	82.33468	178.1183	188.5054	0.150134
Nov	100.5621	44.08056	272.6611	191.9306	0.137472
Dec	102.8936	46.38038	262.1142	181.3629	0.120712

Table 2.16. One-year report of NREL during 2020

Unit	w/m2	w/m2	w/m2	Degree	mbar
Month	Solar Zenith Angle	DHI	DNI	GHI	Surface Albedo
January	101.8527	62.3629	210.4731	174.75	0.123804
February	97.60738	73.79464	213.9851	203.1801	0.130714
March	90.90263	97.12231	209.5793	238.1304	0.132581
April	84.01563	111.5194	166.0639	232.7597	0.147528
May	79.01505	118.8884	153.2782	228.2863	0.143871
June	76.96244	130.1583	123.525	221.1028	0.169458
July	77.95406	140.7876	95.08199	206.8898	0.16207
August	82.07187	130.7191	108.629	207.8616	0.158777
Sept	88.43675	114.4347	133.6528	203.5097	0.154528
Oct	95.34343	77.11962	172.2984	183.8118	0.149489
Nov	100.6613	50.86667	258.3403	192.2208	0.136806
Dec	102.9108	44.18817	288.6411	191.3051	0.12039

After reviewing the reports from NERL and conducting a comprehensive feasibility survey at the study site, Zoram Energy Development Agency (ZEDA) has formulated a proposal for the installation of a solar photovoltaic system. The proposed system includes single and three-phase inverters with varying capacities of 10 kVA, 15 kVA, 20 kVA, and 25 kVA, as well as valve regulated lead-acid (VRLA) battery banks with different specifications such as 120V 500Ah 60000 kWh, 96V 500Ah 48000 kWh, and 240V 500Ah 120000 kWh, depending on the feasibility. The battery bank is designed to provide a power backup time of 12 hours. Table 2.17 shows the available solar capacity for installation in different locations within the study system.
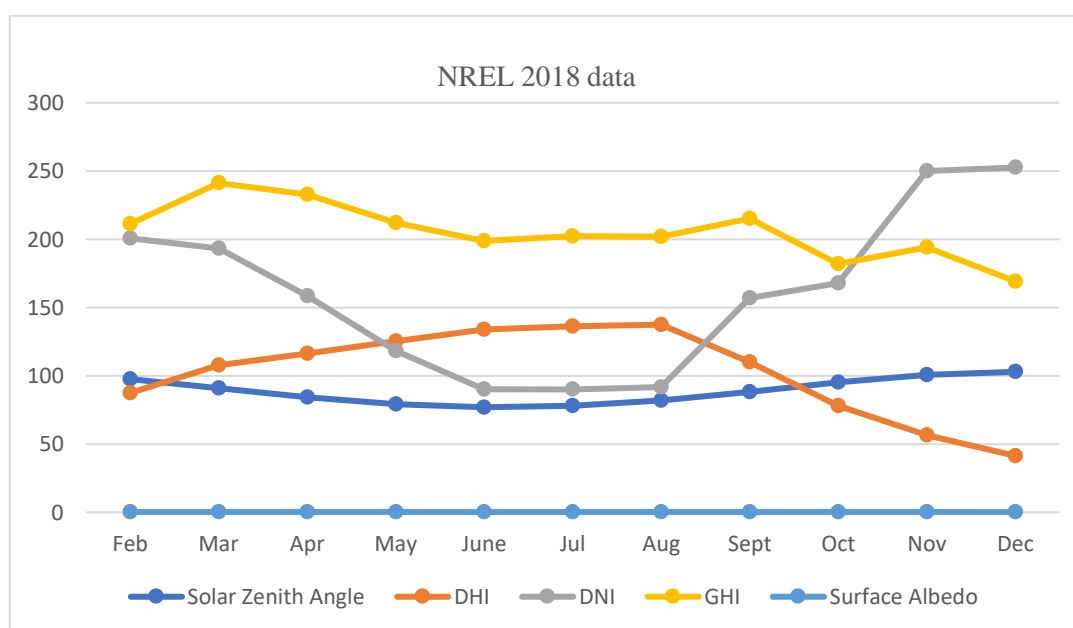
Figure 2.18. NREL solar data in 2018.
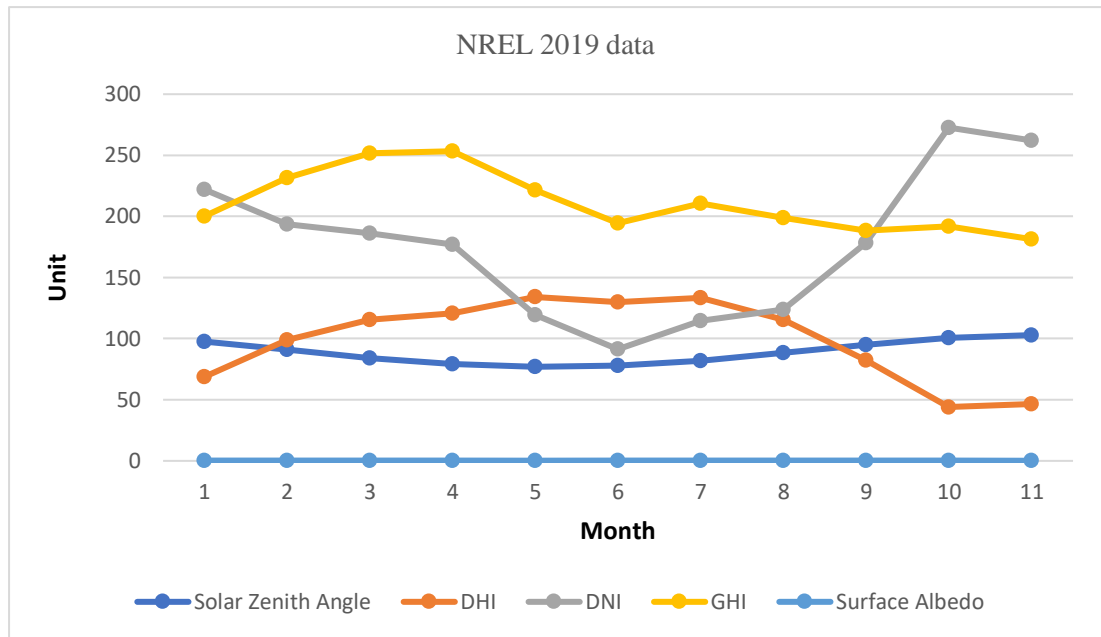
Figure 2.19. NREL solar data in 2019
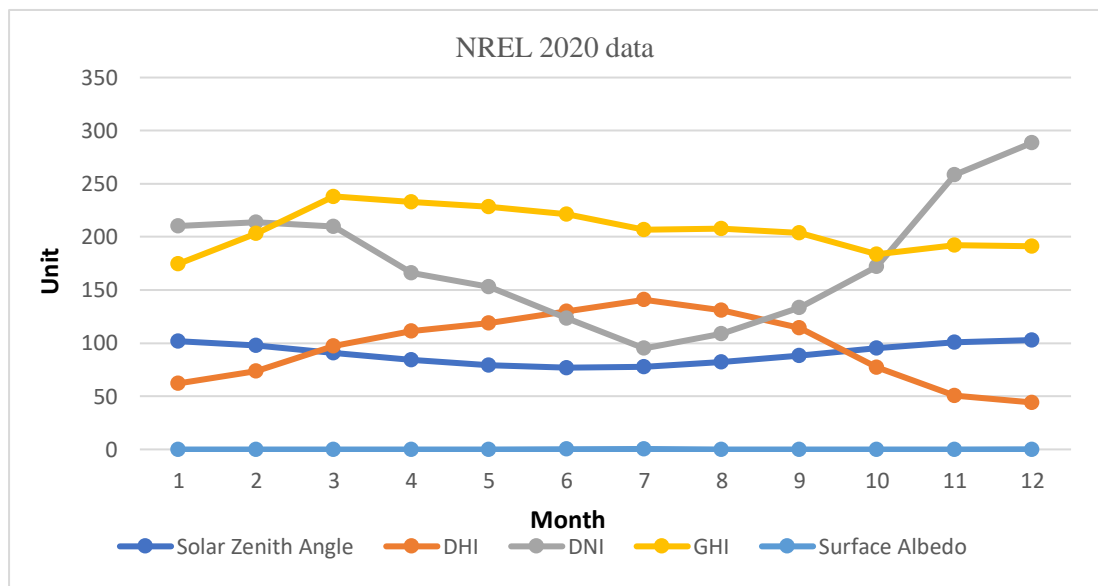
Figure 2.20. NREL solar data in 2020

Table 2.17. Available solar capacity at site

Sl. No	Location	Existing source of Power	Availability of Space	Average Solar Irridiance at site in kWh/sqm/day	Capacity of Solar plant as per availability of Space (kW)	Expected Annual Generation (kWh)
GAWSS P-I						
1	Intake	Grid	Available	4.83	10	14640

2	WTP	Grid	Available	4.83	6x20	175680
3	IPS	Grid	Available	4.83	10x25	146400
GAWSS P-II						
1	Intake	Grid	Available	4.84	8x15	175680
2	WTP	Grid	Available	4.84	22x25	512400
GAWSS P-III						
1	Intake	Grid	Available	4.94	15	21960
2	WTP	Grid	Available	4.94	18x25	732000
3	IPS	Grid	Available	4.94	12x25	292800
4	TOTAL				1815	2071560

2.9.2 Cost Analysis

As per the rate analysis carried out by Zoram Energy Development Agency (ZEDA) [118], the cost of a solar photovoltaic unit can be assessed based on various components, including the cost of system hardware, transportation and insurance, civil works and insurance works, installation and commissioning, annual maintenance for 5 years, battery replacement, and other related costs. Table 2.18 provides the total calculated cost for each kWp module, ranging from 1 kWP to 25 kWp. Additionally, Table 2.19 shows the approximate estimate/cost of the SPV system at GAWSS P-I, II & III, which is estimated to be around 29 Crore.

Table 2.18. Total cost for solar module at site

Sl No.	SPV capacity in kWp	Module	Battery	Inverter	Structure	Others	Total
1	1	42,000	50,000	15,000	10,000	60,000	1,77,000
2	5	2,10,000	3,24,000	75,000	55,020	1,23,000	7,87,020
3	6	2,52,000	3,78,000	86,500	71,520	1,43,000	9,31,020
4	8	3,36,000	5,18,400	1,08,800	88,800	1,48,000	12,00,000
5	9	3,78,000	5,72,400	1,20,300	1,05,300	1,68,000	13,44,000
6	10	4,20,000	6,48,000	1,36,000	1,11,000	1,85,000	15,00,000
7	15	6,30,000	9,72,000	2,04,000	1,66,500	2,77,500	22,50,000
8	20	8,40,000	17,28,000	4,50,000	1,88,900	3,86,000	35,92,900
9	25	10,50,000	17,28,000	6,25,000	2,50,000	3,32,000	39,85,000

Every project comes with its own set of risks. However, the risks associated with installing off-grid power plants are relatively low compared to other technologies. It is expected to generate a significant amount of energy over its operational lifespan. Considering the current average cost of energy, the calculated cost is considerably lower than the total energy bill for all three phases of the project in just one year. The uninterrupted availability of power during times of need will have a significant positive

impact on the beneficiaries. Despite the availability of grid power on-site, frequent power outages disrupt the operations, resulting in financial losses, and most importantly, interruptions in water supply in Aizawl city can be avoided with the implementation of the off-grid power plants.

Table 2.19. Total cost of the module for installation of SPV in GAWSS P-I&II&III

Sl. No.	Module kWp	Numbers	Cost in Rs	Total
1	10	1	1500000	1500000
2	15	9	2250000	20250000
3	20	6	3592900	21557400
4	25	62	3985000	247070000
5	Total			290377400
6	Approximate			29 Crore

2.9.3 Wind Feasibility

Based on the findings of the National Renewable Energy Laboratory (NREL), the wind profile in the study region and Mizoram is characterized by low wind power potential. Mizoram Science, Technology & Innovation Council (MISTIC) and Mizoram state climate change cell (SCCC) report that the month of April recorded the highest average wind speed in Mizoram in 2021 at 7.9 km/hr, while December had the lowest average wind speed at 1.9 km/hr [117-118]. Additionally, Zoram Energy Development Agency (ZEDA) data shows that the wind speed at GAWSS P-I, II & III is only around 4.5 m/s. However, the minimum wind speed required for satisfactory electricity generation from wind turbines is generally considered to be around 15 km/hr or 12 m/s. Figure 2.21. shows wind speed data in Aizawl during 2021.
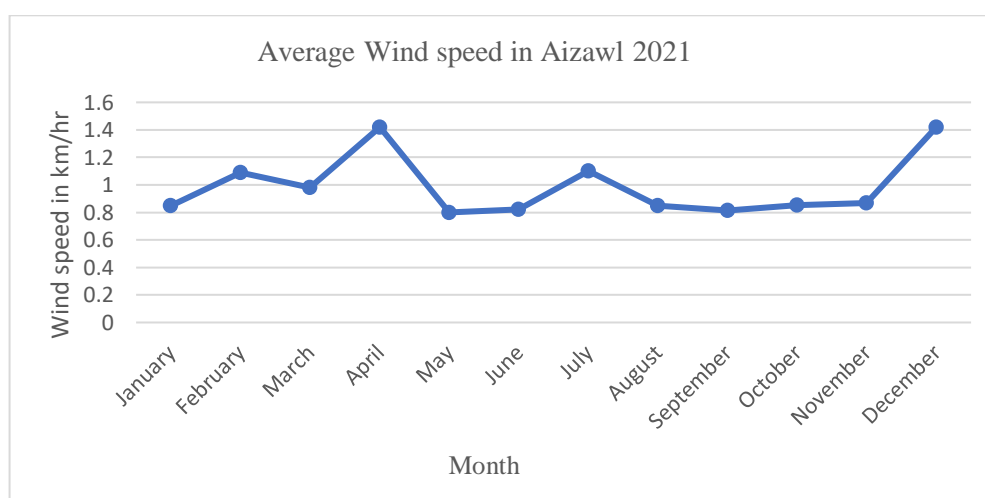
Figure 2.21. Wind speed data in Aizawl during 2021

Given the low wind profile and inadequate wind data, it can be observed that a wind power plant is not feasible for the study system and Aizawl city. Therefore, wind energy is not considered as a viable option in the study system.

2.9.4 Hydro/Water Energy Feasibility

As the study system relies on water as its primary source, with a river intake and high head pumping system in place, the potential for generating hydroelectric power from small and medium-sized hydro power plants is worth considering. This could have a significant impact on optimizing power-related issues and minimizing operational costs associated with energy consumption. In this section, observations and feasibility studies are conducted, taking into account the location of Aizawl and the Tlawng River as the water source, as well as the WTP area, for the implementation of hydro energy sources. Given that Aizawl is located in a hilly terrain, gravity-based hydro power sources offer a significant advantage compared to flat areas.

2.9.4.1 Rainfall Data in Aizawl

The feasibility of implementing a hydro power source relies on several factors, including the annual rainfall report and water quantity of the Tlawng River, as well as the water level throughout the year. The study of rainfall data is obtained from the MISTIC report [119], while the water quantity information is obtained from the PHE department. Figure 2.22 illustrates the trend of annual rainfall from 2002 to 2021.
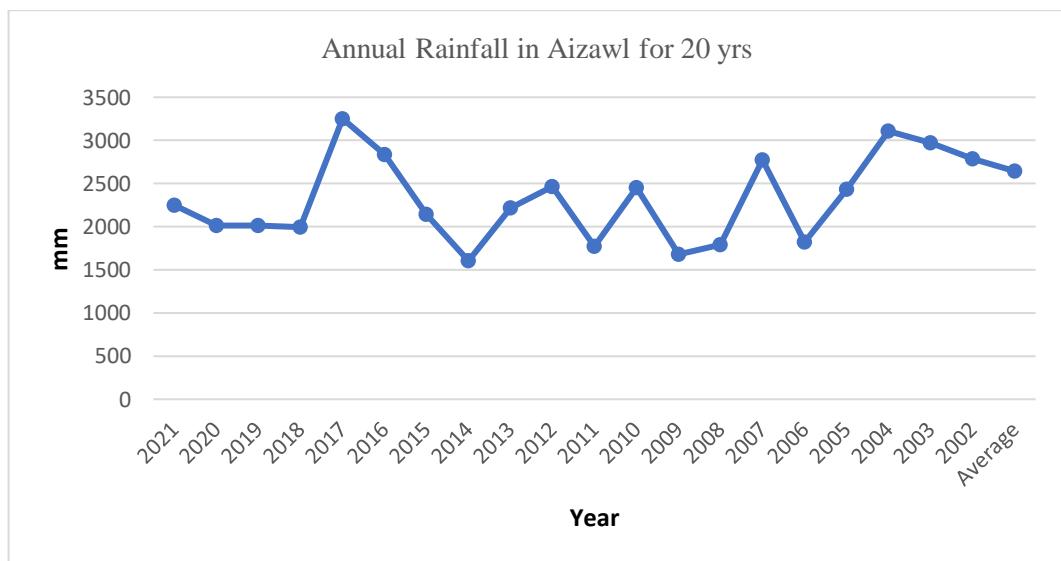
Figure 2.22. Annual rainfall data in Aizawl for 20 years

Over a 20-year period, the highest total annual rainfall was recorded in 2017 with 3251.8 mm, while the lowest was in 2014 with 1604.1 mm. The average annual rainfall received during this period is approximately 2642.5 mm. Table 2.20 presents the annual rainfall data from 2002 to 2021.

Table 2.20. Annual rainfall data in Aizawl from 2002 to 2021

Sl. No.	Year	Annual rainfall in Aizawl in mm
1	2021	2246.3
2	2020	2011.8
3	2019	2012
4	2018	1996.1
5	2017	3251.8
6	2016	2836.5
7	2015	2143.7
8	2014	1604.1
9	2013	2215.8
10	2012	2466.5
11	2011	1769.9
12	2010	2451.6
13	2009	1676.6
14	2008	1790.3
15	2007	2776.9
16	2006	1824.2
17	2005	2436.4
18	2004	3108.3
19	2003	2971
20	2002	2788
21	Average	2642.5

2.9.4.2 Water Availability at Tlawng River

The Tlawng River is the longest river in Mizoram, stretching for around 234 kilometers in a south-north direction before joining the River Barak in the Cachar district of Assam state. It is fed by main tributaries such as Tut, Teirei, and Ngashih. As the Tlawng River runs in close proximity to Aizawl city, it serves as the primary source of water supply for both domestic and agricultural use in the area.

Flow accumulation, an important factor in river systems, varies along the course of the Tlawng River. In the lower reaches, where the channel width is 53 meters and depth is 36 meters, the maximum estimated flow accumulation is 205,431 cubic meters. This section has a gentle gradient. On the other hand, in the upper stream

section at an altitude of 546 meters above mean sea level, the maximum flow accumulation is approximately 2,139 cubic meters. Here, the channel width is 12 meters and depth is 21 meters, and the gradient ranges from moderate to steep. Depending on the channel dimensions and inflow, there may be areas along the river with high flow accumulation.

The following table 2.21 shows the average and projected average water level at River Intake at Phase II and Phase III, due to weir at intake the average water level is considered approximately 8-12 ft for phase II and 10 to 14 ft for phase III throughout the year. However, during rainy seasons, the water level rose above the weir and reaches up to the high flood level of approximately around 49 feet (15 m) from the river bed.

Table 2.21. Average water level at intake river during 2022

Sl. No.	Month	Average Water level at GAWSS P- II in ft (due to silt deposit and weir height at river intake the average water level is approximately 12 ft)	Average Water level at GAWSS P- III in ft (due to silt deposit and weir height at river intake the average water level is approximately 14 ft)
1	January	8-12	10 -14
2	February	8-12	10 -14
3	March	8-12	10 – 14
4	April	8-12	10 -14
5	May	8-12	10 -14
6	June	25-45	25- 49 (High flood level)
7	July	24-35	24 -38
8	August	8-12	10- 14
9	September	8-12	10- 14
10	October	8-12	10- 14
11	November	8-12	10-14
12	December	8-12	10-14

The estimated design capacity for transmitting water, denoting the discharge flow rate at the pump outlet at the reservoir, is approximately 480 m^3/h and for phase I, 810 m3/h, also for phase II, 712 m^3/h and for phase III, 803 m^3/h. Sufficient water has been transmitted and stored in the reservoir and water transmission system. Considering that an average of 60 to 95 litters of water is needed to produce 1 kWh of electricity, depending on the head difference, and taking into account the hilly terrain with significant head difference, it appears feasible to implement a small or medium hydro

power plant in the water supply system. This would require special design considerations for the water transmission line and intermediate sump. Additionally, based on the water level and quantity at the river source intake, installation of a small hydro power plant could be feasible and worth considering in future studies.

Table 2.22 Conclusion summary of the study system

S. N.	Descriptions	GAWSS P-I	GAWSS P-II	GAWSS P-III
1	Operation flow	Intake, (Chemical dosing), Clarifloccultor, Filter house, Pump house I, Pump house II, Reservoir	Intake, Pre settling tank, Pump house I, Aerator, (Chemical dosing), Clarifloccultor, Filter house, Pump house II, Reservoir	Intake, Aerator, Parshal flume, Flash mixer, Clarifloculator, Filter House, Pump House I, Pump house II, Reservoir
2	SCADA system	Cimplicity-Monitoring of process flow	Cimplicity-Monitoring of process flow	Rockwell-Control and Monitoring
3	Intake system HT load	Intake house with 3 nos- 90 kW VT pump	Jack well with 5 nos - 713 kW Submersible Pumps, 3 Nos 713 kW Submersible Pumps and pre setlling tank	Jack well with 3 nos - 550 kW Submersible pump
4	WTP HT load	635 kW	1700 kW	1750 kW
5	IPS HT load	635 kW	-	1850 kW
6	Power Supply	33 kV P&E Dept	33 kV P&E Dept	33 kV P&E Dept
7	SCADA Scope	Water Quality, Water Quantity, Energy consumption	Water Quality, Water Quantity, Energy consumption	Water Quality, Water Quantity, Valve/motor Control with Energy consumption and management
8	Power stepping	132/33 and 33/3.3 kV	132/33 to 33/11 kV	33/11 kV
9	Energy cost	55 Crore annually		73 Crore annually
10	Operation cost	High	High	High
12	Diesel generator set	Yes	Yes	Yes
13	Approximate operational cost	80-90 Crore per year excluding maintenance		110-140 Crore per year excluding maintenance
13	Solar feasibility	Feasible	Feasible	Feasible
14	Wind feasibility	Not Feasible	Not Feasible	Not Feasible
15	Hydro power feasibility	Feasible	Feasible	Feasible

2.10   Conclusion

From the above study of the Aizawl GWSS P-I, II& III, study related to the general SCADA schemes, energy related details as well as power supply status are being focused. Also, feasibility study of renewable energy sources has also been done so as to improve the system efficiency as well as to minimize the energy consumption costs. As shown in the below Table 2.22 the conclusion summary of the study system are shown. Furthermore, field equipment of phase I&II are shown in Appendix -A

Therefore, from the above study and conclusions, implementation of SCADA control and management is done in chapter 3 to improve SCADA system in GAWSS P-I&II as the existing system offers only monitoring scope. Implementation of ladder logic concept in PLC SCADA system is shown in chapter 3. Also, the scope for implementation of microgrid based system considering WTP came into picture for solving various challenges and issues being faced relating to various power related issues in the study WTP. Most of the common issues being faced on the WTP as shown below and it is believed that this can be optimized and improved using introduction of multiarea microgrid concept considering whole water transmission system.

1. High energy consumption
2. High energy bill
3. Interrupted power supply
4. Operational issues due to old and hilly terrain
5. Limited SCADA system for phase I&II (only monitoring)
6. SCADA system without energy management
7. Power back up issues
8. No Renewable energy sources
9. Huge Diesel Engine operation cost due to frequent power interruptions etc.

The corresponding microgrid schemes under consideration of the above concept can be seen in chapter 4, 5 and 6 using ETAP and MATLAB Simulink platform.

CHAPTER

3

Monitoring and Control Strategy of Intake and Water Treatment Plant

---

3.1. Introduction

Modern WTPs are adopting technology-based solutions such as IoT and SCADA to improve their efficiency. By using SCADA, many of the problems associated with operation and maintenance of the WTP can be solved, resulting in reduced manpower requirements. SCADA allows for monitoring and control of every aspect of the pumping stages, leading to an overall improvement in the efficiency of the water treatment process. In particular, the intake structure, which is responsible for the initial stage of water pumping, must be closely monitored to avoid complications due to the seasonal variation of raw water from the source. A classification of different types of intake structures is presented in Table 3.1.

Intake towers are commonly constructed with a vertical tubular structure that includes one or multiple openings to allow raw water to flow in from sources such as rivers, reservoirs, and lakes. The design and construction of the intake structure may vary depending on the region, but generally, it is situated close to the water source. After being conveyed to the WTP, the raw water undergoes filtration processes, and the treated water is then pumped to the main reservoir through IPS, also known as boosters [120].

The power required for each pumping stage in WTPs is typically supplied by the local Power and Electricity department. The specific power requirements depend on the plant's design, such as pump data and head loss calculations. It's worth noting that unlike

other industries, the majority of electrical power consumed by WTPs falls under the HT category, which requires careful monitoring [121].

Table 3.1. Types of Intake

Sl No	Based on type of source	Based on position of Intake	Based on presence of Water in Tower
1	River Intake	Submerged Intake	Wet Intake
2	Canal Intake	Exposed Intake	Dry Intake
3	Reservoir Intake	-	-
4	Lake Intake	-	-

To ensure water quality, various parameters such as salinity, turbidity, and pH are often manually monitored by collecting raw and treated water samples and analyzing them in a laboratory setting. However, many treatment plants have implemented online monitoring using electronic sensors, which could potentially replace conventional laboratory practices [122]. Water quantity monitoring is also crucial for understanding the efficiency of the WTP and forecasting pumping and distribution routines. Monitoring the flow rate is often done through flow meters, with electromagnetic, ultrasonic, and ultrasonic level meters being commonly used in many industries and plants to manage and monitor water supply [123].

The quality of raw water input can vary seasonally, requiring frequent filtration of filter beds. Unfortunately, this process is currently performed manually without a set timing point for filtration. As a result, this manual operation can lead to poor filtration and malfunctioning of the plant process. Furthermore, mechanical LOH monitoring equipment installed for filter beds has been reported to last only a short time without proper maintenance [124].

To address the issues and challenges currently faced in water treatment industries, including training concerns, bacterial control, inadequate monitoring and record-keeping, equipment design and specification, and maintenance problems, the use of advanced technology, such as SCADA systems, is crucial. Given its flexibility and robustness, SCADA has been extensively adopted in many countries. Therefore, research and development focused on its application is crucial, as SCADA offers a wide range of potential applications.

The general concept of the work is presented in Figure 3.1 through a flow chart. The study begins with a literature survey of different intake systems in WTPs. This is

followed by a case study of the SCADA-based intake jackwell power system at Aizawl, which focuses on energy management of the WTP. Implementation of SCADA logic for data retrieval, analysis, and processing is done to collect different energy data related to energy management at the intake and receiving as well as feeding substations. The data is analyzed, and various results are compared, highlighting the advantages and disadvantages of the SCADA system compared to the non-SCADA system. The findings of the study are used to draw conclusions and identify areas for further analysis and improvement.
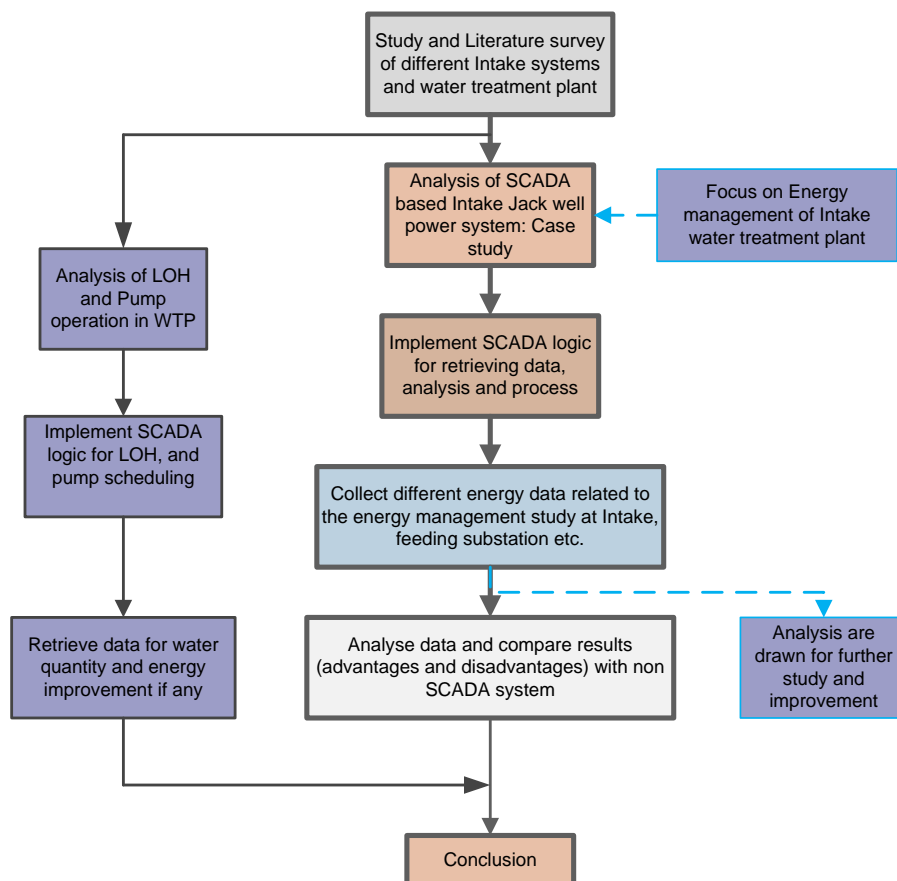
Figure 3.1. Flow chart of the work

3.2. Jack-well Intake Structure

The intake structure of a WTP is usually situated at the river source to ensure maximum water availability throughout the year. It is also located at a safe distance to withstand floods and other natural calamities. The intake collects raw water and then pumps it to the WTP for filtration. The selection of the appropriate intake structure is

crucial for the design and implementation of the WTP. One commonly used intake structure is the jack-well type, which is generally cylindrical in shape [125]. The intake tower structure of the jack-well collects water that is almost at the same level as the source, such as a river, lake, or reservoir. Figure 3.2 shows a typical single well jack-

well intake structure.
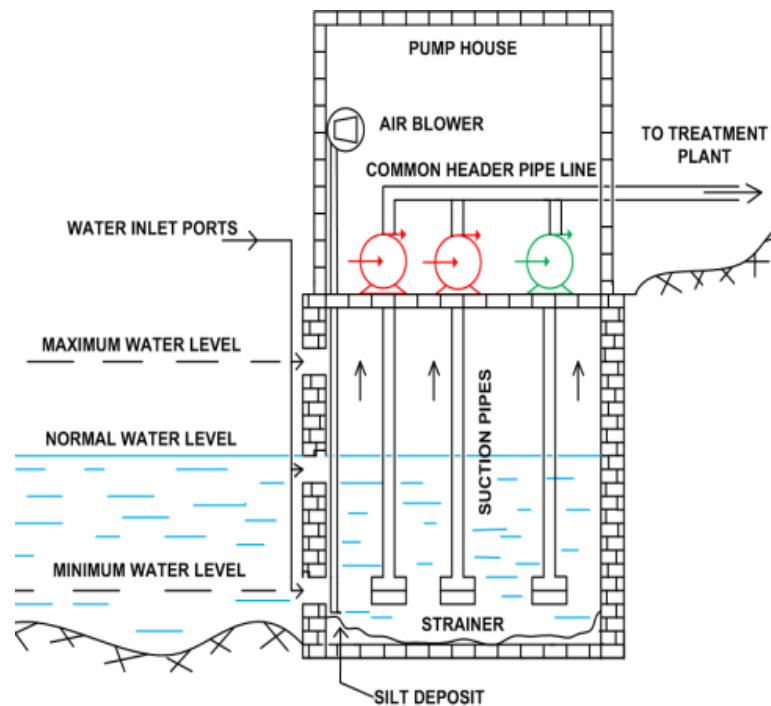
Figure 3.2. Typical Jack-well structure

The jack-well intake structure consists of an underground or underwater structure that collects water from the source. The height of the jack-well is determined by the location of the pump and high flood level. Generally, the top of the jack-well should be 1.0 meter above the high flood level or 0.3 meters above ground level, whichever is higher. The pump house located on top of the structure includes the pump, blower, and electrical panels. The pump can be either submersible or vertical turbine type. The design of the jack-well capacity and pump capacity depend on the WTP's design.

The inlet ports of the jack-well intake structure are situated at different heights on the wall, allowing water to enter the well at different water levels depending on the season. For example, the minimum water level during dry season, the normal water level for spring and rainy season, and the maximum water level during heavy monsoon and rainfall season. The level of water inside the well is usually proportional to the level of the water source. A strainer is located at the tip of the suction pipe to act as a screening

medium for removing dirt and unwanted large particles. Raw water in the Jack-well is pumped through suction pipes and transported to the WTP for further treatment. Silt deposits at the bottom of the well can be removed using submersible pumps or air blowers, as depicted in Figure 3.2.

3.3. Pump Concept

A pump is a mechanical device that transforms mechanical energy into hydraulic energy to transfer fluids such as water, chemicals, slurries, and liquid wastes from one point to another. The selection of a pump is crucial and is determined by factors such as flow rate (i.e., the volume of fluid to be pumped) and head (i.e., the distance between the delivery and receiving ends). Pumps are used in various stages and for different purposes in water supply projects [126].

Pumps are classified based on their principle of operation as follows:

1. Displacement pumps (reciprocating, rotary)
2. Velocity pumps (centrifugal, turbine, and jet pumps)
3. Buoyancy pumps (air lift pumps)
4. Impulse pumps (hydraulic rams)

The pump suction of the intake is designed in accordance with the HI (Hydrological Institute) standard, as depicted in Figure.3.3 and figure 3.4

Minimum pump inlet belt submergence S is in (3.1),

$$S=D(1.0+2.3F_D) \tag{3.1}$$

Where, D (1.5 O.D to 2.5 O.D) is an inlet belt design outside diameter, and F_D equals to V/(gD)0.5, 'V' is the velocity in m/s and 'g' is the acceleration due to gravity 9.81 m/s^2. Also, Minimum Liquid depth H is in (3.2),

$$H=S+C \tag{3.2}$$

Where, C (0.2D to 0.5D) is the distance between the inlet bell and floor. Also, A(5D) is the distance of the pump inlet belt center line to the intake structure entrance, Similarly, B (0.75 D) is the distance from the back wall to the pump inlet belt center line.

Now, Work done by the pump H.P. is in (3.3),

$$HP=\frac{gQH}{75} \tag{3.3}$$

Where, g is the specific weight of water kg/m^3, Q is the discharge of pump, m^3/s and H is the total head against which pump has to work.
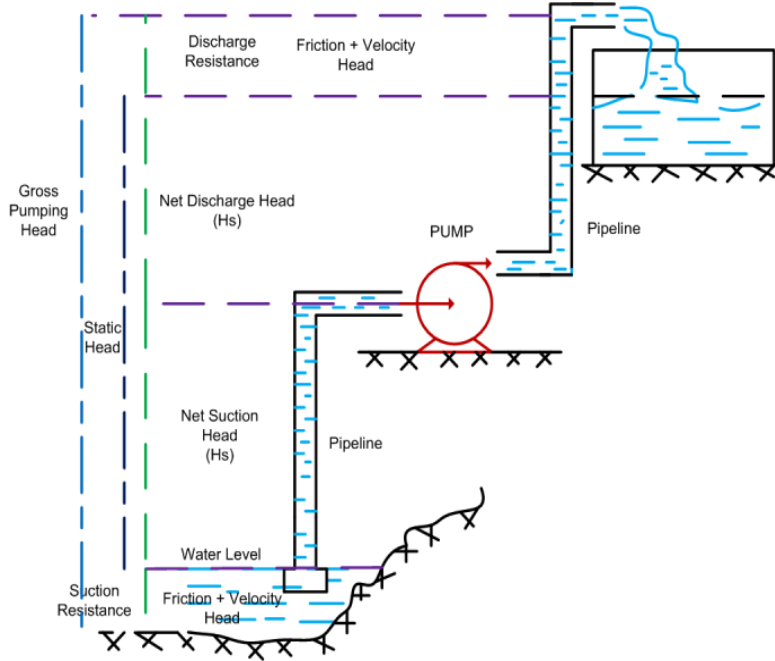
Figure 3.3. Typical pump suction

Also, from Figure.3.3

$$H = H_s + H_d + H_f +$$
$$\text{(losses due to exit, entrance, beds, valves, etc)} \tag{3.4}$$

Where, H_s is the suction head, H_d is the delivery head, and H_f is the friction loss.

Also, Efficiency of the pump (E) is in (3.5),

$$E = \frac{gQH}{\text{Brake HP}} \tag{3.5}$$

Where, total brake horse power (HP) required is given as gQH/E.

Generally, for design of water supply conduits, Hazen-William's formula for pressure conduits and Manning's formula for free flow conduits are used, depending on the resistance to flow, available pressure or head, and allowable velocities of flow. Hazen-William's formula is in (3.6),

$$U = 0.85 \, C \, (r_H)^{0.63} (S)^{0.54} \tag{3.6}$$

Also, Manning's formula is in (7),

$$U = \frac{1}{n} (r_H)^{\frac{2}{3}} \sqrt{s} \, \frac{1}{n} (r_H)^{\frac{2}{3}} \sqrt{s} \tag{3.7}$$

Where, U is the velocity, m/s; r_H is the hydraulic radius, m; S is the slope, C is the Hazen-William's coefficient, and n is the Manning's coefficient. Like ways, the electrical pump power calculation can be done by using the below formula (3.8)
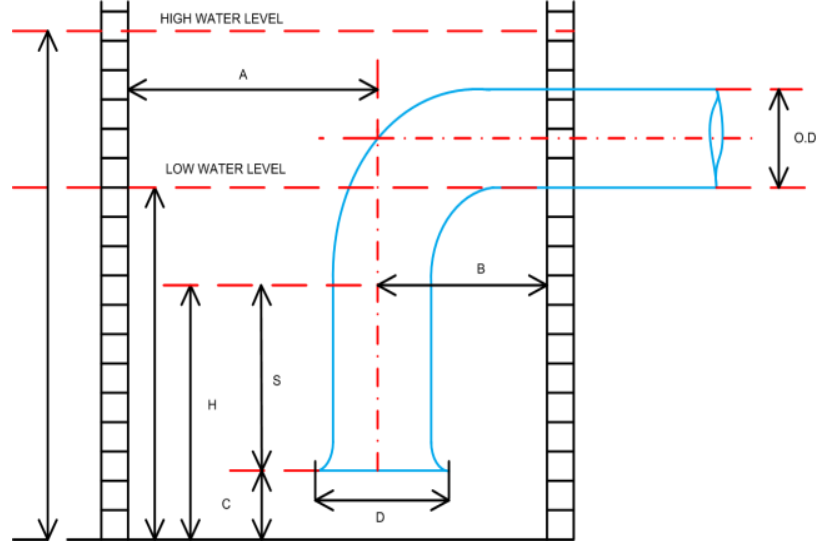
Figure 3.4 Typical Inlet pump principle

$$P_{(kW\_motor)} = \frac{q_{(m^3/hr)} \times \rho_{(kg/m^3)} \times g_{(m^2/s)} \times h_{(m)} \times p_{(pa)}}{3600000}$$ (3.8)

Where, $P_{(kW-motor)}$ is pump power in kilowatts, $q_{(m^3/hr)}$ is the rate of flow in cubic meter per hour, $\rho_{(kg/m^3)}$ is fluid density in kilogram per cubic meter, $g_{(m^2/s)}$ is gravity in m^2/s, $h_{(m)}$ is pump differential head in meter and the differential pressure $p_{(Pa)}$ in Pascal or N/m^2

Also, the shaft power can be given as in (3.9),

$$P_{(kW-shaft)} = \frac{P(kW)}{\eta}$$ (3.9)

The required motor power in kW can be written as (3.10)

$$P_{(kW\_motor)} = \frac{q_{(m^3/hr)} \times \rho_{(kg/m^3)} \times g_{(m^2/s)} \times h_{(m)} \times p_{(pa)}}{(3600000 \times \eta)}$$ (3.10)

3.4. Power Supply

The single line diagram (SLD) of a typical power supply for Intake is shown in Figure.3.5 The power supply system consists of the following four major components,

such as raw power supply from the grid, Control and relay panels, power backup and LT and HT loads.
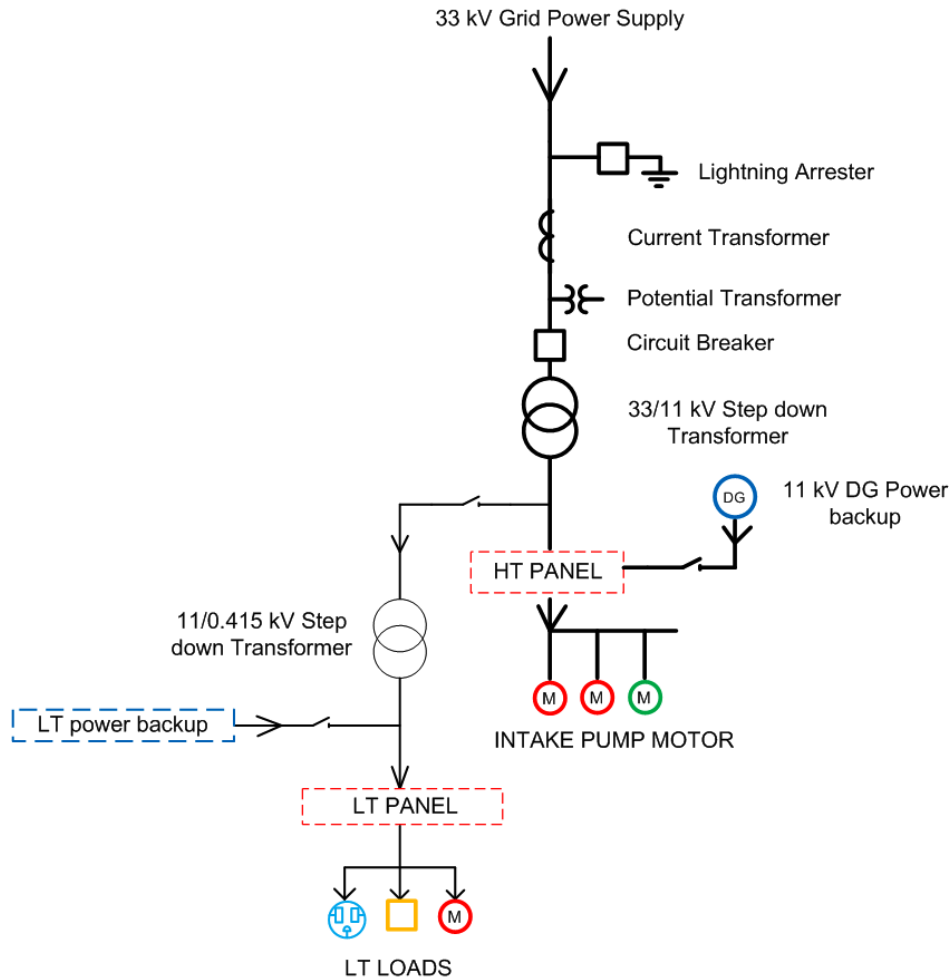
Figure 3.5 Typical SLD of intake power supply.

The intake facility is powered by the grid through a 33/11 kV substation that includes various switchgear equipment, such as lightning arrester, current transformer (CT), potential transformer (PT), and circuit breaker. The incoming 33 kV voltage is stepped down to 11 kV by a step-down transformer, and the output is fed to the 11 kV pump motors via an 11 kV HT panel. An auxiliary transformer is also used to step down the voltage to 0.415 kV for auxiliary loads through LT panels. Additionally, the system includes key devices like HT and LT motor starters and an automatic power factor corrector panel for efficient power management. Control and numerical relay panels connected to the SCADA system monitor and control the switchyard equipment like CT, PT, and breaker. The HT and LT transformer sides are also protected using temperature control, earth fault, Buchholz relay, etc.
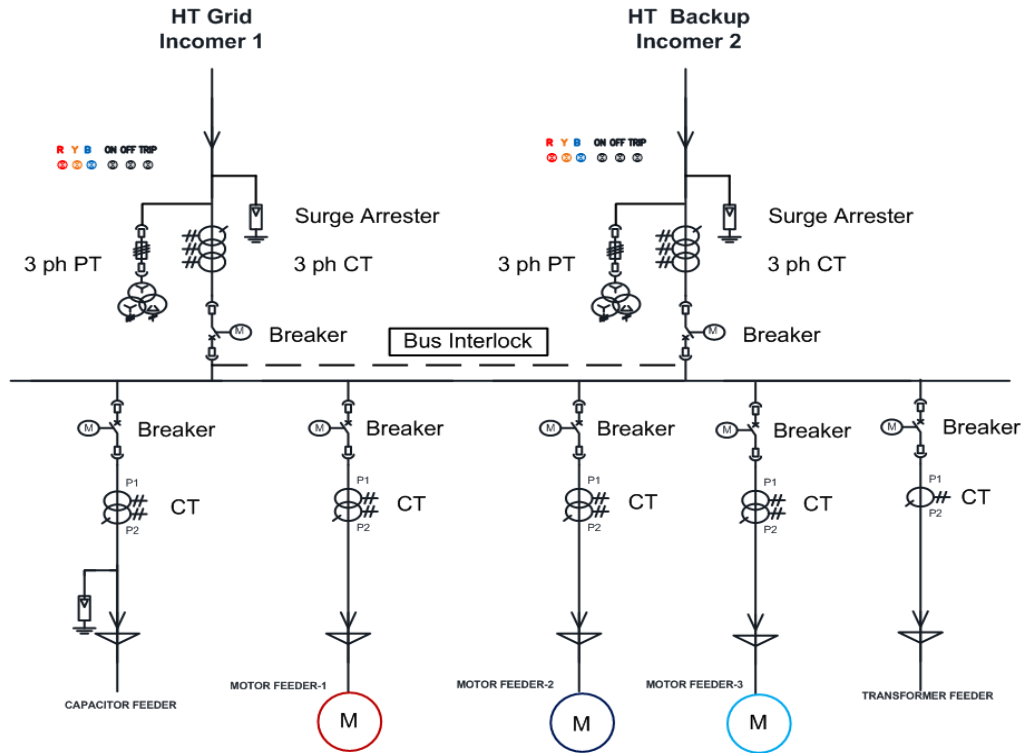
Figure 3.6 SLD of typical HT panel.

A typical HT panel for the intake power supply system is shown in Figure 3.6. Two HT incomers (incomer 1 - 11 kV from the main grid and incomer 2 - 11 kV power backup like DG set) supply the panel and breaker, which automatically isolates the bus and each feeder in case of faults. Surge arrester with CT and PT are installed at the incomer side to monitor the incomer parameters, which are linked to the SCADA system. The bus interlocking system isolates each incomer to prevent any unwanted dual operation of the sources during switching and normal operation period.

Feeder 1, 2, and 3 from the intake power supply system are connected to the HT motor pumps through starters, while the capacitor feeder supplies the Automatic Power Factor Corrector (APFC) panel. An auxiliary step-down transformer feeder is also included for other applications. The breakers, CT, and PT of each feeder are connected to the SCADA system for automation and control from the SCADA station [127-128].

The SLD of a typical LT panel for an intake system is depicted in Figure 3.7. The LT panel, like the HT panel, contains two or more incomers for grid supply and power backup (e.g. DG, Solar, etc.). An interlocking system is incorporated with MCCBs for safety. Outgoing feeders are connected to each of the LT loads and LT motors. Important

sensors for the incomer and outgoing feeders are connected to the SCADA station for control and monitoring of the system.
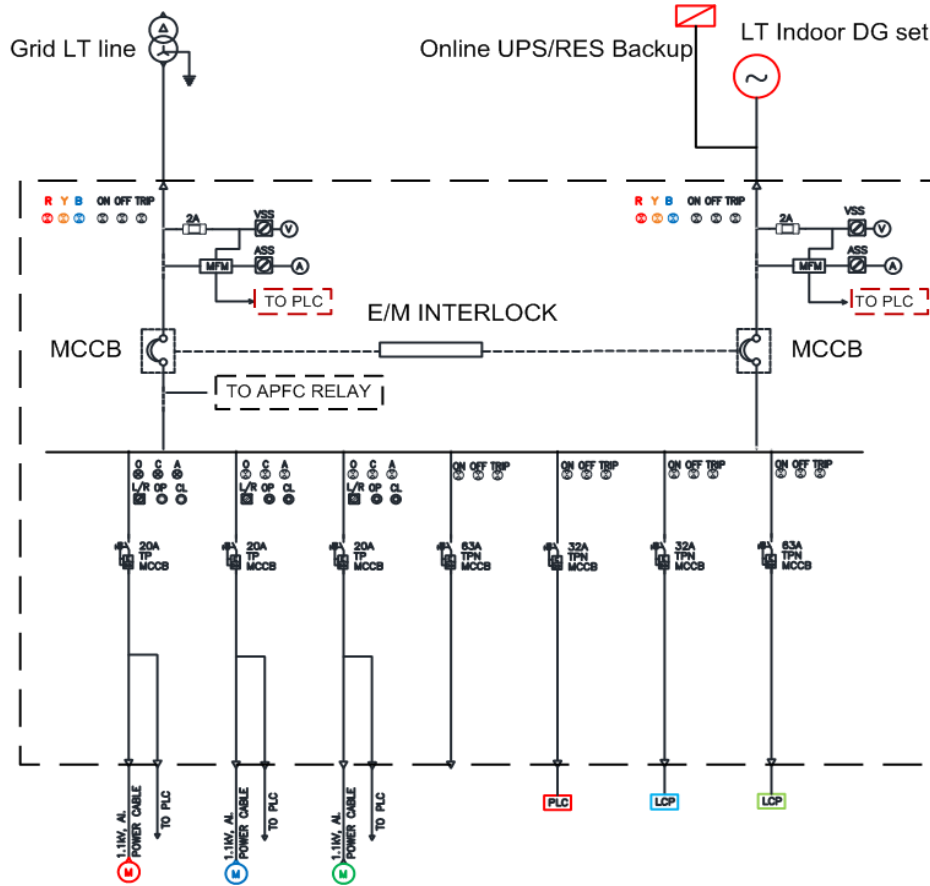
Figure 3.7 SLD of typical LT panel

3.5. Jack-well Monitoring Strategies

In order to understand monitoring strategies of Intake, the working principle of jack-well intake is discussed in the following sections.

3.5.1. Intake tower operation

An illustration showing the operation of the intake tower based on different river water level is shown in the following Figure 3.8, figure 3.9 and figure 3.10.

A. Normal Water Level Operating Condition

The normal operation of a jack-well tower under normal water level is illustrated in Figure 3.8. The tower's inlet port allows water to enter, and the water level must be between the minimum level and just below the top inlet ports. During this condition, all ports are open, and most of the water flows through the middle port. Typically, the water

level inside the tower and outside the tower is the same, which is observed during winter, spring, and autumn, although it may vary depending on the region.
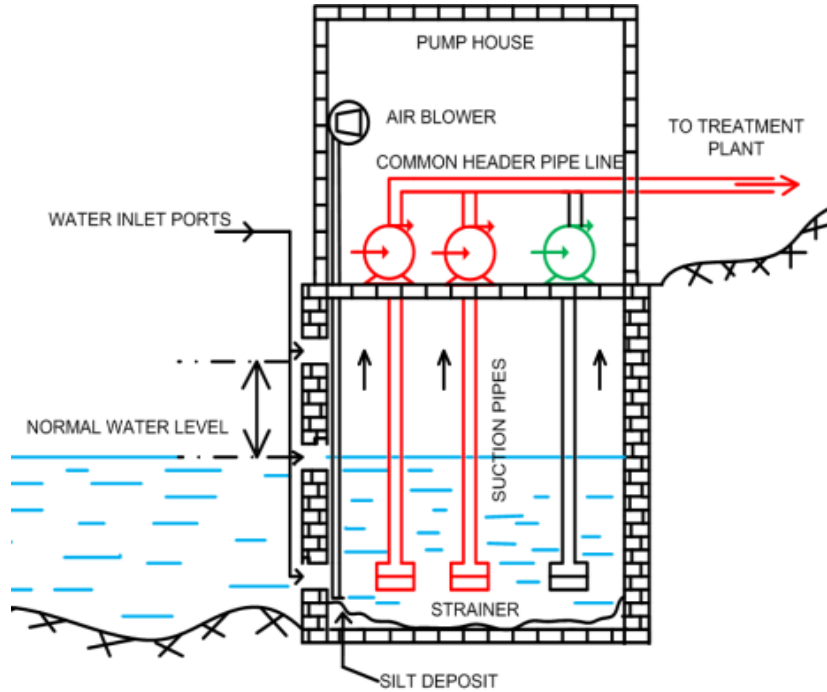
Figure 3.8. Normal water level operating condition

B. Maximum Water Level Operating Condition

Figure 3.9 depicts the functioning of the Jack-well tower under the condition of maximum water level. In this case, the external water level rises to the top inlet port, and the water level inside the tower reaches its maximum. To prevent excessive silt deposits within the tower, water flows only through the top inlet port, and all other ports are closed. This situation generally occurs during the rainy or monsoon season. However, it is crucial to halt the operation if the water level at the source reaches the base of the pump house, where the pump motors are installed.

C. Minimum Water Level Operating Condition

During the dry season, the water level from the source is significantly low, and only the lowest inlet port allows water to enter the tower. As a result, less water is available in the well. If the water level at the well is above the minimum permissible level, which is one (1) meter from the bottom of the well, the pumps are usually operated. However, if the water level drops below 1 meter, the pumps are not operated. In addition, if the silt deposit at the bottom of the well exceeds the permissible level, pumping must be

stopped, and the silt deposit must be removed. Figure 3.10 demonstrates the cleaning of the intake jack well during the dry season by activating blowers. Typically, this operation is observed during the summer and rainy seasons.
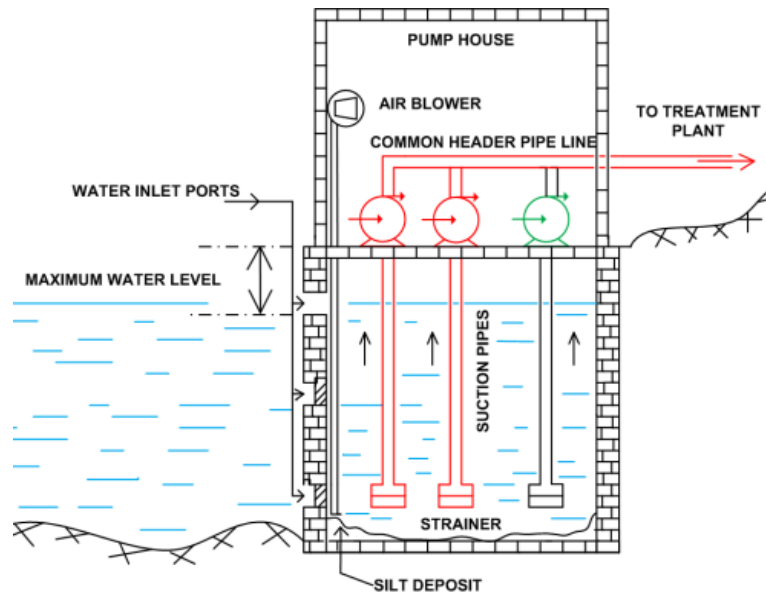
Figure 3.9. Maximum water level operating condition
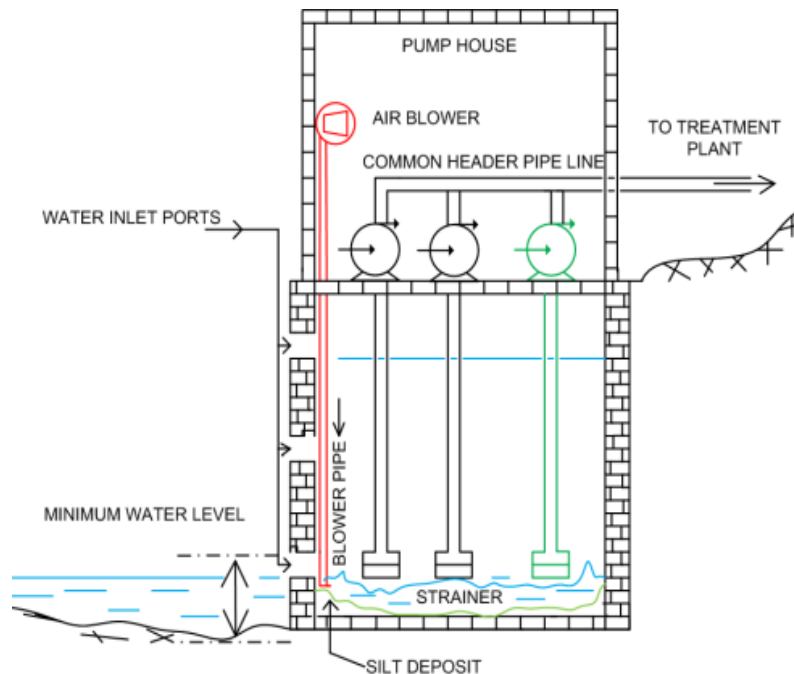
Figure 3.10 Minimum water level operating condition

3.5.2. Pump Operation

Pumps can be operated in single, double, or triple combinations depending on the availability and demand for water. The duration of pump operation can be set for a single

day or more and may vary according to seasons and water levels at the source. Table 3.2 shows an example of the operating hours per day for a typical three VT pump, taking into account the different combinations. The electrical panel feeds each pump of the jack-well intake and can be operated manually or automatically through SCADA.

Table 3.2. Typical pump operation of intake

Sl. No.	Pump combination	Working hours/day	Proposed Season
1	Single (1 pump)	8,12,24 hrs /day	Dry season
2	Double (1&2, 2&3, 3&1)	8,12hrs/day	Normal Season
3	Triple (1&2&3)	4,8,12 hrs /day	Rainy season

3.5.3. SCADA Architecture of Intake Jack-well

Figure 3.11 illustrates a typical SCADA architecture for intake (jack-well) that explains the working principle of the SCADA system. The PLC is responsible for controlling and computing the process flow of the system based on the set of instructions provided by the user through a program. The input and output of the PLC are connected to the field equipment such as pressure transmitter, level transmitter, flow transmitter, energy meter, and analyzer panel, as well as other SCADA components.
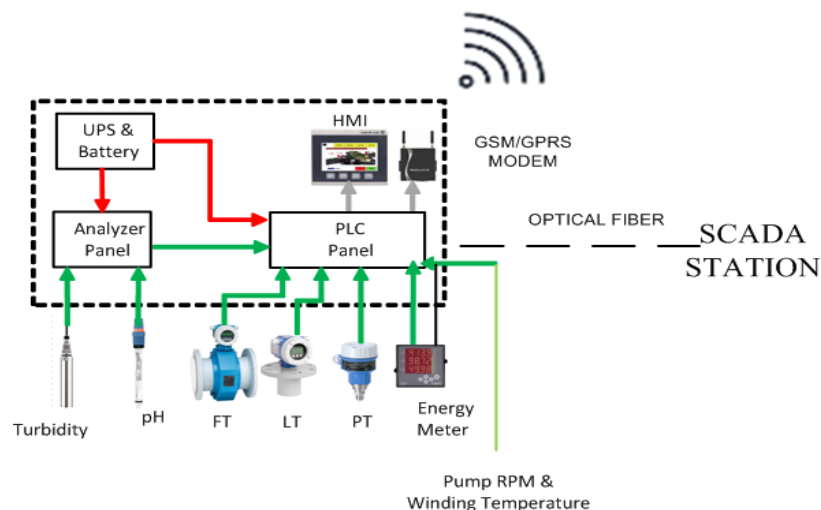
Figure 3.11 Intake SCADA architecture

The HMI serves as a platform for direct interaction between users and machines through touch screens and push buttons. An online uninterruptible power supply (UPS) with battery backup is typically included to ensure power reliability and backup during

power failures. GSM/GPRS and optical fiber media are employed for communication with the SCADA station.

3.5.4. Monitoring of Jack-well Tower

A. Water inlet ports monitoring

The inlet ports of Jack-well intake are crucial for the efficient functioning of the water supply system. Their design ensures that the water entering the well is of good quality, while allowing maximum flow rate. To prevent the entry of silt and debris, the inlet ports are designed with appropriate measures. During heavy rainfall or floods, the lower gates of the inlet port must be closed to prevent the entry of large objects and heavy silt deposits. Motorized inlet gates with SCADA system can be installed for automated open or close of the gate, which can be controlled by the water level meter alarm system. However, in most cases, the inlet port gates are designed to be operated manually.

B. Silt Deposit Monitoring and Removal

Regular cleaning of the intake jack-well is necessary to remove silt deposits and maintain water quality. During dry seasons, field staff manually remove silt deposits from the well. However, the use of SCADA systems can improve efficiency and reduce the need for manpower. Figure 3.10 shows a typical silt deposit removal method using the SCADA system. Blowers can be installed along with the pump to disturb the silt deposit and allow it to float along with the water. During this time, another submersible pump or one of the existing pumps can be used to remove the silt deposit from outside the intake tower well. The timing and monitoring of the process can be done using a level meter and turbidity sensor. Currently, visual inspection is used to determine the amount of silt deposit content in the well.

C. Water Quality Monitoring

Water quality is crucial for WTPs, and improving it is a key objective and criterion. To optimize the treatment process and enhance efficiency, monitoring and measurement of water quality are vital. pH sensor, Turbidity sensor and conductivity sensor are commonly used methods for monitoring water quality.

In addition to these water quality monitoring devices, other devices like temperature sensors, dissolved oxygen monitors, and coliform monitors can also be installed as per

the specific requirements and conditions of the site. These devices can also be integrated into a SCADA system to monitor water parameters and ensure the quality of both raw and treated water.

D. Water quantity monitoring

The effectiveness of a treatment plant is determined by various factors, including its design capacity, pipe diameter, pump capacity, filter bed design, and power supply, as well as the amount of water received at the reservoir each day. As a result, it is crucial to measure and monitor water quantity at various stages of the treatment process, from intake to the main reservoir. Flow meter, pressure transmitter, Level meter are the commonly used water quantity monitoring devices that can be installed at the intake. Commonly used sensor details as discussed above are shown in Appendix -B

E. Power Related Monitoring

The power substation of a WTP contains various protection devices, such as lightning arresters, isolators, CTs, PTs, circuit breakers, and numerical relays. These devices are connected to the SCADA system through PLC, and continuous monitoring of parameters such as current, voltage, and power consumption is done through the SCADA system. Additionally, the SCADA system is used to monitor various parameters of the power transformer, such as efficiency, oil temperature, oil pressure, overcurrent, and restricted earth faults. The data received from field equipment is used for alarm and protection settings, including the trip settings of the numerical relay, overcurrent and undercurrent protection, overvoltage and under voltage protection, and REF settings.

HT electrical panels are used to provide power supply to various HT electrical devices, such as pump motors and distribution panels. Step-down CT, PTs, and energy meters are used to monitor the incoming voltages and bus voltages, as well as the active and reactive power, power factor, frequency, current, and voltage values of the bus. The alternate power backup feeder for Diesel Engine Generator (DEG) or renewable energy sources is also monitored through the HT panels, and the mechanical or electromechanical interlock system status of the main bus is constantly monitored through the SCADA system.

Low Tension (LT) electrical panels distribute power from the transformer or diesel generator to electrical equipment or other distribution panels. The LT panel serves as a

power distribution panel for lighting and auxiliary loads, such as sample analyzer pump and LT blower, in the intake. The SCADA system can be used to monitor the energy consumption as well as the operation of LT equipment through PLC and HMI [129-130].

3.6. Case Study

This section presents a case study of the monitoring strategies implemented using SCADA system in the Intake Jack-well for GAWSS P- II, which is part of the Aizawl Water supply system in India. The purpose of this case study is to illustrate the operation of the intake and pump, as well as the SCADA architecture used in the system. The following sections also describe the ladder logic implemented for monitoring the water quantity using two electromagnetic flow meters and energy meter of the intake, as well as the substation monitoring and mapping strategies.

3.6.1. Instrument Data Mapping

The PHE department utilizes various field instruments for monitoring water parameters using a SCADA system. These instruments include level meters, flow meters, and pressure transmitters for monitoring water quantity, as well as turbidity and pH sensors for raw water quality monitoring. Energy meters are used to monitor the power consumption of the pump. Real-time data from these field instruments are connected to a PLC panel and monitored from a SCADA station located in the control room. CIMPLICITY 10.0 software is used for programming the PLC logic using ladder logic. It is important to periodically clean and maintain these instruments in order to retrieve accurate readings, and reliable power supply is necessary for the vulnerable electronic components embedded in the sensors. Qualified and experienced personnel are required for the cleaning and maintenance work for each field equipment.

3.6.2. Flow Chart Data Mapping

Figure 3.12 shows a flow chart that outlines the equipment data mapping for monitoring water quality using flow meters at the jack well intake, and the operation of the pump using ladder logic is explained in this section. Also, Table 3.3 shows the port allocation of magnetic flow meter and energy meter in the PLC.

To begin with, the program initializes the mapping of real-time data from field equipment by using the MOVE REAL command, as shown below:

1. Start

2. Map Flow Meter-1 input and output data

3. Map Flow Meter-2 input and output data

4. Map Energy Meter phase line current data

5. Map Energy Meter phase active current data

6. Map Energy Meter phase reactive current data

7. Map Energy Meter active, reactive, and apparent power data

8. Map Energy Meter RYB phase voltage data

9. Map Energy Meter average power factor data

10. Map Energy Meter frequency data

11. Check for the activation of automatic settings of Pump-1

12. Check for the activation of automatic settings of Pump-2

13. Check i/p (start/stop) command; if the condition is true for all, start/stop Motor-1

14. Check i/p (start/stop) command; if the condition is true for all, start/stop Motor-2

15. Stop

3.6.3. Ladder logic

The ladder logic shown in Figure 3.13 is used for equipment data mapping and automatic pump ON/OFF operations. The logic uses a MOVE REAL block to collect input data from the electromagnetic flow meter, including flow rate and totalizer value, from input ports W00003, W00005, W00013, and W00015. This real-time data is then sent to the PLC and computer at the SCADA station using assigned tag names/numbers.

Similarly, pump energy data such as line and phase current, active power, reactive power, apparent power, phase voltage, power factor, and frequency are also collected by the PLC. The logic diagram shows the monitoring of the current state and automatic operation, such as ON and OFF control, of two feedback pumps based on different conditions. This same concept can be applied to monitor and control SCADA systems using ladder logic in any other treatment plant.

3.7. Observations

This section discusses the real-time data collected from the intake of GAWSS P- II over a 24-hour period. The observations were made by analyzing the daily report of a

specific sensor data, namely the electromagnetic flow meter and energy meter, using ladder logic through SCADA.

3.7.1. Flow Meter

The flow meter reading for a 24-hour period at the GAWSS P- II intake is presented in Table 3.4. The totalizer value shows the cumulative sum of all flow rates in cubic meters, which can be used to calculate the total water quantity flowing through a pipeline during a specific time period. The flow rate represents the speed of water flowing through the pipeline and is measured in cubic meters per hour. Figure 3.14 illustrates the graph of totalizer readings and flow rate (Y-axis) versus time (X-axis), which shows that the flow rate of raw water remains stable during pumping hours. The totalizer curve gradually increases, indicating the summation of all flow rates over time. The flow rate and totalizer value depend on various factors such as pump type, pipe diameter and configuration, and water quality. The time interval for data generation is adjustable based on specific requirements.

3.7.2. Energy Meter Reading

The energy meter reading for the intake jack-well over a 24-hour period is provided in Table 3.5, along with a graphical representation in Figure 3.15. The graph shows the behavior of various system parameters, such as line current, active power, power factor, line voltage, and frequency during pumping hours and intervals. It also reveals a drop in power and current for three hours from 7:00 A.M. to 10:00 A.M., which is attributed to the switching or scheduling of the pump.

To prevent unwanted tripping of the breaker, alarm settings for upper and lower limits can be implemented in the SCADA system. In addition, SCADA settings can be customized to change plot intervals for each data, and daily report curves and alarm settings can be tailored according to the user's needs. This provides a robust platform for monitoring various parameters and scheduling of the WTP.

3.7.3. Substation Feeder Monitoring

In this section, we will discuss the data collected for the substation feeders. Figures 3.16, 3.17, and 3.18 show the monitoring of feeder substation parameters, such as voltage, phase currents, frequency, real and reactive power, power factor, etc. Additionally, Tables 3.6, 3.7, and 3.8 present the 132/33 kV power substation incomer

and feeder energy meter readings of the outgoing feeders I & II that were monitored for the operation of the WTP.

Similar to the energy meter readings shown in the previous section, the data collected from the incoming 132 kV line and 33 kV outgoing feeder I and II are plotted against time for 24 hours. The droop in the graph is due to the transition of pumping from dual-single-dual or triple-dual-triple operation of the pump. Normally, only one or two pumps are operated to optimize the pumping schedule for a given period of time. The figure shows that pumps are operated in single mode from 1:00 P.M. to 9:00 P.M. and continue in dual operation mode for the rest of the day. The operating hours depend on various factors such as the health of the pump, different seasons, load demand, and availability of water, etc.
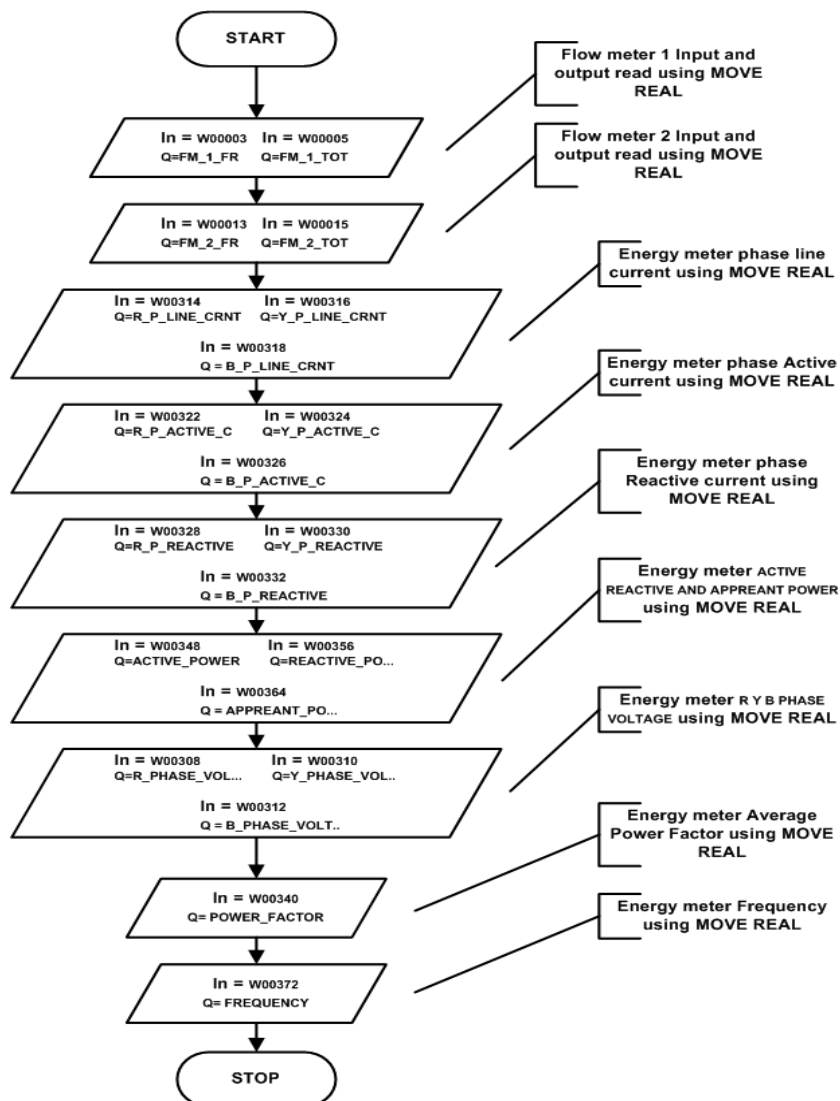
Figure 3.12 Flow chart for data mapping

Table 3.3 Port allocation of PLC

Sl. No.	Port (In)	Port Allocation
1	Magnetic Flow meter	
1.1	W00003	Flow meter 1 Flow rate
1.2	W00005	Flow meter 1 Totalizer
1.3	W00013	Flow meter 2 Flow rate
1.4	W00015	Flow meter 2 Totalizer
2	Energy meter	
2.1	W00314	R Phase Line Current
2.2	W00316	Y Phase Line Current
2.3	W00318	B Phase Line Current
2.4	W00322	R Phase Active Current
2.5	W00324	Y Phase Active Current
2.6	W00326	B Phase Active Current
2.7	W00323	Active Power
2.8	W00356	Reactive Power
2.9	W00364	Apparent Power
2.10	W00308	R Phase Voltage
2.11	W00310	Y Phase Voltage
2.12	W00312	B Phase Voltage
2.13	W00340	Power Factor
2.14	W00372	Frequency
3	Pump mapping	
3.1	100001	Auto Feedback pump 1

3.8. Implementation of Pump and Backwash Scheduling

This section discusses the implementation of pump and backwash scheduling in the WTP for improved pump operation and reduced operation costs. Priority options in the SCADA screen were used along with ladder logic to achieve this. Additionally, ladder logic was used to implement backwash scheduling, which increased the efficiency of the filter bed and reduced backwash time.

3.8.1. Optimization of Pump and Backwash Scheduling

The SCADA system for Greater Aizawl Water Supply System phase I & II not only monitors water quality and quantity online but also detects faults through alarm systems. Furthermore, the implementation of pump scheduling and backwash scheduling methods through the SCADA system has enhanced the overall efficiency of the WTP. These methods keep track of the operational schedule of pumps to reduce operational costs and backwash timing for filter beds at Dihmunzawl and Lawipu filter houses

.
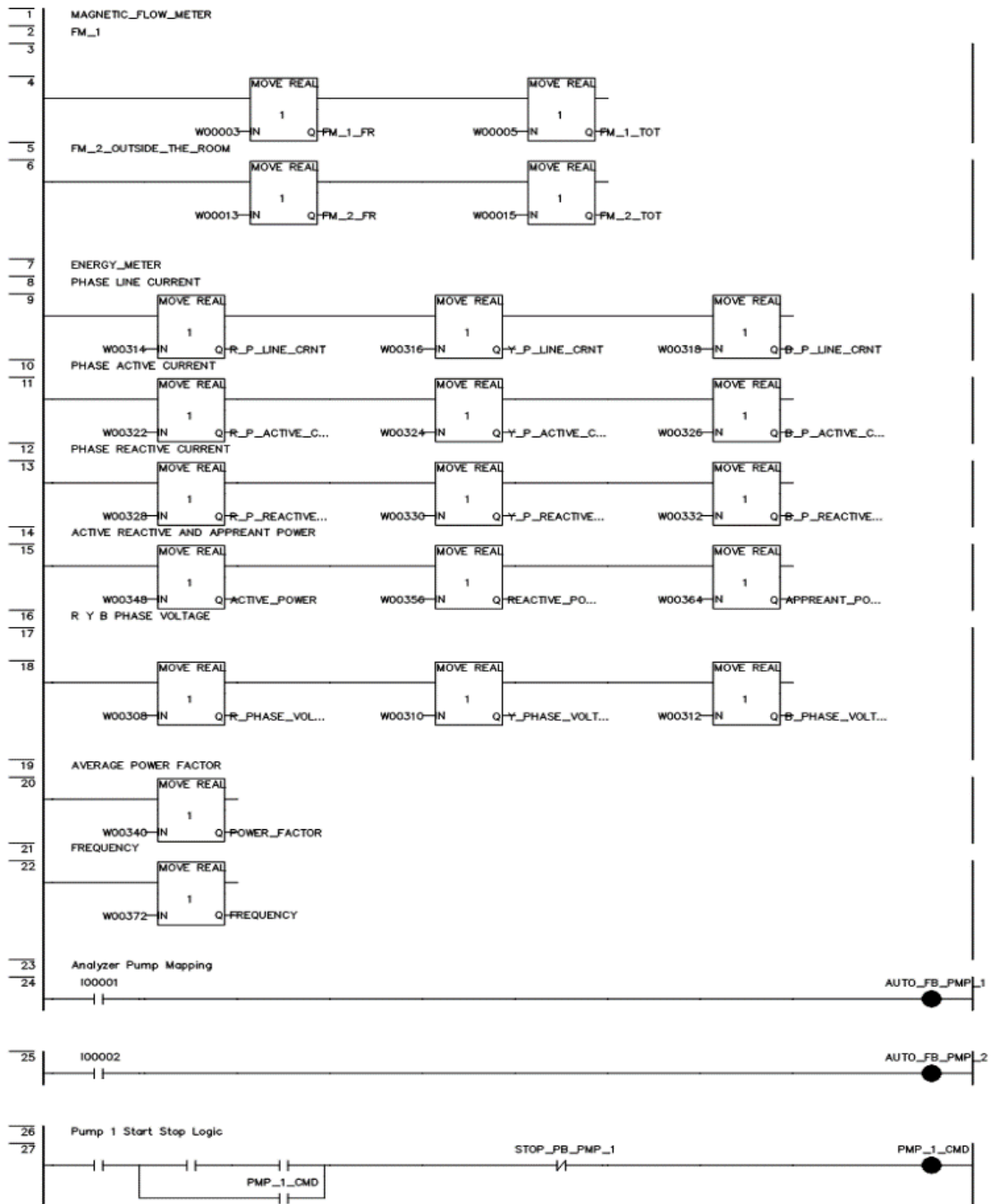
Figure 3.13. Ladder logic for the study system

Table 3.4 Flow meter-I readings of intake

Sl. No	Time	Totalizer in m³	Flow rate m³/hr (x11580)
1	12:00	4606167.000	398.091
2	01:00	4606563.000	398.091
3	02:00	4606959.000	398.091
4	03:00	4607354.000	398.091
5	04:00	4607750.000	398.091
6	05:00	4608145.500	398.091

7	06:00	4608541.000	398.091
8	07:00	4608936.500	398.091
9	08:00	4609337.500	398.091
10	09:00	4609741.000	398.091
11	10:00	4610133.000	398.091
12	11:00	4610520.500	398.091
13	12:00	4610907.000	398.091
14	13:00	4611294.000	398.091
15	14:00	4611680.500	398.091
16	15:00	4612068.000	398.091
17	16:00	4612453.000	398.091
18	17:00	4612840.500	398.091
19	18:00	4613227.500	398.091
20	19:00	4613614.000	398.091
21	20:00	4614000.500	398.091
22	21:00	4614385.500	398.091
23	22:00	4614771.000	398.091
24	23:00	4615156.500	398.091
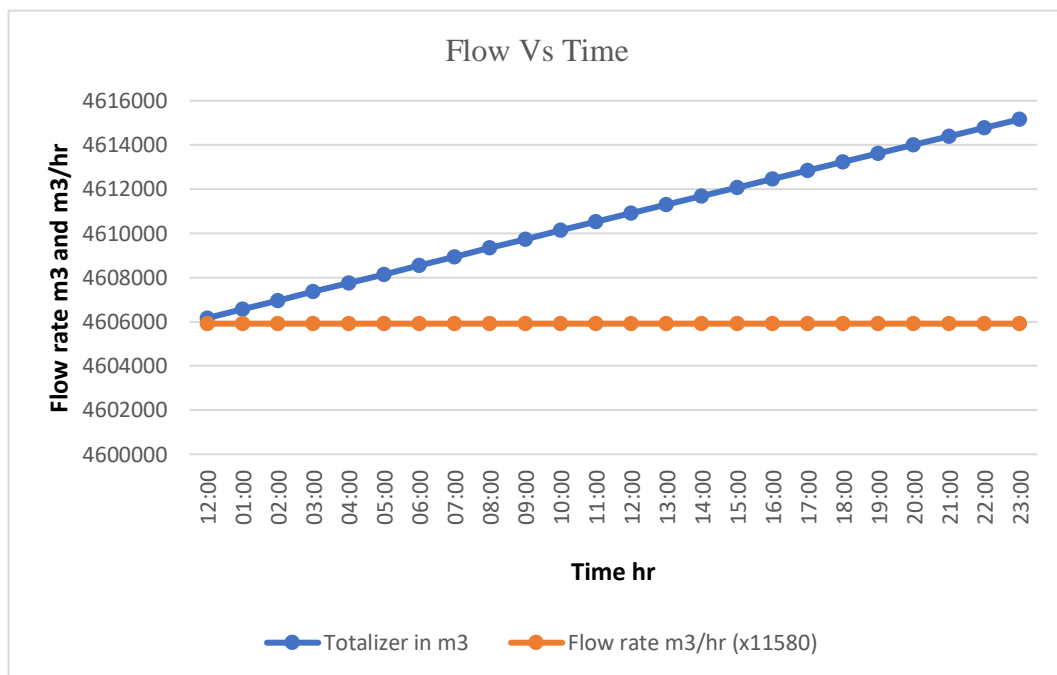
Figure 3.14 Flow Rate Vs Time

Table 3.5. Intake Energy meter data

Sl. No.	Time	Pump 1 current Ampere	Pump 1 active power kW	Pump 1 power factor	Pump 1 R phase to neutral voltage (V)	Pump 1 Y phase to neutral voltage (V)	Pump 1 B phase to neutral voltage (V)
1	00:00	364.915	196.931	0.790	405.007	406.595	403.681
2	01:00	365.539	197.531	0.784	408.493	410.051	407.226
3	02:00	364.932	196.950	0.779	410.308	411.798	408.982
4	03:00	365.708	197.371	0.776	411.742	413.308	410.492
5	04:00	366.619	198.091	0.775	412.593	414.228	411.317

6	05:00	367.097	197.582	0.773	413.401	414.909	411.914
7	06:00	363.028	194.418	0.781	407.418	408.991	406.047
8	07:00	362.852	197.693	0.798	402.051	404.229	401.155
9	08:00	363.676	196.456	0.802	399.144	400.591	397.884
10	09:00	250.313	135.937	0.797	404.777	406.604	403.686
11	10:00	249.485	136.057	0.797	405.331	406.893	404.186
12	11:00	252.027	137.465	0.794	407.988	409.424	406.636
13	12:00	251.874	137.855	0.799	406.184	407.578	404.975
14	13:00	249.962	135.494	0.787	407.593	408.941	406.126
15	14:00	247.946	137.549	0.798	405.583	407.210	404.414
16	15:00	372.397	201.802	0.802	397.645	399.079	396.381
17	16:00	253.529	139.684	0.802	403.111	404.560	401.795
18	17:00	253.354	138.881	0.806	400.874	402.691	399.504
19	18:00	253.928	141.507	0.810	402.274	404.575	401.205
20	19:00	256.867	139.935	0.813	398.713	401.511	397.109
21	20:00	253.039	139.241	0.811	398.881	401.577	398.120
22	21:00	253.087	139.400	0.805	402.431	404.659	401.366
23	22:00	252.832	139.452	0.800	405.837	407.538	404.494
24	23:00	253.499	139.826	0.793	409.524	411.345	408.157
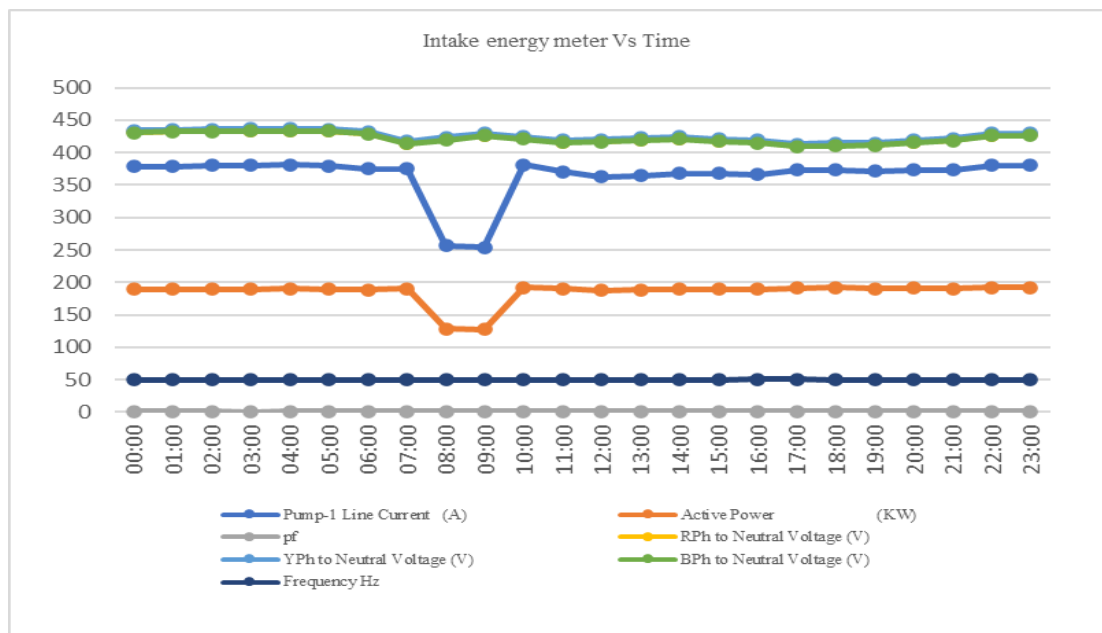
Figure 3.15. Intake Energy meter readings

Table 3.6. 132 kV Feeder Vs Time

Time	Voltage (KV)	R_{Ph}(A)	Y_{Ph} (A)	B_{Ph} (A)	Frequency (Hz)	Power (Mw)	Mvar	Pf
1.00	137.26	35.12	34.80	36.70	50.11	7.66	5.76	0.904
2.00	136.92	35.02	34.74	36.64	50.06	7.60	5.72	0.904

3.00	137.36	34.98	34.72	36.63	50.00	7.64	5.74	0.903
4.00	137.21	35.08	34.81	36.65	50.00	7.64	5.70	0.904
5.00	137.53	34.84	34.57	36.45	50.06	7.62	5.72	0.903
6.00	137.50	34.87	34.67	36.53	50.01	7.62	5.72	0.903
7.00	137.48	34.86	34.58	36.57	50.05	7.62	5.70	0.904
8.00	137.34	35.04	34.58	36.46	50.08	7.64	5.72	0.903
9.00	137.38	34.98	34.52	36.53	50.06	7.64	5.70	0.903
10.00	136.18	34.86	34.65	36.48	50.06	7.64	5.70	0.903
11.00	136.08	35.44	34.71	36.94	50.08	7.64	5.66	0.906
12.00	133.56	35.43	34.91	37.39	50.11	7.64	5.50	0.910
13.00	130.92	24.06	23.71	25.30	50.10	5.94	4.28	0.932
14.00	129.72	24.28	24.09	25.50	50.07	5.26	3.78	0.944
15.00	130.25	24.19	23.45	25.56	50.09	5.30	3.80	0.923
16.00	130.57	23.69	23.60	24.92	50.16	5.18	3.78	0.943
17.00	131.57	23.54	23.39	24.54	50.13	5.12	3.78	0.943
18.00	131.22	23.35	23.34	24.48	50.00	5.12	3.78	0.943
19.00	131.62	27.32	27.19	28.44	49.96	5.90	4.34	0.931
20.00	131.87	36.01	35.99	37.45	50.07	7.62	5.50	0.912
21.00	131.97	36.02	35.89	34.46	50.08	7.62	5.52	0.912
22.00	132.17	35.77	35.65	37.14	50.07	7.60	5.54	0.911
23.00	132.25	36.02	35.9	37.59	49.98	7.66	5.58	0.911
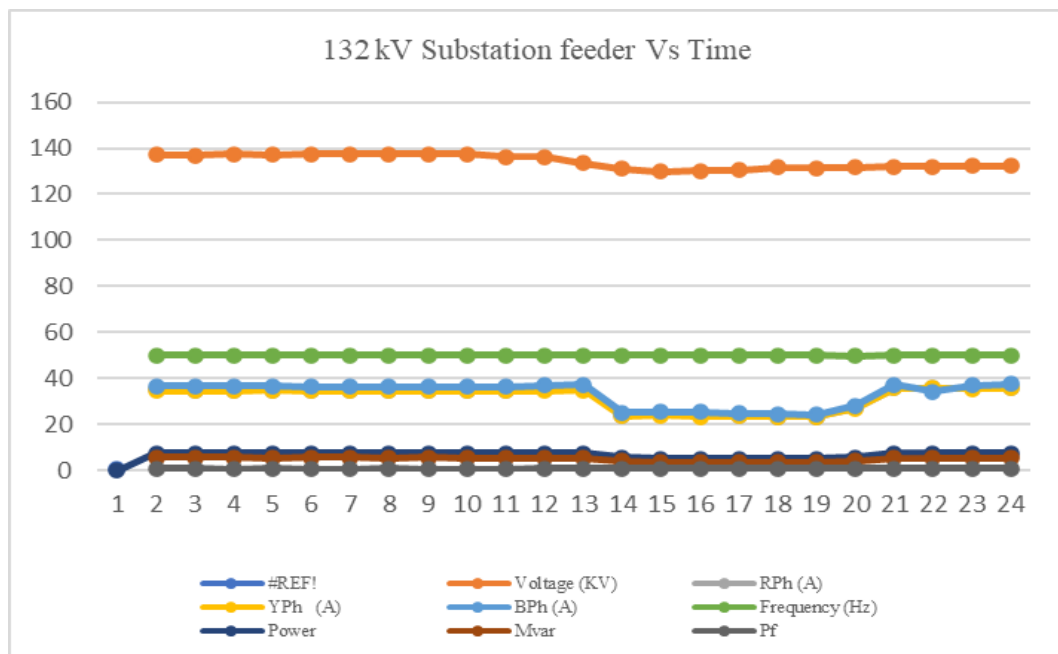
Figure 3.16. 132 kV Feeder Vs Time

Table 3.7. 33 kV Feeder I Vs Time

Time	Voltage (KV)	R_{Ph} (A)	Y_{Ph} (A)	B_{Ph} (A)	Frequency (Hz)	Power (MW)	Mvar	pf
1.00	33.95	52.22	51.12	55.10	50.07	2.95	0.92	0.955
2.00	33.94	51.87	50.78	54.66	49.99	2.93	0.92	0.954
3.00	33.96	52.18	50.70	54.67	50.07	2.95	0.92	0.955
4.00	33.95	52.14	51.07	54.88	50.05	2.95	0.92	0.954

5.00	34.03	51.67	50.47	54.53	50.05	2.93	0.92	0.954
6.00	34.01	51.52	50.13	54.20	50.03	2.92	0.92	0.955
7.00	34.04	51.68	50.18	54.38	50.07	2.93	0.92	0.954
8.00	34.05	51.67	50.46	54.52	50.08	2.92	0.92	0.955
9.00	33.95	51.67	50.11	54.02	50.03	2.92	0.92	0.954
10.00	33.88	51.64	50.38	54.04	50.04	2.93	0.92	0.956
11.00	33.62	51.69	50.26	54.73	50.02	2.92	0.92	0.956
12.00	33.00	51.95	51.35	56.33	50.11	2.93	0.92	0.958
13.00	32.45	52.38	52.82	57.12	50.11	2.91	0.92	0.959
14.00	32.25	38.80	38.21	42.06	50.10	2.18	0.92	0.983
15.00	32.38	38.80	38.21	42.40	50.20	2.19	0.92	0.983
16.00	32.66	38.91	38.86	41.32	50.17	2.18	0.92	0.983
17.00	32.70	38.15	37.85	41.47	50.04	2.19	0.92	0.982
18.00	32.56	38.21	37.93	41.48	50.00	2.19	0.92	0.983
19.00	32.65	38.30	37.96	55.86	50.08	2.89	0.92	0.958
20.00	32.61	52.78	52.16	55.96	50.10	2.89	0.92	0.959
21.00	32.67	52.79	52.29	56.22	50.04	2.88	0.92	0.958
22.00	32.67	53.77	53.11	56.07	50.05	2.89	0.92	0.957
23.00	32.73	53.81	57.26	55.89	50.06	2.88	0.92	0.958
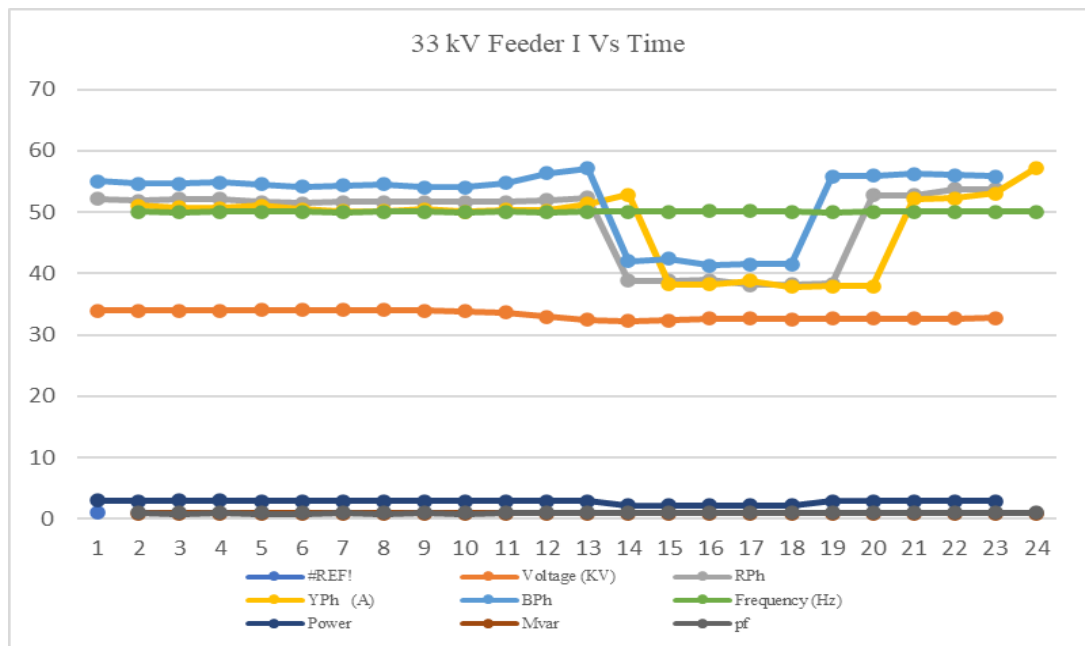
Figure 3.17. 33 kV Feeder I Vs Time

Table 3.8. 33 kV Feeder II Vs Time

Time	Voltage (KV)	R_{Ph} (A)	Y_{Ph} (A)	B_{Ph} (A)	Frequency (Hz)	Power (MW)	MVAR	pf
1.00	33.31	92.75	87.5	88.26	50.02	4.64	2.37	0.891
2.00	33.28	92.32	87.03	88.08	49.98	4.61	2.36	0.890
3.00	33.52	92.03	87.08	87.81	50.08	4.60	2.36	0.889
4.00	33.51	92.26	87.11	88.01	50.00	4.62	2.36	0.890
5.00	33.59	92.27	87.24	88.19	50.00	4.62	2.37	0.889

6.00	33.54	92.06	87.09	87.73	50.02	4.61	2.37	0.889
7.00	33.51	92.32	87.02	87.81	50.08	4.61	2.36	0.890
8.00	33.57	92.28	86.96	88.18	49.98	4.62	2.37	0.889
9.00	33.46	91.88	86.77	87.74	50.00	4.6	2.36	0.890
10.00	33.28	91.77	86.92	87.85	50.08	4.61	2.32	0.890
11.00	33.19	92.62	87.36	88.52	49.98	4.62	2.31	0.893
12.00	32.52	94.64	88.63	89.35	50.11	4.63	2.24	0.900
13.00	32.03	60.95	56.70	57.69	50.11	3.02	1.28	0.920
14.00	32.00	61.51	57.37	57.66	50.10	3.01	1.26	0.922
15.00	32.14	61.61	57.67	57.84	50.20	3.04	1.27	0.922
16.00	32.24	59.75	55.83	56.31	50.17	2.95	1.25	0.921
17.00	32.42	59.18	55.6	56.14	50.04	2.94	1.25	0.923
18.00	32.4	58.55	55.44	55.69	50.00	2.93	1.25	0.919
19.00	32.5	58.66	55.61	56.04	50.08	2.94	1.26	0.919
20.00	32.15	95.50	91.22	91.17	50.10	4.66	2.22	0.902
21.00	32.21	94.79	90.21	90.56	50.04	4.63	2.23	0.901
22.00	32.25	94.85	90.37	90.35	50.05	4.63	2.22	0.902
23.00	32.29	94.96	90.09	90.34	50.06	4.64	2.23	0.901
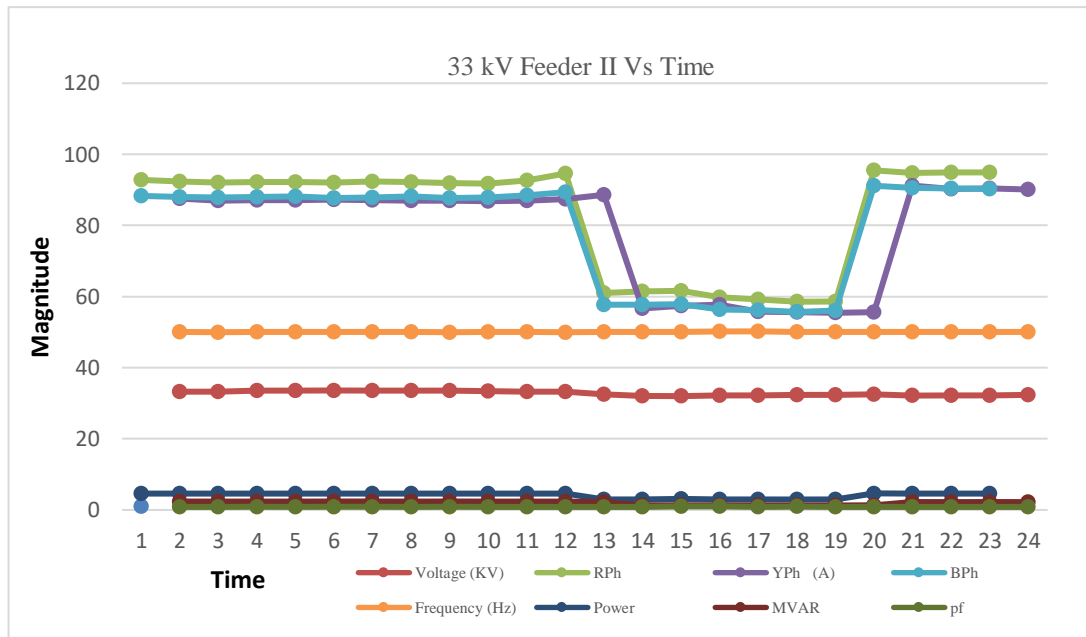
Figure 3.18. 33 kV Feeder II Vs Time

A. Pump Scheduling
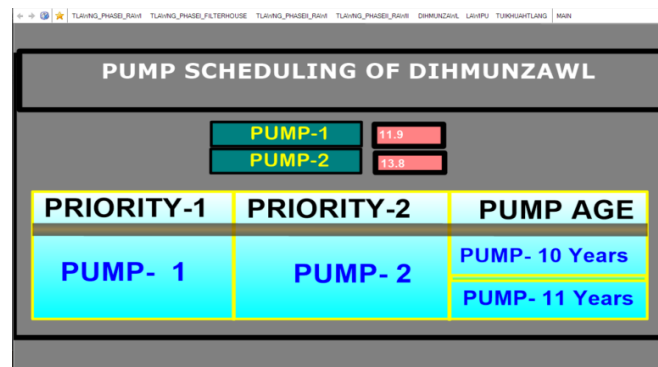
Although there is no specific optimization method implemented for monitoring the energy efficiency of the WTP, pump scheduling is a crucial aspect of the plant's operation in reducing costs and improving efficiency. The SCADA system employs a priority list method to optimize the pump unit commitment, where the most efficient

unit is prioritized, followed by the less efficient units in an orderly manner. This priority order is based on the average energy consumption versus output flow of a single pump, ignoring startup costs and slight fluctuations. The primary goal of pump scheduling optimization is to consume less energy per produced water flow quantity of the pump.

Table 3.9. General cases for Pump scheduling

Pump	Case 1	Case 2	Case 3	Case 4
Pump 1	Electrical	Soft starter	10 years	11.9 (P/f)
Pump 2	Electrical	Star delta	11 years	13.8(p/f)
Pump 3	Diesel	DOL	10 years	NIL
Pump 4	Diesel	DOL	10 years	NIL

The water supply system of GAWSS P- I & II consists of 6 pumping stations with a total of 23 pumps, including diesel engine-driven pumps of varying capacity, efficiency, and age, at each pumping level. To understand the concept of pump scheduling implemented in the SCADA system, pump optimization constraints for a specific area, Dihmunzawl, are constructed and presented in Table 3.9.

Figure 3.19. Pump scheduling of Dihmunzawl

Among the four pump sets, pumps 1 and 2 are electrical-driven pumps with soft starters and the same manufacturer and capacity. These pumps are healthy enough to run continuously, whereas pumps 3 and 4 are diesel-driven and are not recommended to run except during power failures. The energy consumption versus outflow of the pipeline for pumps 1 and 2 is slightly different, and based on the calculation of the energy versus outflow of each pump, pump 1 is considered as the first priority, and pump 2 is considered as the second priority. The pipeline allows two pumps to work together. All the constraints are considered for the optimization algorithm, and the

results of the optimization process are presented in Figure 3.19 as a table for optimal pump unit scheduling of the Dihmunzawl area.

B. Backwash Scheduling

The backwash scheduling method implemented in the GAWSS P- I&II is designed to improve the filtration process and maintain the health of the filter bed. The commonly used LOH method has limitations due to equipment malfunctioning, therefore a new method was developed based on the set points of installed equipment such as Level meter, open channel flow meter, and Turbidity value. When these water parameters reach the set points, the backwash timer is triggered, and the duty personnel in the SCADA station proceeds with the backwash operation. This method ensures relevant timing for backwash and helps to maintain the efficiency of the filter bed.

I. Filtration Concept of the WTP

WTPs typically contain multiple filter beds for removing impurities from clarified water, and the Greater Aizawl Water Supply System Phase I has four filter beds within its filter house. Clarified water enters the beds and is filtered through a filter media, with clean water collected at the bottom and transported to the clear water sump via an open channel water line. Figure 3.20 provides an example of a filter bed and its functions within GAWSS P- I.
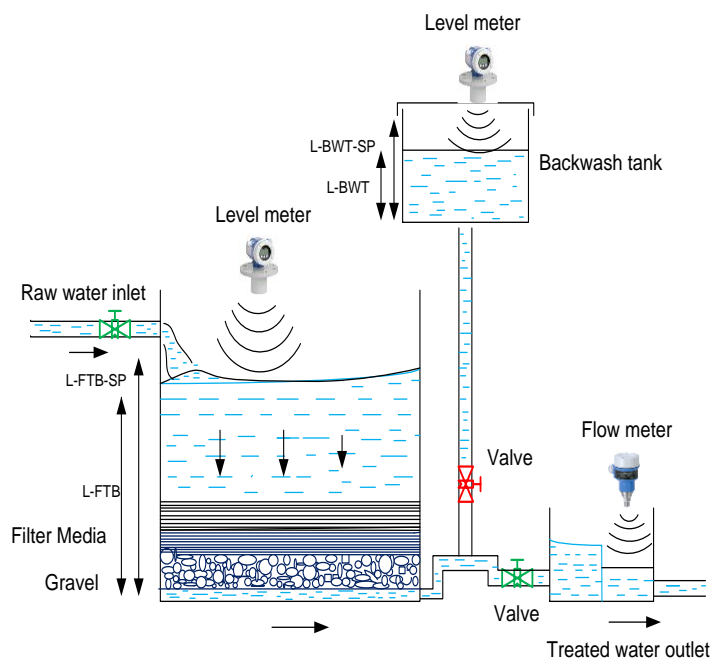
Figure 3.20 Filter bed.

Each filter bed and backwash tank is equipped with an ultrasonic level meter to measure water level, with a set point range established at the SCADA station for monitoring purposes. An open channel flow meter is also installed to measure the outflow rate from the filter bed, with set point ranges established for the treated water outlet flow rate. During normal operation, the inlet and outlet valves remain open while the backwash valve is closed, and backwash processes are only initiated when the plant operates outside of the established set point ranges.

II.   Backwash Scheduling

The primary purpose of backwash operation is to clean the filter bed, as depicted in Figure 3.21. To initiate backwash, the PLC/HMI and SCADA station apply various set points for filter bed level, backwash tank level, and outflow rate, as shown in Table 3.10. Prior to commencing backwash operation, the program verifies the availability of the aforementioned set point data from the filter bed. If all set point constraints are met in the SCADA program, the backwash operation is started by closing the inlet and outlet valves and opening the backwash valve. This enables water from the backwash tank to pass through the filter media in reverse, facilitating further backwash operations. In addition to this, the air blower is operated to produce scour air, which plays a critical role in the backwash operation. However, the figure below does not show the operation of the air blower.
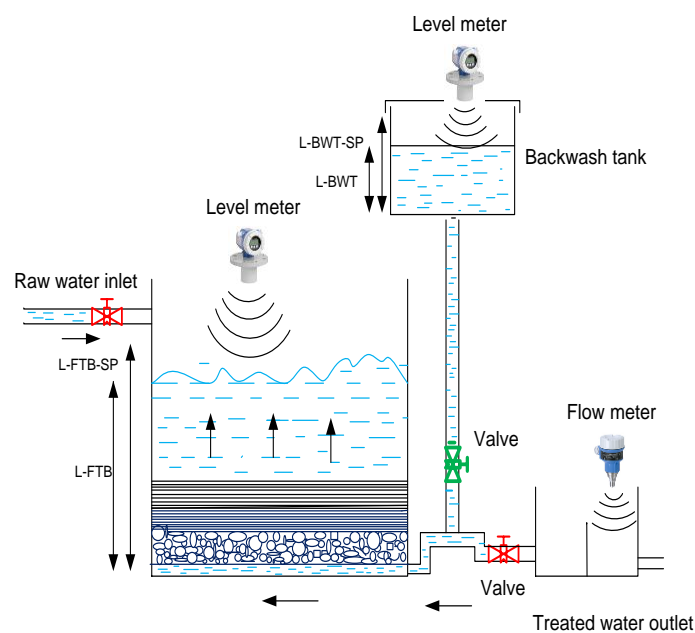
Figure 3.21 Backwash operation

In Figure 3.22, the flow chart for backwash operation using SCADA system is presented. The program begins by checking the Backwash tank level to determine if the water level is above the setpoint values or not. If it is below the set point value, the program signals to start the pump to refill the backwash tank until the set point is reached. Once the condition meets the set point value, the program checks the level of filter bed starting from bed no. 1 until bed no. n and stops if the count equals n.
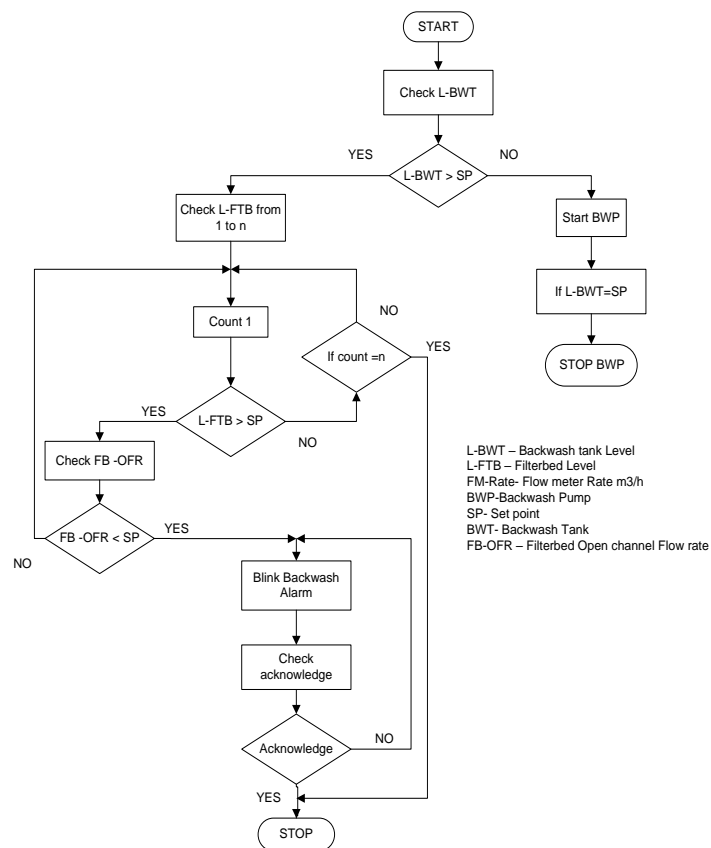
Figure 3.22 Backwash Flow chart

Table 3.10 Set points for filter bed

Description	SP-1 (min)	SP-2 (optimum)	SP- 3 (maximum)
L-BWT- SP	0.2 m	1.8 m	2 m
L-FTB – SP	1 m	2.4 m	2.8 m
FB-OFR – SP	20 m3/h	25m3/h	30 m3/h

If the level of the filter bed is greater than the set point, the program then checks the filter bed open channel flow rate by comparing it with the given set point. If the flow rate value is below the set point, the program initiates a signal for backwash

operation by sending an alarm to the filter section in the SCADA screen. If the condition does not meet the set points, the program returns to the loop search.

Table 3.11. Average Turbidity reading at Tuikhauhtlang reservoir

Date	May-20 Average Turbidity	Jun-20 Average Turbidity	May-19 Average Turbidity	Jun-19 Average Turbidity
1- May/June	0.982	2.086	3.21	2.63
2- May/June	1.045	2.429	3.25	3.87
3- May/June	1.763	2.735	4.16	3.45
4- May/June	1.561	2.039	4.22	4.22
5- May/June	1.862	1.897	2.15	2.87
6- May/June	1.692	1.871	3.56	3.45
7- May/June	1.245	1.822	3.87	4.12
8- May/June	1.241	1.876	3.45	4.68
9- May/June	0.994	1.91	2.55	4.28
10- May/June	0.983	2.334	2.45	5.41
11- May/June	0.784	2.359	2.15	4.66
12- May/June	2.014	3.012	3.75	4.25
13- May/June	1.632	2.411	3.12	6.54
14- May/June	1.982	2.083	3.22	6.55
15- May/June	0.998	2.25	2.58	6.23
16- May/June	0.956	2.137	2.69	5.46
17- May/June	0.992	2.385	3.55	5.26
18- May/June	1.436	2.279	4.22	4.65
19- May/June	1.865	2.368	3.89	3.55
20- May/June	1.732	2.656	3.22	5.42
21- May/June	1.674	2.728	2.56	5.31
22- May/June	1.224	2.226	2.11	5.66
23- May/June	1.245	1.983	1.89	4.52
24- May/June	0.983	1.954	4.25	4.55
25- May/June	1.452	2.038	3.33	4.78
26- May/June	1.874	1.932	3.52	3.86
27- May/June	1.456	2.014	3.45	3.24
28- May/June	1.843	1.890	2.88	2.88
29- May/June	1.842	2.031	2.98	2.98
30- May/June	2.068	1.89	3.66	3.58
31- May/June	2.337	-	3.21	-
Average Turbidity Value	1.476	2.187	3.19	4.43

Once all the conditions for backwash operation are met, the SCADA system will alert the operator by initiating an alarm and displaying a blinking filter bed on the screen. This will help the operator understand the timing for backwash. To acknowledge the backwash process, the operator can click the acknowledge button to stop the alarm and blinking. If the operator does not acknowledge the alarm, it will continue to revert back to the loop until the backwash operation is completed. The

minimum, optimum, and maximum set point values for the level of backwash tank, level of filter bed, and filter bed open channel flow rate are shown in Table 3.10.
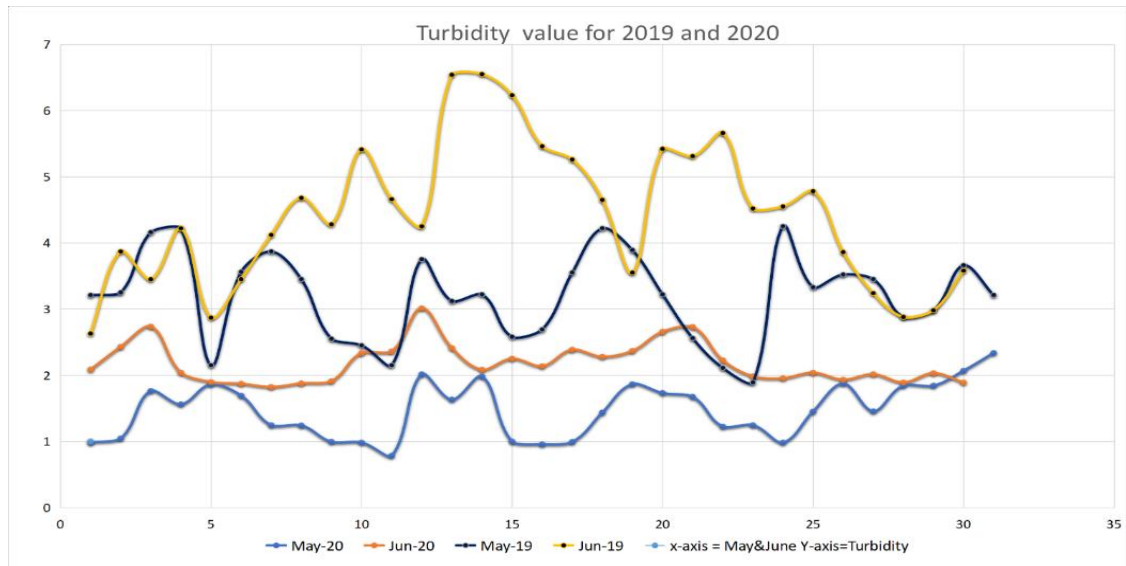
Figure 3.23. Turbidity value comparison
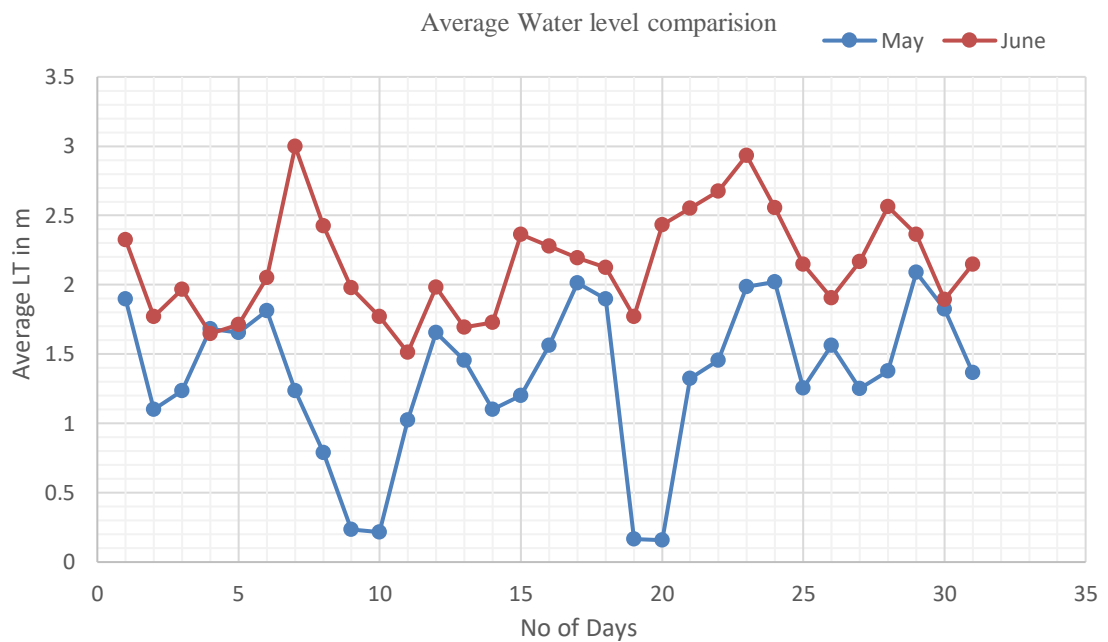
Figure 3.24. Water Level May Vs June.

Table 3.11 and Table 3.12 compare the average Turbidity and Level Transmitter readings at the reservoir for the months of May and June after implementing pump scheduling and backwash scheduling. The results show an improvement in both the

quantity and quality of treated water. Figure 3.23 and Figure 3.24 depict the corresponding graphs.

Table 3.12. Average water level reading at Tuikhuahtlang reservoir

May		June	
Date	Average LT reading(mtr)	Date	Average LT reading(mtr)
1-May-20	1.897	1-Jun-20	2.324
2-May-20	1.101	2-Jun-20	1.772
3-May-20	1.235	3-Jun-20	1.966
4-May-20	1.684	4-Jun-20	1.647
5-May-20	1.654	5-Jun-20	1.714
6-May-20	1.812	6-Jun-20	2.053
7-May-20	1.234	7-Jun-20	2.997
8-May-20	0.789	8-Jun-20	2.426
9-May-20	0.234	9-Jun-20	1.979
10-May-20	0.216	10-Jun-20	1.772
11-May-20	1.025	11-Jun-20	1.511
12-May-20	1.657	12-Jun-20	1.983
13-May-20	1.456	13-Jun-20	1.695
14-May-20	1.102	14-Jun-20	1.727
15-May-20	1.203	15-Jun-20	2.364
16-May-20	1.564	16-Jun-20	2.278
17-May-20	2.013	17-Jun-20	2.193
18-May-20	1.897	18-Jun-20	2.123
19-May-20	0.165	19-Jun-20	1.771
20-May-20	0.158	20-Jun-20	2.431
21-May-20	1.325	21-Jun-20	2.551
22-May-20	1.456	22-Jun-20	2.675
23-May-20	1.987	23-Jun-20	2.934
24-May-20	2.021	24-Jun-20	2.557
25-May-20	1.254	25-Jun-20	2.149
26-May-20	1.564	26-Jun-20	1.906
27-May-20	1.253	27-Jun-20	2.169
28-May-20	1.378	28-Jun-20	2.564
29-May-20	2.089	29-Jun-20	2.364
30-May-20	1.825	30-Jun-20	1.894
31-May-20	2.092	-	-
Average LT reading	1.365	Average LT reading	2.149

3.9. Conclusion

To ensure precise measurement and analysis of water quality and quantity in the water treatment process, a range of equipment is installed, including electromagnetic flow meters, open channel flow meters, level meters, pressure sensors, analyzers for pH, chlorine, and turbidity, energy meters, PLCs, HMIs, and UPS power backup systems with isolation transformers. The data collected from these devices can be calibrated to optimize pump scheduling and backwash scheduling, which play a crucial role in the overall efficiency of the plant process.

The efficiency of WTPs greatly benefits from the integration of SCADA systems in the intake system. The Appendix provides a list of measurement devices used in the system. The real-time data obtained from SCADA, including energy meter readings of the intake and substation feeders, demonstrate significant improvements in overall efficiency in terms of water quality and quantity to the tune of $10-20\%$ compared to non-SCADA. All data from sensors are stored in a local server at SCADA stations, allowing operators to generate reports at any time for future water management and energy management plans, thereby enhancing the water supply system.

However, one of the main challenges of the system is the requirement for skilled engineers and technically capable manpower to handle any technical issues that may arise during operation and maintenance. Additionally, the remote and hilly location of the study region, incur a risk of data loss due to internet and optical fiber issues. However, this challenge can be mitigated by implementing GSM/GPRS modems and improving internet connectivity. Proficient field staff to handle technical issues and conducting regular operation and maintenance activities can also improve the reliability, efficiency, and longevity of the equipment. Moreover, the development of online web-based and mobile applications could provide a platform for remote monitoring from any location, enabling smart solutions and swift responses to any issues.

CHAPTER 4

Analysis of Water Treatment Plant Considering Solar PV, SVC and Current Limiting reactor

4.1. Introduction

In this chapter, ETAP 19.0.1 simulation software is used to investigate and analyse an existing water treatment facility. The primary goals are to assess and apply the ETAP model of the GAWSS P-III electrical system of the Aizawl WTP in Mizoram, India. LFA, short circuit analysis, and relay discrimination settings of the system are performed with and without consideration of DERs such as solar, wind, and so on, in order to conduct extensive analysis and make distinguished improvements in the study system. The study demonstrates the analysis and practicality of a microgrid-based water treatment idea applied to enhance the efficiency of a WTP, which can be considered a significant framework for reducing various challenges encountered in WTPs as well as operational cost.

As the demand for electricity continues to grow steadily, it becomes crucial to not only construct more power plants, but also upgrade and remodel the existing power grids. Load flow studies play a crucial role in this process, as they provide valuable insights into the behavior and performance of power systems. The ETAP is a reliable and comprehensive software tool that can be used to conduct load flow studies, offering precise and dependable results [131-132].

ETAP offers a wide range of electrical design features, such as transient consistency, transfer coordination, LFA, transient stability, cable ampacity, and more. These tools enable engineers to analyze the complex interactions of electrical

components within a power system, helping them make informed decisions for optimal system performance [133].
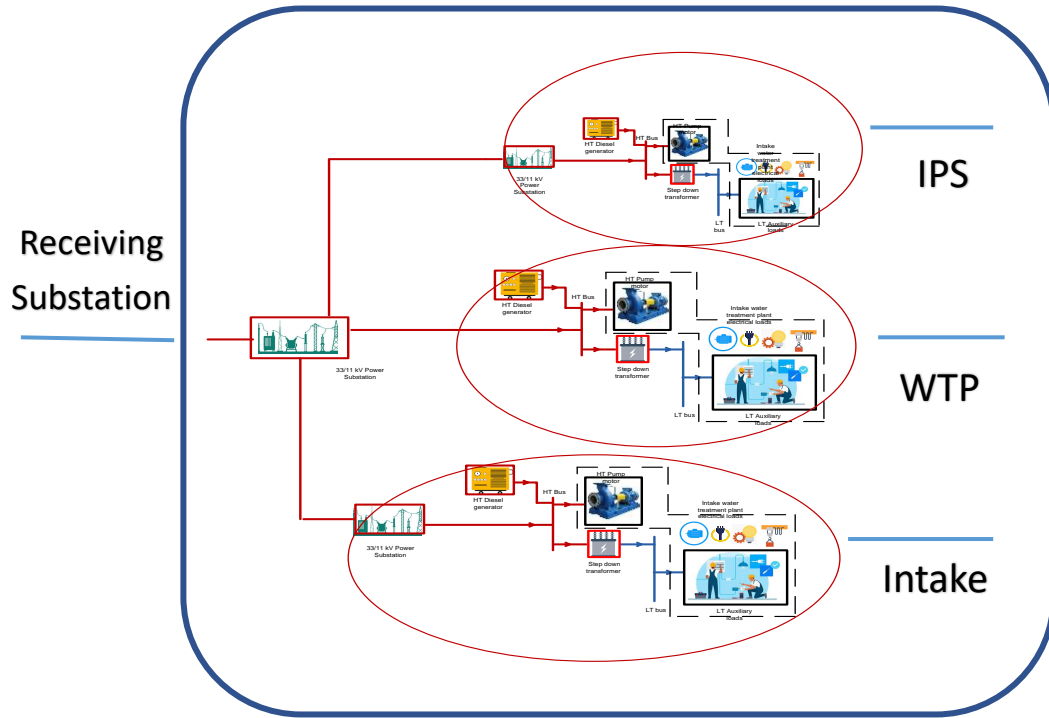
Figure 4.1. Schematic diagram of WTP electrical system

The increasing demand for energy is particularly evident in rapidly urbanizing regions and expanding economies, such as in developing countries like Pakistan, where power generation struggles to keep up with the demand. Insufficient analytical capabilities are often a limiting factor in addressing the energy scarcity issue. However, utilizing advanced software like ETAP for load flow studies can provide valuable insights for effective planning and management of power systems, ultimately helping to bridge the gap between supply and demand. [134-135]. Voltage fluctuations are a significant concern in power systems, as reactive power cannot be easily transmitted over long distances, especially under heavy loads. Reactive power needs to be generated as close as possible to the point of use due to the inability to transmit it efficiently over vast distances. This is because any variation in voltage creates the flow of reactive power (VARS) in the electrical network, and there is a subtle difference between the rated and actual voltage on the network, which can result in the circulation of reactive power over long distances [136].

When reactive power is absent at the point of load, it can cause voltage drops, which can be detrimental to the operation of various equipment, such as motors, as it can force them to operate at higher temperatures, leading to potential damage or failure. The voltage drop can also result in system instability and disintegration, further impacting the reliability and performance of the power system. Therefore, accurate analysis of reactive power and voltage fluctuations using tools like load flow studies, such as ETAP, can help identify and mitigate potential issues related to voltage fluctuations and their effects on the power system. [137]. In recent years, computer-based software has become a significant driving force in electrical engineering studies, including the analysis of power systems in WTP. One such software that has been used for this purpose is the ETAP. ETAP has been employed in the examination and analysis of power systems in WTP, both with and without the inclusion of renewable energy sources (RES) for microgrid concept power distribution [138].
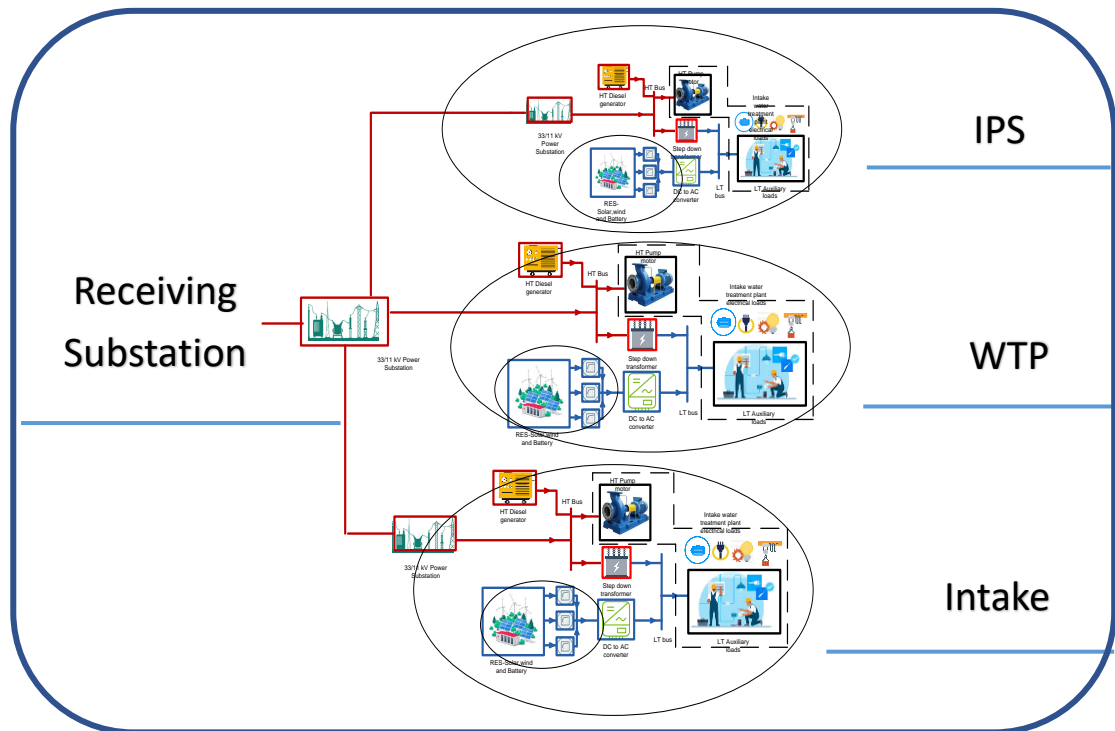
Figure 4.2. Schematic diagram of proposed WTP electrical system

In the simulation and modeling process using ETAP, the single-line diagram of the study system is initially prepared based on-site conditions and the internal and external values of the system. Real ratings of substations, circuit breakers, CT, PT, isolating switches, and load values, including motor rated values, are obtained from the Greater

Aizawl Water Supply Schemes Phase III in Aizawl, India. These data are input into ETAP for accurate analysis and assessment of the power system in the WTP, considering the inclusion or exclusion of RES-based systems for microgrid power distribution.

Figure 4.1 and figure 4.2 shows the schematic diagram of power system in WTP with and without RESs. The WTP and its facilities are mainly connected to the main power grid. However, in most cases, the only backup power source available is a traditional DEG, which is not only expensive to operate but also emits greenhouse gases [139]. With the growing focus on renewable energy sources (RES) as a solution for energy conservation and reducing greenhouse gas emissions, incorporating RES into the existing DG system while considering the microgrid concept in the WTP could potentially lower power consumption and offset various losses. This approach aims to address the limitations and environmental impact of traditional DEG backup power, and promote a more sustainable and efficient energy management system for water treatment facilities [140].

The WTP in the cities is facing several issues, including unplanned outages caused by a congested distribution system shared by utilities and treatment units, as well as frequent disruptions in the supplying utility. Additionally, the power management and control system in the feeding substation has deteriorated due to outdated facilities, leading to inadequate visualization and controls for the interconnected tie to the grid. In this paper, ETAP is introduced as a tool for conducting power system studies to investigate power flow, operational issues, and provide recommendations for improving system performance. ETAP also facilitates the investigation of system performance under various DERs to assess microgrid compatibility.

Therefore, considering various literature and from the above points, the contribution of this chapter are shown in the below points

1. To implement Single Line Diagram of the existing WTP, i.e. GAWSS P-III power supply system.

2. Implement RES such as Solar to in the existing system

3. To perform LFA under different scenarios with and without RES.

4. Compare and improve the system performance by implementing various compensation techniques

5. To perform Short circuit analysis under different scenarios with and without RES.

6. Implement improvement of the short circuit analysis using various technique

7. To perform relay coordination settings.

4.2. Power System Analysis

4.2.1. Load Flow Analysis

Load flow studies play a crucial role in the planning and design of power systems, providing steady-state solutions for the voltages at all buses under specific load conditions. Different solutions can be obtained for different operating conditions, aiding in the planning, design, and operation of the power system. Typically, load flow studies are focused on the transmission system, which involves the bulk power transmission [141]. Table 4.1 shows the classification of Buses for LFA, the load at the buses is assumed to be known, and load flow studies provide insights into various aspects of system operation, such as violation of voltage magnitudes at buses, overloading of lines and generators, reduction in stability margin indicated by power angle differences between interconnected buses, and the effects of contingencies such as line voltages and emergency shutdown of generators. Load flow studies are also essential for economic operation and transient stability studies of power systems. Load flow studies play a vital role in power system analysis. The load flow problem involves determining the power flows (both real and reactive) and voltages for a given network configuration and load conditions. At each bus in the network, there are four key quantities that need to be determined for further analysis: real power, reactive power, voltage magnitude, and phase angle [142]. Due to the nonlinearity of the algebraic equations that describe the power system, iterative methods are commonly used for their solution.

There are several constraints that can be placed on load flow solutions, including ensuring that Kirchhoff's relations are satisfied, considering the capability limits of reactive power sources, accounting for the tap-setting range of tap-changing transformers, incorporating specified power interchange between interconnected systems, and selecting appropriate initial values, acceleration factors, and convergence

limits. These constraints are essential in obtaining accurate and reliable load flow solutions for power system planning, design, and operation [143-144].

<div align="center">Table 4.1 Classification of Buses for LFA</div>

Sl No.	Bus Types	Specified Variables	Unspecified Variables	Remarks
1	Slack/ Swing bus	$|V|, \delta$	P_G, Q_G	$|V|, \delta$ are assumes if not specified as 1.0 and 0^0
2	Generator/Machine/PV Bus	$P_G, |V|$	Q_G, δ	A generator is present at the machine bus
3	Load/PQ Bus	P_G, Q_G	$|V|, \delta$	About 80% buses are of PQ type
4	Voltage Controlled Bus	$P_G, Q_G, |V|$	Δ, a	'a' is the % tap change in tap-changing transformer

4.2.2. Data for load flow

The data required for load flow studies is common regardless of the solution method used, and is typically in per unit (pu). It includes system data such as the number of buses (n), number of PV buses, number of loads, number of transmission lines, number of transformers, number of shunt elements, slack bus number, voltage magnitude of slack bus (angle is generally taken as 0°), tolerance limit, base MVA, and maximum permissible number of iterations.

1. Generator bus data for PV buses includes the bus number, active power generation (PG$_i$), specified voltage magnitude (V$_i$), minimum reactive power limit (Q$_{i,min}$), and maximum reactive power limit (Q$_{i,max}$).

2. Load data includes the bus number, active power demand (P$_{Di}$), and reactive power demand (Q$_{Di}$) for all loads.

3. Transmission line data includes the starting bus number (i) and ending bus number (k) for each transmission line, as well as the resistance, reactance, and half line charging admittance.

4. Transformer data includes the starting bus number (i) and ending bus number (k) for each transformer, as well as the resistance, reactance, and off-nominal turns-ratio (a).

5. Shunt element data includes the bus number where the element is connected, and the shunt admittance (G$_{sh}$ + jB$_{sh}$).

The Newton-Raphson (N-R) method is a widely used iterative approach for solving the power flow problem in power system analysis. Unlike other methods, it is based on Taylor's series and partial derivatives, making it a more accurate and efficient solution technique. One of the major advantages of the N-R method is its convergence rate, which is faster compared to other methods like Gauss-Seidel (G-S). It requires fewer iterations to reach convergence, resulting in less computational time and cost. Additionally, the N-R method is less sensitive to factors such as slack bus selection and regulating transformers, making it more robust in different system scenarios [145].

Another advantage of the N-R method is that the number of iterations required for convergence is almost independent of the system size. This makes it suitable for analysing both small and large power systems without significant differences in computational effort. Overall, the Newton-Raphson method is considered to be a sophisticated and important technique for solving the power flow problem, offering advantages such as faster convergence, higher accuracy, and robustness in various system conditions [146].

In LFA, the primary objectives are to calculate the complex powers and nodal voltages. These problems involve finding the phasors of node voltages when a specific complex power is applied.

$$P_p - j Q_p = \underline{U}_p \sum_{i=1}^{n} \underline{Y}_{pi} \underline{U}_i, p = 1,....,n \tag{4.1}$$

Where "p" represents nodes in the corresponding system, excluding the reference or slack bus. The admittance matrix elements and the complex voltage equations can be expressed in terms of their real and imaginary parts, as shown below in (4.2)

$$\left. \begin{aligned} \mathbf{P}_p &= \sum_{i=1}^{n} \left[U_p' \left(U_i' G_{pi} + U_i'' B_{pi} \right) + U_p'' \left(U_i'' G_{pi} - U_i' B_{pi} \right) \right] \\ \mathbf{Q}_p &= \sum_{i=1}^{n} \left[U_p' \left(U_i' G_{pi} + U_i'' B_{pi} \right) + U_p'' \left(U_i'' G_{pi} - U_i' B_{pi} \right) \right] \end{aligned} \right\} \tag{4.2}$$

By applying a finite difference approximation, the following matrix equation form can be obtained in below (4.3)

Equation (4.3) below is solved iteratively by applying the Newton Raphson method through ETAP software package.

$$
\begin{bmatrix} \Delta P_1 \\ \Delta Q_1 \\ \vdots \\ \Delta P_n \\ \Delta Q_n \end{bmatrix} = \begin{bmatrix} J_{11}^1 & J_{11}^2 & \cdots & J_{1n}^1 & J_{1n}^2 \\ J_{11}^3 & J_{11}^4 & \cdots & J_{1n}^3 & J_{1n}^4 \\ \cdots & \cdots & \cdots & \cdots & \cdots \\ J_{ns}^1 & J_{ns}^2 & \cdots & J_{nn}^2 & J_{1n}^4 \\ J_{n1}^3 & J_{n1}^4 & \cdots & J_{nn}^3 & J_{nn}^4 \end{bmatrix} \cdot \begin{bmatrix} \Delta U_1^{'} \\ \Delta U_1^{''} \\ \cdots \\ \Delta U_n^{'} \\ \Delta U_n^{''} \end{bmatrix}
\tag{4.3}
$$

Where,

$$
\left.\begin{array}{l}
J_{pi}^1 = \dfrac{\partial P_p}{\partial U_p^{'}} = U_p^{'}G_{pi} + U_p^{''}B_{pi} \quad J_{pi}^2 = \dfrac{\partial P_p}{\partial U_i^{''}} = -U_p^{'}B_{pi} + U_p^{''}G_{pi} \\[4mm]
J_{pi}^3 = \dfrac{\partial Q_p}{\partial U_i^{'}} = -U_p^{'}B_{pi} + U_p^{''}G_{pi} \quad J_{pi}^4 = \dfrac{\partial Q_p}{\partial U_i^{''}} = -U_p^{'}G_{pi} - U_p^{''}B_{pi}, i \neq p
\end{array}\right\}
\tag{4.4}
$$

4.2.3. Short Circuit Analysis

Short-circuit currents, also referred to as faults, can result in the introduction of substantial amounts of destructive energy in the form of heat and magnetic forces into a power system. A short circuit occurs when there is a low-resistance path that bypasses a part of a circuit, causing the bypassed part to stop working. The reliability and safety of electric power distribution systems rely on accurate knowledge of short-circuit fault currents that may be present, as well as the performance of protective devices in interrupting these currents. It is crucial for engineers responsible for planning, design, operation, and troubleshooting of distribution systems to have a thorough understanding of computational methods used in power system analysis [147].

Electric power systems are designed to minimize faults through meticulous system and equipment design, appropriate installation practices, and regular equipment maintenance. However, despite these measures, faults can still occur due to various reasons, including:

  a) Presence of animals, such as birds and insects, in equipment

  b) Loose connections leading to equipment overheating

  c) Voltage surges

  d) Deterioration of insulation due to aging

  e) Voltage or mechanical stresses applied to the equipment

  f) Accumulation of moisture or other contaminants

g) Intrusion of metallic or conducting objects into the equipment, such as grounding clamps, fish tape, tools, jackhammers, or pay-loaders

h) Assorted "undetermined causes"

i) Overloading of equipment

j) Human error during installation or maintenance work

k) Inadequate cooling

l) Natural disasters like heavy rain, wind storms, floods, etc.

When a short-circuit occurs in an electric power distribution system, it can result in various outcomes, as discussed below.

The generation of very high short-circuit currents, which introduce a significant amount of energy into the fault location. Arcing and burning at the fault location, potentially causing damage to adjacent equipment and posing a hazard to personnel working on the equipment. Flow of short-circuit current from rotating machines in the electrical distribution system to the fault location. Thermal and mechanical stresses on components carrying the short-circuit currents, which can result in damage [148-149]. These stresses depend on the square of the current magnitude and the duration of the current flow. Voltage drops in the system proportional to the magnitude of the short-circuit currents flowing through the system elements. The maximum voltage drop occurs at the fault location (potentially dropping to zero for a bolted fault), but voltage drops can occur throughout the power system to varying degrees.

When gathering data for short-circuit studies in an electrical system, the first step is to create a one-line diagram. In a balanced three-phase system, the circuit impedance for each phase is identical, allowing for the representation of the entire system using a single-phase drawing. The short circuit current waveform for different types of faults is typically asymmetrical, comprising of both a unidirectional DC component and a symmetrical AC component. The DC component decays over time, while the amplitude of the symmetrical AC component reaches a constant value in steady-state conditions [150-151]. The peak value of the short circuit current can be calculated using a multiplier based on the X/R ratio of the network and the steady-state fault current value.

$$MF_{peak} = \sqrt{2}\left(1 + e^{\frac{2\pi}{X/R}}\right) \tag{4.5}$$

Where τ is the instant of time when fault occurs, for maximum peak fault current values τ should be equal to $\frac{1}{2}$ Cycles.

4.2.4. Relay Coordination Settings

The primary goal of power system protection is to promptly isolate the faulty section of the electrical power system from the rest of the live system to prevent further damage due to fault currents. Circuit breakers are responsible for automatically opening during fault conditions, triggered by signals from protection relays. The philosophy of protection is to interrupt the flow of fault current by quickly disconnecting the short-circuit path from the system [152].

To minimize the extent of the power system that is disconnected during a fault, protection is arranged in zones. Ideally, these protection zones should overlap to ensure that no part of the power system is left unprotected. However, due to practical, physical, and economic limitations, CTs may only be available on one side of the circuit breakers in some cases.

4.2.4.1. Numerical relay

Numeric protection relays play a crucial role in safeguarding power and distribution transformers from a wide range of faults, such as distance safety, line differential, pilot wire, low impedance busbar, high impedance differential, frequency, voltage, circuit breaker failure, auto reclosing, and faults in synchronicity. These relays, which are digital systems, maintain constant communication with substation automation systems through menu-driven interfaces. They feature binary inputs, outputs, and programmable logic configurability, and are capable of tracking, calculating, and reporting electrical values, faults, delays, and events. With high-speed operation and multifunctionality, numerical safety relays offer improved selectivity and reliability. They can automatically detect faults, making power systems highly reliable, compact in size, and low in power consumption. These relays are essential automated systems that communicate through menu-driven interfaces with substation automation systems, providing efficient tracking, calculation, and recording of electrical values, faults, disruptions, and events. Their automatic fault detection capabilities make power systems highly efficient, while being compact in size and consuming minimal power [153-154].

4.2.4.2. Overcurrent relay

An Over-Current Relay is a protective relay that detects and responds to overcurrent conditions in a power system. It uses a CT to measure the current of a load and compares it with preset values to determine if it exceeds a specific threshold. If the current exceeds the preset value, the relay sends a signal to a circuit breaker to open its contacts and disconnect the protected equipment. Depending on the type of relay, it can operate instantly (in the case of instant overcurrent relays) or have a time delay before issuing a trip signal (in the case of time-delayed overcurrent relays). This time delay, also known as the relay's operating time, is calculated by the relay's microprocessor-based protective algorithm. Numerical overcurrent relays typically offer customization of time-current characteristics through graphical or tabular settings. These relays are equipped with multiple microprocessors that perform various software functions, such as executing protective algorithms, processing sensor signals, controlling output relays, and managing the human interface [155-156].

4.2.4.3. Relay Coordination

It is crucial to achieve coordination between overcurrent phase and earth fault relays to accurately identify and clear faults in power systems. These relays must be able to distinguish between normal operating currents and fault currents, including short-time currents that may arise from normal equipment operation. They need to operate rapidly to isolate the faulted section of the network, while ensuring uninterrupted operation of healthy circuits. In case of primary relay failure, backup relays should operate with sufficient time discrimination to allow for the operation of primary relays. Therefore, coordination between primary and backup protection devices is essential. The settings of the relays should be flexible and optimized to achieve the objectives mentioned above [157].

There are various types of protective relays used in power systems, including:

a. Electromagnetic Relays: These relays utilize an armature, induction cup, or induction disc.

b. Static Relays: These relays process analog input signals using solid state devices.

c. Digital/Numerical Relays: These relays employ programmable solid state devices based on digital signal processing.

Based on their characteristics, protective relays can be categorized as:

a. Definite time relays.

b. Inverse time relays with definite minimum time (IDMT).

c. Instantaneous relays.

d. IDMT with inst.

e. Stepped characteristic.

f. Programmed switches.

g. Voltage restraint over current relay.

4.2.4.4. Problem definition and mathematical formulation

As per the guidelines set by the International Electrotechnical Commission (IEC) standard, the time-current characteristics (TCCs) of overcurrent relays can be broadly described. These characteristics are typically represented by various types of curves or graphs that illustrate the behaviour of the relay with respect to time and current. The TCCs are designed to determine the operating time of the relay for different fault currents, aiding in the coordination of protective relays in a power system [158]. From the following equation (4.6)

$$OT = \frac{T_D \cdot \alpha}{\left(\dfrac{I_F}{I_P}\right)^n - 1} \tag{4.6}$$

The relay tripping time (OT) and fault current (I_F) are defined in seconds (s) and amperes (A), respectively. The parameters "α" and "n" are fixed values that depend on the type of relay characteristics, such as long inverse (LI), extremely inverse (EI), very inverse (VI), and normally inverse (NI). The coordination of overcurrent relays can be formulated as a nonlinear optimization problem, with an objective function and a set of constraints. The ultimate goal of this formulation is to minimize the total operating time of main relays for faults occurring within their primary protection area [159]. Also, the objective function (OF) can be written as shown in (4.7).

$$OT = \min imized\left(\sum_{i=1}^{N} OT_{P,i}\right) \tag{4.7}$$

The operating time of the ith primary relay for a fault near that relay is denoted as OTP; I, where I represents the relay number. N is the total number of main relays in the system being studied. The objective function of this formulation is to minimize the total operating time of main relays for faults occurring within their primary protection area. This objective function is subject to a set of constraints, which will be defined in the subsequent sections.

4.2.4.5. Relay setting constraints

The relay setting constraints encompass limits on TD (time dial setting) and IP (pickup current setting), as depicted in equation (4.8) and (4.9) respectively. Furthermore, the type of relay characteristic is selected as defined in equation (10).

$$T_{Di}^{\min} \leq T_{Di} \leq T_{Di}^{\max} \dots \forall i \in N \tag{4.8}$$

$$I_{Pi}^{\min} \leq I_{Pi} \leq I_{Pi}^{\max} \dots \forall i \in N \tag{4.9}$$

$$\text{Re} laycurve_i \in \{NI, VI, EI, LI\} \dots \forall i \in N \tag{4.10}$$

The equation above defines the variables used in the coordination of overcurrent relays. T_{Di} represents the time dial setting of the ith relay, while $T^{\min}{}_{Di}$ and $T^{\max}{}_{Di}$ denote the minimum and maximum time dial settings of the ith relay, respectively. IP_i represents the pickup current setting of the ith relay, and $I^{\min}{}_{Pi}$ and $I^{\max}{}_{Pi}$ represent the minimum and maximum pickup current settings of the ith relay, respectively. It is crucial to note that the pickup current setting (I_{Pi}) should be set above the maximum expected load current (I_L) to ensure reliable relay operation during fault conditions and to allow for full capacity operation of the equipment protected by the ith relay [160].

4.3. Power Supply of WTP (Case Study)

4.3.1. Power supply system

The power supply details of GAWSS P-III was discussed in the previous chapter, the geographical representation and a substation schematic diagram of a power supply system for the Greater Aizawl Water Supply Schemes Phase III structure is shown in figure nos. 4.3 & figure 4.4. and figure 4.5 shows the substation diagram of IPS. The power supply system consists of the following three major components, 1. Power supply from the grid and receiving substation, 2. Control and Relay panels and 3. Backup power supply system.

The 33/11 kV substation serves as the entry point for power supply from the grid to a facility. It is equipped with essential switchgear devices such as lightning arresters (LA), CT, PT, and circuit breakers (VCB/SF6) to ensure proper functioning of the power system. The incoming 33 kV power is stepped down to 11 kV using a power transformer, and the output is then fed to the HT load, such as 11 kV pump motors, through an 11 kV HT panel. Additionally, an auxiliary transformer is used to further step down the voltage from 11 kV to 0.415 kV (Indian standard) for three-phase power supply to auxiliary loads through low tension (LT) panels.

To ensure smooth operation of the power system for both HT and LT loads, important devices such as HT and LT motor starters and automatic power factor correction (APFC) panels are also installed in the facility. These devices help in controlling and maintaining the power factor of the load, ensuring efficient and reliable operation of the electrical system. The control and numerical relay panel is an essential component of the switchgear system in the substation. It is linked to the SCADA system, which allows for monitoring and control of various equipment such as CT, PT, and circuit breakers. This enables efficient management of the substation operation.
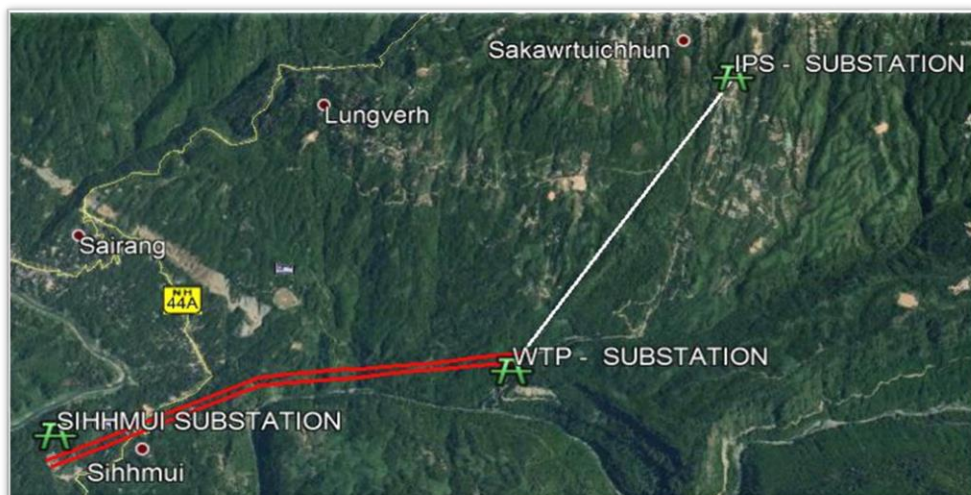
Figure 4.3 Map of power line in WTP phase III.

Transformer protection for both the HT and LT sides is crucial, and it includes measures such as temperature control, earth fault detection, and Buchholz relay monitoring. These protection mechanisms provide live data to the PLC, which allows for control and monitoring of the substation. The typical HT panel for the intake power supply system shown in figure 4.6 includes two HT incomers for the main grid and HT

power backup sources such as diesel generators (DG sets) or renewable energy sources (RES). Surge arresters, along with CT and PT, are installed at the incomer side to monitor the parameters, which are then linked to the SCADA system for real-time monitoring.
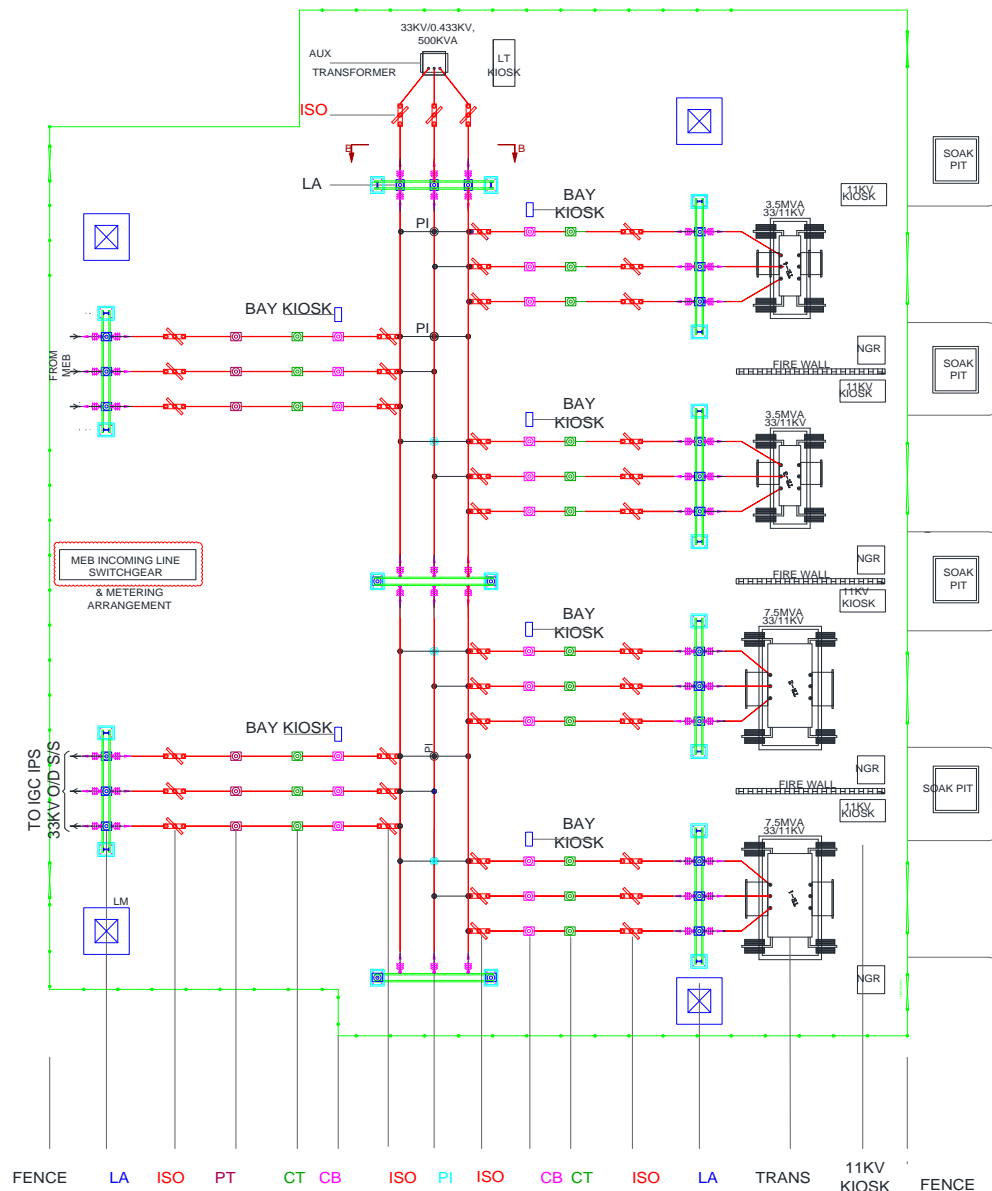
Figure 4.4 33 kV Substation Layout.

To ensure safe operation, a bus interlocking system is implemented in the HT panel to prevent unwanted dual operations of the sources during switching and normal operation periods. The incoming power is then fed to the outgoing feeders for various purposes such as HT pump motors, blowers, automatic power factor correction

(APFC), and auxiliary transformers. The breakers, current, and voltage of each feeder are linked to the SCADA system for automation and control, allowing for efficient operation of the substation. In designing the panels, calculations for current and safety considerations are essential factors to be taken into account.
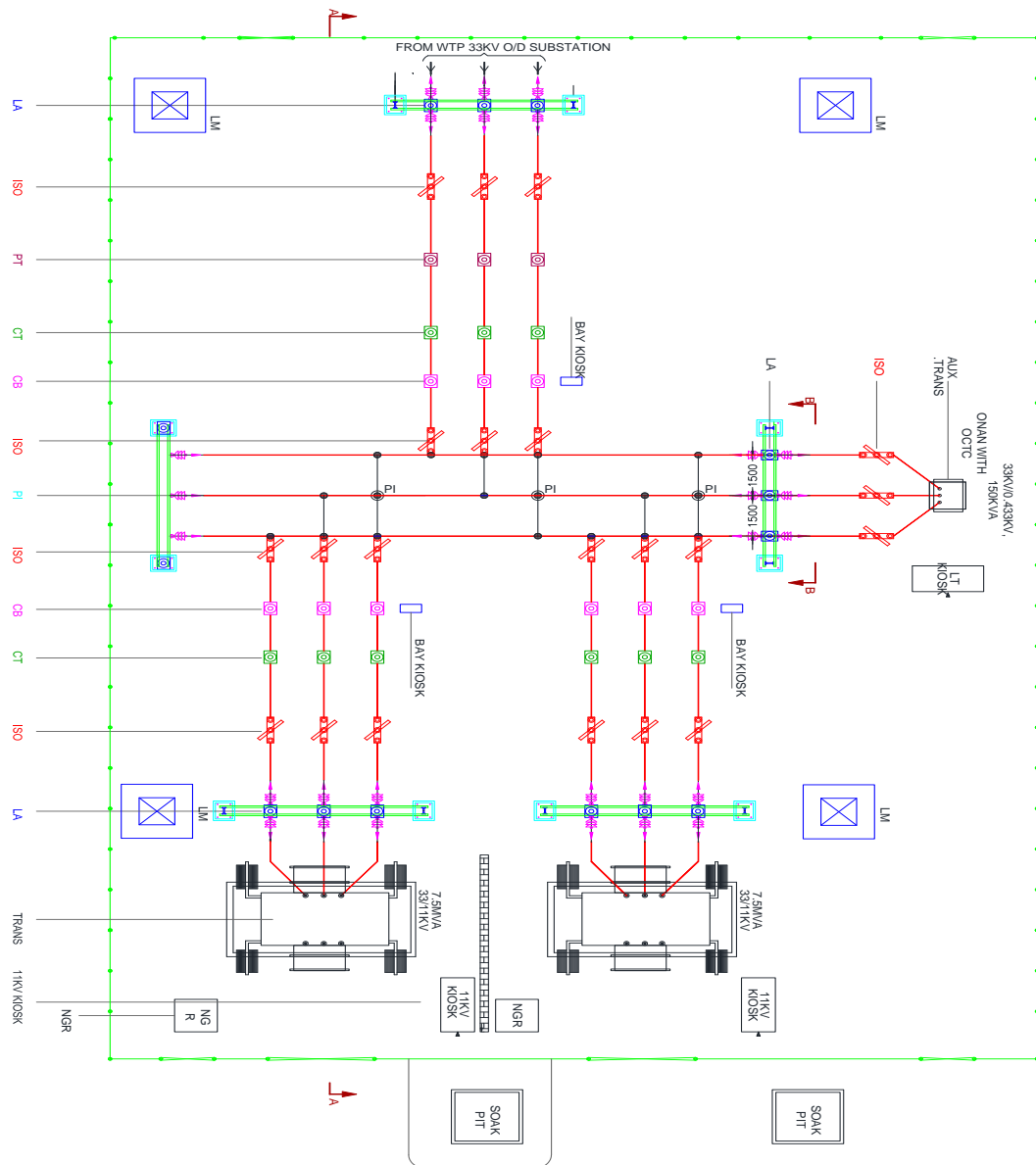
Figure 4.5 IPS Substation layout

The principal of a SLD of a standard Low Tension (LT) panel is similar to the HT panel, the LT panel comprises two or more incomers for grid supply and power backup sources such as diesel generators (DG), solar panels, etc. To ensure safety, an interlocking system is in place in conjunction with the Moulded Case Circuit Breakers

(MCCB). The outgoing feeders from the LT panel are connected to various LT loads, motors, and other equipment. Similar to other panels, important sensors are installed at the incomer and outgoing feeders, which provide data to the SCADA station for efficient control and monitoring of the system. This allows for real-time monitoring of the LT panel's performance and ensures smooth operation of the intake system. 33 kV Substation Layout side view, SLD of 33 kV Switchyard of Phase III power supply and SLD of LT MPCC is shown in appendix-C.

4.4. Implementation of the Study system

4.4.1 SLD of the ETAP study system

Figure 4.7 shows the Single line diagram of the study system. Description as well as load details are discussed in the previous chapter. The plant is powered by the utility source at a voltage of 33 kV, with two incomers designated as 01 and 02 incomers. There is a total of 2nos of 3500KVA transformers and 4nos of 7500KVA transformers in the system. The 3500KVA transformers are connected to the RWPH (Raw Water Pump House) panel, while the 7500KVA transformers are divided into two sets. Two of them are connected to the CWPH-1 (Clear Water Pump House 1) panel, and the other two are connected to the CWPH-2 (Clear Water Pump House 2) panel. These transformers are further connected to downstream panels and distribution boards for power distribution within the plant. Also, Solar photo voltaic power backup system is incorporated in the load side of the system as shown in the figure. Table 4.2 shows system description of the SLD.

Table 4.2 System Description of a SLD

System Description		
Total no of Buses	Swing	1
	Diesel Generator	1
	Load	4
Branches	Transmission line	3
	Transformer	9
Diesel Generators		1
Loads		7
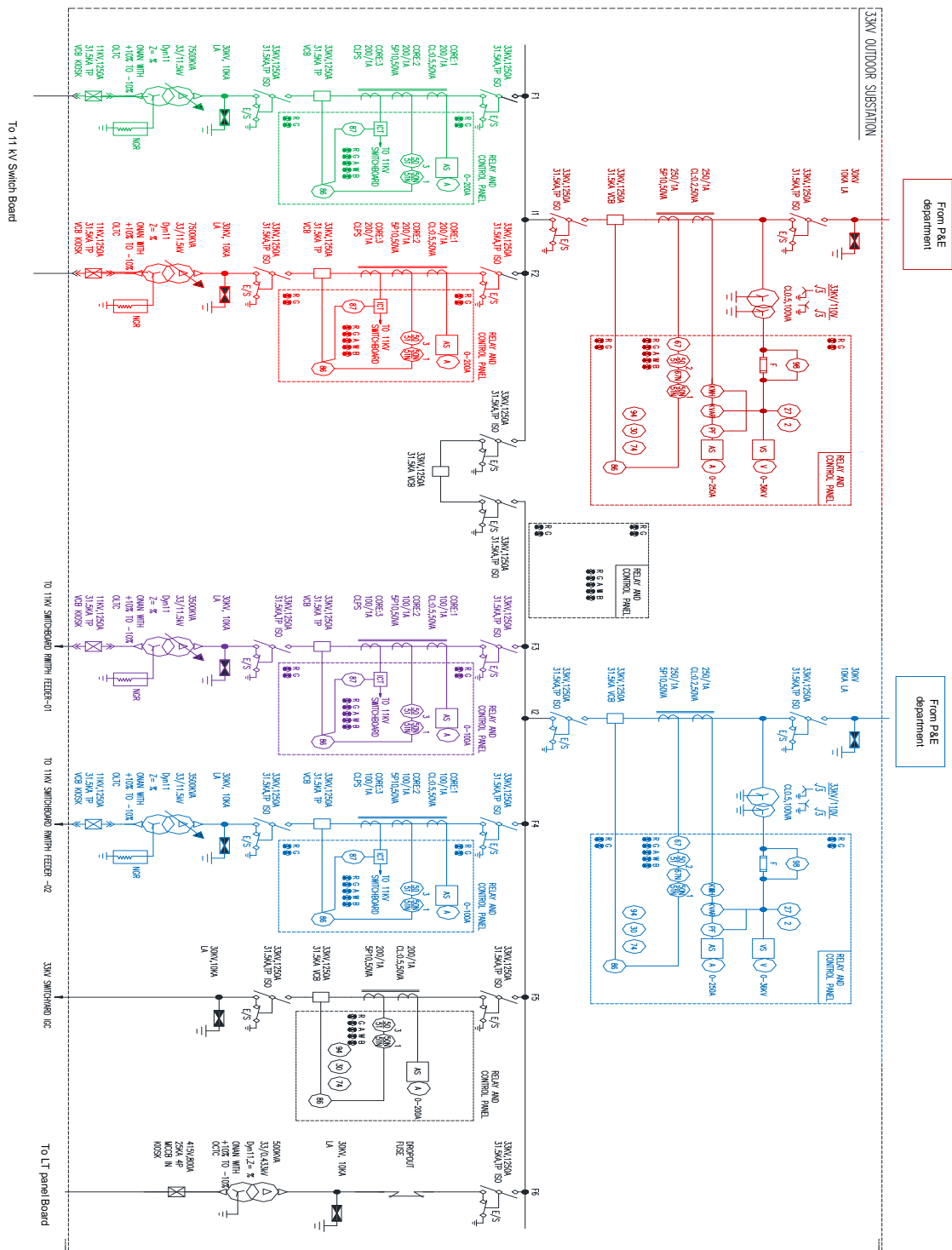
Figure 4.6 33 kV Substation panel layout

4.5. Load flow analysis of WTP

The study involves utilizing computer-based power system analysis software, specifically ETAP version 19.0.1 developed by Operation Technology Inc. (OTI), to

analyze and examine the power distribution system. The objective is to create an equivalent one-line diagram network representation based on the SLD, allowing for detailed analysis and evaluation of the system's performance.

The Design Consideration for performing LFA is as under

- Cable Sizes and lengths are modelled as per the Cable sizing Calculation.
- Grid Voltage is considered for 100 % for the Load flow study.
- Loads are modelled as per the Load schedule.
- Loading of each bus is considered as per Load analysis, Distribution Transformer considered as OCTC, Transformer impedance values are given in the table 4.3.

Table 4.3 Transformer impedance values

S. No.	Transformer Rating	% Impedance	X/R ratio	Tapping
1	Distribution Transformer 3500 kVA	7.15 % (no negative tolerance)	11.41 %	Nominal
2	Distribution Transformer 7500 kVA	7.15 % (no negative tolerance)	14.23 %	Nominal

4.5.1. Study Cases

Case-1: Incomer 1 and 2 is in ON condition. DG is in OFF condition.

Case-2: Incomer 1 is in ON condition and Incomer 2 is in OFF condition. DG is in OFF condition.

Case-3: Incomer 1 and 2 is in OFF condition, DG is in ON condition.

Case-4: Incomer 1 and 2 is in ON condition, IPS Area is in OFF condition. DG is in OFF condition.

Case-5: Incomer 1 and 2 is in ON condition, DG is in OFF condition. Solar panel 1 and 2 is in ON condition.

In order to avoid lengthy report, Case 1, Case 3 and Case 5 are shown and discussed in this chapter.

Case-1: Incomer 1 and 2 is in ON condition. DG is in OFF condition.

Figure 4.8 (a) and figure 4.8 (b) shows the single line diagram of the case study system before and after study condition. Where, both the incomer 1 and 2 are in ON condition. The load flow report of case-1 is shown in Appendix -C. Also, Table 4.4 shows the total summary of generation, loading and demand under case1.
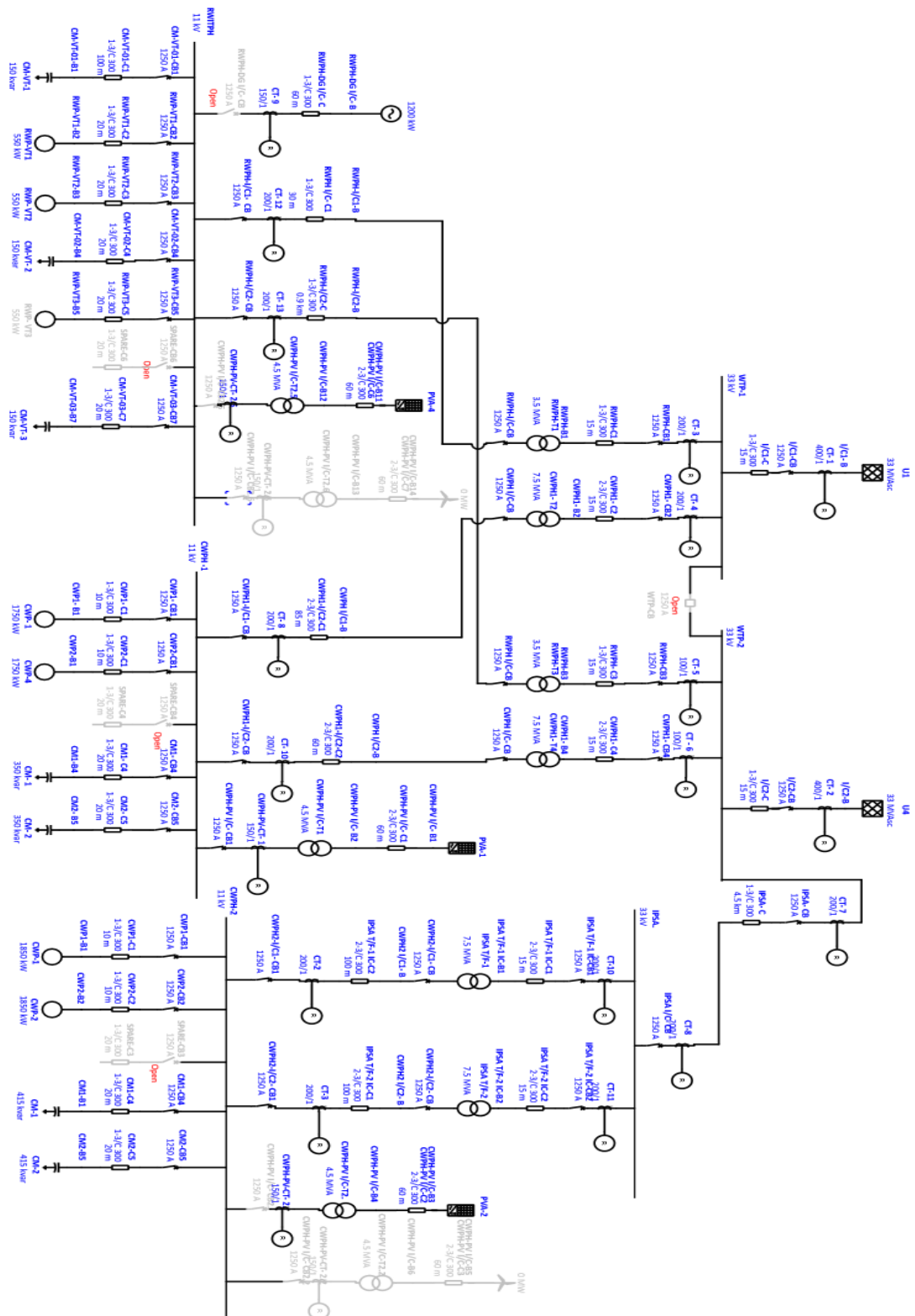
Figure 4.7 SLD of the WTP electrical system (ETAP model)
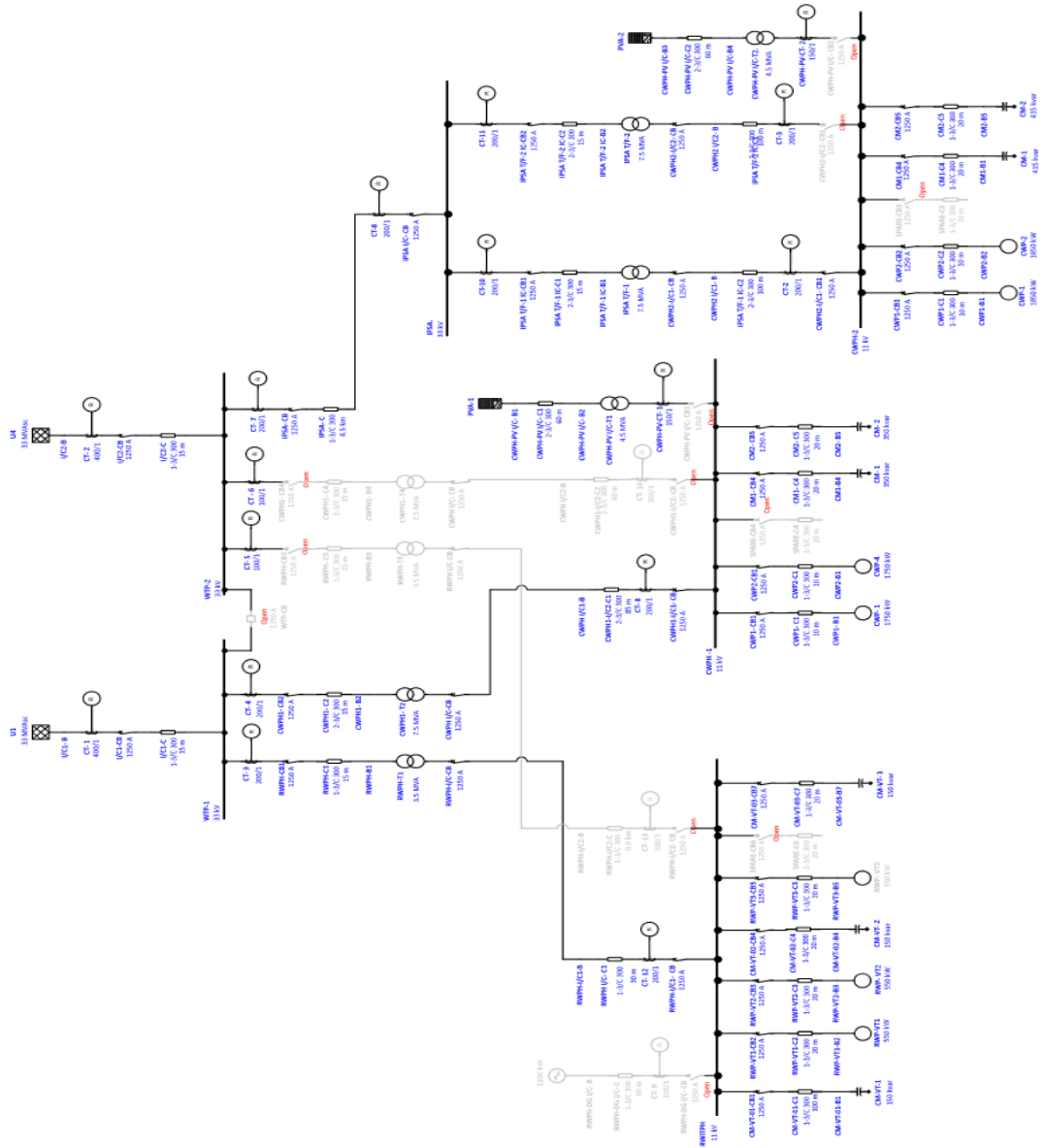
Figure 4.8 (a) SLD of Case 1 (ETAP model)

Table 4.4 Summary of case 1

Sources	MW	Mvar	MVA	% PF
Source (Swing Buses):	8.806	2.854	9.257	95.13 Lagging
Source (Non-Swing Buses):	0.000	0.000	0.000	
Total Demand:	8.806	2.854	9.257	95.13 Lagging
Total Motor Load:	8.773	4.935	10.066	87.16 Lagging
Total Static Load:	0.000	-1.919	1.919	0.00 Lagging
Total Constant I Load:	0.000	0.000	0.000	-
Total Generic Load:	0.000	0.000	0.000	-
Apparent Losses:	0.033	-0.162		-
System Mismatch:	0.000	0.000		-
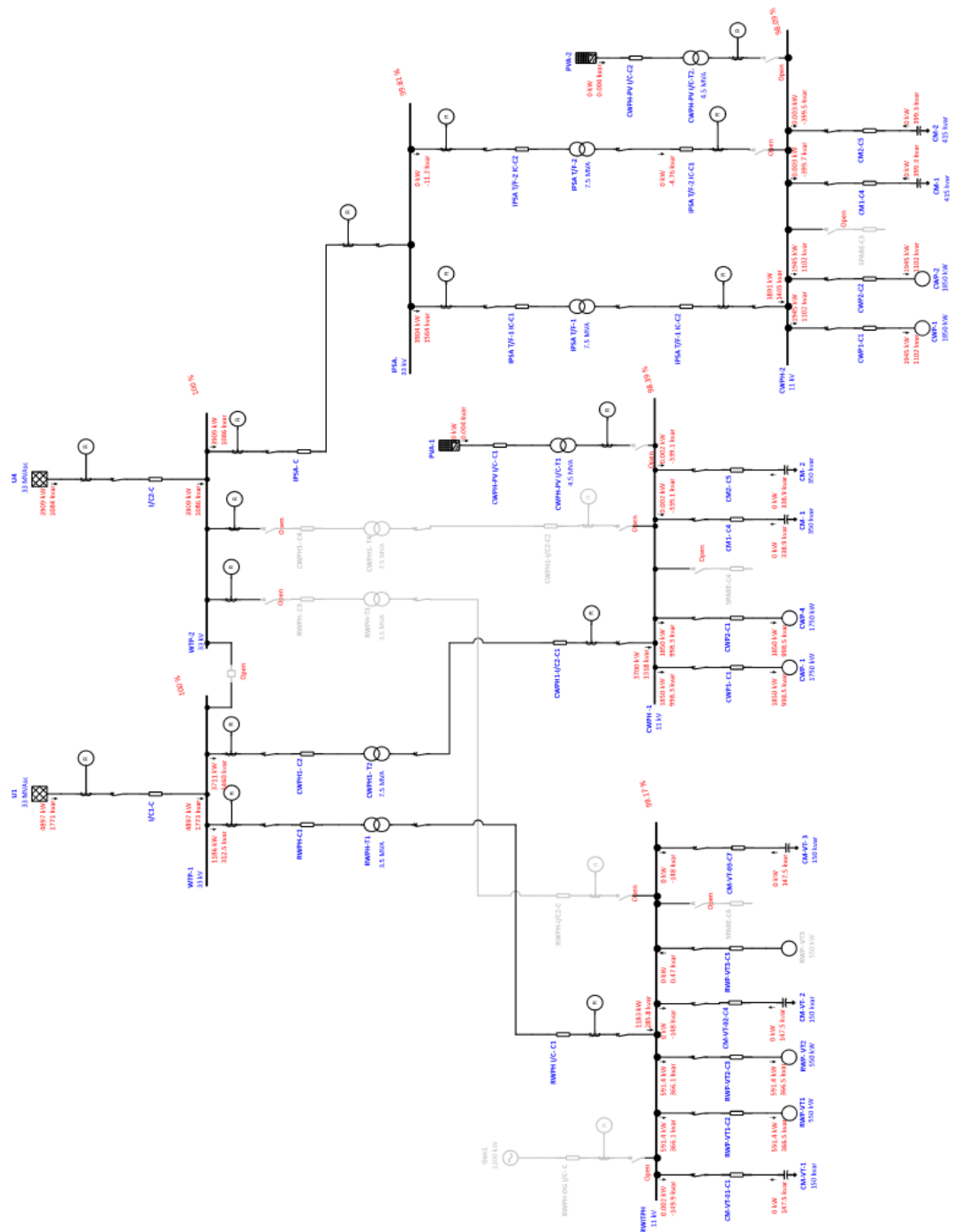
Figure 4.8 (b) SLD of Case 1 under study (ETAP model)

Case-3: Incomer 1 and 2 is in OFF condition, DG is in ON condition.

Figure 4.9 (a) and figure 4.9 (b) shows the single line diagram of the case 3 study system before and after study condition. Where both the incomer 1 and 2 are in OFF condition. Where in Case 3, the loading of the system is considered for Intake pump

motors, the 1500 kVA diesel engine generator came into operation for feeding power supply to Intake pumps On the other hand, during this period WTP and IPS are considered to be operated under diesel engine driven pump motors located at WTP and IPS. Moreover, the Solar power plant is not considered under this case. The Load Flow Report of case 3 is shown in Table 4.5. Furthermore, Table 4.6 shows the branch connection details under case 3 and Table 4.7 shows the total summary of generation, loading and demand under case 3.

Figure 4.9 (a) SLD of Case 3 (ETAP model)

Figure 4.9 (b) SLD of Case 3 under study (ETAP model)

Case-5: Incomer 1 and 2 is in ON condition, DG is in OFF condition. Solar panel 1 and 2 is in ON condition.

Figure 4.10 (a) and figure 4.10 (b) shows the single line diagram of the case 5 study system before and after study condition. Where both the incomer 1 and 2 are in ON condition. Also, in this case solar panel on bus 5th and 6th are in operational. Where in Case 5, the loading of the system is considered for all the sites viz. Intake, WTP, and

IPS. Moreover, the power supply from the grid are considered to be operated for pumping the water in all sits. Furthermore, the Solar power plant is considered under this case. The Load Flow Report of case 5 is shown in Appendix -C. Furthermore, the table 4.8 shows the branch loss summery report under case 5 and Table 4.9 shows the total summary of generation, loading and demand under case 5.

Table 4.5 Load Flow Report of case 3

Bus	Voltage			Generation		Load		Load Flow				
ID	kV	% Mag.	Ang.	MW	Mvar	MW	Mvar	ID	MW	Mvar	Amp	%PF
CM-VT-01-B1	11.00	99.993	0	0	0	0	-0.15	RWITPH	0	0.150	7.9	0.0
CM-VT-02-B4	11.00	99.92	0	0	0	0	-0.15	RWITPH	0	0.15	7.9	0.0
CM-VT-03-B7	11.00	99.92	0	0	0	0	-0.15	RWITPH	0	0.15	7.9	0.0
* CWPH-PV I/C-B1	0.415	100.00	0	0	0	0	0	CWPH-PV I/C-B2	0	0	0.0	0.0
CWPH-PV I/C-B2	0.415	100.00	0	0	0	0	0	CWPH-PV I/C-B1	0	0	0.0	0.0
* CWPH-PV I/C-B3	0.415	100.00	0	0	0	0	0	CWPH-PV I/C-B4	0	0	0.0	0.0
CWPH-PV I/C-B4	0.415	100.00	0	0	0	0	0	CWPH-PV I/C-B3	0	0	0.0	0.0
RWITPH	11.00	99.92	0	0	0	0	0	CM-VT-01-B1	0	-0.15	8.0	0.0
								CM-VT-02-B4	0	-0.15	7.9	0.0
								CM-VT-03-B7	0	-0.15	7.9	0.0
								RWP-VT1-B2	0.58	0.24	33.5	92.3
								RWP-VT2-B3	0.59	0.36	36.5	85.0
								RWP-VT3-B5	0	0	0.0	0.0
								RWPH-DG I/C-B	-1.1	-0.15	62.5	99.1
RWP-VT1-B2	11.00	99.99	0	0	0	0.58	0.24	RWITPH	-0.5	-0.24	33.5	92.2
RWP-VT2-B3	11.00	99.99	0	0	0	0.59	0.36	RWITPH	-0.5	-0.36	36.5	85.0
RWP-VT3-B5	11.00	99.99	0	0	0	0	0	RWITPH	0	0	0.0	0.0
* RWPH-DG I/C-B	11.00	100.0	0	1.18	0.15	0	0	RWITPH	1.18	0.15	62.5	99.1

Table 4.6 Branch connection details of Case 3

Bus ID	CKT/ Branch	Connected Bus ID		% Impedance, Pos. Seq., 100 MVA Base			
ID	Type	From Bus	To Bus	R	X	Z	Y
CM-VT-01-C1	Cable	RWITPH	CM-VT-01-B1	1.02	0.99	1.42	0.0023900
CM-VT-02-C4	Cable	RWITPH	CM-VT-02-B4	0.20	0.20	0.28	0.0004780
CM-VT-03-C7	Cable	RWITPH	CM-VT-03-B7	0.20	0.20	0.28	0.0004780
CWPH-PV I/C-C1	Cable	CWPH-PV I/C- B1	CWPH-PV I/C- B2	215.77	208.82	300.27	0.0000041
CWPH-PV I/C-C2	Cable	CWPH-PV I/C-B3	CWPH-PV I/C-B4	215.77	208.82	300.27	0.0000041
RWP-VT1-C2	Cable	RWITPH	RWP-VT1-B2	0.20	0.20	0.28	0.0004780
RWP-VT2-C3	Cable	RWITPH	RWP-VT2-B3	0.20	0.20	0.28	0.0004780
RWP-VT3-C5	Cable	RWITPH	RWP-VT3-B5	0.20	0.20	0.28	0.0004780
RWPH-DG I/C-C	Cable	RWPH-DG I/C- B	RWITPH	0.61	0.59	0.85	0.0014340

Table 4.7 Summery of Case 3

Source	MW	Mvar	MVA	% PF
Source (Swing Buses):	1.180	0.157	1.191	99.13 Lagging
Source (Non-Swing Buses):	0.000	0.000	0.000	
Total Demand:	1.180	0.157	1.191	99.13 Lagging
Total Motor Load:	1.180	0.613	1.330	88.74 Lagging
Total Static Load:	0.000	-0.450	0.450	0.00 Lagging
Total Constant Load:	0.000	0.000	0.000	
Total Generic Load:	0.000	0.000	0.000	
Apparent Losses:	0.000	-0.006		
System Mismatch:	0.000	0.000		

4.5.2. Discussions and summary of Load flow Results

LFA for the above cases were conducted considering that all transformers are operating at their nominal tap positions and the load flow results were analyzed. ETAP Generated reports, in standard format are attached in Appendix-C. for all study cases of Load flow, which is carried out in line with Study cases specified above. The voltages at the different HV and LV buses for the Various Operating Conditions are

tabulated. Table 4.10 shows the load flow results and summery. From LFA, it is found that the steady state voltages are within the specified limit range for all the cases specified above. However, improvement of the system performance is done under implementation/ incorporation of Shunt capacitor and Static Var Compensator.
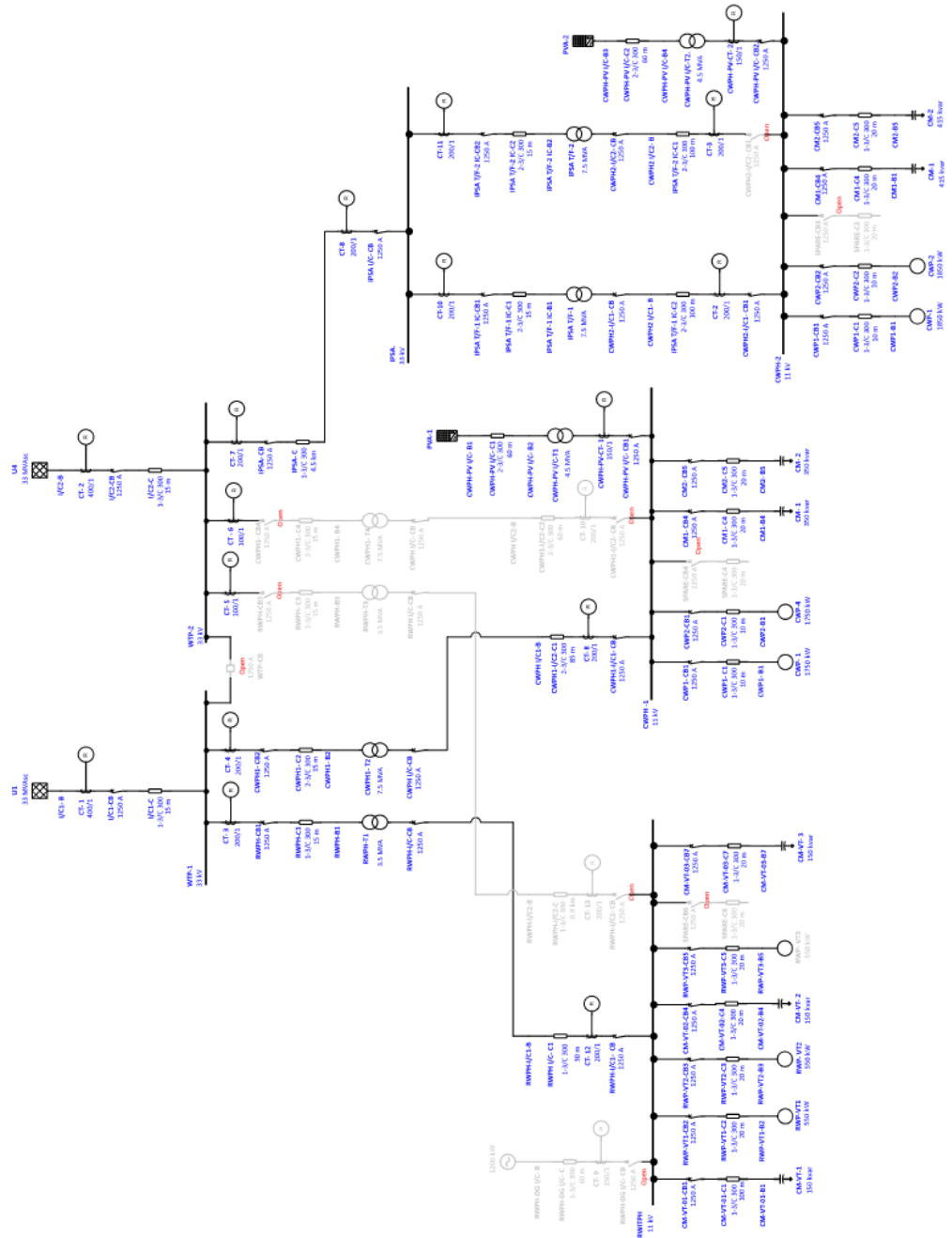
Figure 4.10 (a) SLD of Case 5 (ETAP model)
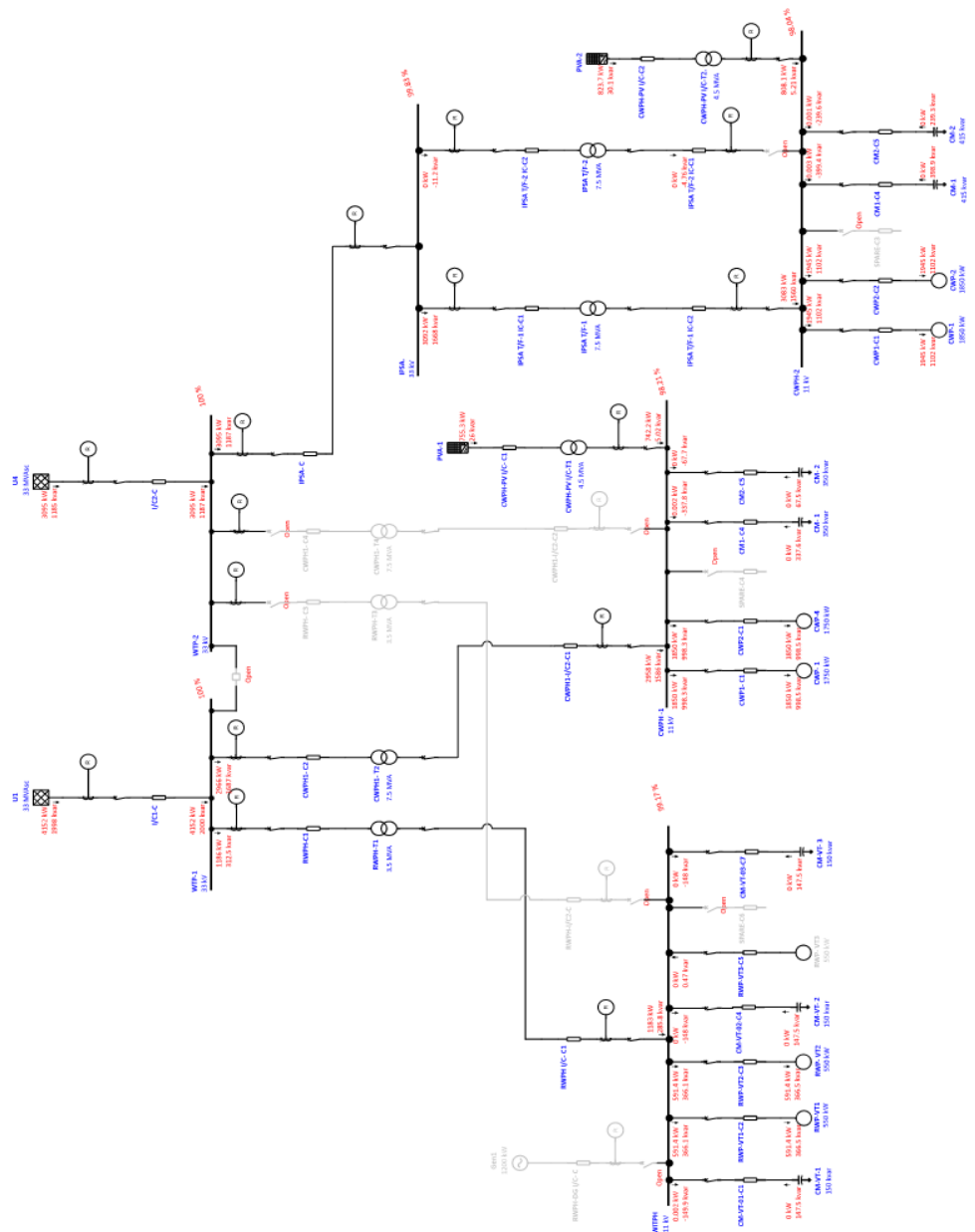
Figure 4.10 (b) SLD of Case 5 under study (ETAP model)

Table 4.8 Branch loss summary report of case-5

Branch ID	From-To Bus Flow		To-From Bus		**Losses**		% Bus Voltage		% Drop in Vmag
	MW	Mvar	MW	Mvar	kW	kvar	From	To	
CM1- C4	0.000	0.339	0.000	-0.339	0.0	-0.2	98.4	98.4	0.00
CM1-C4	0.000	0.399	0.000	-0.400	0.0	-0.5	98.1	98.1	0.00
CM2- C5	0.000	0.339	0.000	-0.339	0.0	-0.2	98.4	98.4	0.00
CM2-C5	0.000	0.399	0.000	-0.400	0.0	-0.2	98.1	98.1	0.00
CM-VT-01-C1	0.000	0.148	0.000	-0.151	0.0	-2.4	99.4	99.4	0.00
CM-VT-02-C4	0.000	0.148	0.000	-0.149	0.0	-0.5	99.4	99.4	0.00
CM-VT-03-C7	0.000	0.148	0.000	-0.149	0.0	-0.5	99.4	99.4	0.00

CWP1- C1	-1.850	-0.998	1.850	0.998	0.0	-0.2	98.4	98.4	0.00
CWP1-C1	-1.945	-1.102	1.945	1.102	0.1	-0.2	98.1	98.1	0.00
CWP2-C1	-1.850	-0.998	1.850	0.998	0.0	-0.2	98.4	98.4	0.00
CWP2-C2	-1.945	-1.102	1.945	1.102	0.1	-0.2	98.1	98.1	0.00
CWPH1- C2	-2.985	-1.461	2.985	1.454	0.0	-6.4	100.0	100.0	0.00
CWPH1- T2	-2.978	-1.356	2.985	1.461	7.4	105.0	98.4	100.0	1.55
CWPH1-I/C2-C1	-2.977	-1.359	2.978	1.356	0.5	-3.5	98.4	98.4	0.02
CWPH-PV I/C- C1	0.735	-0.022	-0.723	0.033	11.7	11.3	100.0	98.5	1.53
CWPH-PV I/C-C2	0.000	0.000	0.000	0.000	0.0	0.0	100.0	100.0	0.00
CWPH-PV I/C-T1	-0.723	0.041	0.723	-0.033	0.8	8.6	98.4	98.5	0.04
I/C1-C	4.168	1.642	-4.168	-1.643	0.0	-1.6	100.0	100.0	0.00
I/C2-C	3.909	1.084	-3.909	-1.086	0.0	-1.6	100.0	100.0	0.00
IPSA- C	-3.904	-1.553	3.909	1.086	5.4	-467.1	99.8	100.0	0.19
IPSA T/F-1	-3.892	-1.402	3.904	1.571	11.9	169.0	98.1	99.8	1.69
IPSA T/F-1 IC-C1	-3.904	-1.571	3.904	1.564	0.0	-6.4	99.8	99.8	0.00
IPSA T/F-1 IC-C2	-3.891	-1.405	3.892	1.402	0.9	-3.7	98.1	98.1	0.03
IPSA T/F-2	0.000	0.005	0.000	-0.005	0.0	0.0	99.8	99.8	0.00
IPSA T/F-2IC-C1	0.000	-0.005	0.000	0.000	0.0	-4.8	99.8	99.8	0.00
IPSA T/F-2 IC-C2	0.000	0.005	0.000	-0.011	0.0	-6.4	99.8	99.8	0.00
RWPH I/C- C1	-1.180	-0.164	1.180	0.163	0.0	-0.7	99.4	99.4	0.00
RWPH-C1	-1.183	-0.192	1.183	0.189	0.0	-3.2	100.0	100.0	0.00
RWPH-DG I/C- C	0.000	-0.001	0.000	0.000	0.0	-1.4	100.0	100.0	0.00
RWPH-T1	1.183	0.192	-1.180	-0.163	2.6	29.2	100.0	99.4	0.57
RWP-VT1-C2	0.589	0.246	-0.589	-0.247	0.0	-0.5	99.4	99.4	0.00
RWP-VT2-C3	0.591	0.366	-0.591	-0.367	0.0	-0.5	99.4	99.4	0.00
RWP-VT3-C5	0.000	0.000	0.000	0.000	0.0	-0.5	99.4	99.4	0.00

Table 4.9 Total summary report of case 5

Sources	MW	Mvar	MVA	% PF
Source (Swing Buses):	8.812	2.703	9.217	95.60 Lagging
Source (Non-Swing Buses):	0.000	0.000	0.000	-
Total Demand:	8.812	2.703	9.217	95.60 Lagging
Total Motor Load:	8.771	4.815	10.005	87.66 Lagging
Total Static Load:	0.000	-1.922	1.922	0.00 Lagging
Total Constant Load:	0.000	0.000	0.000	-
Total Generic Load:	0.000	0.000	0.000	-
Apparent Losses:	0.041	-0.190		-
System Mismatch:	0.000	0.000		-

Table 4.10 Load Flow Results summery of all cases

SI.NO	BUS ID	KW	KVAR	KVA	AMPS	PF IN %	BUS VOLTAGE IN %
				LOAD FLOW STUDY			
				CASE 1			
1	WTP-1	4897	1773	5208	91.1	94.03	100
2	WTP-2	3909	1086	4057	71	96.35	100
3	RWITPH	1183	285.8	1217	64.4	97.2	99.17
4	IPSA	3909	1086	4057	71	96.35	99.81
5	CWPH-1	3700	1318	3928	209.5	94.2	98.39
6	CWPH-2	3891	1405	4137	221.4	94.05	98.09
				CASE 2			
1	WTP-1	8806	2857	9258	162	95.12	100
2	WTP-2	3909	1084	4057	71	96.36	100
3	RWITPH	1183	285.8	1217	64.4	97.2	99.17
4	IPSA	3909	1086	4057	71	96.35	99.81
5	CWPH-1	3700	1318	3928	209.5	94.2	98.39
6	CWPH-2	3891	1405	4137	221.4	94.05	98.09
				CASE 3			
1	WTP-1	NA	NA	NA	NA	NA	NA
2	WTP-2	NA	NA	NA	NA	NA	NA
3	RWITPH	1183	278.3	1215	63.8	97.34	99.99
4	IPSA	NA	NA	NA	NA	NA	NA
5	CWPH-1	NA	NA	NA	NA	NA	NA
6	CWPH-2	NA	NA	NA	NA	NA	NA
				CASE 4			
1	WTP-1	3711	1460	3988	69.8	93.06	100
2	WTP-2	1187	294.1	1223	21.4	97.06	100
3	RWITPH	1183	286.6	1217	64.5	97.19	99.08
4	IPSA	NA	NA	NA	NA	NA	NA
5	CWPH-1	3700	1318	3928	209.5	94.2	98.39
6	CWPH-2	NA	NA	NA	NA	NA	NA
				CASE 5			
1	WTP-1	4152	2000	4608	80.6	90.09	100
2	WTP-2	3095	1187	3315	58	93.37	100
3	RWITPH	1183	285.8	1217	64.4	97.2	99.17
4	IPSA	3095	1187	3315	58	93.37	99.83
5	CWPH-1	3700.2	1591.02	4098.2	219.1	94.06	98.21
6	CWPH-2	3891	1565.21	4263.1	228.3	94.61	98.04

4.5.3. Implementation of Static VAR Compensator

As shown in the previous section, different voltages at different HV and LV buses tabulated in the above table shows the load flow results are within the specified limit range for all the cases specified above. However, it is necessary to improve the system performance due to various uncertainties and unpredictable nature of the power system, Therefore, improvement under implementation/ incorporation of Shunt capacitor and Static Var Compensator is done in case 5 above as shown in the following figure 4.11. where the SVC are incorporated in the load side of the system, i.e. Intake, WTP and IPS bus. The load flow results summery is shown in the below table 4.11
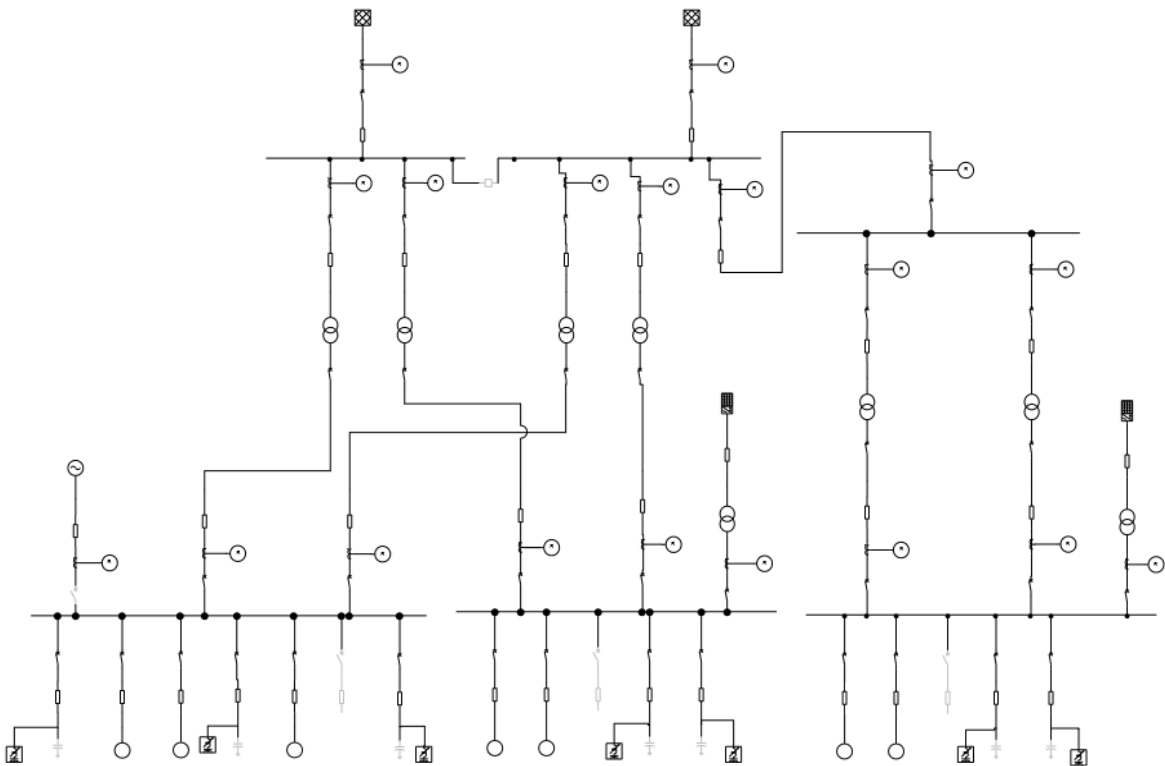
Figure 4.11 SLD under Static Var Compensator model

4.5.4. Comparison of various compensator Performance

Table 4.12 as shown below indicates the comparison statement of the LFA under case 5, the result shows the performance of each buses. Performance comparison is done for the following case such as 1) without any compensator, 2) with capacitor bank and 3) with static var compensator. The performance of SVC shows improvement in

maintaining system voltage under change in load in all the buses. Figure 4.12 shows the bus voltage comparison in percentage for various compensator.

Table 4.11 Load flow study under Static Var Compensator

Load flow study under SVC							
Sl No	BUS ID	kW	kVAR	kVA	AMPS	Pf in %	Bus Voltage in %
CASE 5							
1	WTP-1	4152	2000	4608	81.6	92.49	100.015
2	WTP-2	3095	1187	3315	58.12	95.63	100.015
3	RWITPH	1183	285.8	1217	64.01	98.25	99.25
4	IPSA	3095	1187	3315	58.24	94.34	99.92
5	CWPH-1	3700.2	1591.02	4098.2	219.01	95.54	98941
6	CWPH-2	3891	1565.21	4263.1	228.023	94.81	99.52

Table 4.12 Bus Voltage in % Comparison of various compensator Performance

Sl no	Bus Type	Without Compensator	With Capacitor bank	With Static Var Compensator	With Addition of all compensator
1	Slack /Swing		100	100.015	102.790
2	Load	82.863	100	100.015	104.143
3	Load	80.147	99.17	99.25	103.922
4	Load	89.078	99.83	99.92	103.909
5	Load	86.527	98.21	98.941	103.929
6	Load	85.416	98.04	99.52	105.000
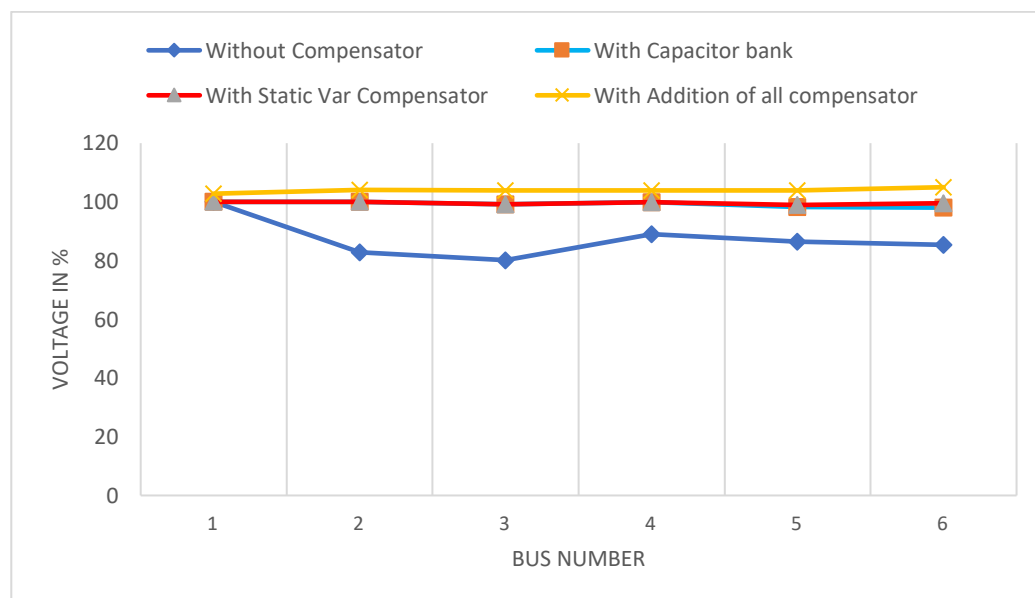
Figure 4.12 Comparison of bus voltages under various compensator

4.6. Short Circuit Analysis

In order to understand the system performance with and without consideration of

microgrid system, a short circuit analysis is performed on the singe line diagram as shown in the figures 4.13 the design consideration are as follows.

1. Loading of each bus is considered as per Short Circuit analysis

2. Distribution Transformer considered as OCTC mode.

3. Transformer impedance values are given in the table

4. The extent of modelling the LV system is shown as per SLD

5. Cable Sizes and lengths are modelled as per the Cable sizing Calculation.

6. Short circuit study evaluates the 3 phase - Fault current, Line to ground fault of the system and Check the withstand capacity of the Breaker Peak and Symmetrical Short Circuit and Ground Fault current.

7. The type of fault is considered as three phase bolted fault with zero impedance as this result in maximum fault current value is calculated.

4.6.1 Study Cases

The study deals with the equivalent one line diagram network representation based on the Single line Diagram. This report considers computer-based Power System study to analysis and examine the Power distribution system. ETAP version 19.0.1 developed by Operation Technology Inc. (OTI) is used for the System analysis. Short circuit studies for the above cases were conducted considering that all transformers are operating at their nominal tap positions and the interim short circuit results were analyzed. Figure 4.13 (a) and figure 4.13 (b) shows the short circuit analysis under three phase fault and Line to Ground fault. Moreover, Table 4.13 shows the short circuit analysis report under different cases as explained in the previous section.

From table 4.13 it can be seen that the short circuit currents in each bus are within standard range and as per limit range of the system ampere ratings. However, Improvement in the Short circuit analysis values can be done by installing series reactor or current limiting reactor in the system, the following table 4.14 shows the comparison of various current before and after implementation of current limiting reactor, from the report it can be seen that the current limiting reactor reduce the fault current in each busses and can improve the system performance, especially under such fault conditions.
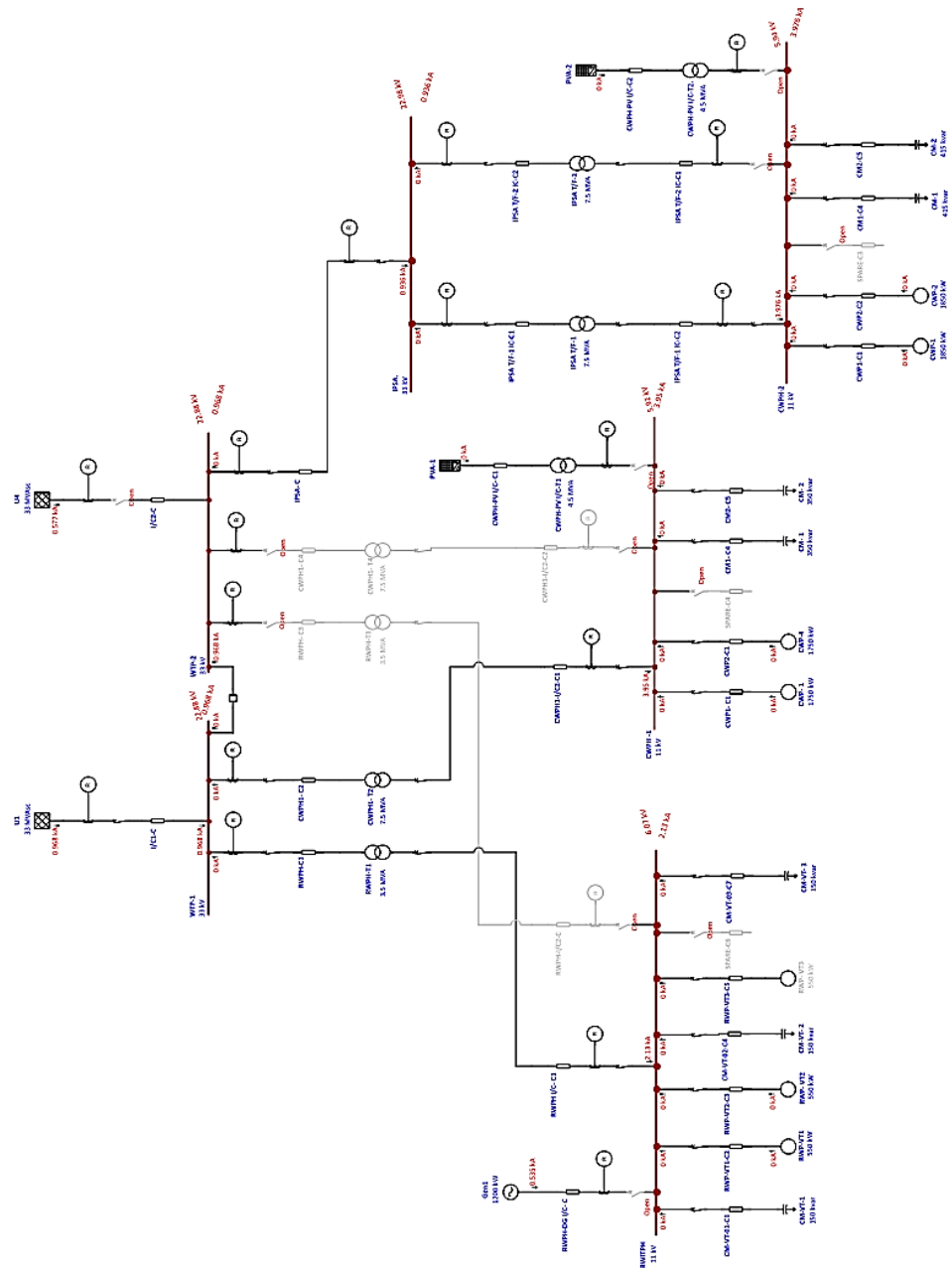
Figure 4.13 (a) Short Circuit analysis three phase fault

Table 4.13 Short circuit results summary

Short circuit current			
S.NO	BUS ID	3-PHASE in kA	L-G fault in kA
CASE 1			
1	WTP-1	1.07	0.833
2	WTP-2	0.97	0.791
3	RWITPH	1.749	1.956
4	IPSA	0.965	0.773

5	CWPH-1	2.938	3.47
6	CWPH-2	2.822	3.36
CASE 2			
1	WTP-1	1.463	0.968
2	WTP-2	1.463	0.968
3	RWITPH	1.965	2.13
4	IPSA	1.433	0.936
5	CWPH-1	3.474	3.95
6	CWPH-2	3.506	3.976
CASE 3			
1	WTP-1	NA	NA
2	WTP-2	NA	NA
3	RWITPH	0.809	0.898
4	I P 44	NA	NA
5	CWPH-1	NA	NA
6	CWPH-2	NA	NA
CASE 4			
1	WTP-1	0.956	0.785
2	WTP-2	0.691	0.648
3	RWITPH	1.41	1.619
4	IPSA	NA	NA
5	CWPH-1	2.749	3.292
6	CWPH-2	NA	NA
CASE 5			
1	WTP-1	1.133	0.841
2	WTP-2	1.031	0.799
3	RWITPH	1.768	1.972
4	IPSA	1.026	0.781
5	CWPH-1	3.18	3.871
6	CWPH-2	2.822	3.36

Table 4.14 Comparison with and without current limiting reactor

Bus No	Bus Type	3 phase fault current kA	L-G fault current kA	With current limiting reactor 3 phase current (kA)	With current limiting reactor L-G fault current (kA)
1	WTP-1	1.133	0.841	0.933	0.692
2	WTP-2	1.031	0.799	0.731	0.429
3	RWITPH	1.768	1.972	0.628	0.862
4	IPSA	1.026	0.781	0.142	0.436
5	CWPH-1	3.18	3.871	1.716	2.648
6	CWPH-2	2.822	3.36	1.614	2.187
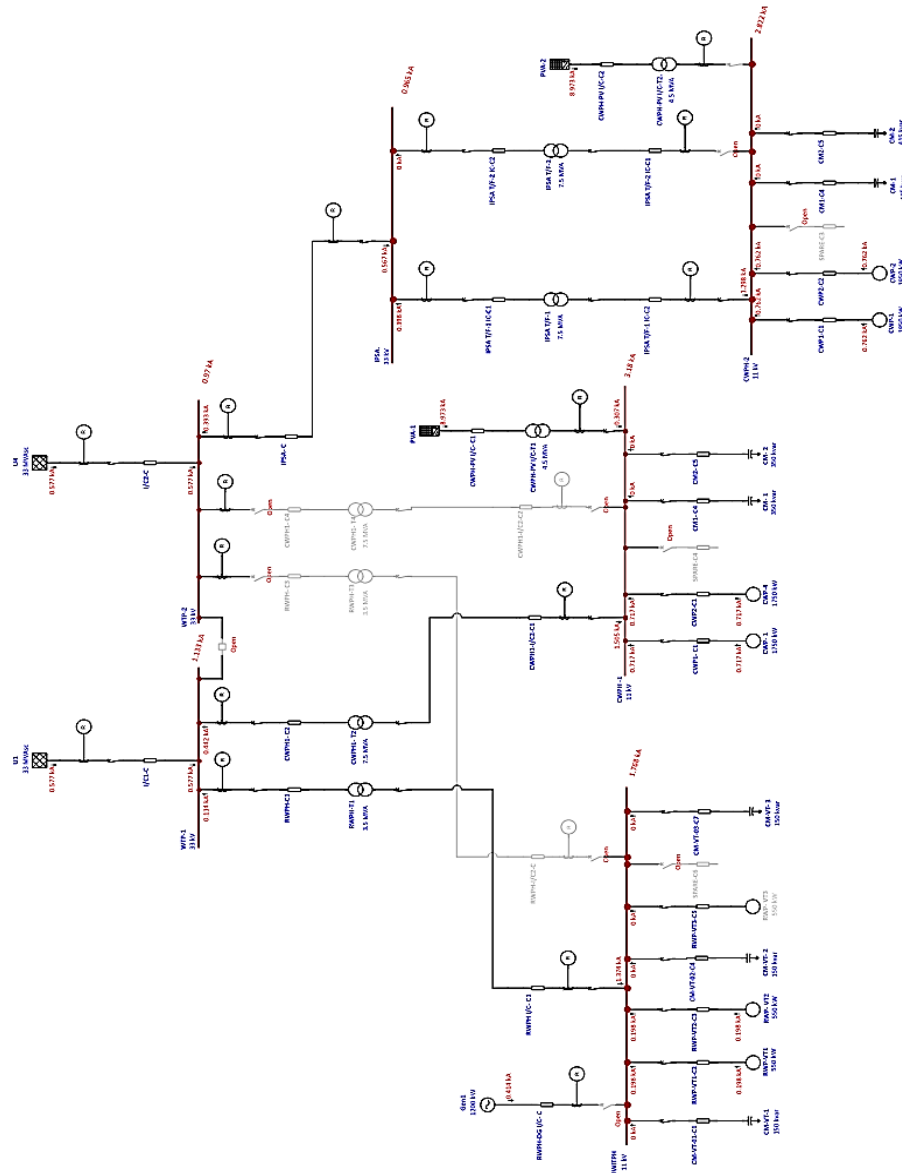
Figure 4.13 (b) Short circuit analysis L-G fault

4.7. Relay Coordination

Relay coordination settings has not been yet properly implemented in the power system of WTP. Because of this unexpected tripping of relays and coordination issue is being faced in the existing system. Causing various issues in the operation of the treatment plant. Therefore, in order to properly coordinate the system at various locations in times of fault and unwanted events, relay coordination settings have been done using ETAP software. Various relay coordination settings for Intake, WTP and IPS are discussed below. Various calculation and settings such as under voltage

settings, hysteresis settings, time delay settings, earth fault settings etc. are shown below. Table 4.15 below shows various settings such as Restricted Earth faults, HV Ref settings etc. Similarly, the corresponding figure 4.14, 4.15 and 4.16 shows relay coordination settings done for CWPH1& CWPH2, RWPH Intake transformer and CWPH-1 transformer as shown in the Single Line Diagram discussed in the previous sections.

4.7.1 Under Voltage Protection Setting

4.7.1.1 Calculation of (33kV) Protection Relay - REF-615

In order to properly set the relay co-ordinations each and every set values need to be chalked out properly before settings of the respective relays, various settings and calculations are shown in this section.

A. System Data taken from the WTP substation, Aizawl

Bay Reference (33kV Incoming feeders)	=	H05, H10
(33kV Bus Sections)	=	H07 & H13
(33kV Cable feeders)	=	H06, H09, H12 & H15
System Voltage	=	33 kV

B. Voltage Transformer (VT) data

Voltage Ratio	=	$(33000 / \sqrt{3}) / (110/\sqrt{3})$
Accuracy Class	=	0.5 / 3 P
Burden	=	100 VA

C. Relay Data

Make	=	ABB
Model	=	REF-615

4.7.1.2 Undervoltage Alarm Setting

Power system under-voltages on may occur due to:

System faults, an increase in system loading and non-energized power system e.g. Loss of an incoming transformer. Therefore, Undervoltage/DTL elements can be used to detect abnormal undervoltage conditions due to system overloads. To confirm loss of supply, the undervoltage elements should be set to values safely below that where a normal system voltage excursion can be expected

Hence, selected voltage setting is 80% of the nominal

voltage.   = $0.8 \times (110/\sqrt{3}V)$

                                   =   50.8 V

Gn 27/59-1 setting   =   51 V (Alarm)

4.7.1.3 Time delay settings

A time delay is required to ensure voltage dips due to remote system faults do not result in an unnecessary alarm. The time delay for undervoltage element is recommended as 60 sec.

Gn 27/59-1 Delay (Alarm)   =   60 sec (Alarm)

4.7.1.4. Hysteresis Setting

The variable hysteresis setting allows the user to vary the pick-up/drop-off ratio (or drop-off / pick-up ratio) of the element.i.e. it affects the reset ratio. Care has to be taken to ensure that with undervoltage elements, the reset level of the element is not set to a value higher than that at which the system rated voltage is expected to operate. The Hysteresis setting for undervoltage element is set as 2% as per relay manufacturer recommendation,

Gn 27/59-1 Hysteresis = 2.00%

4.7.1.5. U/V Guard Setting

Voltage elements can be blocked if all phase voltages fall below the 27/59 U/V Guard settings,

Gn 27/59-1 U/V Guarded = Yes

4.7.1.6. O/P Phases Setting

The settings determines whether the time delay is initiated for operation of any phase or only when all phases have detected the appropriate voltage condition,

Gn 27/59-1 O/P Phases = Any

4.7.2. Undervoltage Setting for Earth Switch Interlock

This setting is used for the the earth switch interlock of the cable feeders. Therefore, selected voltage setting is 30% of the nominal voltage,

$$= 0.3 \times (110/\sqrt{3}V) = 19.1 \text{ V}$$

Gn 27/59-2 setting   = 19 V

4.7.2.1. Time Delay Setting

A time delay is required to ensure the absence of voltage in the cable The time delay for undervoltage element is recommended as 1 sec

Gn 27/59-2 Delay = 1 sec

4.7.2.2. Hysteresis Setting

The variable hysteresis setting allows the user to vary the pick-up/drop-off ratio (or drop-off / pick-up ratio) of the element.i.e. it affects the reset ratio. The Hysteresis setting for is set as 2%.

Gn 27/59-2 Hysteresis = 2.00%

4.7.2.3. U/V Guard Setting

Voltage elements can be blocked if all phase voltages fall below the 27/59 U/V Guard settings,

Gn 27/59-2 U/V Guarded = No

4.7.2.4. O/P Phases Setting

The settings determine whether the time delay is initiated for operation of any phase or only when all phases have detected the appropriate voltage condition.

Gn 27/59-2 O/P Phases = All

Table 4.15 various Settings for relay co-ordinations

RESTRICTED EARTH FAULT PROTECTION		
Relay type used	=	REF 615 ABB Make
System Details (3500 KVA TRANSFORMER)		
Transformer Capacity in MVA	=	3.5
Transformer % Impedance	=	7.15%
HV Side Phase side CT reference- primary	=	200
HV Side Phase side CT reference- secondary	=	1
HV Side Voltage reference in kV	=	33
HV full load current in Amps	=	3.5MVA/(1.732*33*10^3)
	=	61
HV REF Settings:		
Maximum Fault Current in Amps	=	61/(0.0715)
	=	853
Equivalent Fault Current in Sec. in Amps	=	4.27
REF Pickup current in Amps	=	20% of full load current
	=	0.20*61
	=	12.2
Equivalent secondary current in Amps Is	=	12 /200
	=	0.06
station transformer - HV standby EF protection		
Relay type used	=	REF 615 ABB Make

System Details		
Transformer Capacity in MVA	=	3.5
Transformer % Impedance	=	7.15%
HV Side Phase side CT reference- primary	=	200
HV Side Phase side CT reference- secondary	=	1
HV Side Voltage reference in kV	=	33
HV full load current in Amps	=	3.5MVA/(1.732*33*10^3)
	=	61
Standby Earth fault setting:		
Pick up Setting in Amps	=	20% of rated current
	=	0.2*61
	=	12.2
Pick up Setting in secondary	=	0.1
Delay Type	=	DT
Operating Time	=	0.5 s
The above SBEF protection needs to be combined with a neutral over voltage protection to prevent nuisance		
Relay type used	=	REF 615 ABB Make
System Details (7500 KVA TRANSFORMER)		
Transformer Capacity in MVA	=	7.5
Transformer % Impedance	=	7.15%
HV Side Phase side CT reference- primary	=	200
HV Side Phase side CT reference- secondary	=	1
HV Side Voltage reference in kV	=	33
HV full load current in Amps	=	7.5MVA/(1.732*33*10^3)
	=	131

HV REF Settings:		
Maximum Fault Current in Amps	=	131/(0.0715)
	=	1832
Equivalent Fault Current in Sec. in Amps	=	9.16
REF Pickup current in Amps	=	20% of full load current
	=	0.20*131
	=	26.2
Equivalent secondary current in Amps Is	=	26/200
	=	0.13
station transformer - HV standby EF protection		
Relay type used	=	REF 615 ABB Make
System Details		
Transformer Capacity in MVA	=	7.5
Transformer % Impedance	=	7.15%
HV Side Phase side CT reference- primary	=	200
HV Side Phase side CT reference- secondary	=	1
HV Side Voltage reference in kV	=	33
HV full load current in Amps	=	7.5MVA/(1.732*33*10^3)
	=	131
Standby Earth fault setting:		
	=	20% of rated current

Pick up Setting in Amps	=	0.2*131
	=	26.2
Pick up Setting in secondary	=	0.1
Delay Type	=	DT
Operating Time	=	0.5 s
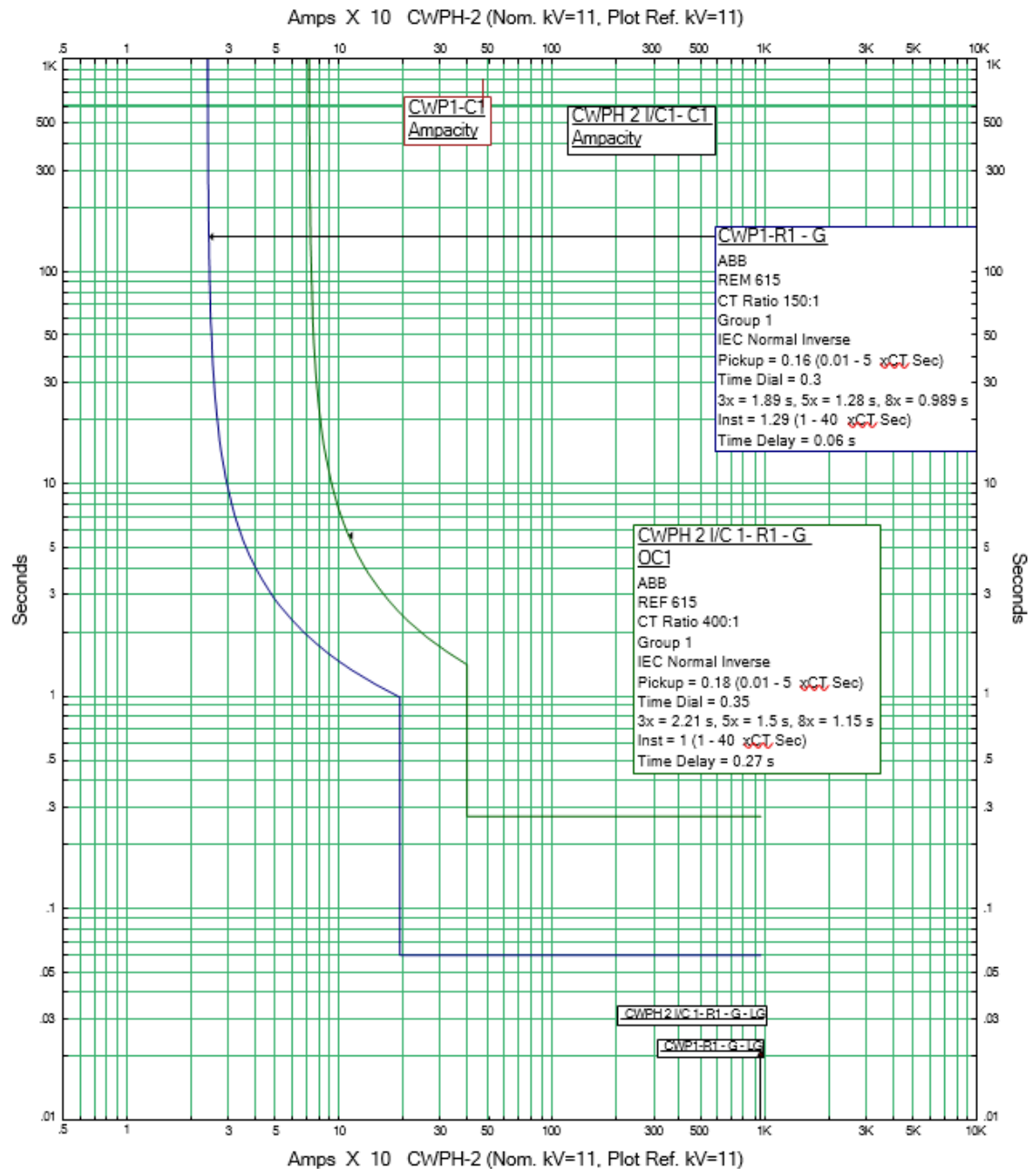
Figure 4.14 Relay settings for CWPH1& CWPH2

Figure 4.15 Relay settings for RWPH intake Transformer
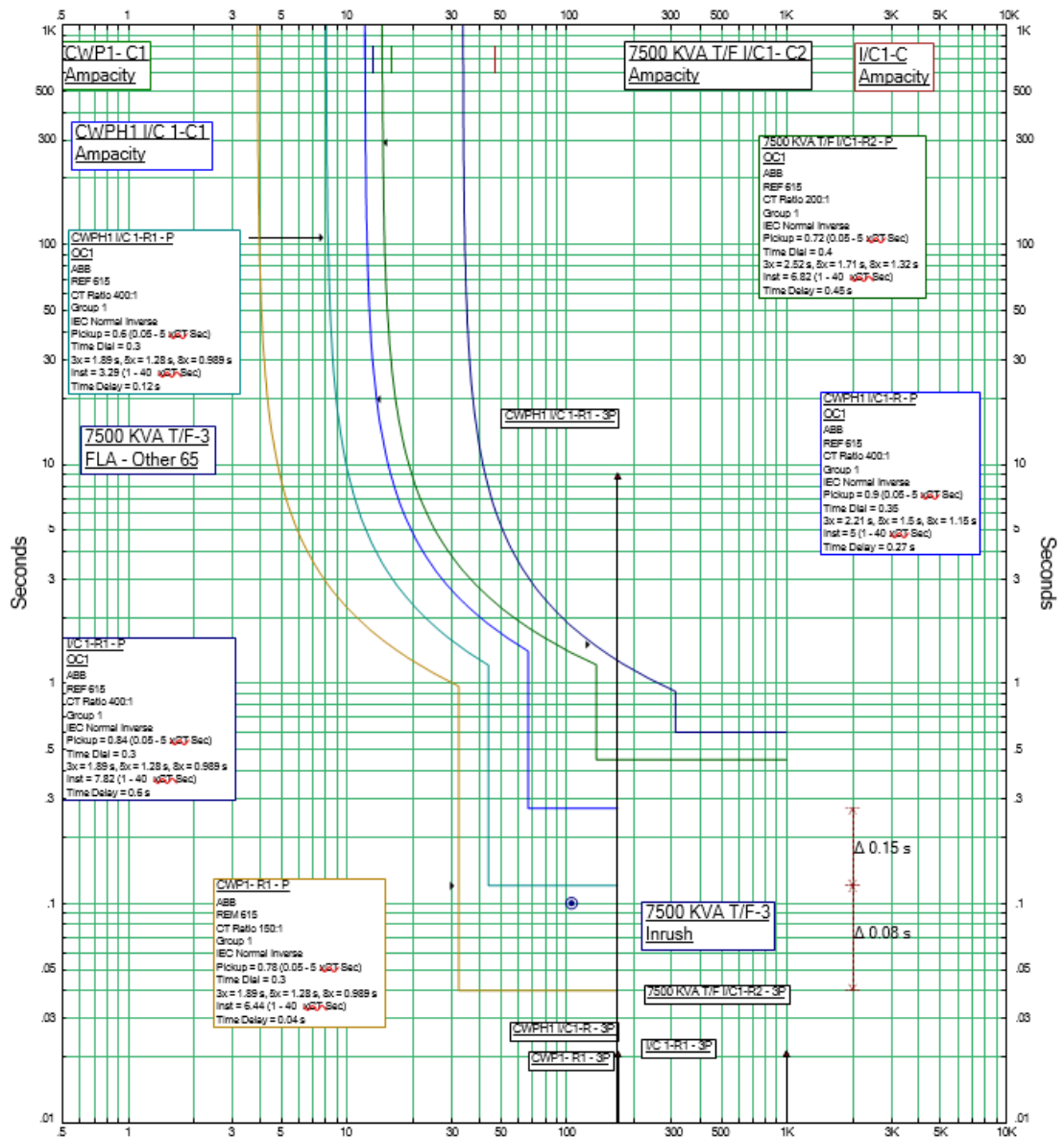
Figure 4.16 Relay settings for CWPH-1 Transformer

4.8. Conclusions

In this chapter, analysis / study of existing WTP is done using ETAP software, study such as load flow, short circuit analysis and relay settings are presented. As per site survey no proper analysis as well as plan for RES installation is not yet done in the existing system. Therefore, ETAP software offers efficient tool for various analysis and to solve the coordination problem of overcurrent relays. All power substation, load

and transmission data are considered and used as per actual data in the analysis and report, The analysis report of Load flow, short circuit analysis and relay coordination of Intake, WTP and IPS including 33kV electrical system of around 8.3 MVA capacity and SPV shows possibilities and strategies for improvement in system performance as well as current status of existing system.

With reference to Schneider Electric's, the LFA, short circuit analysis, and relay setup approach provided here is the method utilised in general in industries. This report's relay coordination technique is based on industrial guidelines (Alstom protection guide) and IEEE publications. ETAP is used to get simulation results.

The main protection devices in a distribution system are overcurrent relays (phase and earth fault), improvement in the analysis such as load flow results using a static variable compensator, and short circuit results using a current limiting reactor is done in this chapter. The overcurrent relay coordination problem in a radial network is a very difficult optimisation issue. The relays in the power system must be correctly coordinated in order to offer main and backup protection while avoiding malfunction and therefore avoiding an unnecessary outage of a healthy component of the system. Also, analysis with and without RES i.e. Solar shows system analysis under consideration of Microgrid concept.

CHAPTER

5

Solar PV, Wind, Battery based AC Microgrid system considering Intake of Water Treatment Plant

5.1 Introduction

Conservation of water sources and sustainable management of WTPs have become increasingly important due to the effects of climate change and pollution in the environment. The rising consumption of fossil fuels such as coal, natural gas, and oil has resulted in higher energy costs, which is a significant consideration for public WTPs and industries. Typically, a water supply system comprises raw water pumping station, a WTP, intermediate pumping stations, and a main reservoir. Power for each pumping station is obtained from the grid through distribution companies or the power and electricity department. The power requirements for each pumping station are determined by the plant design and pump capacity.

In the case of public WTPs, the power requirement is classified under the HT category and stepped down to low tension (LT) for auxiliary loads. The figure 5.1 depicts a SLD of a typical intake. A HT diesel generator is provided for standby power supply, and step-down power transformers are used to feed various auxiliary loads, which typically account for 5-20% of the total loads. Since public WTPs are bulk consumers, the government and municipalities bear the operating and energy costs. However, the use of a diesel generator set alone contributes significantly to the operational cost, which is a financial burden for many WTPs [161].

Apart from financial considerations, the use of diesel generators also contributes to environmental pollution, particularly the release of CO_2 gas into the atmosphere. Therefore, sustainable treatment and power supply are crucial for ensuring reliable public water supply while reducing the burden on each municipal.

DER or distributed generation (DG) are playing a significant role in resolving various challenges in the power sector, including those encountered in water supply systems. These resources have gained popularity due to their flexibility and decentralization, allowing them to meet the ever-increasing energy demand. They are integrated into the main grid through control panels and power electronic devices such as converters [162]. The microgrid concept has the potential to revolutionize power sectors by addressing various issues, and it can be incorporated into various applications. A microgrid is an independent energy system that comprises different loads and one or more DERs, such as wind turbines, solar panels, battery energy storage systems, generators, and others. Microgrids typically operate in synchronization with the grid but isolate themselves in case of a fault on the line or grid side, ensuring that the system continues to receive a continuous power supply. Examples of microgrid applications include university campuses, industrial complexes, military complexes and treatment plants etc. among others [163].
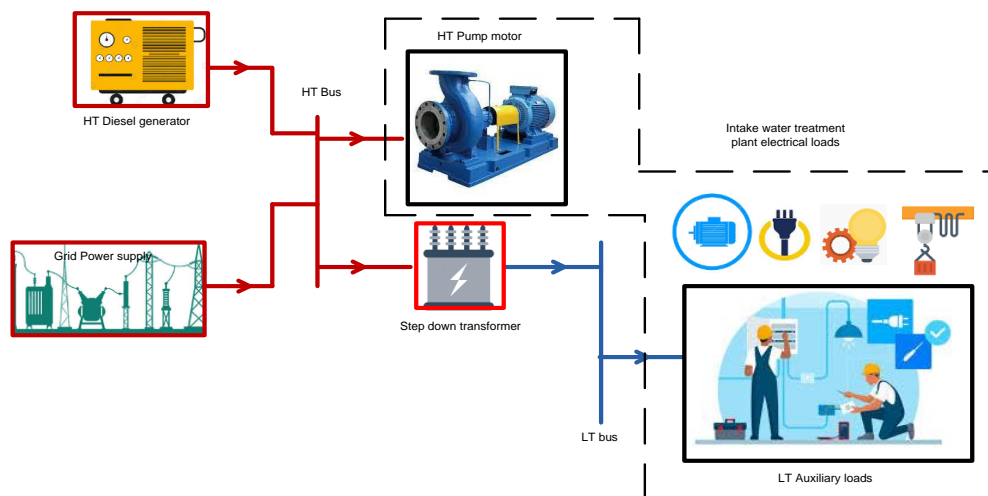

Figure 5.1. SLD of typical Intake system

In a microgrid system, maintaining system frequency, voltage, and stability poses significant control challenges. To address these challenges, various control techniques

are available for both grid-connected and isolated modes of operation. Energy management is the primary objective in grid-connected mode, whereas frequency and voltage control become the top priority in islanded mode while ensuring energy demand is met. In traditional power networks, centralized control architecture is widely used, especially in generating stations [164-165] However, decentralized control architectures are commonly applied in DER/DG applications. In the absence of synchronous machines in microgrid systems, inverters play a critical role in providing frequency and voltage control, particularly in islanded mode of operation. Control strategies such as Active Power (P) and Reactive Power (Q) control, and voltage frequency control (V/f) are utilized in grid-connected mode and are quickly switched to frequency and voltage control when islanded mode is activated. [166-167].

When designing a low voltage (LV) based microgrid system, the line impedance at various voltage levels is crucial in considering droop control. Typically, the lines are assumed to be resistive, and therefore, a relationship between active power (P), voltage (V), and (P-V) is considered. Similarly, a relationship between reactive power (Q), frequency (f), and (Q-f) is taken into account. Hence, the combinations of P-V and Q-f droop and their relationships are considered for voltage and frequency control in microgrid systems. These relationships are vital in regulating voltage and frequency in microgrid systems, ensuring efficient and stable system operation [168-169].

In contrast to low voltage (LV) microgrid systems, medium voltage (MV) microgrid systems are designed with lines that are assumed to be more inductive. As a result, the relationship between active power (P) and frequency (f) is considered through (P-f) droop, while the relationship between reactive power (Q) and voltage (V) is considered through (Q-V) droop. To improve the efficiency and stability of the microgrid system, more advanced droop methods, such as P-f and Q-V droops and their variations, are utilized for frequency and voltage control [170-171].

In terms of WTPs, the intake system can be viewed as a separate unit that consists of a combination of low voltage and medium voltage loads. Consequently, the line's resistance and inductance are taken into account, and the respective P-f and Q-V droops are considered for regulating frequency and voltage in the intake microgrid system [172-173].
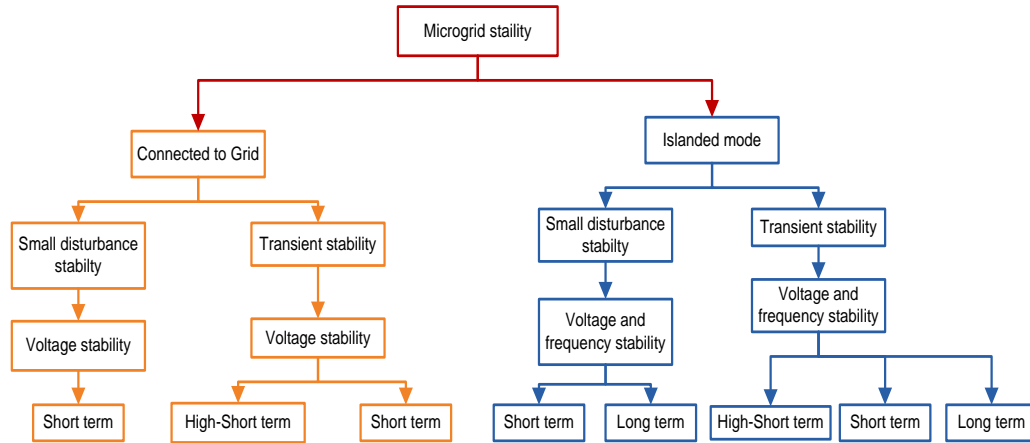
Figure 5.2. Microgrid stability

Studies have shown that renewable sources, such as wind and solar, have a periodic and fluctuating nature, causing the power producing capacity of Distributed Generators (DGs) to be varying and periodic. Therefore, it is crucial to monitor and compensate for reactive power to avoid problems such as voltage change, transient stability, and voltage collapse. Figure 5.2 illustrates different classifications of Microgrid (MG) stability, which can be divided into two phenomena: short-term phenomena lasting only a few seconds and long-term phenomena. Stability issues that extend beyond the short-term phenomena are categorized as long-term stability [174]. To prevent instability, different control methods are available as per the specific requirements. To address the stability issues of microgrid systems, researchers have proposed several solutions in various papers. Microgrid systems typically integrate renewable energy sources and power electronic devices, with improved energy storage elements incorporated to compensate for energy deviations.

The droop control technique is widely used in microgrid systems to regulate voltage and frequency for achieving power sharing. However, the generalized droop control technique is only effective under grid-connected mode. This is because it relies on the inverter output impedance and line impedance between DGs and loads, and determining the accurate line impedance value between multiple DG units and their corresponding loads can be challenging [175]. Furthermore, droop control has limitations such as high droop coefficients, which can cause voltage and frequency deviations and compromise the stability of the grid. Additionally, implementing droop

control in microgrid systems can be difficult due to the complex transformation of microgrid parameters [176]. To mitigate the limitations of the droop control technique and overcome the dependency on line parameters, various intelligent methods such as artificial neural network (ANN), ANFIS, and fuzzy logic have been proposed as alternatives [177]. These methods are being researched as potential solutions for improving the performance of microgrid systems.

Various control schemes have been proposed in recent studies for improving power quality in grid-connected mode, as well as regulating voltage and frequency in islanded mode. Intelligent-based frequency control techniques have also been introduced in many scenarios, which have shown to improve system response compared to conventional methods. For instance, in some literature, ANN and fuzzy logic controller (FLC) based frequency regulation in an islanded microgrid has been implemented [178]. Many studies have also suggested the use of energy storage elements such as batteries, electric vehicles, fuel cells, capacitors, flywheel storage, etc. for regulating frequency. This research paper focuses on developing a battery storage-based frequency regulation system for a microgrid that supplies power to a public water supply intake. The microgrid comprises a permanent magnet-based wind turbine and a solar photovoltaic system. To regulate the microgrid's frequency, the paper proposes a droop control technique that employs an ANFIS [179]. The paper aims to address the issue of frequency deviations in the microgrid system caused by the primarily motor load of the water supply intake. Although intelligent techniques such as ANNs, Fuzzy Logic Control (FLC), and ANFIS have been employed in other microgrid systems, this paper focuses on an application in the water supply system that has not been explored in existing literature.

The goals and objectives of this chapter include:

1. Examining a WTP (intake) under consideration of a microgrid concept.

2. Implementing distributed generators (DGs) into the microgrid system.

3. Employing droop control and utilizing the ANFIS technique for improving the system performance.

4. Evaluating the results with the generalized droop control (GDC) method.

5.2. Intake microgrid configuration and modeling (topology)

Maintaining a balance of power flow between supply and demand is a key objective of microgrid systems, particularly in islanded mode of operation. This balance can be achieved by load shedding or adjusting the power generation from various sources, such as non-renewable (e.g., natural gas, diesel, thermal, nuclear) or renewable energy sources (e.g., wind, solar, hydro). Utilizing these sources can enhance the performance of the microgrid system. Wind energy, for instance, generates fewer harmonics in the system compared to other renewable energy sources. However, in standalone systems, the low inertia of the system makes it susceptible to frequency fluctuations.
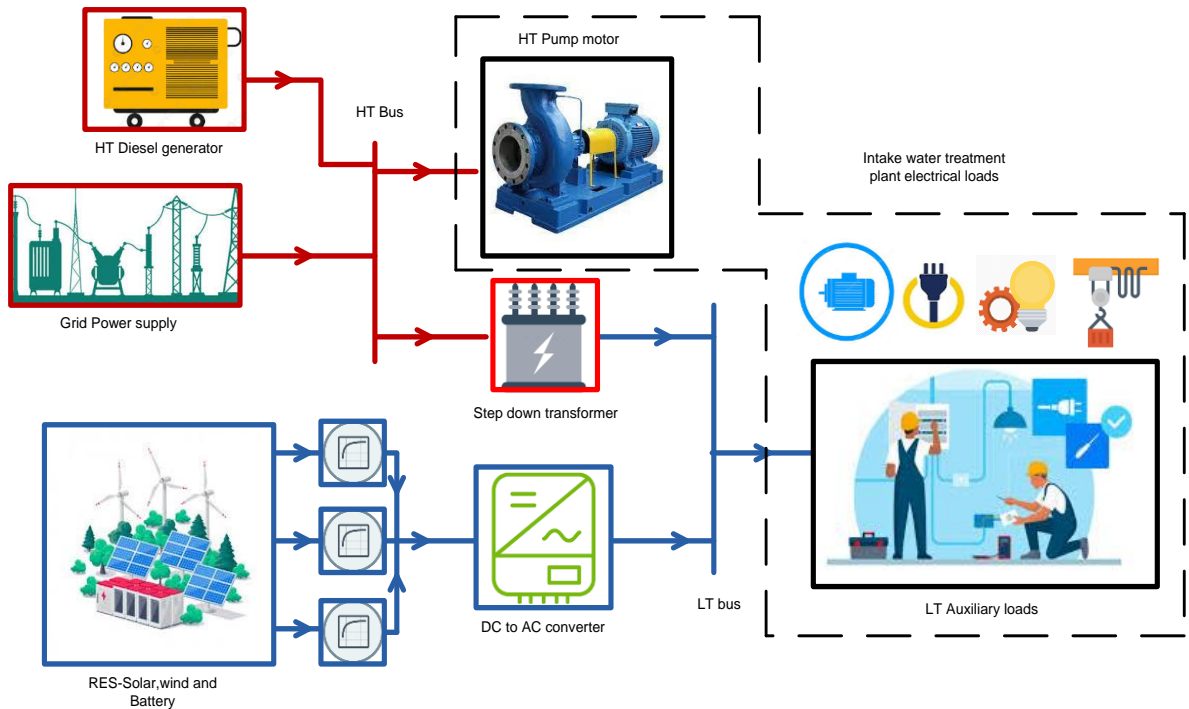
Figure. 5.3. Single line configuration of the proposed microgrid system.

The proposed intake microgrid system configuration is depicted in Figure 5.3. The system is designed to function as a microgrid with HT loads and auxiliary low-tension (LT) loads. In grid-connected mode, the power supply from the grid is stepped down to feed the various HT and LT loads. The system has two voltage levels. The first level is the HT power system, consisting of a parallel combination of the HT grid (such as 11 kV) and an HT diesel generator, which provides power supply to HT loads such as

pumps. The second level is the LT power voltage, which is provided through a step-down power transformer that feeds various LT loads such as compound lighting, quarters, and offices. In the LT side of the microgrid, backup power sources are implemented, including various distributed generators (DGs) such as a SPV system, a BESS, and permanent magnet synchronous generator (PMSG) based permanent magnet wind turbine generator. The figure shows the arrangement of the proposed microgrid system. The DGs, including the SPV system, BESS, and PMSG, are connected to a boost converter through a voltage source converter.

The BESS is coupled to the converter using a bidirectional DC to DC converter. The boost converter for the SPV array extracts the maximum available power using maximum power point tracking, while the bidirectional converter allows for charging and discharging of the battery. The BESS keeps the converter's DC-link voltage constant, providing the required power supply despite changes in SPV power output. The PMSG-based wind turbine generator is connected to the converter's DC side through a boost converter. The converters are linked to the DC-AC converter through the DC link. The output of the converter is connected to the LT bus via an LC filter and a coupling inductor, and various LT loads are connected at the LT bus or point of common coupling.

Table 5.1. Various loads of the microgrid system

Sl. No.	Load	Power	Unit
1	Raw water pump 1	350	kW
2	Raw water pump 2	350	kW
3	Indoor & outdoor lighting	2.5	kW
4	Sludge pump	2.8	kW
5	Auxiliary load	1.9	kW

Table 5.2. Various DGs of the microgrid system

Sl. No.	Source	Value	Unit
1	Solar	2.5	kW
2	Battery	1.5	kW
3	Wind	1	kW
4	HT Diesel generator	1000	kVA

The proposed microgrid system includes both HT and LT combinations, and a Diesel engine generator alone can provide power backup for both HT and LT loads. However, due to high operational and maintenance costs, the Diesel generator is

considered only for HT load. Therefore, various DGs are proposed for the LT side only, and the control strategy of the system is designed only for the LT side of the microgrid system. Table 5.1 and 5.2 provide details of the various loads and DGs connected to the intake microgrid system. Since the microgrid system operates in both grid-connected and islanded modes, the proposed intake microgrid system is designed to operate in both modes. Table 5.3 shows the operation of the microgrid in both grid-connected and islanded modes. In grid-connected mode, various loads such as motor loads, pumps, and lighting loads operate as per the system's requirements to pump the maximum amount of water from the river.

In the proposed intake microgrid system, the main power supply from the grid is utilized fully and excess energy from the renewable energy sources (RES), such as the SPV and Wind energy, is stored in the BESS and used to power the system. In addition, any surplus energy from the RES can be used to offset the power cost from the grid. In islanded mode, the system is disconnected from the main grid and the Diesel generator and RES provide the full power supply to the system. The converters in the system are crucial for controlling and converting energy. The stability and power flow optimization is achieved by performing droop control in both modes of operation.

5.2.1. Modeling and control of PV with battery system

Nowadays, various renewable energy technologies are widely adopted and utilized. Among them, SPV systems are one of the most important sources of renewable energy and are commonly used in many countries. The benefits of SPV systems include being pollution-free, requiring less maintenance, having no fuel costs, being easy to install, and contributing positively to environmental concerns such as the reduction of greenhouse gases. Therefore, SPV systems are an ideal and valuable alternative source of energy for replacing fossil fuel generation [180].

When operating in grid-connected mode, the primary concern regarding control is the proper distribution of power between the load and the source. However, in islanded or stand-alone mode, voltage and frequency control, as well as power sharing, become very important. To achieve this, a properly designed and calculated microgrid system is necessary, taking into account the dynamics of the loads and power sources [181].

Under islanded mode, it may not always be possible for the SPV system to operate at its maximum power point, additional energy source such as a BESS is required to satisfy the requirements of both linear and nonlinear loads. In this paper, a combination of a SPV system and BESS is considered to achieve maximum power output, and DC link voltage control is achieved through the use of electronic converters.

Table 5.3. Operation timeline of microgrid in grid connected and islanded mode

Sl. No.	Grid connected (0-0.5)	Islanded (0.5-1)	Load (HT/LT)	Operation time (s)
1	On	On	Raw water pump 1	0-1
2	On	On	Raw water pump 2	0-1
3	Off	On	Indoor & outdoor lighting	0-0.6
4	Off	On	Sludge pump	0.2-0.8
5	Off	On	Auxiliary load	0.4-0.9

The schematic diagram of the stand-alone SPV, BESS and Wind turbine system is shown in Figure 5.4. The system includes a SPV and a BESS that are connected to a DC link capacitor, which then connects to a three-phase inverter (DC-AC). To meet the system requirements, a DC to DC boost converter is utilized to boost the solar output voltage magnitude and drive the SPV output power. A bi-directional DC-to-DC converter is also connected to the battery energy storage system, which allows the converter to switch between charging and discharging the battery while achieving the DC link voltage. Finally, a three-phase inverter is used to convert DC voltage to AC voltage and control the load voltage magnitude. The system is implemented in MATLAB Simulink environment, and various loads analogous to intake LT loads are considered.

5.2.2. Solar photo voltaic (SPV) System

Table 5.4 displays the designed parameters for the SPV, battery and wind stand-alone system. The nonlinear model equation of the SPV system, which relates the SPV current to the terminal voltage, is defined in the following equations.

Table 5.4. Parameters of the stand-alone Wind, SPV and Battery system

Solar			
Parameters	Values	Parameters	Values
Θ	289°k	n_p	249
q	$1.602e^{-19}$C	I_{src}	8.12A

S	1.2	Θ_r	300° k
I_{rs}	1.8e^{-7}	n_s	238
A	1.692	k_θ	0.0014
K	1.38e^{-23} J/K		
Battery			
Parameters	**Values**	**Parameters**	**Values**
C_{b1}	49000F	R_{b3}	0.0019 Ω
C_{b2}	1.5 F	R_{b4}	0.045 Ω
R_{b1}	0.045Ω	V_b	46V
R_{b2}	0.001 Ω		
Wind			
Parameters	**Values**	**Parameters**	**Values**
$V_{w\text{-}rated}$	8.5 m/s	β	0 deg
P	1.204 kg/m^3	n_{gear}	5.8
R	4.6	$P_{T\text{-}rated}$	22.9 kW

$$I_{pv} = n_p I_{ph} - n_p I_{rs}[exp\left(\frac{q}{k\theta A}\frac{V_{pv}}{n_s}\right) - 1] \tag{5.1}$$

$$I_{ph} = [I_{scr} + k_\theta(\theta - \theta_r)]\frac{S}{100} \tag{5.2}$$

The equation describing the nonlinear model of the solar SPV system is given as:

I=Irs {[exp((V+I×Rs)/AΘ)]-1} + (T-Tref) × Isc / (kΘ × ns× np) + Gs $\tag{5.3}$

where I_{pv} represents the output current of the SPV system, I_{rs} is the reverse saturation current, Θ represents the temperature of the p-n junction, A is the ideality factor, I_{scr} is the short-circuit current of a single SPV cell, S is the solar irradiation level, n_s and n_p are the series and parallel number of SPV cells in a string, q (1.602e^{-19}C) and k (1.38e^{-23} J/K) are the unit electric charge and Boltzmann's constant, respectively. T is the operating temperature of the SPV system, T_{ref} is the cell temperature reference, kΘ is the temperature coefficient, and Gs represents the SPV cell conductance [182-183]

Similarly, equations for Boost Converter and the SPV System can be defined as follows,

When S_1 is ON (S_1 =1),

$$C_{pv}pV_{pv} = I_{pv} - I_1 \tag{5.4}$$

$$V_{pv} = L_1 pI_1 + R_1 I_1 \tag{5.5}$$

When, S_1 is Off (D_1 =1),

$$C_{pv}pV_{pv} = I_{pv} - I_1 \tag{5.6}$$

$$V_{pv} = L_1pI_1 + R_1I_1 + V_{dc} \tag{5.7}$$

Therefore, from the above equations ($D_1 = 1 - S_1$),

$$C_{pv}pV_{pv} = I_{pv} - I_1 \tag{5.8}$$

$$V_{pv} = L_1pI_1 + R_1I_1 + (1-S_1)V_{dc} \tag{5.9}$$
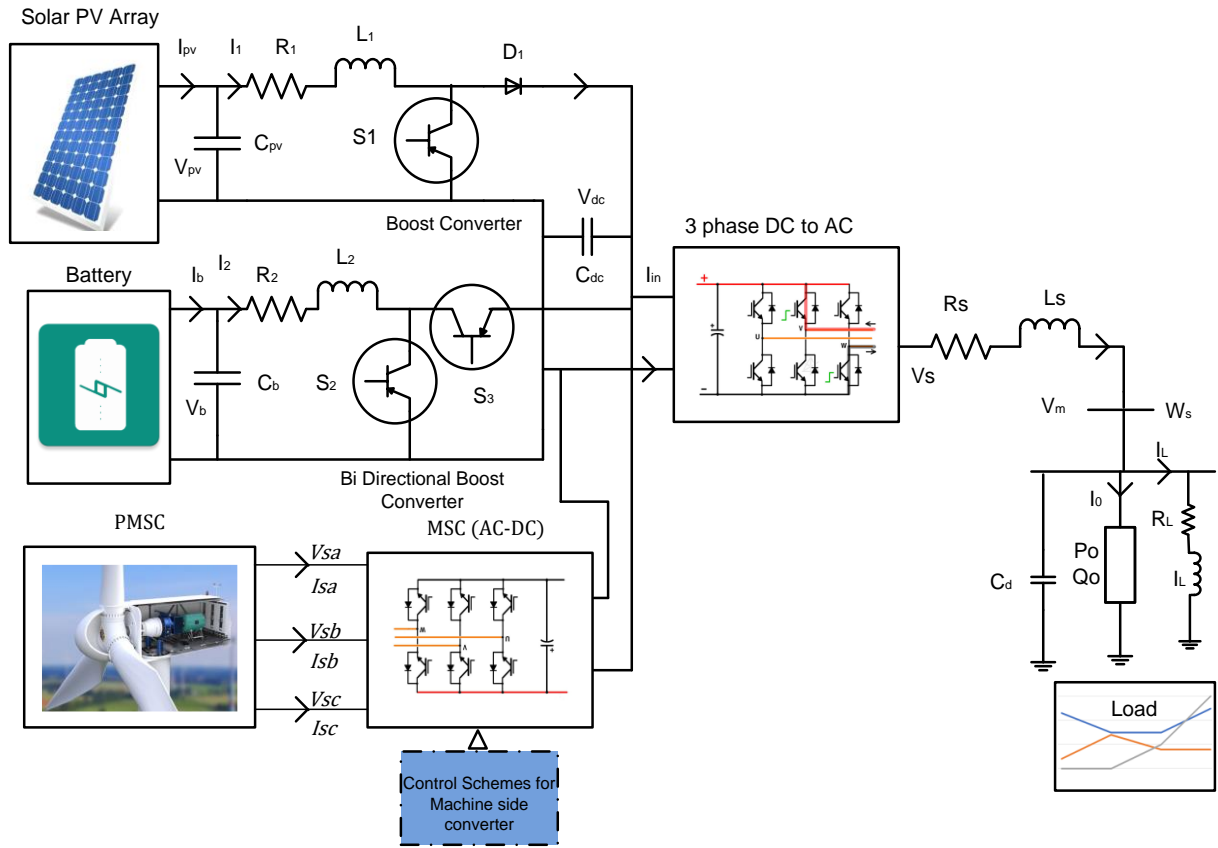
Figure 5.4. Wind-solar-Battery Stand-alone System.

5.2.3. Battery Energy Storage System (BESS)

The SPV system is connected to the battery energy storage system through a bidirectional converter, as shown in Figure 5.4. The converter is a DC to DC converter, and it is also connected to the DC link. The equivalent circuit of the battery is shown in Figure 5.5, and the equations that define the characteristics of the battery are provided below [192]. The parameters of the battery are given in Table 5.4.

$$R_{b1}I_{b1} - V_{b1} - V_{cb1} = 0$$

$$R_{b2}I_{b2} - V_{cb2} = 0$$

$$V_{cb1} + V_{cb2} + (R_{b3} + R_{b4})I_b + V_b = 0 \tag{5.10}$$

$$I_{b1} = I_b - C_{b1}pV_{cb1}$$

$$I_{b2} = I_b - C_{b2}pV_{cb2}$$

$$R_{b1}(I_b - C_{b1}pV_{cb1}) - V_{b1} - V_{cb1} = 0$$

$$R_{b2}(I_b - C_{b2}pV_{cb2}) - V_{cb2} = 0 \tag{5.11}$$

$$V_b = -V_{cb1} - V_{cb2} - (R_{b3} + R_{b4})I_b$$

$$R_{b1}C_{b1}pV_{cb1} = R_{b1}I_b - V_{b1} - V_{cb1}$$

$$R_{b2}C_{b2}pV_{cb2} = R_{b2}I_b - V_{cb2} \tag{5.12}$$

$$V_b = -V_{cb1} - V_{cb2} - (R_{b3} + R_{b4})I_b$$

The bidirectional boost converter for the battery is given by

When, S_2 is on ($S_2 = 1$, $S_3 = 0$),

$$C_b pV_b = I_b - I_2 \tag{5.13}$$

$$V_b - V_{dc} = L_2 pI_2 + R_2 I_2 \tag{5.14}$$

When S_2 is off ($S_2 = 0$, $S_3 = 1$)

$$C_b pV_b = I_b - I_2 \tag{5.15}$$

$$V_b = L_2 pI_2 + R_2 I_2 \tag{5.16}$$

After combination of the two modes of operation ($S_3 = 1-S_2$)

$$C_b pV_b = I_b - I_2 \tag{5.17}$$

$$V_b - S_2 V_{dc} = L_2 pI_2 + R_2 I_2 \tag{5.18}$$

From the above the DC link voltage equation can be given as

$$C_{dc}pV_{dc} = (1 - S_1)I_1 + S_2 I_2 - I_{in} = (1 - S_1)I_1 + S_2 I_2 - \frac{3}{4}(M_q I_{sq} + M_d I_{sd}) \tag{5.19}$$
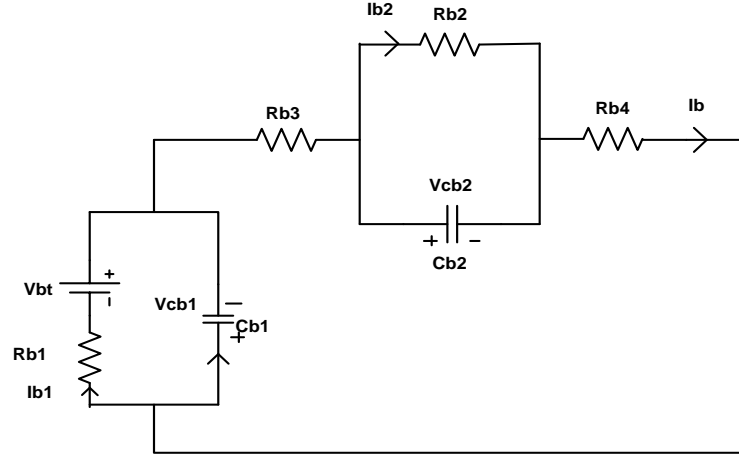
Figure 5.5. Battery equivalent circuit [192]

5.2.4. Control schemes for SPV and Battery

5.2.4.1. SPV Voltage and current Control

Figure 5.6 depicts the block diagram of a SPV DC-DC boost converter control system. The primary goal of the photo voltaic control is to track and maintain the maximum power point (MPP). The voltage controller's output is formulated using a specific equation,

$$C_b p V_b = I_b - I_2 \tag{5.20}$$

Therefore,

$$C_{pv} s V_{pv} = I_{pv} - I_1 = K_{pvv}(s)(V_{pv} * - V_{pv}) = \beta_{pvv} \tag{5.21}$$

In the SPV DC-DC boost converter control system, the SPV voltage reference (V_{pv}*) is obtained from the maximum power point tracking (MPPT) mechanism. The outer voltage PI controller's coefficients and the reference current for the inner controller are defined as part of the system's design.

$$
\left.
\begin{aligned}
K_{Ppvv} &= 2\lambda\omega_n C_{pv} \\
K_{Ipvv} &= W_n^2 C_{pv} \\
I_1^* &= I_{pv} - \beta_{pvv}
\end{aligned}
\right\} \tag{5.22}
$$

The controller parameters for the SPV DC-DC boost converter control system are set to $\lambda = 0.7$ and $\omega_{n1} = 0.2\pi f_{swdc}$, where f_{swdc} denotes the switching frequency of the DC-DC converter. In this case, the value of f_{swdc} is chosen to be 5 kHz for both DC-DC converters.

Figure 5.6. Block diagram of SPV DC-DC boost converter control

5.2.4.2. For current control

We have,

$$L_1 s I_1 + I_1 R_1 = V_{pv} - (1 - S_1^*)V_{dc} = K_{pv}(s)(I_1^* - I_1) = \beta_{pv} \tag{5.23}$$

Where S_1^* is the average duty ratio of the converter,

Also,

$$\begin{cases} K_{Ppv} = 2\lambda\omega_n L_1 - R_1 \\ \quad K_{Ipv} = W_n^2 L_1 \end{cases} \tag{5.24}$$

Where, $S_1^* = 1 - \dfrac{V_{pv} - \beta_{pv}}{V_{dc}}$, for further inner current control $\omega_{n2} = 0.4\pi f_{swdc}$.

5.2.4.3. DC link battery control

To ensure that the DC link voltage is properly regulated, the battery DC-DC converter in the SPV DC-DC boost converter control system should be responsible for controlling the voltage. Figure 5.7 and Table 5.5 provide additional information on the block diagram of the battery converter control unit and the relevant battery system parameters. If this method is utilized, the dynamics of the DC link voltage can be effectively managed and regulated.

$$C_{dc} s V_{dc} = (1 - S_1 *)I_1 + S_2 * I_2 - \frac{3}{4}\left(M_q I_{sq} + M_a I_{sd}\right)$$

$$= K_{dc}(s)(V_{dc} * - V_{dc}) = \beta_{dc} \tag{5.25}$$

Also,

$$\begin{cases} K_{Pdc} = 2\lambda\omega_n C_{dc} \\ \quad K_{Idc} = \omega_n^2 C_{dc} \end{cases} \tag{5.26}$$

Table 5.5 controller coefficient values and system parameter values

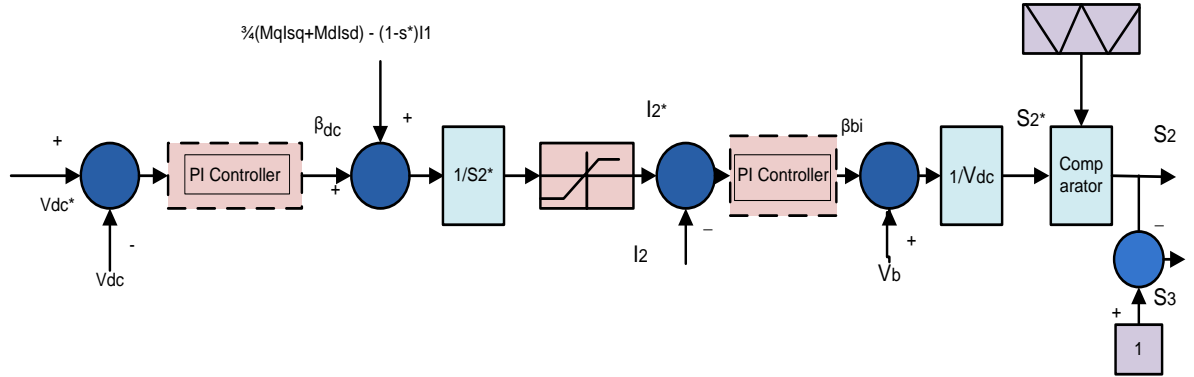| PI controller Coefficient Parameters of a system			
Parameters	Values	Parameters	Values
K_{pm}	0.457	K_{ppvv}	0.0578
K_{ps}	34.45	K_{ppv}	0.457
K_{pdc}	0.127	K_{lm}	0.128
K_{pb}	2.476	K_{ls}	3.447
K_{ppll}	0.821	K_{lpvv}	0.748
M_p	3 e^{-4}	K_{lpv}	0.487
K_{ldc}	0.463	K_{lpll}	0.348
K_{lb}	0.297	N_q	21 e^{-4}
Parameter value of a system			
Parameters	Values	Parameters	Values
R_s	0.245Ω	C_d	210 e^{-6}F
L_s	4.4 e^{-3}H	C_{dc}	5.8 e^{-6}F
R_L	10.248 Ω	R_1	0.248 Ω
L_L	0.4863H	L_1	3.4 e^{-3}H
C_{pv}	120 e^{-6}F	R_2	0.348 Ω
C_b	110 e^{-6}F	L_2	3 e^{-3}H

Figure 5.7. Block diagram of battery DC-DC converter control part

Similarly, for Current control of Battery Converter

$$L_2 s I_2 + I_2 R_2 = V_b - S_2 * V_{dc} = K_b(s)(I_2^* - I_2) = \beta_{bi} \tag{5.27}$$

Also, we have

$$\left. \begin{array}{c} K_{Pb} = 2\lambda\omega_n L_2 - L_2 \\ K_{ib} = \omega_n^2 L_2 \end{array} \right\} \tag{5.28}$$

Where, $S_2 * = \dfrac{V_b - \beta_b}{V_{dc}}$

In addition to fault protection, implementing an inner current loop controller for the battery converter in the SPV DC-DC boost converter control system can effectively regulate the battery's charge and discharge currents. This is a critical factor in determining the battery's overall lifespan. By utilizing this approach, the battery's

current flow can be limited, which can help to improve its longevity and optimize its performance.

5.2.5. Modelling and control of wind turbine generator

In recent years, there has been a growing interest in the use and development of renewable energy sources such as geothermal, solar, and wind power. Among these sources, wind energy generation has seen significant improvements and advancements over the past decade. Wind turbines are typically based on either synchronous generators or doubly fed induction generators (variable speed), with permanent magnet (PM) based generators being a popular choice due to their excitation-free operation, high efficiency, and reliability when compared to other generators. [184-185].

The wind turbine system connected with SPV and battery described in Figure 5.4 includes blades, a generator, and converters. The PMSG (Permanent Magnet Synchronous Generator) type wind turbine system is considered and it converts the mechanical energy produced by the gear system from the shaft of the turbine blades into electrical energy. This electrical energy is then connected to the electrical system via a machine-side converter (MSC) that converts AC to DC, and a Load-side converter (LSC) explained in the following sections, that converts DC to AC.

The MSC plays a vital role in controlling the speed of the wind turbine rotor and tracking the maximum power point of the available power, thus minimizing power losses. Meanwhile, the LSC maintains the DC link voltage and regulates the flow of reactive power to the load according to the system's requirements. [186-187].

To determine the mechanical power (P_T) generated by a wind turbine at a specific wind speed (V_ω), you can use the following mathematical equation:

$$P_T = \frac{1}{2}\rho A C_P(\lambda, \beta)V_\omega^3 \tag{5.29}$$

The provided formula includes several variables: ρ (kg/m), which denotes the air density; A (= πr^2), which represents the blade swept area; r, which is the wind turbine radius; V_ω (m/s), which stands for the wind velocity; C_P, which is the power coefficient; and λ and β, which represent the tip ratio and blade pitch angle, respectively.

To compute the power coefficient and tip ratio, equations (5.30) and (5.31) can be used, respectively

$$C_P = \frac{1}{2}(\lambda - 0.22\beta^2 - 0.5)e^{(-0.17\lambda)} \tag{5.30}$$

$$\lambda = \frac{R * \omega_T}{V_\omega} \tag{5.31}$$

5.2.6 PMSG wind turbine modeling

The model for the permanent magnet synchronous generator (PMSG) involves the application of the Park transformation method, which allows for the transformation of the three-phase abc reference frame to a two-phase dq reference frame [188]. Using this method, we can obtain the voltage equations for the PMSG.

$$V_{sd} = R_s I_{sd} + L_d \frac{dI_{sd}}{dt} - \omega_e L_q I_{sd} \tag{5.32}$$

$$V_{sq} = R_s I_{sq} + L_q \frac{dI_{sq}}{dt} - \omega_e \psi_{fl} + \omega_e L_d I_{sd} \tag{5.33}$$

In the context of the dq reference frame, the stator voltages are identified as V_{sd} and V_{sq}, while the stator currents are denoted by I_{sd} and I_{sq}. Additionally, L_d and L_q refer to the inductances of the dq axis, and R_s represents the resistance of the stator. The angular frequency is given by $\omega_e = np$, where np corresponds to the number of poles, and ψ_{fl} stands for the permanent flux linkage.

We can derive the electrical torque equation as follows:

$$T_e = 1.5n_p[\psi_{fl} I_{sq} + (L_d - L_q)I_{sd}I_{sq}] \tag{5.34}$$

Assuming that the PMSG is surface-mounted, where Ld equals Lq, we can write the expression for the electrical torque as follows

$$T_e = 1.5n_p\psi_{fl} I_{sq} \tag{5.35}$$

Rewriting the mechanical torque equation of PMSG

$$T_m = T_e + Bw_m + J\frac{dw_m}{dt} \tag{5.36}$$

The equation describes the relationship between the mechanical torque (T_m) and electrical torque (T_e), where J represents the moment of inertia and B denotes the friction coefficient.

Regarding the steady-state conditions, we can express both the active and reactive powers of the PMSG using the following equations:

$$P_s = \frac{3}{2}\left(V_{sd}I_{sd} + V_{sq}I_{sq}\right) \tag{5.37}$$

$$Q_s = \frac{3}{2}\left(V_{sq}I_{sd} - V_{sd}I_{sq}\right) \tag{5.38}$$

5.2.7. Control schemes for wind Turbine

5.2.7.1. Machine side controller

The primary goal of connecting the MSC to a wind turbine is to extract the maximum power available from the wind. Depending on the wind turbine's parameters, different conditions may arise. If the wind turbine's design perfectly matches that of the generator, the maximum power of both the generator and the wind turbine at nominal wind speed will be at the same point as the nominal speed of the generator. However, in other cases, the maximum power may occur either before or after the nominal speed of the generator [189]. For the purposes of this discussion, we assume that both the generator and the wind turbine are perfectly matched.

Power electronic devices are commonly used in wind turbine systems to convert the output of a permanent magnet synchronous generator (PMSG) from three-phase AC to DC power that can be linked to the DC bus [190]. This conversion process is essential for effective energy management and distribution within the system. By using power electronics, the generated power can be efficiently regulated and converted to the appropriate form for distribution or storage.
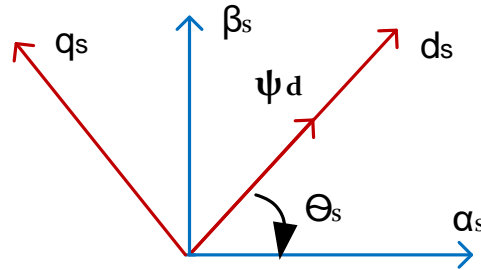

Figure5.8 Phasor diagram for MSC

the terms α_s and β_s are used to describe the stationary reference frame, while d_s and q_s refer to the synchronously rotating reference frame. Additionally, ψ_d represents

flux aligning with the d-axis, and ψ_q represents flux aligning with the q-axis. Figure 5.8 provides a phasor diagram illustrating these concepts. In this context, the primary flux can be mathematically expressed using the following equation.

$$\psi = \psi_d + j\psi_q \tag{5.39}$$

Assuming that the primary flux is aligned with the d-axis, it follows that the value of ψ_q, which represents flux aligning with the q-axis, is zero. This leads to a modification of Equation (5.39), which describes the relationship between the stator voltage phasor and the rotor flux phasor in the dq reference frame. Specifically, the new equation can be expressed as.

$$\psi_d = \psi \tag{5.40}$$

If the value of ψ_d, aligned with the d-axis, is equal to the primary flux ψ, and the stator voltage phasor along the d-axis (V_d) is zero, then the stator voltage phasor along the q-axis (V_q) is equal to V. Substituting these values into Equation (5.37) yields a modified version of the equation, which can be expressed as.

$$P = \frac{3}{2}V_q I_q \tag{5.41}$$

Assuming that Vq is held constant, it is possible to control the active power by regulating the current along the q-axis (Iq). This is because, when Vd is equal to zero, Equation 3.58, which describes the relationship between the stator current phasor and the rotor flux phasor in the dq reference frame, can be rewritten as.

$$Q = -\frac{3}{2}\left(V_q I_d\right) \tag{5.42}$$

This modified equation demonstrates that the active power is directly proportional to the current along the q-axis and the component of the rotor flux phasor along the d-axis (ψ_d).

Equation 5.42 indicates that it is possible to control the reactive power by regulating the current along the d-axis (I_d). Figure 5.9 shows a block diagram of the machine side controller, which is designed to maximize power output at varying wind velocities using a Perturb and Observe (P&O) algorithm-based Maximum Power Point Tracking (MPPT) technique [191]. The control scheme for the machine side involves calculating the reference speed ($\omega_m{}^*$) at which maximum power is achieved, in order to optimize performance.
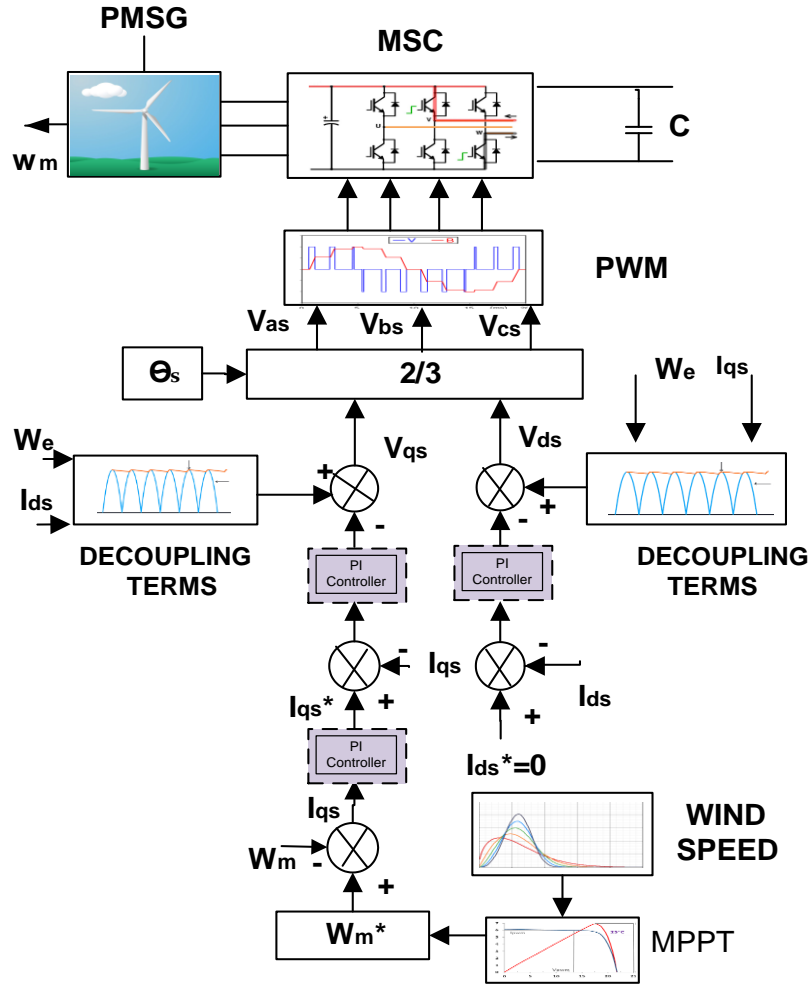
Figure 5.9 Machine side converter controller

5.2.7.2 Load side controller

The figure depicted in Figure 5.12 shows the block diagram of a typical power system based on a standalone converter. This system employs a voltage source converter to convert a DC input into an AC output voltage, which is then used to power a linear RL load and a constant load via a transmission line. To ensure that the voltage across the load is smooth, a capacitor is connected across it. Considering the abc reference frame, the dynamic equations of the transmission line are described by

$$
\left.
\begin{aligned}
V_{sa} &= V_{ma} + L_s p I_{sa} + R_s I_{sa} \\
V_{sa} &= V_{mb} + L_s p I_{sb} + R_s I_{sb} \\
V_{sa} &= V_{mc} + L_s p I_{sc} + R_s I_{sc}
\end{aligned}
\right\}
\tag{5.43}
$$

Also, Linear load of DG1 (L1) equations are defined as

$$
\left.\begin{array}{l}
V_{ma} = R_L I_{La} + L_L p I_{La} \\
V_{mb} = R_{L1} I_{Lb} + L_L p I_{Lb} \\
V_{mc} = R_L I_{Lc} + L_L p I_{Lc}
\end{array}\right\} \tag{5.44}
$$

Similarly, I_{L1abc} are represented as phase currents of linear load (L$_1$) derived from DG1

Capacitor equations can be given as

$$
\left.\begin{array}{l}
C_d p V_{ma} = I_{Sa} - I_{La} - I_a \\
C_d p V_{mb} = I_{Sb} - I_{Lb} - I_b \\
C_d p V_{mc} = I_{Sc} - I_{Lc} - I_c
\end{array}\right\} \tag{5.55}
$$

The above equation (5.43), (5.44) and (5.55) are converter into dq-axis using Perturb and Observe (P&O) algorithm transformation technique as shown in [192] Also, Figure 5.10. shows the control Scheme for DC-AC 3-phase Converter.

Therefore, we have the following three phase converter equations

$$
\left.\begin{array}{l}
p I_{sq} = \dfrac{1}{L_s}\left(M_q \dfrac{V_{dc}}{2} - V_{mq} - R_s I_{sq} - L_s \omega_s I_{sd}\right) \\[3mm]
p I_{sd} = \dfrac{1}{L_s}\left(M_d \dfrac{V_{dc}}{2} - V_{md} - R_s I_{sd} - L_s \omega_s I_{sq}\right)
\end{array}\right\} \tag{5.56}
$$

Similarly, the qd- synchronous reference frame equations at the voltage source inverter terminal (angular frequency $\omega_{s1)}$ for the inductance -resistance load, the linear load DG1(L1) equation can be given as

$$
\left.\begin{array}{l}
p I_{Lq} = \dfrac{1}{L_L}\left(\dfrac{V_{dc}}{2} - V_{mq} - R_L I_{Lq} - L_L \omega_s I_{Ld}\right) \\[3mm]
p I_{Ld} = \dfrac{1}{L_L}\left(\dfrac{V_{dc}}{2} - V_{md} - R_L I_{Ld} - L_L \omega_s I_{Lq}\right)
\end{array}\right\} \tag{5.57}
$$

Also, for the load capacitor the qd equation can be given as

$$
\left.\begin{array}{l}
p V_{mq} = \dfrac{1}{C_d}\left(I_{sq} - I_{Lq} - I_{0q} - C_d \omega_s I_{md}\right) \\[3mm]
p V_{md} = \dfrac{1}{C_d}\left(I_{sd} - I_{Ld} - I_{0d} - C_q \omega_s I_{mq}\right)
\end{array}\right\} \tag{5.58}
$$

Also, PI voltage controller is designed and shown as below in order to follow the load reference voltage at rated value

$$C_d pV_{mq} = I_{sq} - I_{Lq} - I_{0q} - C_d \omega_s I_{md} = K_{mq}(s)(V_{mq}^* - V_{mq}) = \sigma_{mq}$$
$$C_d pV_{md} = I_{sd} - I_{Ld} - I_{0d} - C_q \omega_s I_{mq} = K_{md}(s)(V_{md}^* - V_{md}) = \sigma_{md}$$

(5.59)

Where, the PI voltage controllers are

$K_{mq}(s), K_{md}(s)$

Similarly, after performing control of the load voltage the current controller will follow its reference after the current reference are defined.

The qd axis dynamic equations of the inner current controller are given below

$$L_s s I_{sq} = R_s I_{sq} = M_q \frac{V_{dc}}{2} - V_{mq} - L_s \omega_s I_{sd} = K_{sq}(s)(I_{sq}^* - I_{sq}) = \sigma_{sq}$$
$$L_s s I_{sd} = R_s I_{sd} = M_d \frac{V_{dc}}{2} - V_{md} - L_s \omega_s I_{sq} = K_{sd}(s)(I_{sd}^* - I_{sd}) = \sigma_{sd}$$
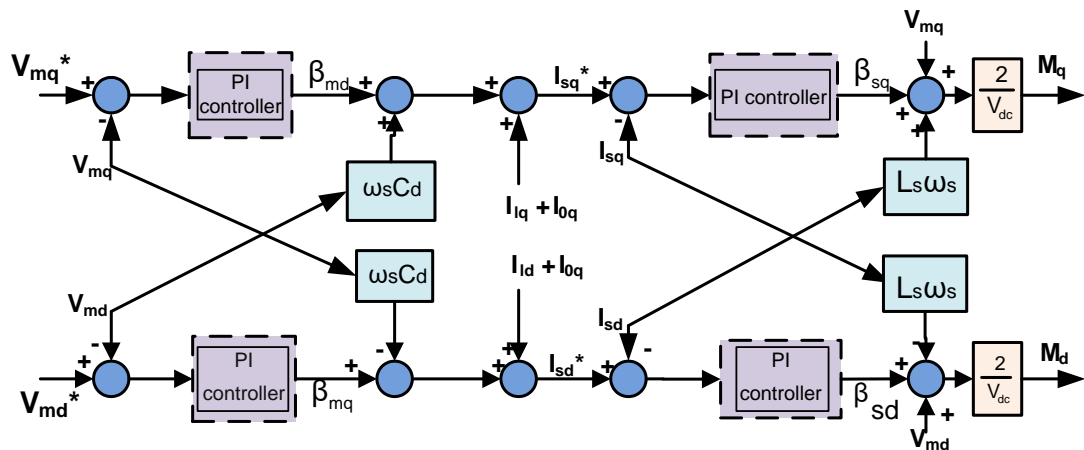
(5.60)

Figure 5.10. Control Scheme for Load side Converter

5.3. Control unit diagram

The generalized droop control (GDC) unit diagram for the microgrid system is presented in Figure 5.11. In this system, the output DC voltage from the renewable energy sources (RES) is converted to AC voltage through the GDC, ensuring that the voltage magnitude and frequency of each DG unit align with the total load's characteristics [193-194]. The converter is fed by a crucial feedback loop consisting of four significant components: the droop controller, which determines the total power balance between generation and load; the voltage control and current control, which

regulate the control voltage and current within acceptable limits; and the phase lock loop (PLL), which measures the local frequency while aligning the load voltage in the reference frame of the q-axis [195].
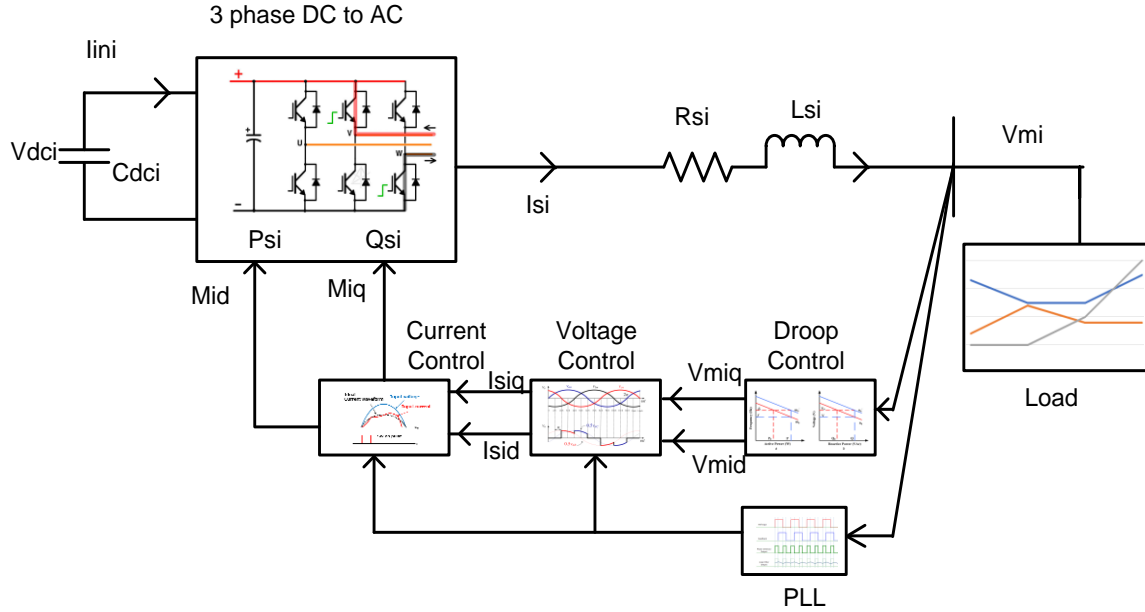

Figure. 5.11. GDC unit diagram

5.3.1 Generalized Droop Control (GDC)

The droop control technique is commonly applied in power generation plants to distribute the total active power of the load among various generators. By adjusting the frequency, the output active power of the converter can be drooped, which is related to the frequency and considered a function of converter output active power. Similarly, the voltage output magnitude of the converter can also be drooped as per requirements to distribute the total reactive power of the load among the DGs. This method ensures load sharing and control of the required operational range of voltage and frequency in the system. Typically, the cut of frequency is around 10% of the nominal frequency, which is considered reliable in producing the average output power value and eliminating fluctuations. [196-198].

Consider a single DG system as depicted in figure 5.12. The system consists of a DG unit, DG_1, connected to a load, with V_2 representing the voltage at the PCC located at the load side. The VSC in the circuit transforms the DC voltage into AC voltage as

required by the system, and the output voltage, V₁, is considered at point A. The line impedance, Z_L, and the reactive power, Q_A, and real power, P_A, at point A can be expressed as follows:

$$P_A = \frac{V_1}{R_L^2 + X_L^2}[R_L(V_1 - V_2 \cos \delta) + X_L V_2 \sin \delta] \tag{5.61}$$

$$Q_A = \frac{V_1}{R_L^2 + X_L^2}[-R_L V_2 \sin \delta + X_L(V_1 - V_2 \cos \delta)] \tag{5.62}$$

The equations to calculate the real power (PA) and reactive power (QA) at point A in a single DG system, as shown in Figure 5.12, are shown in the above equations

Where, V_1 is the inverter output voltage at point A, V_2 is the voltage at the point of common coupling (PCC), δ is the power angle, and Θ is the phase angle of the line impedance Z_L. X_L and R_L represent the reactance and inductance of the line, respectively. Typically, either X_L or R_L is neglected in the equations, leading to the development of P-V/Q-f or P-f/Q-V relations for the droop characteristics [199].
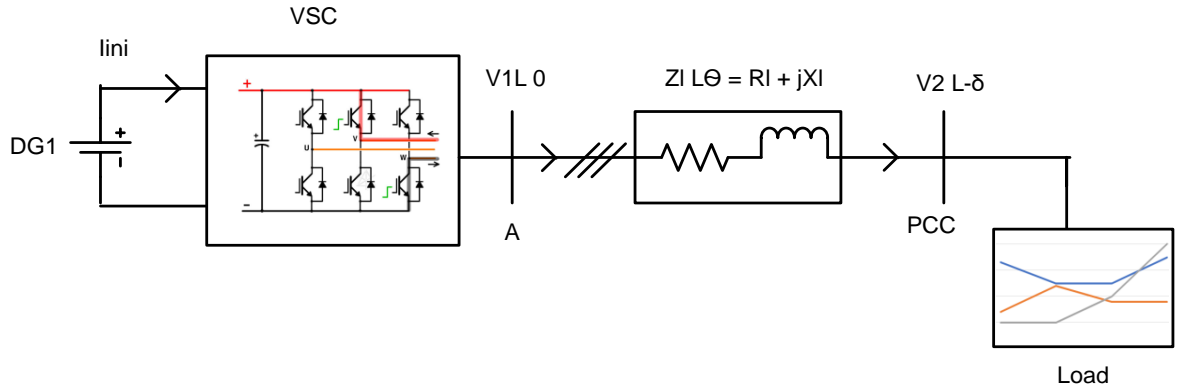

Figure 5. 12. Structure of a single DG system

Additionally, the virtual reactive power Q_{vir} and real power P_{vir} can be calculated as:

$$P_{vir} = \frac{X_L}{Z_L}P_A - \frac{R_L}{Z_L}Q_A \tag{5.63}$$

$$Q_{vir} = \frac{R_L}{Z_L}P_A - \frac{X_L}{Z_L}Q_A \tag{5.64}$$

From above, equation 31 and 32 becomes

$$\delta = \frac{Z_L P_{vir}}{V_1 V_2} \tag{5.65}$$

$$V_1 - V_2 = \frac{Z_L Q_{vir}}{V_1} \tag{5.66}$$

From the above equation, the P_{vir} and Q_{vir} can be used to regulate the frequency and voltage of the microgrid system. Therefore, the generalized droop relation becomes

$$f = f^* - k_{pf}(P_{vir} - P^*) \tag{5.67}$$

$$V = V^* - k_{qv}(Q_{vir} - Q^*) \tag{5.68}$$

Also, from the above equations, we have droop control relations

$$\Delta f = \frac{1}{K_f}\left(\frac{Z}{X}P' - P_0\right) + K_R K_V \, \Delta V_s + K_R Q_0 \tag{5.69}$$

$$\Delta V_s = \frac{1}{K_v}\left(\frac{Z}{X}Q' - Q_0\right) - K_R K_f \, \Delta f + K_R P_0 \tag{5.70}$$

5.3.2. Simulation of the GDC system

The results of the simulation for the GDC Intake microgrid system have been presented in figures 5.13 to 5.18. Figure 5.13 shows the power flow between the load and the source, where battery power compensates for the power flow as per the requirements. In Figure 5.14, the V&I vs time graph has been plotted at the point of common coupling, and a sudden change in current is observed at 0.5 seconds. The modulation index waveform of the inverter side control schemes has been illustrated in Figure 5.15. Additionally, Figure 5.16 shows the DC link voltage at different switching times during grid connected mode and islanded mode. The frequency response of the microgrid system under switching conditions has been demonstrated in Figure 5.17, and Figure 5.18 represents the reactive and active power response of the microgrid system.

The power flow graph in the figure depicts the changes in solar power, wind power, and battery power with varying load demand. During off-peak conditions, the battery continuously charges to balance the power flow while maintaining the frequency. As the frequency nears nominal levels, the battery begins to charge. In general, the generalized droop control scheme performs well in grid-connected mode of operation. However, severe fluctuations may occur during islanded mode if the line parameters are not correctly set. Studies have also shown that the sharing of actual real and reactive power may become problematic due to the high reliance on the output impedance and line impedance between DG units and the load [200-201]. To address

this issue, a new intelligent approach utilizing an ANFIS-based microgrid system is proposed in the following section.
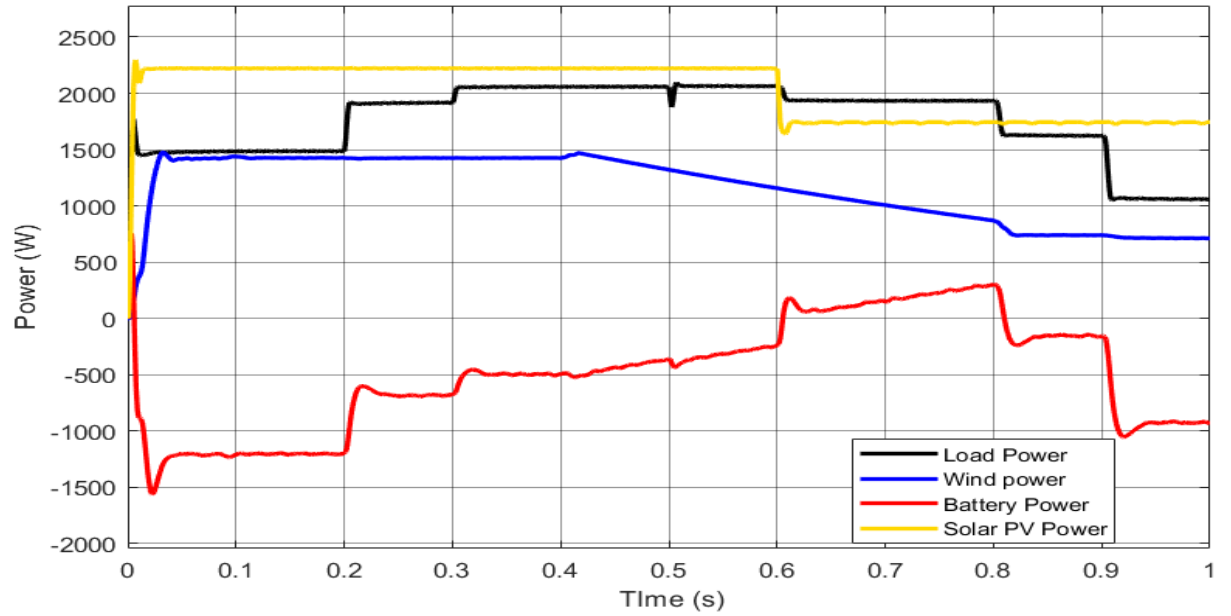

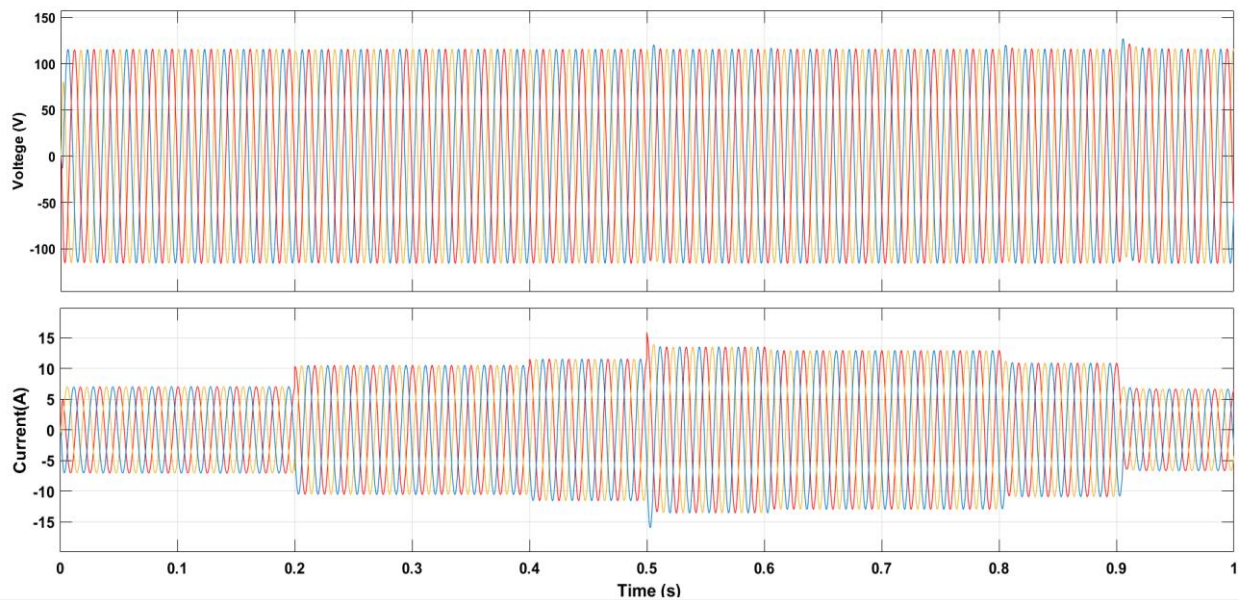Figure 5.13. Load Vs Source power

Figure. 5.14. V&I at point of common coupling (PCC)
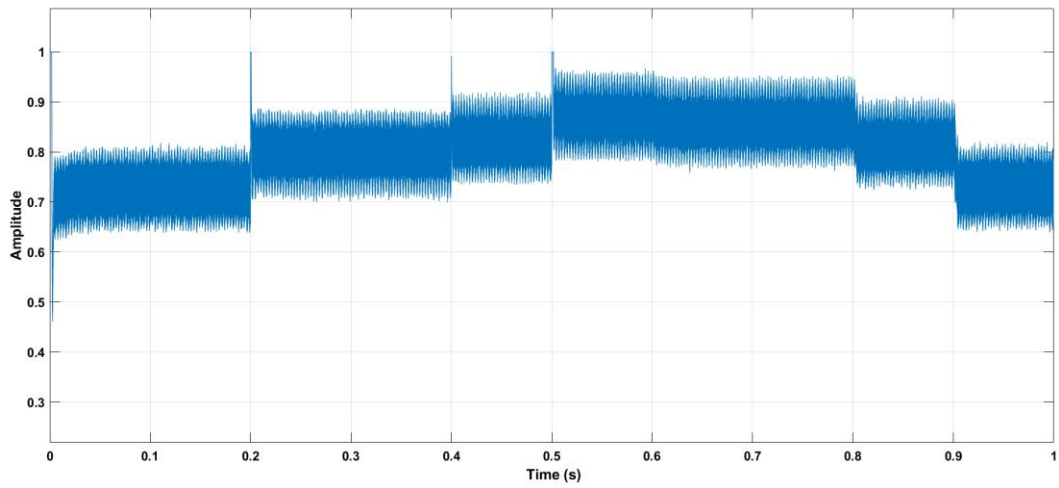
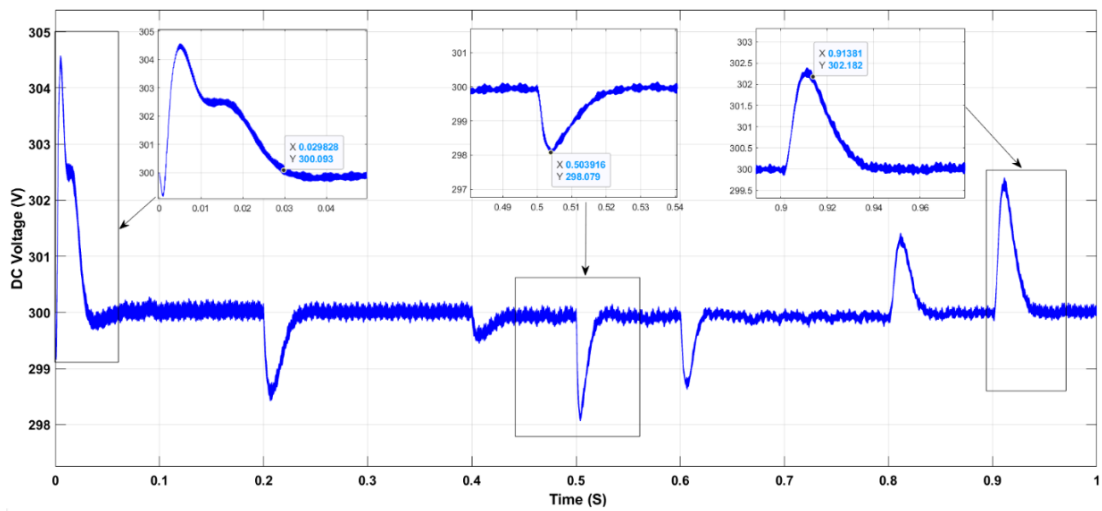Figure 5.15. Modulation index waveform
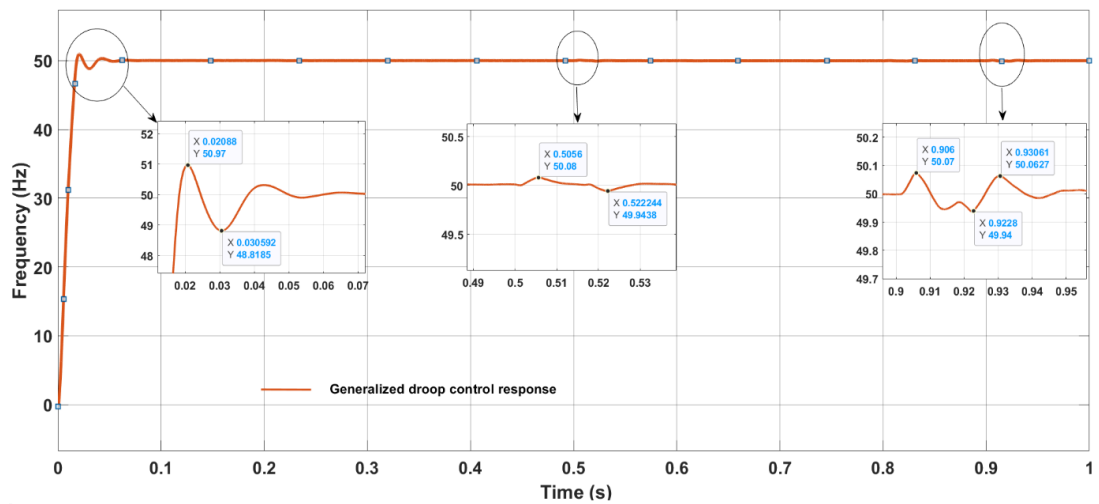

Figure 5.16. DC link voltage
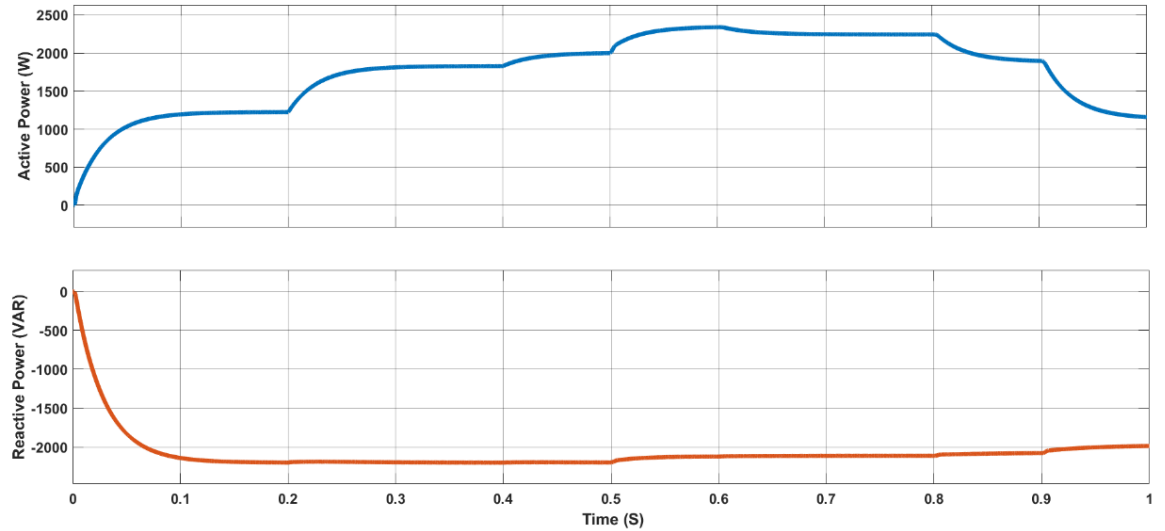

Figure 5.17. GDC Frequency

Figure 5.18**.** Active and Reactive Power

5.4. ANFIS Based Droop Control Approach

5.4.1. ANFIS Architecture and controller

ANFIS is an Artificial Intelligence (AI) system that combines Neural Networks (NN) and Fuzzy Logic (FL) techniques. It is commonly used in solving complex and nonlinear systems in various fields. ANFIS uses an adaptive modeling method to learn information from a set of input data [202-203]. During the training process, the membership functions (MFs) and Fuzzy rules are obtained by adjusting the parameters of the MFs using selected data sets. The system uses hybrid or back propagation learning methods to determine the parameters of the adaptive system.

The ANFIS in this study is trained using two input variables, active power (P) and reactive power (Q), to predict the corresponding output variables, frequency (f) and voltage (V). A hybrid learning algorithm is used for each input variable to determine the ANFIS parameters. One of the benefits of using ANFIS is that it does not require any prior information about the membership function rules if the ANN is appropriately calibrated. Furthermore, ANFIS can automatically choose the membership function parameters based on the application. In this study, the parameters of the membership functions are determined using the product of two sigmoidal membership functions (psigmf) and triangular membership function (trimf) method.

The ANFIS structure depicted in Figure 5.19 is a Multi Input Single Output (MISO) configuration and consists of five layers. The two active and reactive power inputs are denoted by P and Q respectively, while A1 and A2 are the membership functions of input P and B1 and B2 represent the membership functions of input Q. The first layer of the ANFIS structure comprises the membership function of each individual input. In the second layer, the AND operation is performed for both the MFs of input one and input two, following which the corresponding rules for the input can be formed as: [204-205].

• *Rule no 1: If P is A1 and Q is B1, then $f_1 = p_1P + q_1Q + r_1$,*

• *Rule no 2: If P is A2 and Q is B2, then $f_2 = p_2P + q_2Q + r_2$*

From the above rules, p_1, q_1, r_1 and p_2, q_2, r_2 represents the parameters of each of the output functions. Each node of these output is referred as firing strength of a rule. The corresponding layers of the ANFIS are explained in the followings

Layer 1 of the ANFIS structure consists of square nodes, each containing a node function. The fuzzy sets are obtained by applying the input variables in proportion to their values. The membership value of each input is represented by a function in each node i of the layer. The output of each node is described as follows:

$$
\begin{aligned}
O_{1,i} &= \mu A_i(P); \ i=1, \\
O_{1,i} &= \mu B_{i-2}(Q); \ i=3,4
\end{aligned}
\tag{5.71}
$$

Where Q and P, are the input variables for node i, and B_i (or A_i) is the linguistic label, such as "small" or "large". $O_{1,i}$ represents the membership function of A_i, and it determines the degree to which it satisfies the quantifier A_i. Typically, μA_i is chosen in a bell-shaped form with a maximum limit of 1 and a minimum limit of 0. The membership function $\mu A_i(P)$ is expressed as follows, according to sources [206-207].

$$
\mu A_i(P) = \frac{1}{1+(\frac{P-c_i}{\alpha_i})^{2\beta}}
\tag{5.72}
$$

Where, α_i, β_i, c_i are known as the premise parameters and are called parameter set, as the values of these parameters change, they exhibit several forms of membership functions on A_i or linguistic label.

Layer 2: Each node in the second layer multiplies the outputs from the nodes in the first layer and sends the product as output. Mathematically, it can be represented as:

$$Q_{2,i} = W_i = \mu_{Ai}(P) \times \mu_{Bi}(Q); \quad i=1,2 \tag{5.73}$$

Each node output represents the firing strength of a rule, i.e. W_i. The signals from the incoming are i^{th} line with the precursor (if) of the rule.
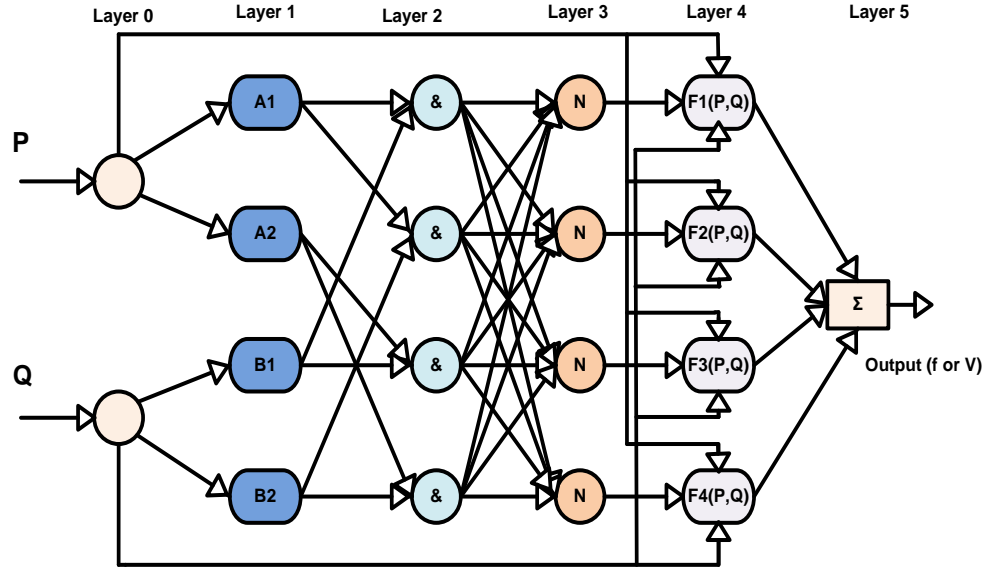
Figure 5.19. ANFIS typical structure

Layer 3: The third layer consists of circular nodes labeled as N. Each node represents the activity of a fuzzy rule, and the number of nodes in this layer is equal to the number of fuzzy rules in the system. The output of this layer is a normalized version of the previous layer. The output of the ith node in this layer is calculated as the ratio of the ith rule's firing strength to the sum of firing strengths of all rules, as given below.

$$O_{3,i} = \overline{w_i} \ \frac{w_i}{\sum_j w_j} \tag{5.74}$$

Layer 4: The fourth layer of the ANFIS model involves computing the fractional output values, which are the products of the output nodes in layer 0 and layer 3. The output nodes in this layer are Takagi-Sugeno type and can be represented as follows:

$$O_{4,i} = \overline{w_i} f_i = \overline{w_i}(p_i P + q_i Q + r_i) \tag{5.75}$$

Whereas, $\overline{w_i}$ is the output of the fourth layer, p_i, q_i, r_i are the parameter set, denoted as consequent parameters

Layer 5: The final ANFIS output is obtained in the fifth layer. The output is nothing but the summation of the incoming signals from the layer four as shown below.

$$O_5 = \sum_i \overline{w_i} f_i \qquad (5.76)$$

The fifth layer of ANFIS is the defuzzification layer responsible for computing the final output. The node function of this layer has minimal constraints except for piecewise differentiability in an adaptive network, which must be feed forward in configuration. These constraints make ANFIS suitable for a wide range of instant and practical applications [208-209].

5.4.2 Implementation of ANFIS and validation

The ANFIS structure can be used to implement the generalized droop control structure, which is shown in Figure 5.11. The ANFIS model for the droop control structure is depicted in Figure 5.20. After validating the model, the ANFIS-based controller can be utilized for droop control, as illustrated in the figure. APPENDIX - D shows MATLAB simulation figures and various control schemes
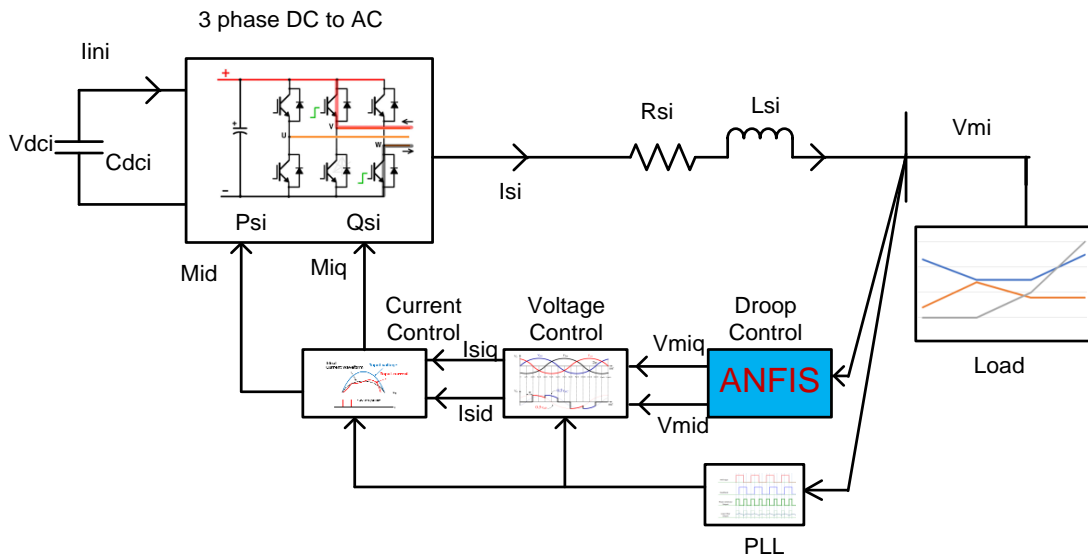
Figure 5.20. ANFIS droop control model

The ANFIS-based droop control model requires input and output data sets for training [210]. The droop control unit has two input data, namely active and reactive power, and two output data, namely frequency and voltage amplitude. Two ANFIS blocks are separately applied for controlling the voltage and frequency outputs. ANFIS can only operate on multi-input-single-output (MISO) signals. The input and output

data sets are generated and stored in the system, and the corresponding ANFIS models are generated and trained. The ANFIS is continuously trained until the error tolerance values are evaluated and the minimal training RMSE result shows that ANFIS has been successfully trained. Once the ANFIS is successfully trained, the conventional controllers are replaced with the trained ANFIS controllers. The active and reactive loads are changed by switching various loads, and the system output frequency and voltage are compared to the conventional droop results. ANFIS training data for frequency control and voltage control are shown in table 5.6 and table 5.7, respectively.

Table 5.6. ANFIS train data: for frequency control

Sl. No.	Details	Data	Details	Data
1	Input Numbers of MFs	6 3	Error tolerance	0
2	Input MFs type	Product of two sigmoidal membership function (psigmf)	Epochs	200
3	Output MFs type	Constant	Optimization method	Hybrid

Table 5.7. ANFIS train data: for Voltage control

Sl. No.	Details	Data	Details	Data
1	Input Numbers of MFs	6 3	Error tolerance	0
2	Input MFs type	Triangular membership function (trimf)	Epochs	200
3	Output MFs type	Linear	Optimization method	Hybrid

5.5. Results and Discussion

To evaluate the effectiveness of the ANFIS-based droop control system, simulations were conducted using MATLAB Simulink environment under various loading conditions. The droop controller's output, P&Q, was trained with ANFIS function and after successful training, the corresponding controllers were set and tuned in the Simulink model. The microgrid system operated in grid connected mode from 0 to 0.5 seconds and in islanded mode from 0.5 to 1 second during the simulation period. The results were compared with the GDC results and the DC link voltage, frequency response, active and reactive power were analyzed. These results are presented in figures 5.21, 5.22, and 5.23.
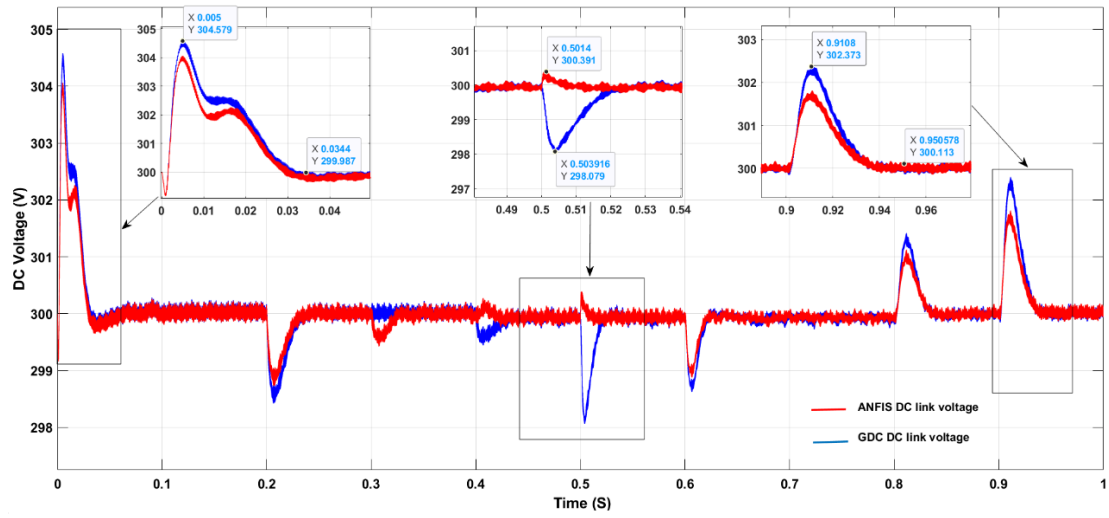
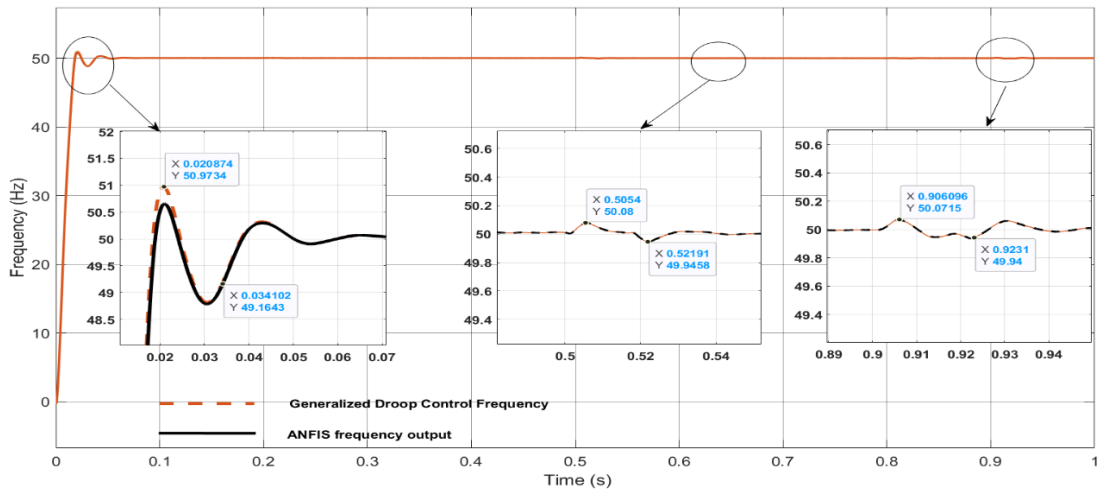Figure 5.21. Comparison of DC link voltage

Figure 5.22. Comparison of Frequency GDC Vs ANFIS
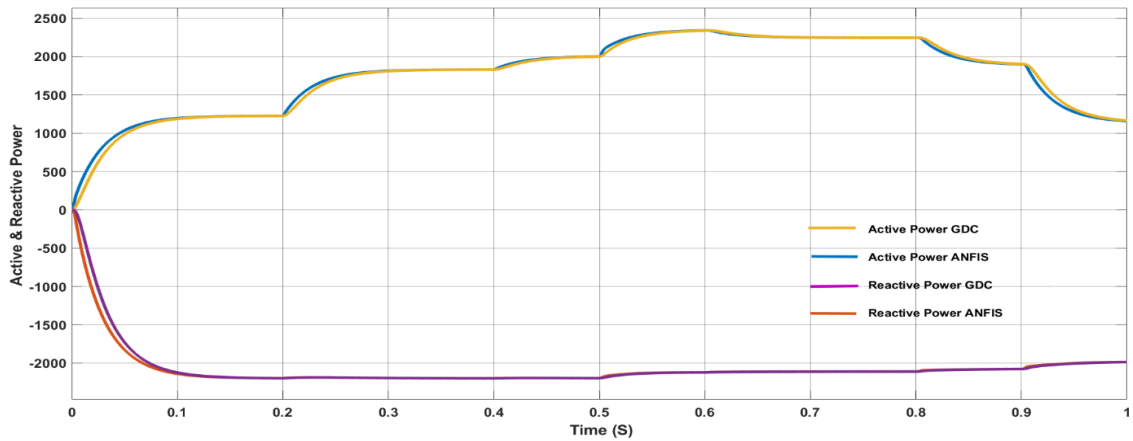
Figure 5.23. Comparison of Active and Reactive power vs Time

During the ANFIS training process, data for both the P-F and Q-V relations of the droop controller are stored and trained separately using MATLAB. After successful tuning and training, the individual fuzzy systems for both P-F and Q-V relations are configured separately. The trained ANFIS data plots for both MFs, such as surface plot, fuzzy rules, and membership function plot, are shown in Figure 5.24, Figure 5.25, and Figure 5.26. Similarly, Table 5.8 presents the corresponding training data for both P-F and Q-V droop characteristics in the ANFIS platform.

Table 5.8. ANFIS structure train data of Q-V and P-F

Sl. No.	Parameters	P-f ANFIS data	Q-V ANFIS data
1	Number of nodes	59	43
2	Number of linear parameters	54	36
3	Number of nonlinear parameters	36	21
4	Total number of parameters	90	57
5	Number of training data pairs	500172	500172
6	Number of fuzzy rules	18	12
7	Number of checking data pairs	0	0
8	Minimal training RMSE	0.002753	0.001753
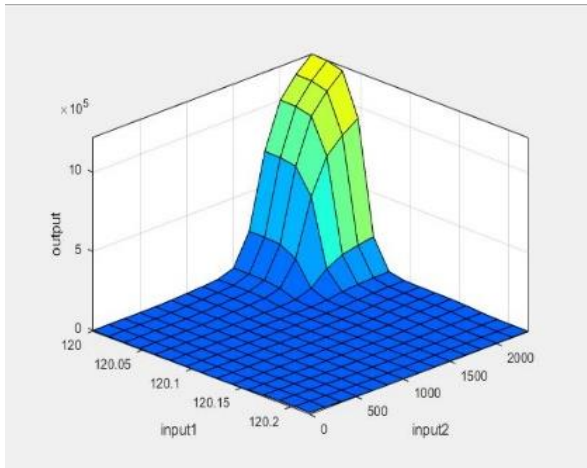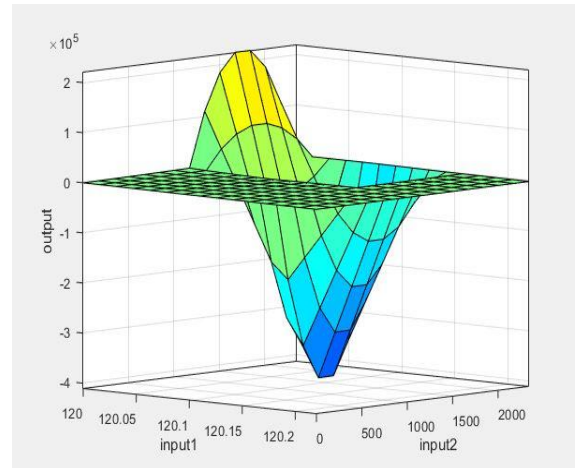
(a)   (b)

Figure 5.24 Surface plot (a) P-F ANFIS, (b) Q-V ANFIS
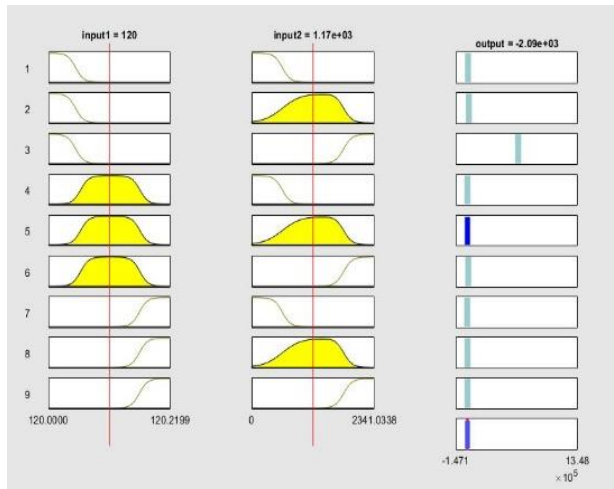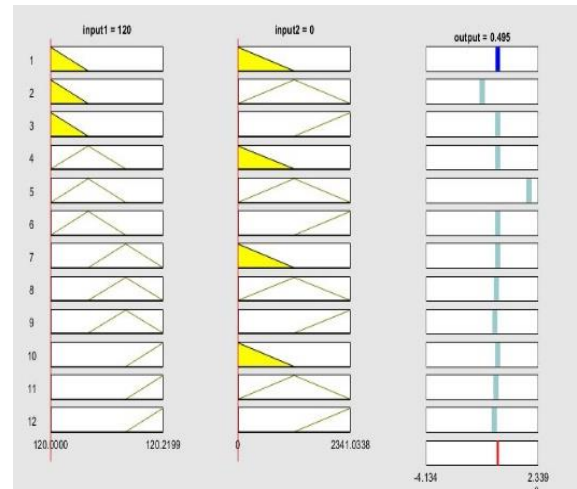
(a)   (b)

Figure 5.25 Fuzzy rules (a) P-F ANFIS, (b) Q-V ANFIS
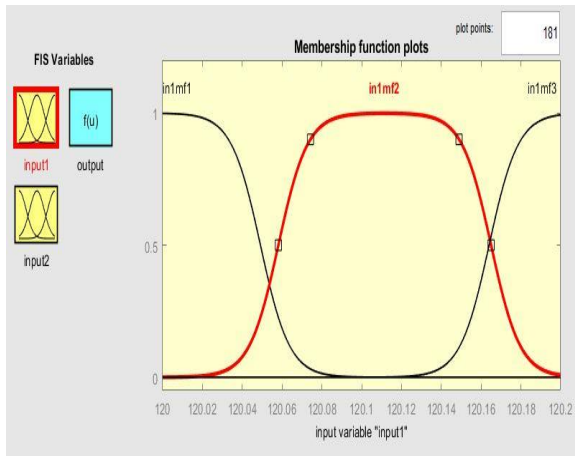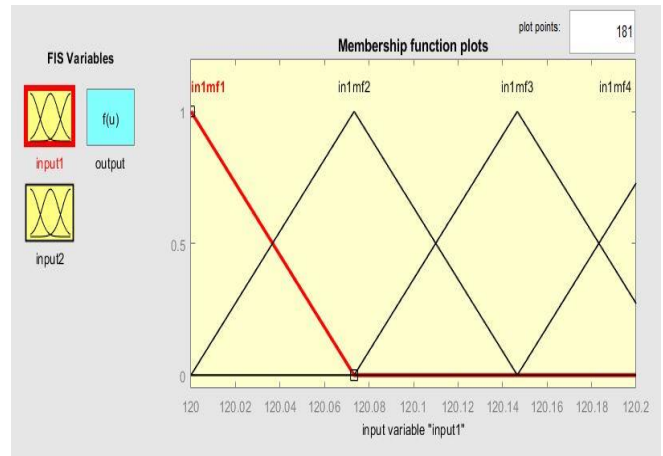
(a)   (b)

Figure 5.26 Membership function plot (a) P-F ANFIS, (b) Q-V ANFIS

The results obtained from the simulation of the ANFIS-based droop controller show significant improvements in the performance of the microgrid system. As seen in Figure 5.21, the DC link voltage shows reduced transients during switching operations in both grid-connected and islanded modes of operation. Figure 5.22 shows a decrease in frequency deviations during different switching conditions, thus improving the frequency response. Furthermore, Figure 5.23 indicates an improvement in both active power (P) and reactive power (Q) under the ANFIS droop technique. The ANFIS method demonstrates better and more reliable results compared to the GDC, as observed from the various system response tests conducted under different switching time frames.

5.6. Conclusions

The present study investigates the application of ANFIS-based droop control technique in a microgrid system operating under different loading conditions. In grid connected mode, sharing of active and reactive power between the source and load is in an important factor, whereas in islanded mode, frequency and voltage control becomes the primary focus. ANFIS-based droop control technique is employed to address this issue. The designed system operates in grid connected mode until 0.5 seconds and islanded mode until 1 second. Only the LT side of the load is considered in the simulation, as the intake system contains both HT and LT loads. The battery system compensates for power sharing between the source and load as various loads change. The trained ANFIS data, such as surface plot, fuzzy rules, membership function plot, and RMSE value for both P-F and Q-V droop, demonstrate successful ANFIS training. The controller units for both P-F and Q-V are then replaced with ANFIS, yielding improved results.

Frequency stability is a crucial aspect to consider when analyzing the performance of a microgrid system. In droop control, the system frequency relies on the balance between active power from the source and load. In the proposed intake microgrid system, the batteries play a vital role in injecting or absorbing real power during frequency imbalances. Additionally, the voltage stability of the system heavily relies on the reactive power balance between the source and the load. The proposed ANFIS-based droop controller shows promising results in regulating the frequency and voltage of an intake microgrid system. To evaluate its reliability, the ANFIS system was compared to the GDC in various loading conditions. The simulation results show that the ANFIS system performs satisfactorily.

The ANFIS-based droop control technique used in WTP-based intake microgrids can have applications beyond its current use. This approach has the potential to address several issues faced by various WTPs, such as high operational costs, power-related issues, and frequent maintenance. Moreover, the ANFIS-based droop control technique can also be applied to various other treatment plants, such as waste water treatment, sewage treatment, and others.

CHAPTER

6

Load Frequency Control of Multi area and multi-source based Water Treatment Plant

6.1. Introduction

The previous section of this study discussed the implementation of droop control using an ANFIS for the intake part of a WTP, which was considered as a microgrid system. The study aimed to improve the power system performance by optimizing the system frequency using various energy sources and a real-time simulation platform. Since the load distribution and operation concept in different pumping stages are similar, the same approach of droop control could be applicable in other pumping stations and independent treatment units.

In line with the study of the water treatment-based multi-area microgrid system, this study also considered a transfer function-based multi-area microgrid system. The microgrid system was supplied with power from renewable energy sources such as solar, battery, and a small hydro power plant. Additionally, a DEG is considered as the primary power backup source. The focus of this chapter is to address frequency issues and deviations, which are commonly observed in existing power systems as well as in multi-area microgrid systems. To control the frequency at the desired value, the study proposed an Enhanced Harris Hawks Optimization Algorithm (EHHO)-based PID controller. The controller considered SPV, small hydro (SHG), BESS, and DEG as power sources for peak demand. The proposed controller was implemented in MATLAB, and its performance was analyzed and compared with existing techniques such as PSO and GWO.

In most cases, facilities such as water treatment systems are connected to the main electrical grid and use conventional energy sources like diesel engine generators as backup during power outages. However, operating these sources at light loads can be expensive and result in the emission of greenhouse gases. As a result, renewable energy sources (RES) have become the primary focus of energy conservation efforts to reduce the impact of greenhouse gases on the environment. Integrating RES with the existing power supply can be complex and requires advanced control systems and additional reliable elements like energy storage systems to compensate for their intermittency.

To ensure a stable and uninterrupted power supply to critical loads like water treatment stations, complex control strategies are needed. Additionally, integrating RES can make frequency control more expensive. The microgrid is an effective way to integrate RES into the electric power system. It's a small-scale power system controlled by a group of interconnected loads and energy storage systems (ESSs) that can be operated in grid-connected or islanded modes. In the grid-connected mode, the utility grid controls voltage and frequency variations, while in the isolated mode, regulation is done through solar and wind energy compensation.

A newer concept is the multi-microgrid (MMG) system, which is a high-level structure formed at the medium-voltage level, comprising several interconnected microgrids for mutual supply. There are three levels of hierarchical control in a microgrid: primary, secondary, and tertiary control. The conventional primary droop control maintains the microgrid's voltage and frequency in islanded mode and shares active and reactive power among the DGs without using communication links. However, it can cause frequency deviation. [211]. Renewable energy sources (RESs) are known for their fluctuating and unreliable power production, resulting in imbalances between power generation and demand. These imbalances cause frequency disturbances that can threaten the security of the power grid [212]. Power engineers face the challenge of maintaining load frequency changes in the power system to regulate the system frequency, consume fewer fuels, and increase the lifetime of batteries. LFC plays an important role in the power system as it brings the frequency deviation to zero and ensures that the exchange power on the tie-line between

interconnected power systems remains at the reference value [199].

Energy storage systems (ESSs) are crucial in safeguarding power quality and the reliability of the power system. Rechargeable batteries are commonly used in autonomous power systems as they have a small daily self-discharge rate, fast response time, and high cycle efficiency. However, load frequency deviation in the microgrid remains unresolved, and various controllers such as conventional PID control, intelligent control, adaptive control, robust control, and MPC control have been applied to DGs of islanded MG to improve LFC response [213-214]. But the performance of these controllers for LFC is inadequate. Therefore, an EHHO approach-based PID controller is proposed in this paper to control load frequency and maintain it at a nominal value, providing a reliable power supply to the WTP.

Based on the above, the main contribution of this chapter are as follows:

1. To consider each pumping station as a three-area WTP based microgrid system.
2. To implement various DGs such as solar, wind Battery and Diesel engine on each pumping stations of the microgrid system
3. To implement 3DOF-FOPIDN, 3DOFTIDN controller and compare the performance with conventional controller
4. To adapt and apply Enhanced Harris Hawks Optimization Technique and compare the performance with conventional optimization techniques
5. To perform stability and robustness analysis of the proposed controller

6.2. Proposed Methodology

This chapter proposes the use of a multi-microgrid system for supplying power to various pumping stages in a WTP. The microgrid system consists of various interconnected power sources such as solar panels, wind turbines, diesel engine generators, battery energy storage systems, and frequency controllers, linked through controllers and connected by tie lines. However, renewable energy sources such as solar panels and wind turbines can cause power fluctuations due to irregular solar irradiation and wind speed. Furthermore, the fluctuating load and low inertia of diesel engine generators can create frequency deviations and fluctuations in the microgrid system. To address these issues, battery energy storage systems and diesel engine

generators can be used to control frequency deviations in the microgrid system.

However, due to the varying and aging parameters, the real-time microgrid parameters may differ from the microgrid parameters. To regulate and balance the frequency deviation of the microgrid system, a PID controller-based frequency controller is used. However, the performance of a PID controller alone may not be enough, and the tuned parameters of the PID controller must be optimized. Therefore, the paper proposes the use of the EHHO algorithm to optimize the gain parameter values of the PID controller. The PID controller's output is then given to the diesel engine generators and battery energy storage systems to regulate the frequency deviation and fluctuations in the microgrid system. Moreover, in line with the above, higher degree controller such as 3DOF-FOPIDN and 3DOF-TIDN controllers are implemented and utilized in the system to optimize the system performance and regulate the frequency.

6.3. Mathematical Modelling

The mathematical models of the proposed systems are described as follows:

6.3.1. Wind Turbine Generator

Wind turbines are typically used to harness kinetic energy from wind and convert it into mechanical energy [215]. This mechanical energy is then transferred to the rotor of the generator via a shaft, and the generator converts the mechanical energy into electrical energy. The mathematical representation of the mechanical output of a wind turbine is shown in equation (5.29) and the wind power coefficient can be expressed as equation (6.1).

$$C_p = \frac{P_m}{P_w} \tag{6.1}$$

where, P_m represents mechanical power derived from the rotor shaft, P_w is the power of wind content in the virtual stream tube consisting Wind turbine [216]. Figure 6.1 represents the block diagram of the first-order transfer function model of WTG.
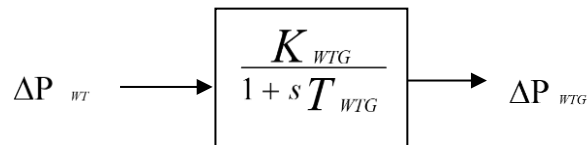
$$\Delta P_{WT} \longrightarrow \boxed{\frac{K_{WTG}}{1 + s\,T_{WTG}}} \longrightarrow \Delta P_{WTG}$$

Figure 6.1 Block diagram of the first-order transfer function model of WTG.

6.3.2. Photo Voltaic Cells

A SPV system is a power generation system that converts sunlight directly into electricity, and can be used for both standalone and grid-connected applications. The increasing popularity of SPV systems in recent years can be attributed to government policies that encourage their use, the high demand for electricity, environmental concerns, low operating costs, and no fuel costs. The amount of power output from a SPV system is dependent on the solar irradiance, ambient temperature, and the conversion efficiency of the SPV panel [217]. The following equations can be used to estimate the power output of a SPV system.

$$T_{ct} = T_{at} + s(t) * \left[\frac{NOCT - 20}{0.8} \right] \tag{6.2}$$

$$I = s(t) * [I_{sc} + K_{ct} * (T_{ct} - 25)] \tag{6.3}$$

$$V = V_{oc} + K_{vt} * T_{ct} \tag{6.4}$$

$$FF = \frac{V_{mp} * I_{mp}}{V_{oc} * I_{sc}} \tag{6.5}$$

$$P_{pv}(s(t)) = \eta_{cells} * FF * V * I \tag{6.6}$$

Where, T_{ct} is the cell temperature in °C, T_{at} is the ambient temperature in °C, s(t) is the random irradiance, NOCT is the nominal cell operating temperature in °C, I_{sc} is the short-circuit current in A, K_{ct} is the current temperature coefficient in mA/°C, V_{oc} is the open-circuit voltage in V, K_{vt} is the voltage temperature coefficient in mV/°C, V_{mp} is the voltage at maximum power in V, I_{mp} is the current at maximum power in A, FF is the fill factor, η_{cells} is the number of SPV cells, V is the terminal voltage, I is the current (A) and $P_{pv}(s(t))$ is the SPV power output (W). The first-order transfer function model of SPV power is given in Figure 6.2.
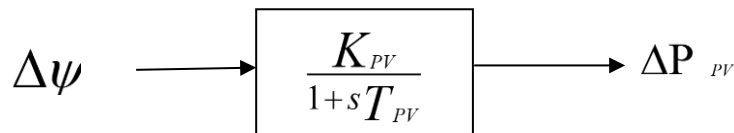
$$\Delta\psi \longrightarrow \boxed{\frac{K_{PV}}{1 + sT_{PV}}} \longrightarrow \Delta P_{PV}$$

Figure 6.2. SPV power's first-order transfer function model

6.3.3. Diesel Engine generator

Diesel generators are a common component in power systems that are used to meet the electricity needs of consumers. These generators offer reliable and long-lasting power solutions for applications ranging from prime power to standby power. Diesel generators are used as backup power sources, emergency and standby units, and for peak shaving because of their unique characteristics such as quick start-up, high availability, reliability, durability, and black start capability [218]. Despite some drawbacks, these features make diesel generators a popular choice in certain locations. The rate of fuel consumption of a diesel generator at any given time t is directly related to its output power, and can be represented mathematically.

$$F = F_0.Y_{dg} + F_1.P_{dg} \tag{6.7}$$

Where, F_0 is the fuel curve intercept coefficient (units/h/kW), F_1 is the fuel curve slope (units/h/kW), P_{dg} is the electrical output of the generator (kW) and Y_{dg} is the rated capacity of the generator (kW).

Figure 6.3 represents the block diagram of the first-order transfer function model of DEG. The equilibrium between power demand and its generation in an autonomous microgrid due to variation in solar power and wind power is maintained by DEG with speed governor control action.
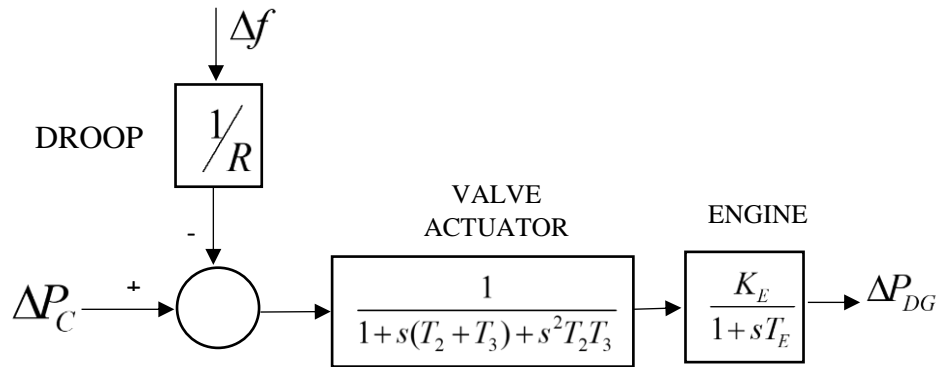
Figure 6.3. Block diagram of the first-order transfer function model of DEG

6.3.4. Battery energy storage system model

BESS are commonly used to improve the primary frequency regulation of autonomous MG. Usually, the primary frequency control task is handled by DEG. However, DEGs have a high time constant and respond slowly to frequency variations, which can cause large overshoot [219]. To address this issue and enhance the primary

frequency response, BESS can be incorporated into the system. The BESS state of charge at any time t and the BESS state of charge limits as a function of optimal BESS capacity ESS_{bess}^{cap}, respectively, are given by:

$$SOC(t) = SOC(t-1)(1 - S_{bess}) + P_{bess}^{ch}(t) * \eta_{bess}^{c} - \frac{P_{bess}^{dis}(t)}{\eta_{bess}^{d}} \tag{6.8}$$

$$SOC_{bess}^{min} = 0.2 * ESS_{bess}^{cap} \tag{6.9}$$

$$SOC_{ptes}^{max} = 0.8 * ESS_{bess}^{cap} \tag{6.10}$$

Where, SOC (t) and SOC (t-1) are the current and previous energy capacity of the BESS over one time step and S_{bess} is the self-discharge rate. P_{bess}^{ch} and P_{bess}^{dis} are the charging and discharging power to and from the BESS which are functions of the energy surplus and deficits from the energy supply system, respectively. η_{bess}^{c} and η_{bess}^{d} are the charging and discharging efficiencies of the BESS.

The first-order transfer function model of BESS is given in Figure 6.4. The BESS can be either in charging mode or discharging mode based on the system frequency as shown in Table 6.1.

Table 6.1. Battery charging status based on system frequency

ΔF	BESS status
Positive	Charging
Negative	Discharging

$$\Delta f \longrightarrow \boxed{\frac{K_{BESS}}{1 + s\, T_{BESS}}} \xrightarrow{\Delta\,P_{BESS}}$$

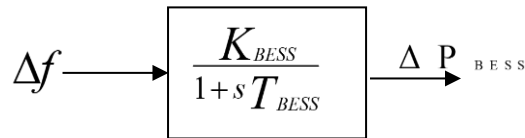Figure 6.4. The first-order transfer function model of BESS

6.4 Frequency Controller (FC)

Before implementing an optimization technique for controller design, it is important to establish the fitness function. There are several performance indices that are commonly used in controller design, including Integrated Absolute Error (IAE), Integrated Time Absolute Error (ITAE), Integrated Square Error (ISE), and Integrated

Time-weighted Square Error (ITSE), as identified in a literature survey. In this particular study, the fitness function used is the integral time absolute error, as presented in Equation (11) for multi area interconnected microgrid system [220].

The objective of this research is to optimize the parameters of the PID-based LFC controller using EHHO, a modern meta-heuristic optimization algorithm. The aim is to achieve nearly zero deviation in frequency and tie-line power flow variations despite load disturbances. The optimization process will consider the frequency deviation of both single and multi-microgrid systems, as well as the tie-line power flow variation, as references for optimal tuning of PID controller gains.

In this study, ITAE criteria is considered as the fitness function for fine-tuning the PID controller gains. This performance index is preferred over other performance indices, such as integral-squared error (ISE), integral absolute error (IAE), and integral time-weighted squared error (ITSE), because ITAE produces smaller overshoots/undershoots and oscillations. On the other hand, ISE gives minimum overshoot but more settling time, IAE produces slower response than ISE in LFC controller design, and ITSE produces larger controller output for sudden changes in input. The fitness function ITAE is defined in Equation (6.11), while the boundaries for gains of the PID controller are defined in Equation (6.12).

Fitness = Minimize {ITAE}

$$=\text{Min}\left\{\int_0^T \left(\left|\Delta F_i\right| + \left|\Delta P_{tie-line,ij}\right|\right).t.dt\right\} \tag{6.11}$$

Subjected to PID gain limits,

$$\left.\begin{array}{l} K_p^{\min} \le K_p \le K_p^{\max} \\ K_i^{\min} \le K_i \le K_i^{\max} \\ K_d^{\min} \le K_d \le K_d^{\max} \end{array}\right\} \tag{6.12}$$

The variables i and j are being utilized in this context to denote area numbers. More specifically, i is limited to the values 1, 2, and 3 while j is restricted to 2 and 3. Additionally, it should be noted that i and j cannot be equivalent (i.e., i is not equal to j). Furthermore, the terms "min" and "max" are being employed to represent the minimum and maximum values of various controllers' parameters.

6.5 PID controller

Generally, proportional (K_P), integral (K_I) and derivative (K_D) gains are the three parameters of the PID controller. Then the PID controller's transfer function can be given as,

$$G_c(s) = \frac{U(s)}{E(s)} = K_p\left[1 + \frac{1}{T_i s} + T_d s\right] \tag{6.13}$$

Where, $K_I = \dfrac{K_p}{T_i}$ and $K_D = K_p T_d$

The regulation of frequency deviation is commonly achieved by utilizing PID controllers. However, it is frequently observed that the performance of PID controllers in regulating frequency deviation is not sufficient to achieve the desired level of accuracy [221]. Therefore, it is necessary to adjust the parameters of the PID controller such as K_p, K_i, and K_d appropriately to enhance its performance in regulating frequency deviation. Therefore, in this chapter, we introduce a technique-based PID controller that has been tuned using the EHHO technique to regulate frequency deviation.

6.5.1 PSO optimization

Kennedy and Eberhart introduced the PSO algorithm as an evolutionary optimization technique, inspired by animal social behaviors, such as the movement of schools of fish or flocks of birds, in finding food and avoiding predators. These creatures possess remarkable traits that are functional and have been optimized through many iterations of a vast optimization algorithm in the DNA of living beings [222]. Consequently, the PSO Algorithm, like other intelligent optimization algorithms, is influenced by nature. The algorithm employs random numbers and is structured in the following way:

The PSO algorithm can be broken down into six steps. The first step is the initialization of the population, which creates a random number to serve as the starting location for each particle or sequence's motif candidate. Step 2 calculates the fitness value for each particle, and parameter pBest stores the particle with the highest fitness value. In Step 3, the global maximum fitness value (gBest) is updated. Step 4 involves

calculating velocities using a randomization approach. In Step 5, each particle's new location is updated using a velocity value. Finally, Step 6 pertains to the termination condition, where the process flow is terminated if the condition is satisfied. Otherwise, the process flow will be repeated from Step 2.

6.5.2. GWO algorithm

Grey wolves are known to be highly skilled predators that excel at locating prey. Their social hierarchy, as depicted in Figure 6.5, is a fascinating characteristic of these animals. The group is organized into a rigid dominating structure, with the most powerful member of the pack being the Alpha, which can be either male or female. The Alpha wolf makes critical decisions about hunting, migration, sleeping locations, and eating [223].

The Alpha wolf is not necessarily the strongest member of the group but must be the best at controlling the pack, emphasizing that organization and discipline are more important than power. The beta wolf is the next level in the hierarchy, and they assist the Alpha wolf in making decisions. When the Alpha wolf becomes ill or dies, the beta wolf takes over as the leader. The beta wolf also serves as the disciplinarian and counsellor to the Alpha wolf. Delta, the third level in the hierarchy, is dominant in omega but must report to the Alpha and beta wolves. Scouts, carers, and hunters fall within the delta category. Omega is at the bottom of the hierarchy and is made the scapegoat, allowing them to eat last. These wolves' absence can lead to internal strife and issues within the group. The GWO flow chart, shown in Figure 6.6, follows this hierarchical structure [224].
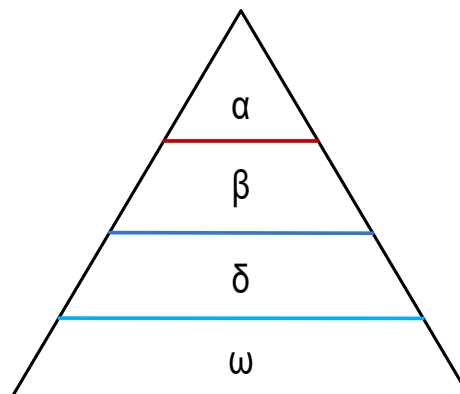
Figure 6.5. GWO hierarchy
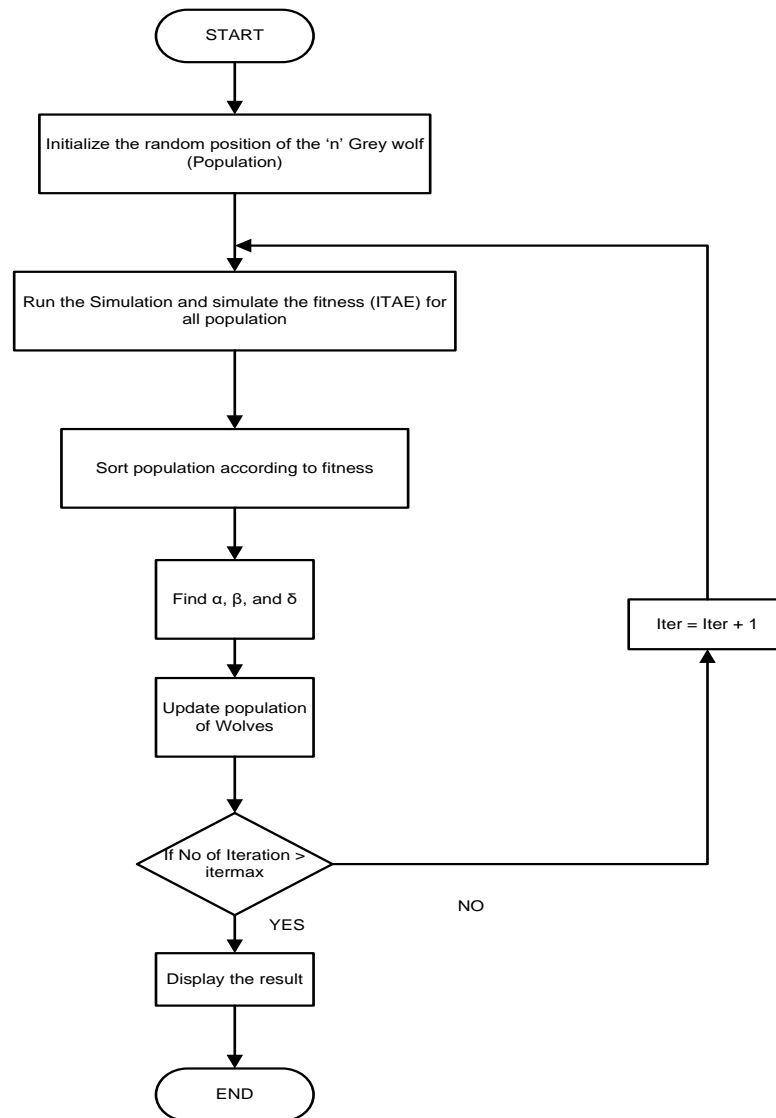
Figure 6.6 Flow chart of GWO algorithm

6.6 Tuning optimal parameters of PID controller using EHHO

An effective EHHO control strategy is presented in this section for the regulation of load frequency deviation in MG systems. The proposed approach involves the use of a PID controller for load frequency deviation regulation. The performance of the PID controller is improved by optimally tuning its parameters, including Kp, Kd, and Ki. To accomplish this, EHHO is utilized to determine the optimal values for these parameters.

HHO algorithm is a population-based optimization method inspired by the cooperative hunting behavior of Harris's hawks in nature. The HHO algorithm is

designed to mimic the surprise pounce technique used by Harris's hawks to catch prey. The hawks cooperate and chase the prey from different directions to surprise it. The HHO algorithm is preferred due to its simplicity and low number of control parameters [224]. The proposed EHHO approach uses the PSO algorithm to enhance the performance of the conventional HHO by improving the updating process. The operation of EHHO is described in detail.

6.6.1. Exploration phase

This section proposes the exploration mechanism of HHO. In nature, Harris's hawks use their powerful eyes to locate and identify their prey, but sometimes, the prey may not be easily visible. Therefore, the hawks perch, observe, and monitor the desert area for several hours to detect a potential prey. In HHO, the candidate solutions are considered as the hawks, and the best solution in each iteration is considered as the target or the ideal prey. In HHO, the hawks randomly perch on various locations and wait to detect a prey based on two strategies. Firstly, they perch based on the positions of other family members (to attack the prey while being close to each other), and the prey, which is represented by Equation (6.14) when $j < 0.5$. Alternatively, they perch on tall trees randomly located within the group's home range, as shown in Equation (6.14) when $j \geq 0.5$.

$$P(s+1) = \begin{cases} P_{rand}(s) - x_1 \mid P_{rand}(S) - 2x_2 P(S) \mid & j \geq 0.5 \\ (P_{rabbit} - P_m(s)) - x_3(lb + x_4(ub - lb)) & j \langle 0.5 \end{cases} \tag{6.14}$$

Where $P(s+1)$ is the position vector of hawks in the next iteration s, $P_{rabbit}(s)$ is the position of rabbit, $P(s)$ is the current position vectors of hawks, x_1, x_2, x_3, x_4 and j are random numbers inside (0,1), which are updated in each iteration, u_b and l_b show the upper and lower bounds of variables, $P_{rand}(s)$ is a randomly selected hawk from the current population, and P_m is the average position of the current population of hawks. The average position of the hawks is attained using the Equation (6.15).

$$P_m(s) = \frac{1}{n} \sum_{i=1}^{n} P_i(s) \tag{6.15}$$

Where $P_i(s)$ indicates the location of each hawk in iteration, s and n denotes the total number of hawks. It is possible to obtain the average location in different ways, but we utilized the simplest rule.

Equation (6.11) is used to calculate the fitness function. The objective is to minimize this function and obtain the optimal values of K_p, K_i, and K_d parameters. The position and velocity of the agent are updated using separation, alignment, and cohesion coefficients after evaluating the fitness function.

6.6.2. Transition from exploration to exploitation

The HHO algorithm can switch between different exploitative strategies depending on the prey's escaping energy, transitioning from exploration to exploitation. The energy of the prey decreases significantly during its escape behavior, and this is reflected in the prey's energy equation.as below:

$$E = E_0\left(1 - \frac{t}{S}\right) \tag{6.16}$$

The energy of a prey is given by the equation E, where E_o is the initial energy, S is the maximum number of iterations, and t is the current iteration. As the prey's energy decreases during the escaping behavior, it becomes less likely to escape. Hence, the hawks adopt different strategies depending on the prey's energy and distance. Exploitation involves soft and hard besieges with perching dives, while exploration is performed randomly using the average positions of searching particles.

6.6.3. Exploitation Phase

During the attacking phase, Harris' hawks perform a surprise pounce on the prey detected in the previous phase. However, preys often try to escape from danger, and the chasing behavior of hawks varies in response to different escaping behaviors. To model the attacking stage in HHO, four possible strategies are proposed based on the escaping behaviors of prey and chasing strategies of hawks. When the absolute value of prey's energy (|E|) is greater than or equal to 0.5, a soft besiege strategy is employed, and when |E| is less than 0.5, a hard besiege strategy is used.

6.6.3.1. Soft besiege

In the scenario where x ≥ 0.5 and |E| ≥ 0.5, the prey tries to escape by making

random jumps, but eventually fails. The Harris' hawks surround the prey during these attempts to make the prey more tired before performing the surprise pounce. This behavior is simulated by the following set of rules:

$$P(s+1) = \Delta P(s) - E \mid i \, \boldsymbol{P}_{rabbit}(s) - P(s) \mid \tag{6.17}$$

$$\Delta P(s) = \boldsymbol{P}_{rabbit}(s) - P(s) \tag{6.18}$$

Where $\Delta P(s)$ is the difference between the position vector of the rabbit and the current location in iteration S, x_5 is a random number inside (0, 1), and $i = 2(1 - x_5)$ represents the random jump strength of the rabbit throughout the escaping procedure. The i value changes randomly in each iteration to simulate the nature of rabbit motions.

6.6.3.2. Hard besiege

When the value of x is greater than or equal to 0.5 and the absolute value of energy E is less than 0.5, it means that the prey is very tired and has low energy to escape. The Harris' hawks approach the prey with caution and perform a surprise pounce to catch it. In such a scenario, the positions are updated using Equation (6.19).

$$P(s+1) = \boldsymbol{P}_{rabbit}(s) - E \mid \Delta P(s) \mid \tag{6.19}$$

6.6.3.3. Soft besiege with progressive rapid dives

The next move of the hawks in delicate besiege is made based on Equation (6.19) and progressive fast dives are made using the leapfrog scheme using Equation (6.21).

$$Q = \boldsymbol{P}_{rabbit}(s) - \mid i \, \boldsymbol{P}_{rabbit}(s) - P(s) \mid \tag{6.20}$$

$$\boldsymbol{R} = \boldsymbol{Q} + \boldsymbol{M}.lf(d) \tag{6.21}$$

Where d is the dimension of the problem, M is a random vector of the size of 1xd, *lf* is the levy flight function calculated by Equation (6.22).

$$lf(p) = \frac{0.01.u.\sigma}{|v|^{\frac{1}{\beta}}} \tag{6.22}$$

Where $\beta = 1.5$ a default constant u and v is are represented as random numbers between 0 and 1. The strategy to update the position is concluded in Equation (6.23).

$$P(s+1) = \begin{cases} Q & if F(Q) < F(P(s)), \\ R & if F(R) < F(P(s)) \end{cases} \tag{6.23}$$

6.6.3.4. Hard besiege with progressive rapid dives

The HHO algorithm has two strategies to attack prey: soft besiege and hard besiege. The hard besiege has similar characteristics to the soft besiege, but its Q and R conditions are different. To visualize the HHO tracking, the vector addition structure is used and shown in Figure 6.7. Additionally, the flow chart of the HHO algorithm is illustrated in Figure 6.8.

$$P(s+1) = \begin{cases} Q & if F(Q) < F(P(s)), \\ R & if F(R) < F(P(s)) \end{cases} \tag{6.24}$$

Where Q and R are calculated by equation (6.25) and (6.26).
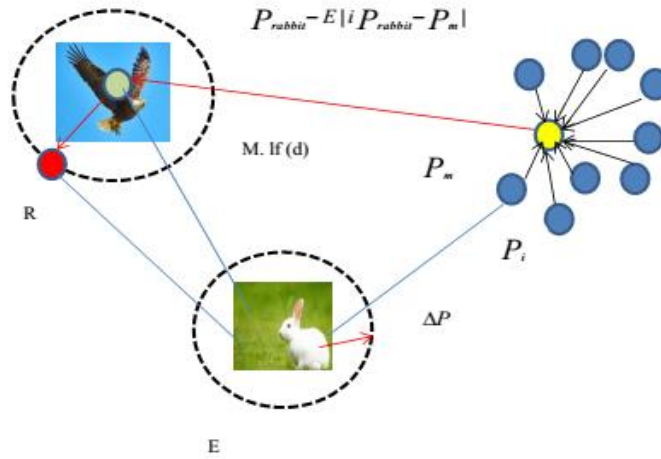
Figure 6.7 Structure of the visualization of HHO tracking with vector addition

$$Q = P_{rabbit}(s) - E \,|\, i\, P_{rabbit}(s) - P(s)| \tag{6.25}$$

$$R = Q + M.lf(d) \tag{6.26}$$

6.6.3.5. Velocity of Hawk Updating Operator

In order to improve the efficiency of the conventional HHO algorithm, an enhancement is proposed by integrating the velocity updating equation of the PSO algorithm into the updating process of HHO.

$$V_{id} = V_{id} + C1^* rand()^*(P_{id} - X_{id}) + c2^* rand()^*(P_{gd} - X_{id}) \tag{6.27}$$

Where, V_{id} is the particle (hawk) velocity; X_{id} is the current particle (hawk) (solution). P_{id} and P_{gd} are pbest and gbest. rand () is a random number between (0,1). cl, c2 are learning factors. Usually c1=c2=2.
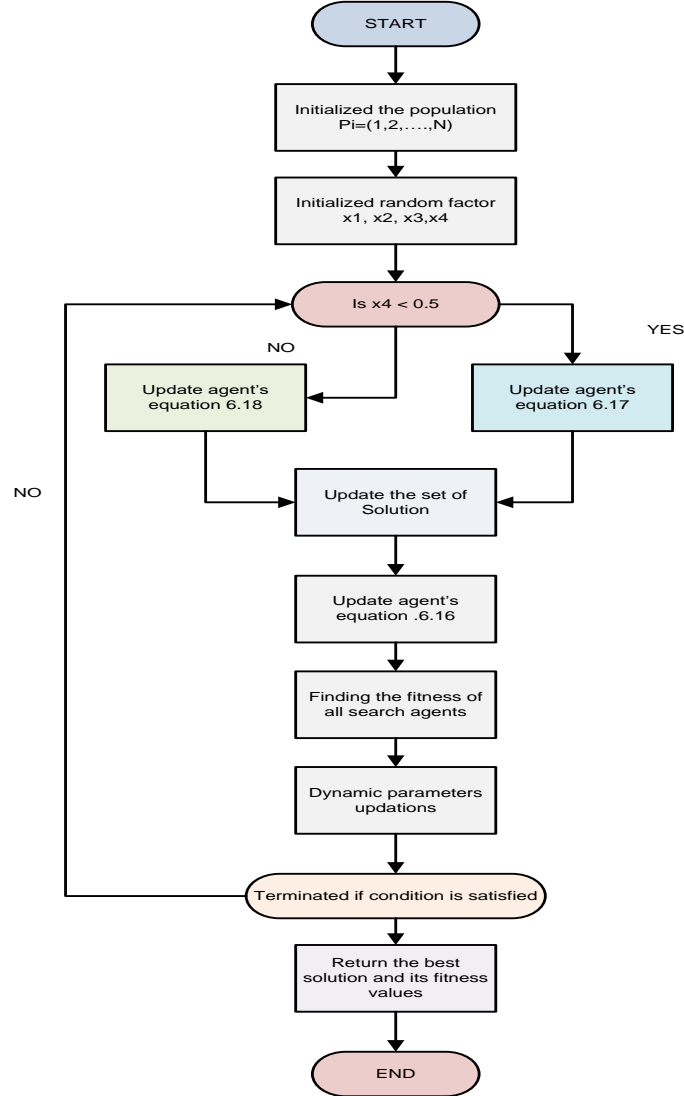
Figure 6.8. Flow chart of HHO algorithm

6.4. Results and Discussions

In this section, we analyze the performance of the EHHO control scheme proposed for controlling frequency deviation in RES-based microgrids. The proposed LFC comprises various renewable energy sources, including SPV, WTG, BESS, and DEG, and considers three microgrid systems for each pumping station with tie line connections. The proposed technique is implemented using MATLAB platform,

Intel(R) Core (TM) i5 processor, and 8GB RAM, and its performance is evaluated. To evaluate the frequency control performance of the proposed EEHO-based PID controller, we compare it with other existing methods, such as GWO and PSO. Figure 6.9 shows the Simulink diagram of the proposed system.

6.4.1 Performance Analysis

6.4.1.1. PSO based Controller

In this sub section, PSO based controller performance is discussed separately for each area of the microgrid sections considering WTP. The values are derived from PSO based multi-microgrid system. The performance of PSO based controller for SPV, WTG, BESS, DEG, load deviation and frequency deviation for each unit as well as tie line within each area is shown in the following figures separately as shown below. The PSO based controller has attained the average output power of SPV and WTG as 0.25 p.u. and 0.36 p.u. respectively. Similarly, the response of BESS and DEG are shown in the figure. The PSO based controller has attained the load deviation between 1.25 p.u to almost 2.1 p.u .Also, the PSO based controller performance for frequency deviation has been attained almost zero value with high deviation.
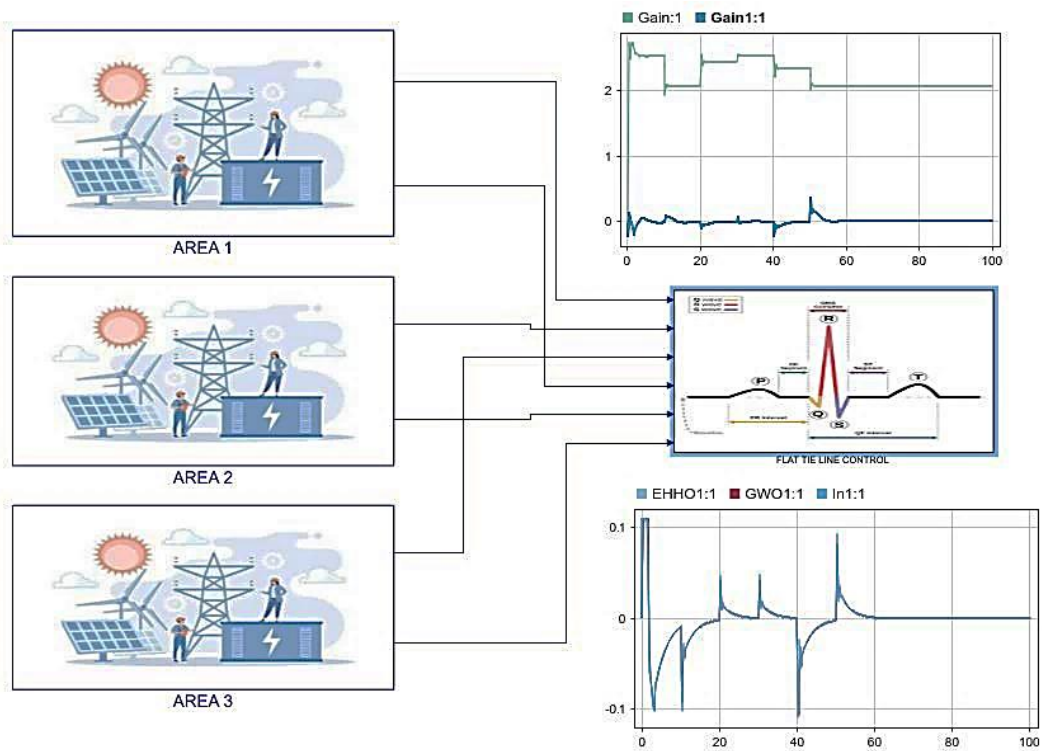
Figure 6.9 Simulink diagram of proposed system.

A. Microgrid area-1

The performance of different power sources and load of Microgrid area 1 under PSO is shown below. Figure 6.10 shows load deviation in P.U and figure 6.11 shows Solar and wind power output in P.U. Figure 6.12 shows output power of BESS and Diesel Engine Generator, Similarly, Figure 6.13 shows frequency deviation of area 1 in Hz, also, Figure 6.14 shows the total output power of Area I in P.U.
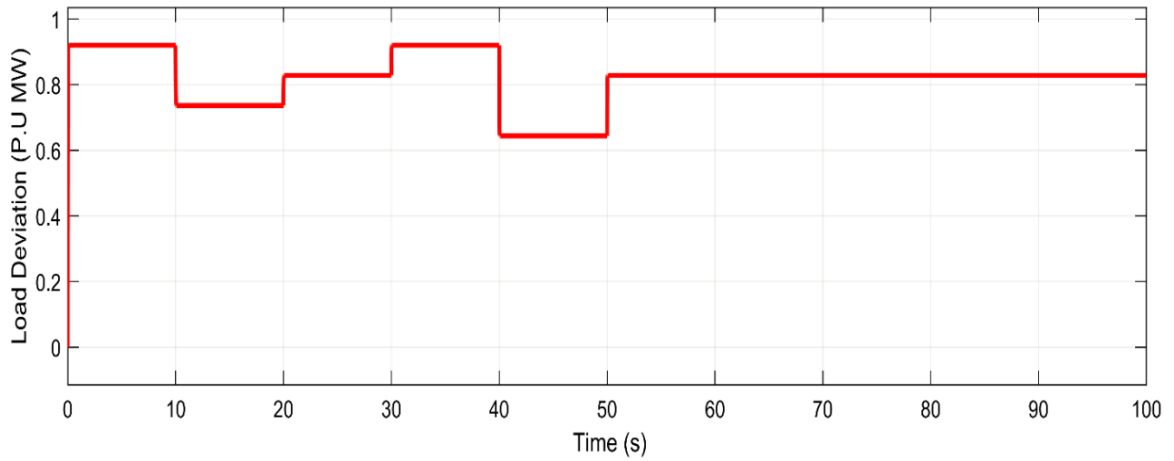
Figure 6.10 Load deviation
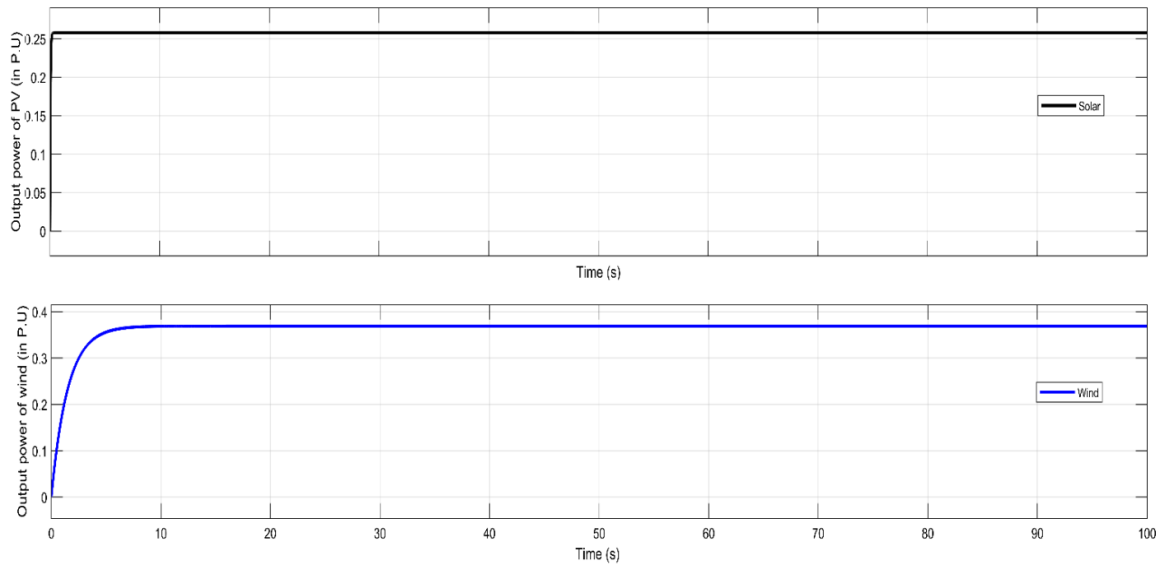
Figure 6.11 Solar and Wind power
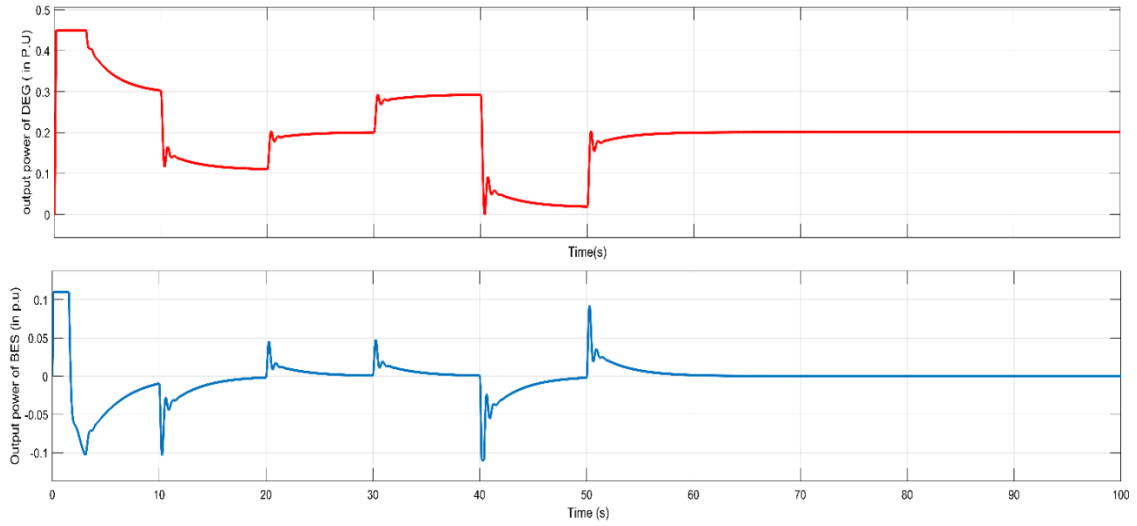
Figure 6.12 Output power of DEG and BESS
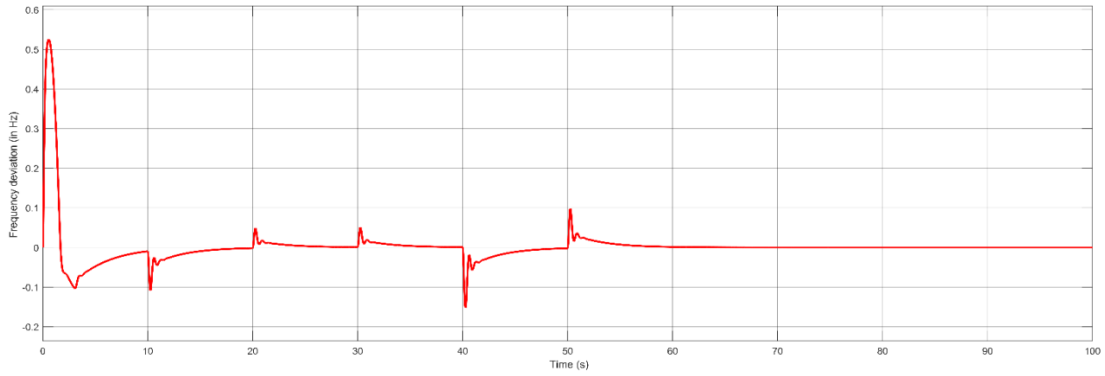
Figure 6.13 Frequency deviation of area 1 in Hz.
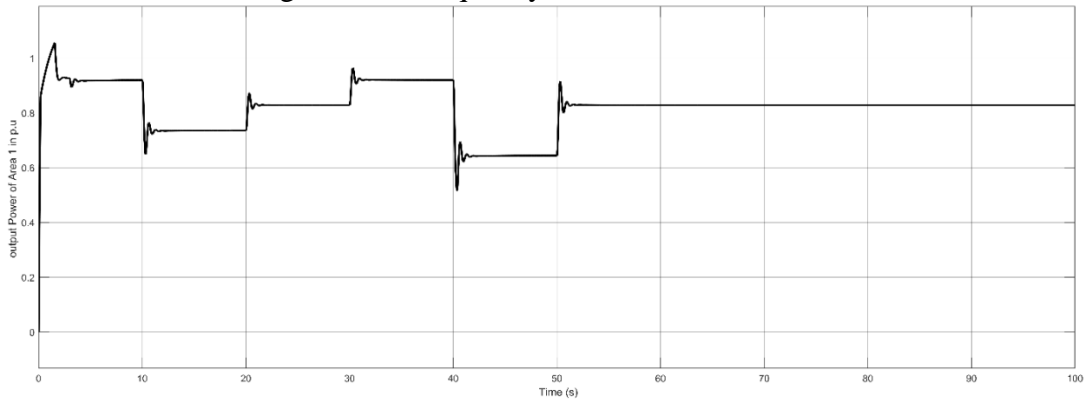
Figure 6.14 Output power of area 1 in P.U.

B. Microgrid Area 2

Similar to Area 1 The performance of different power sources and load of Microgrid area 2 under Particle Swarm Optimization PSO is shown in the following figures. Figure 6.15 shows load deviation of area 2 in P.U and figure 6.16 shows output

power of BESS and Diesel Engine Generator, Similarly, Figure 6.17 shows frequency deviation of area 1 in Hz, also, Figure 6.18 shows the total output power of Area 2 in P.U.
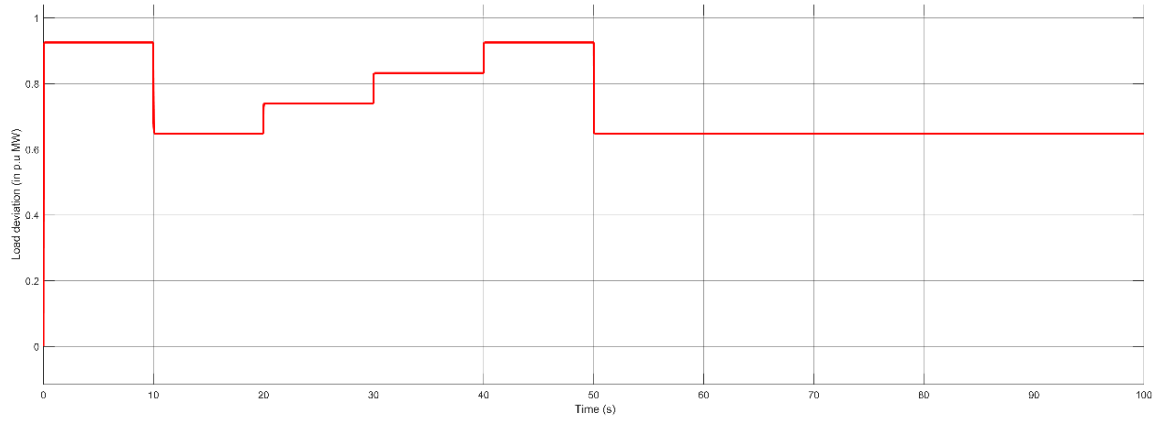
Figure 6.15 Load deviation of area 2 in pu
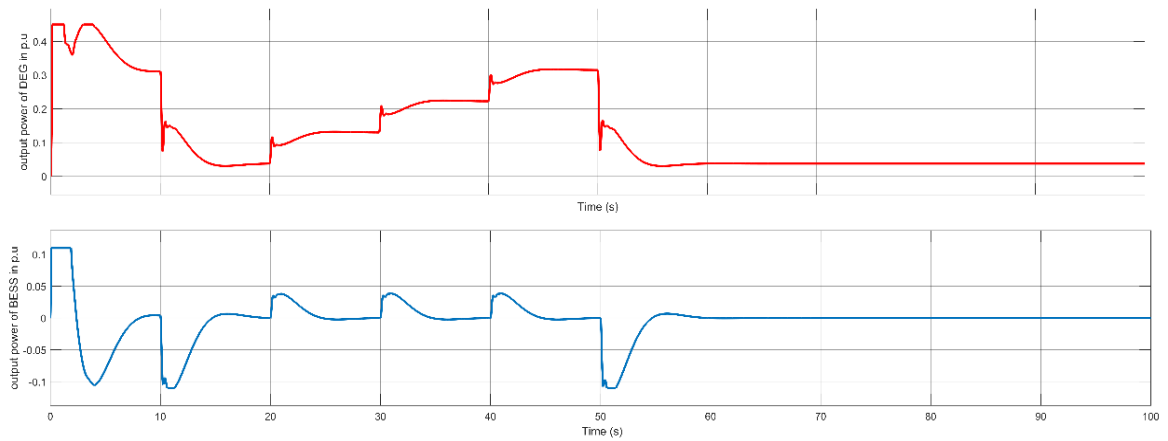
Figure 6.16 BESS and DEG power output in P.U.
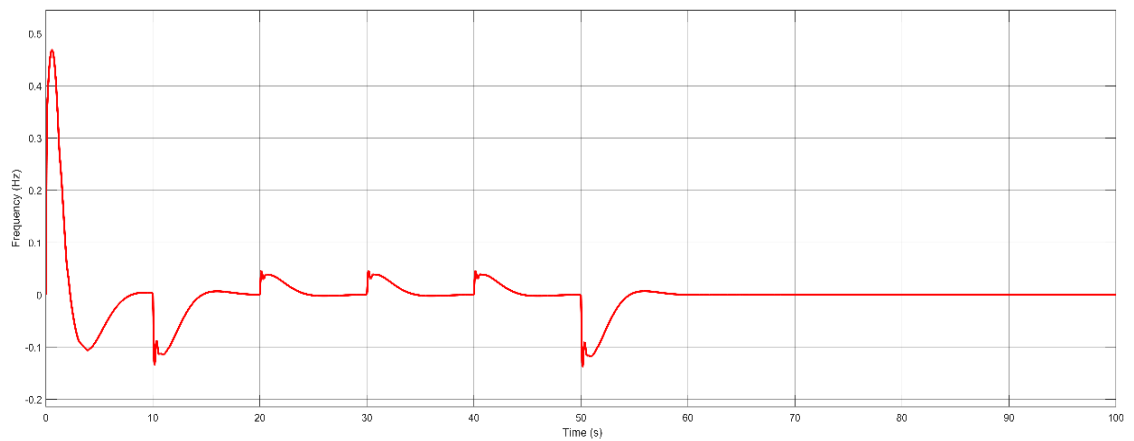
Figure 6.17 frequency deviation of area 2 in Hz.
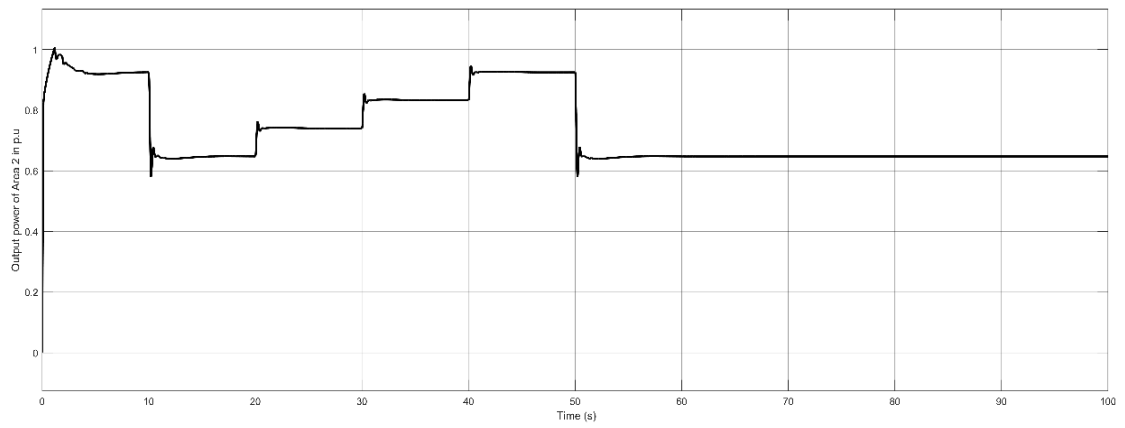
Figure 6.18 total output power of Area 2 in pu.
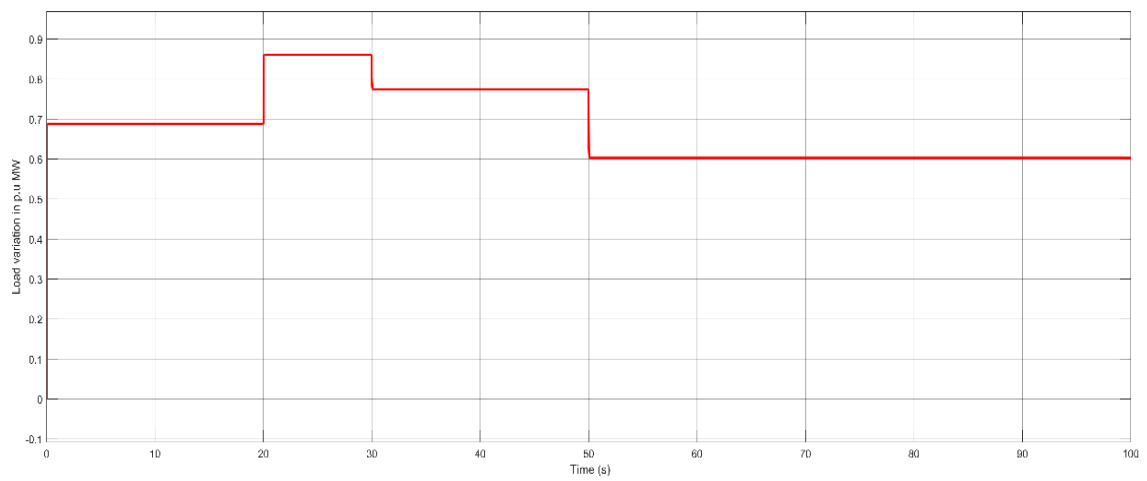
Figure 6.19 load deviation of area 3 in pu
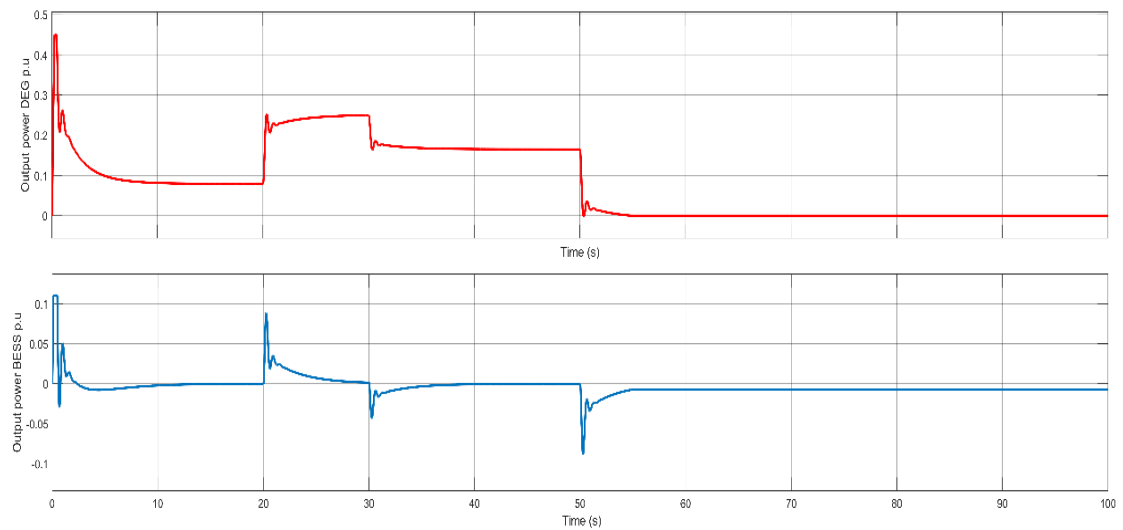
Figure 6.20 Output power of BESS and DEG
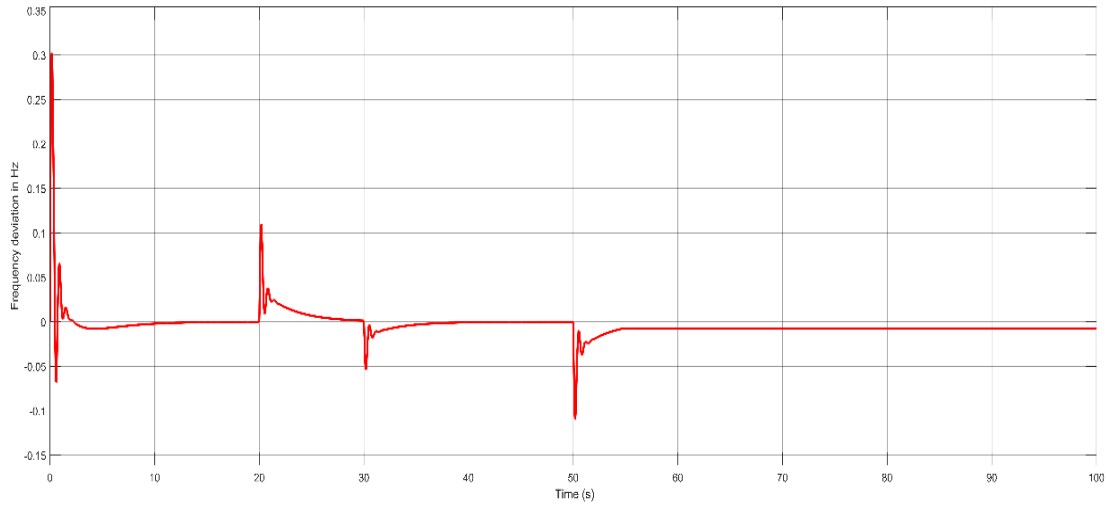
Figure 6.21 frequency deviation of area 3 in Hz.
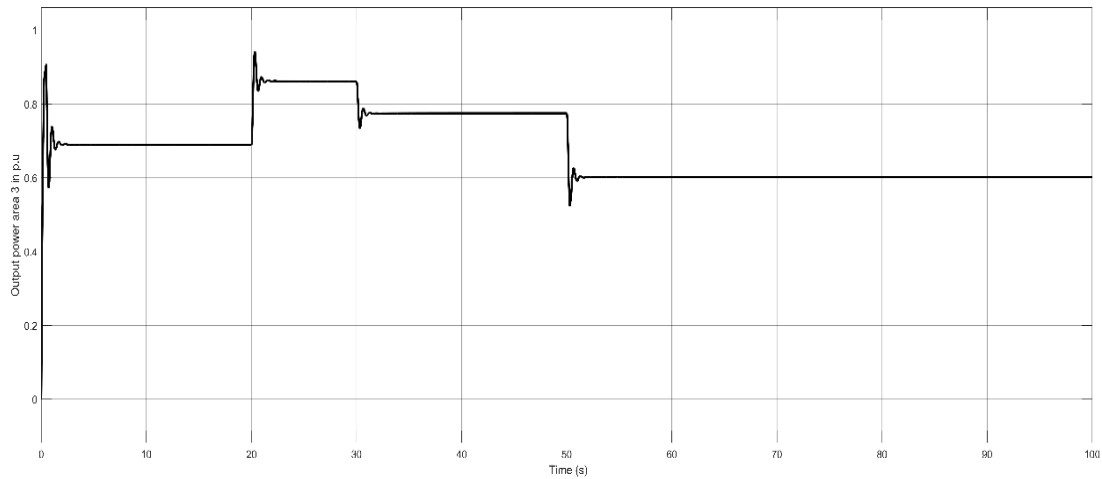
Figure 6.22 total output power of Area 3 in P.U.

A. Microgrid Area 3

Similar to Area 1 and 2, the performance of Microgrid area 3 under PSO is shown in the following figures. Figure 6.19 shows load deviation of area 3 in P.U and figure 6.20 shows output power of a BESS and Diesel Engine Generator, Similarly, Figure 6.21 shows frequency deviation of area 3 in Hz, also, Figure 6.22 shows the total output power of Area 3 in P.U.

B. Tie line values under PSO

The performance of the tie line values such as frequency deviation and power of each of the Microgrid area 1, 2 and 3 under PSO is shown in the following figures.

Figure 6.23 shows the tie line power deviation of each Microgrid such as (a) Area 1 and 2 (b) area 2and 3 (c) area 1 and 3. Similarly, Figure Moreover, the iteration for fitness function convergence of PSO is shown in figure 6.24 showing that at 50 iteration the PSO shows best convergence result.
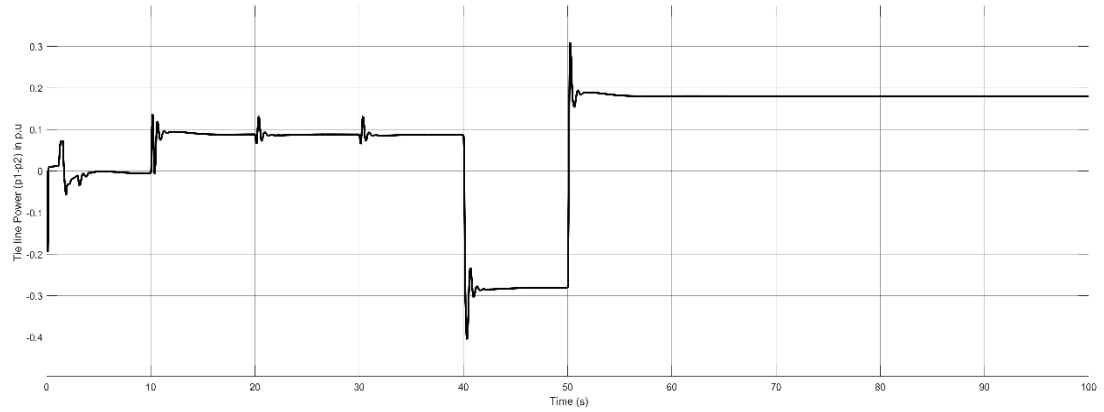
(a)
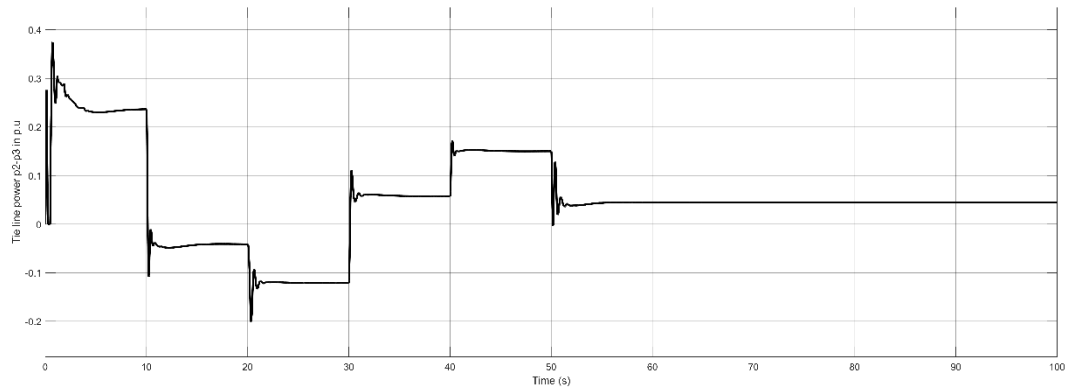
(b)
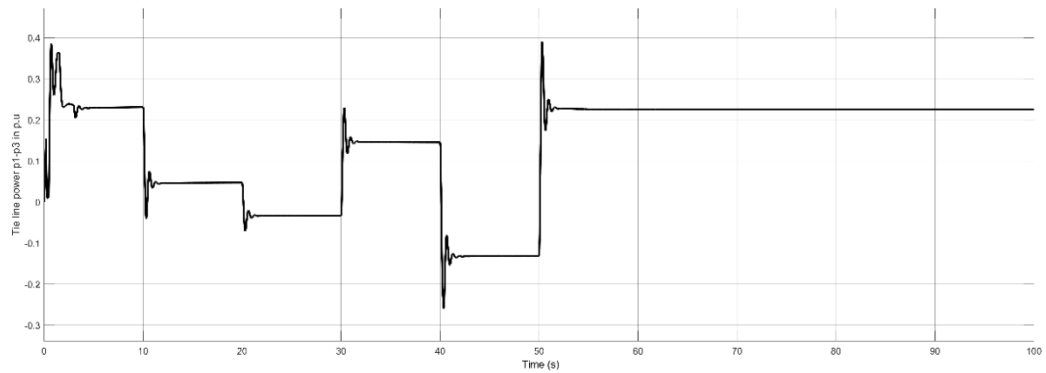
(c)

Figure 6.23 Tie line power deviation (a) Area 1 and 2 (b) area 2and 3 (c) area 1 and 3
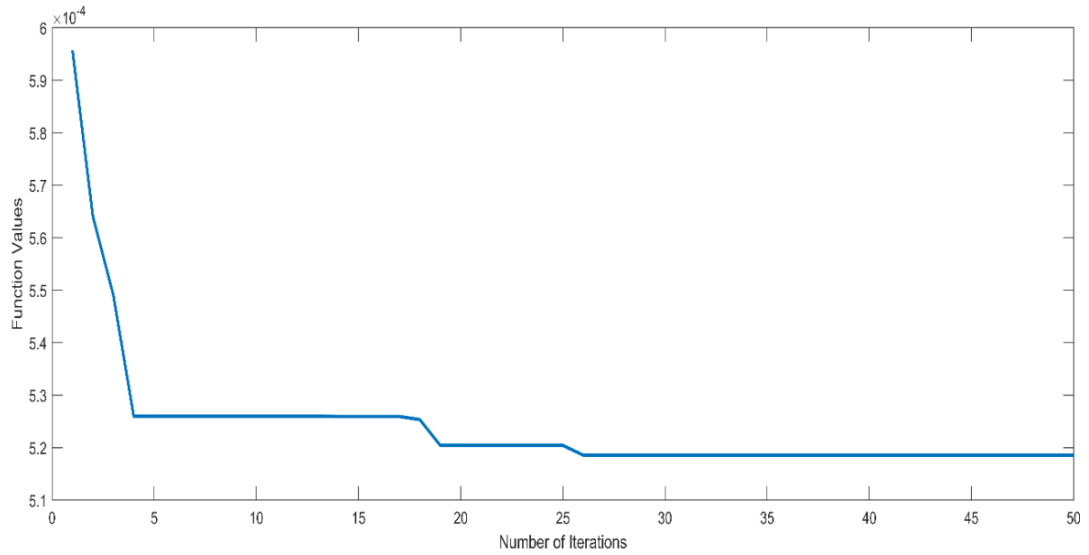
Figure 6.24 convergence plot of PSO.

6.4.1.2. Comparative Analysis

In order to understand the characteristics and performance of each controllers. The performance of the proposed controller and existing controllers such as PSO, GWO and EHHO based controller is compared and evaluated in this sub section. The comparative performance of the proposed and existing controller for each microgrid areas are shown and explained in the following sub sections. The following table 6.2 shows the optimized controller parameters with different algorithms.

Table 6.2. Different parameters optimized with different algorithms

Optimum	PSO	GWO	EHHO
K_{Ts1}	0.6485	1.2498	0.7643
K_{Ts2}	0.1846	1.3486	1.2549
K_{Ts3}	1.4965	1.5879	0.9784
K_{Is1}	0.0125	0.3248	0.1487
K_{Is2}	1.2978	1.4879	1.6458
K_{Is3}	1.2645	0.0489	0.2657
K_{Ds1}	0.3214	0.1458	0.5487
K_{Ds2}	0.8974	0.3456	0.2489
K_{Ds3}	1.2645	2.0216	0.1546
K_{ps1}	0.6458	0.8974	1.0245
K_{ps2}	0.4579	0.9874	0.7854
K_{ps3}	1.2464	1.3654	1.8645
K_{is1}	0.2458	1.5462	1.6548
K_{is2}	0.9567	0.7846	0.9461
K_{is3}	0.4965	0.6478	0.2876
N_{s1}	1.8462	2.0189	2.7842
N_{s2}	2.8426	2.6742	2.1436
N_{s3}	4.1028	3.0456	2.7842

N_{Tf1}	167.4863	142.6872	128.4356
N_{Tf2}	201.5489	238.7268	102.4892
N_{Tf3}	15.4765	24.8462	32.4872

A. GWO based Controller

The performance of GWO based controller for SPV, WTG, BESS, DEG, load deviation and frequency deviation is shown and discussed in the following figures, the output power of SPV and WTG are 0.25 p.u and 0.36 p.u respectively. Also, the BESS and DEG response are shown in the figure. The GWO based controller has attained almost less load deviation compare to PSO. The GWO based controller for frequency deviation performance has achieved almost zero value with less deviation.

B. EHHO based proposed Controller

The performance of EHHO based proposed controller compare with PSO and GWO for SPV, WTG, BESS, DEG, load deviation and frequency deviation of each microgrid area shows that the performance of proposed controller is achieving better results. The performance of the above controllers with respect to each microgrid area in comparison with PSO and GWO is shown in the following figures.

B1. Microgrid Area 1

The performance of Microgrid area 1 under comparison of different optimization method is shown in the following figures. Figure 6.25 shows the output power of DEG and Figure 6.26 shows the output power of BESS Similarly, Figure 6.27 shows the frequency deviation of area 1 in Hz, also, and figure 6.28 shows the total output power of Area 1 in P.U. From the figure it can be stated that the performance of EHHO shows better results compare to other optimization techniques in Area 1.
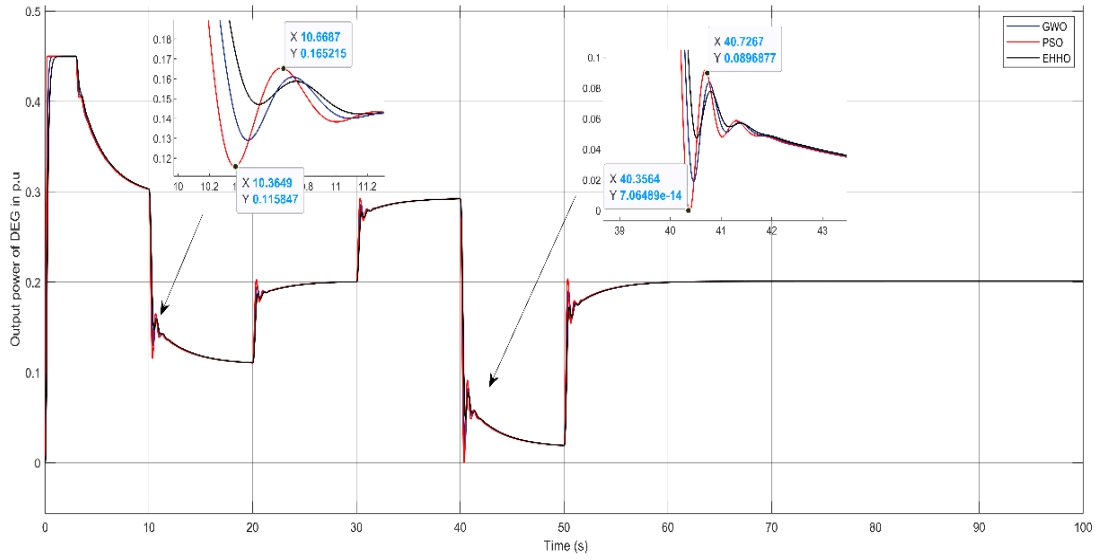
Figure 6.25 Output power of DEG in pu.
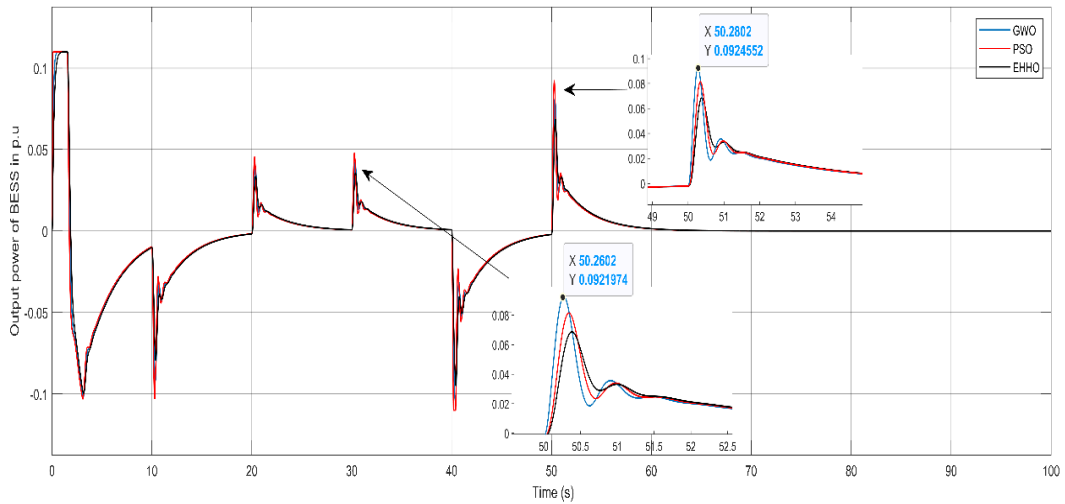
Figure 6.26 Output power of BESS in pu.

B2. Microgrid Area 2

Similar to area 1, the performance of Microgrid area 2 under comparison of different optimization technique is discussed and shown in the following figures. Figure 6.29 shows the output power of DEG and Figure 6.30 shows the output power of BESS Similarly, Figure 6.31 shows the frequency deviation of area 2 in Hz, also, and figure 6.32 shows the total output power of Area 2 in P.U. From the figure it can be stated that the performance of EHHO shows better results compare to other

optimization techniques in Area 2. The output power and frequency deviation compare to area 1 shows better results in Area 2.
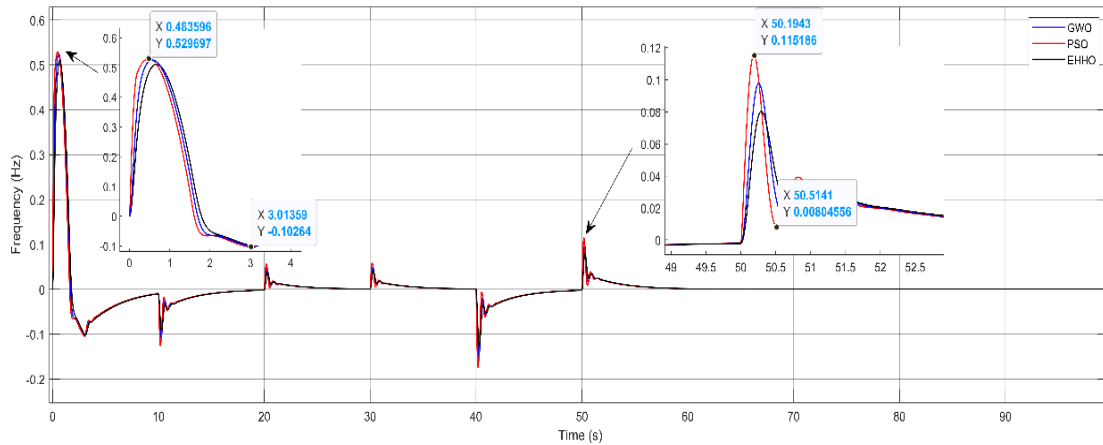
Figure 6.27 frequency deviation of area 1 in Hz
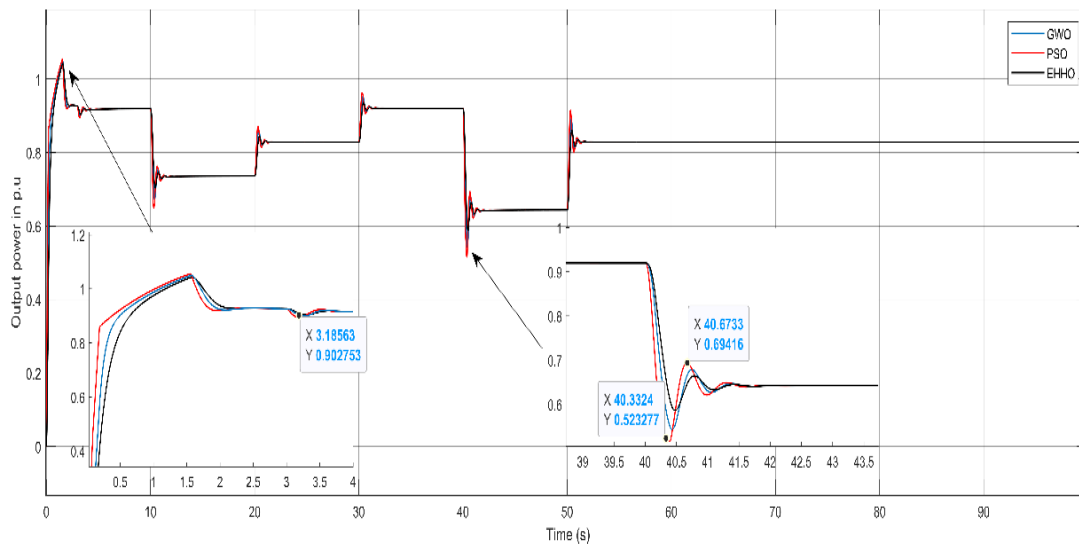
Figure 6.28 shows the total output power of Area 1 in P.U.

B3. Microgrid Area 3

Similar to area 1 and 2, the performance of Microgrid area 3 under comparison of different optimization technique is discussed and shown in the following figures. Figure 6.33 shows the output power of DEG and Figure 6.34 shows the output power of BESS Similarly, Figure 6.35 shows the frequency deviation of area 3 in Hz, also, and figure 6.36 shows the total output power of Area 3 in P.U. From the figure it can be stated that the performance of EHHO shows better results compare to other optimization techniques in Area 3.
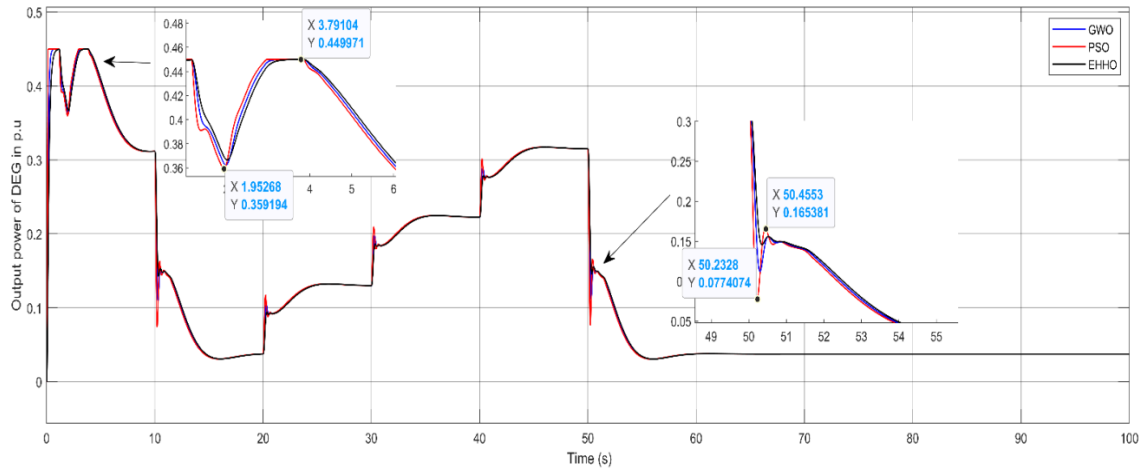
Figure 6.29 Output power of DEG
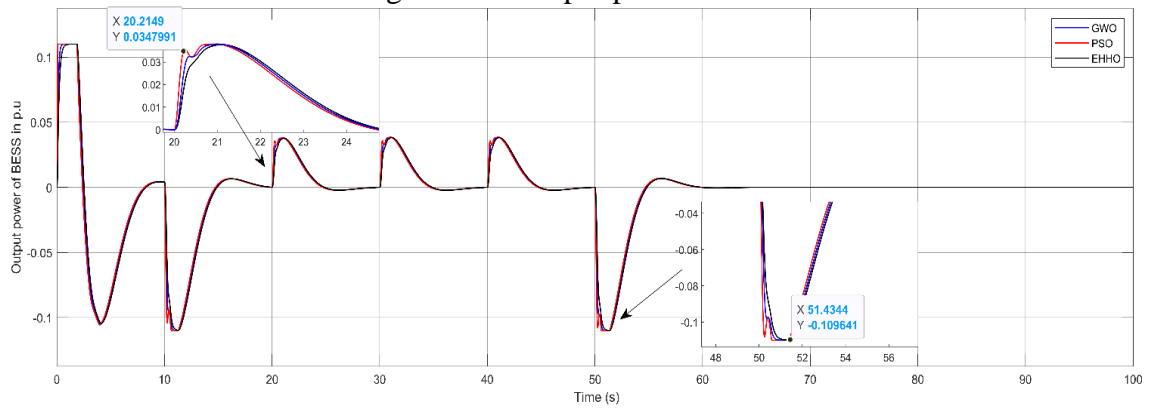
Figure 6.30 Output power of BESS

From the above figures, the proposed controller has attained better results compare to PSO and GWO. The SPV and WTG output for each area are not shown in the comparison due to stand alone configurations. As shown in the figure the response of the DEG and BESS tries to compensate the varying load and produce the corresponding output as per requirement of the system. The response of each area show better steady state with less variations under EHHO optimization schemes. Also, the frequency and output power of each area shown in the figure represents each response of area 1, 2 and 3. It can be seen that the proposed controller shows better results under different loads. The proposed controller is accurately minimize the load frequency deviation, i.e. the value of proposed controller has been almost converged to zero with less steady state error when compared to other methods such PSO and GWO. Therefore, the proposed controller has outperformed than existing techniques such as PSO and GWO
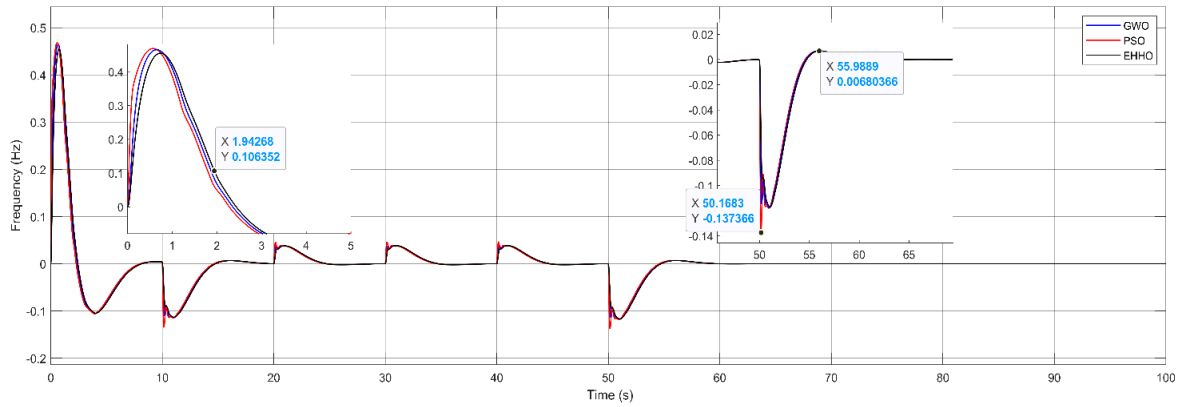
Figure 6.31 Frequency deviation of area 2 in Hz
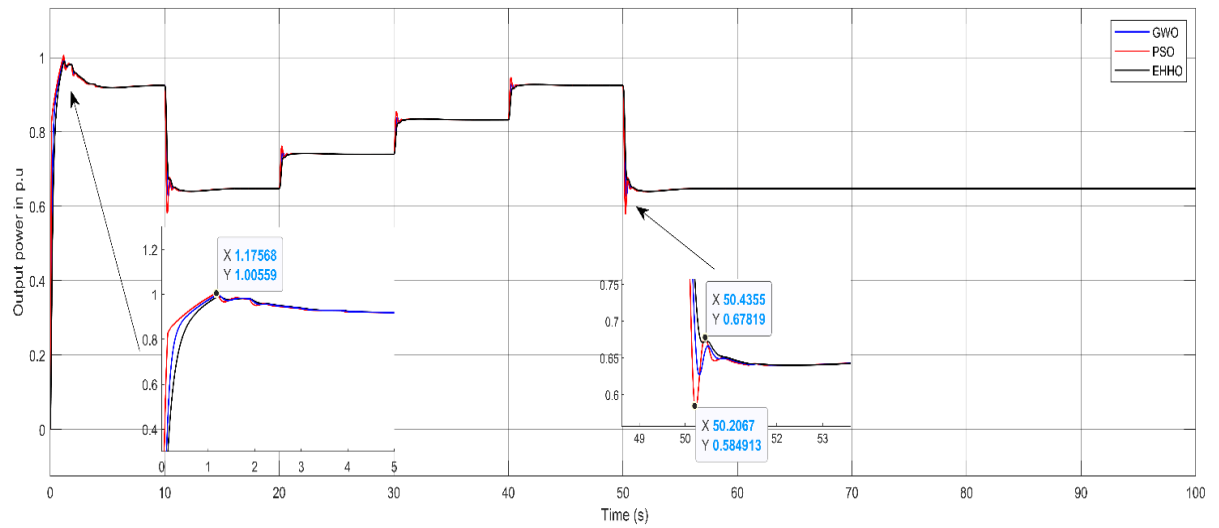
Figure 6.32 The total output power of Area 2 in pu
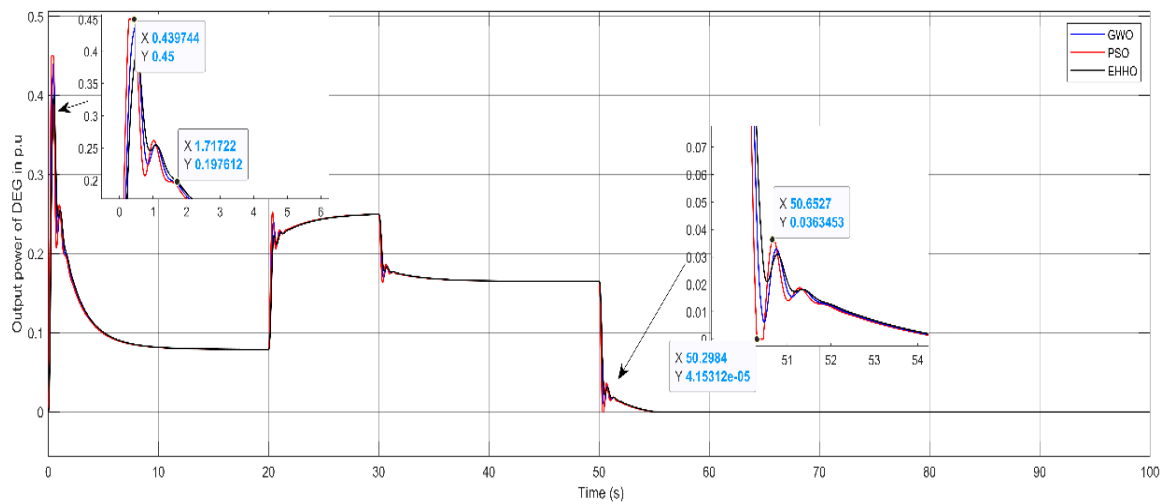
Figure 6.33 Output power of DEG
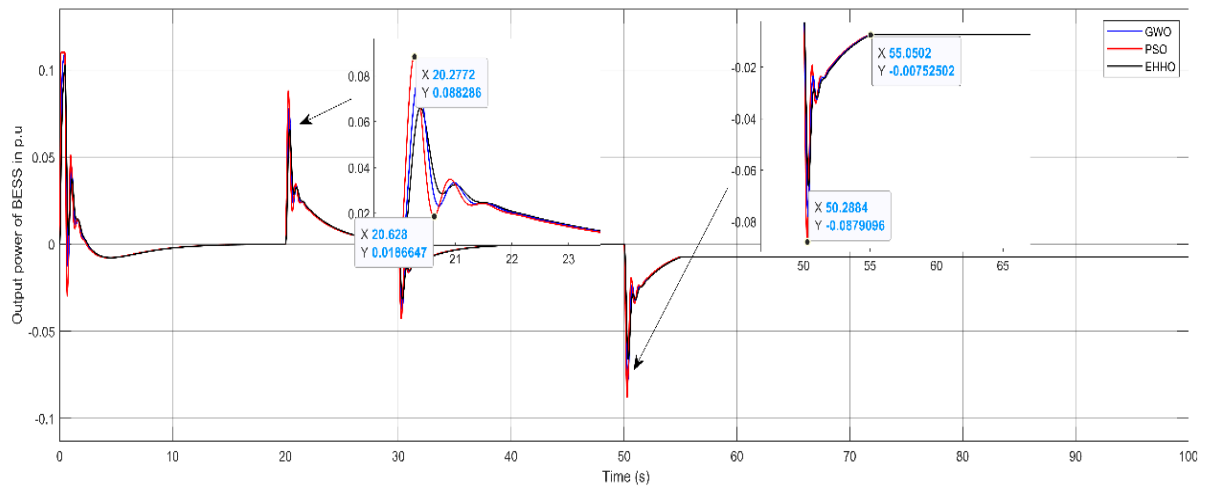
Figure 6.34 Output power of BESS
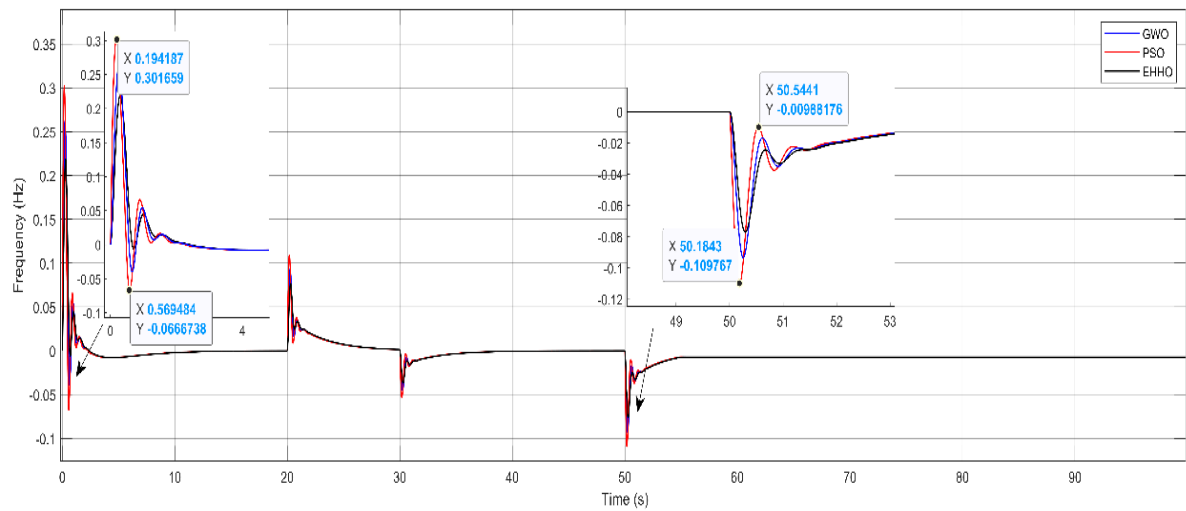
Figure 6.35 shows the frequency deviation of area 3 in Hz
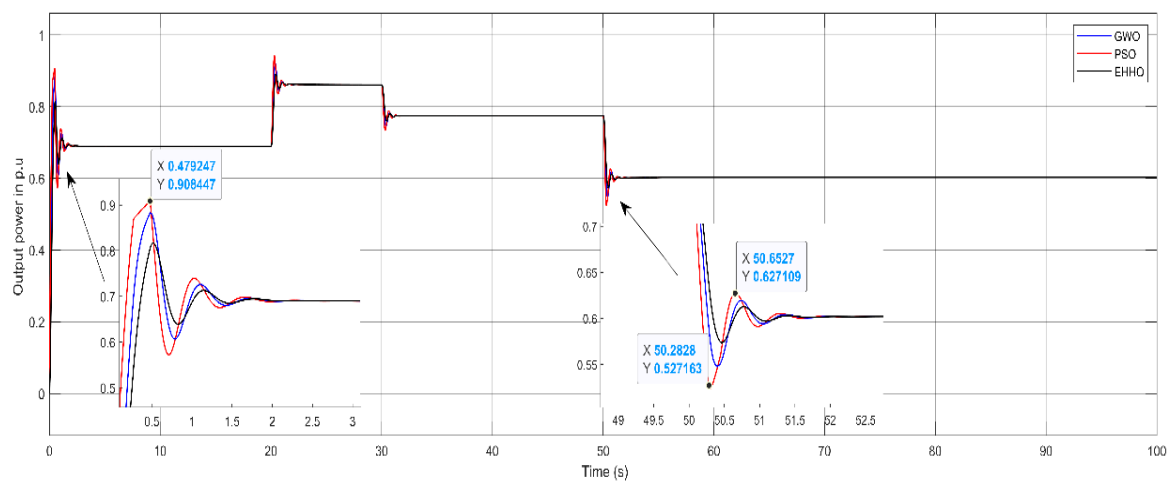
Figure 6.36 Total output power of Area 3 in P.U.

B4. Tie line values

The tie line of a transmission system is defined as the connecting point or parts of different transmission line or different sub-systems, here in microgrid system a tie line represents the connecting points of two or more area or branch for exchanging power for the whole microgrid system. the performance of each three Microgrid area under comparison of different optimization technique is discussed and shown in the previous subsections. However, comparison of each optimization technique in the tie line between each microgrid area is discussed in this section and the following figure shows tie line power and frequency. Figure 6.37 shows the tie line output power of (a) area 1 & 2 (b) area 2 & 3 and (c) area 1 & 3. From the figure it can be stated that the performance of EHHO shows better results compare to other optimization techniques in Area 3. Figure 6.38 shows tie line power deviation of different area under EHHO. Moreover, Figure 6.39 shows convergence plot comparison of PSO, GWO and EHHO optimization technique. The convergence curve shows that the fitness function for EHHO is low compared to other optimization technique and also converge faster. Also, Table 6.3 shows the parameters of each area of the microgrid system.

Table 6.3 Parameter values of each of the microgrid area 1,2 & 3.

Sl. No.	Parameters	Area 1	Area 2	Area 3
1	Wind turbine parameters	$K_{WTG}=1$, $T_{WTG}=1.5$	$K_{WTG}=1.6$, $T_{WTG}=1.47$	$K_{WTG}=1.4$, $T_{WTG}=1.65$
2	SPV Parameters	$K_{PV}=0.0075$, $T_{PV}=0.03$	$K_{PV}=0.1075$, $T_{PV}=0.047$	$K_{PV}=0.0235$, $T_{PV}=0.13$
3	BESS parameters	$K_{BES}=1$, $T_{BES}=0.1$	$K_{BES}=1$, $T_{BES}=0.24$	$K_{BES}=1$, $T_{BES}=0.45$
4	Valve Actuator	$T_1=0.025$, $T_2=2$, $T_3=3$	$T_1=0.125$, $T_2=1.482$, $T_3=2.343$	$T_1=0.045$, $T_2=2.58$, $T_3=3.45$
5	Diesel Engine	$K_E=1$, $T_B=3$	$K_E=1.2$, $T_B=3.4$	$K_E=1.6$, $T_B=3.8$
6	Speed Regulation Constant	$R_1=5\frac{Hz}{P.U\ MW}$, $R_2=5\frac{Hz}{P.U\ MW}$	$R_1=5.5\frac{Hz}{P.U\ MW}$, $R_2=5.5\frac{Hz}{P.U\ MW}$	$R_1=6.5\frac{Hz}{P.U\ MW}$, $R_2=6.5\frac{Hz}{P.U\ MW}$
7	Synchronizing power coefficient	$T_{12}=0.225/7$	$T_{12}=0.315/6$	$T_{12}=0.245/9$
8	Rotor Swing -1	$K_{P1}=60$, $T_{P1}=18$	$K_{P1}=50$, $T_{P1}=21$	$K_{P1}=54$, $T_{P1}=16$
9	Rotor Swing -2	$K_{P2}=60$, $T_{P2}=18$	$K_{P2}=50$, $T_{P2}=21$	$K_{P2}=54$, $T_{P2}=16$
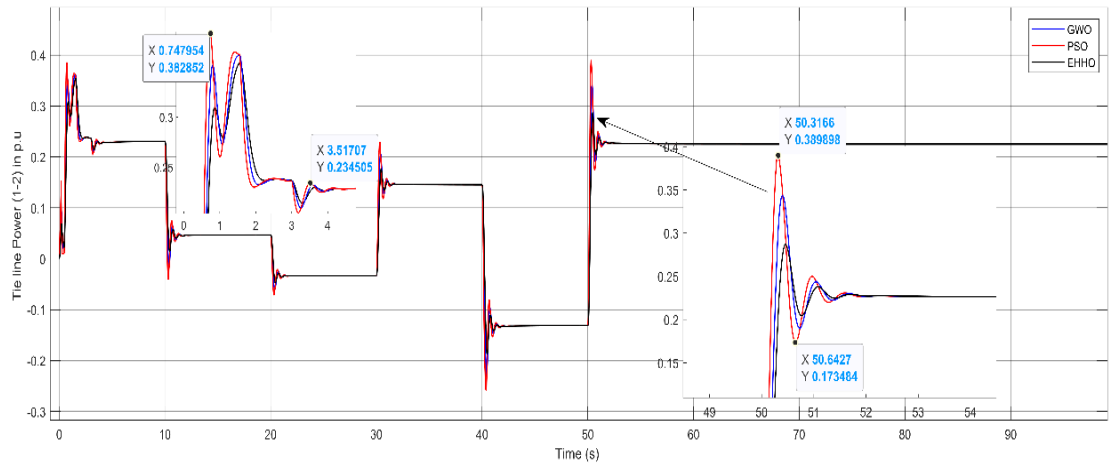
(a)
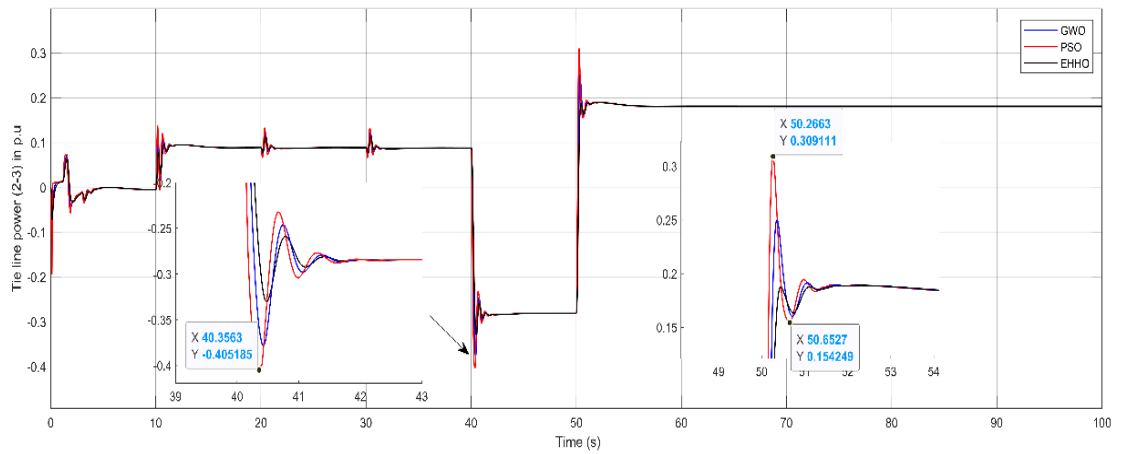
(b)
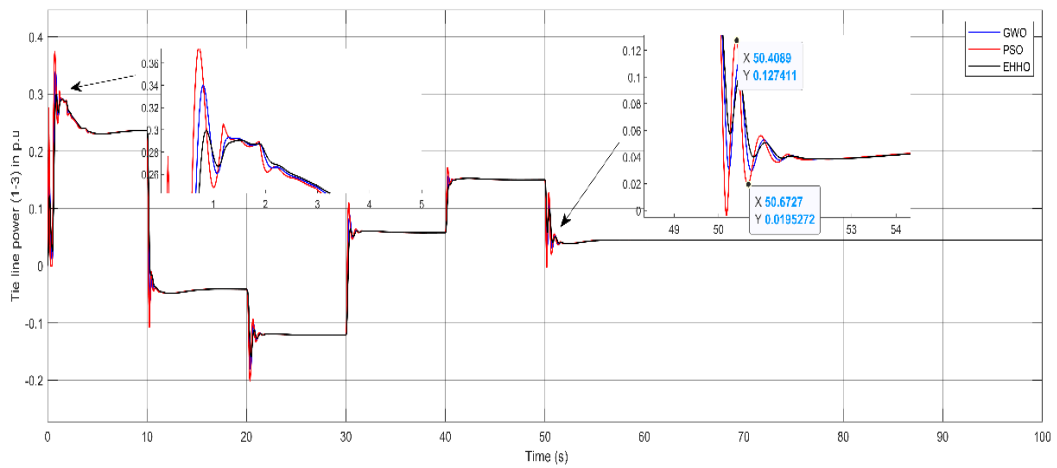
(c)

Figure 6.37 Tie line power of (a) area 1 & 2 (b) area 2 & 3 and (c) area 1 & 3
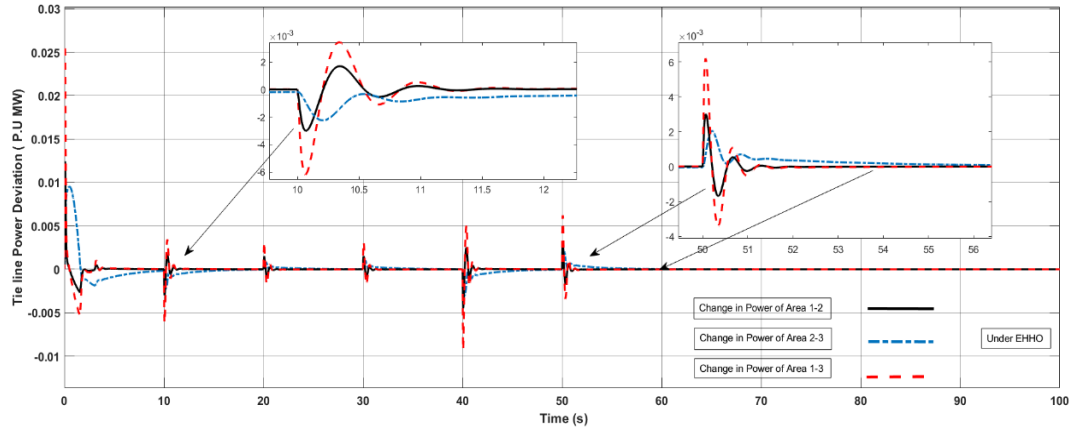
Figure 6.38 Tie line Power deviation of different area under EHHO
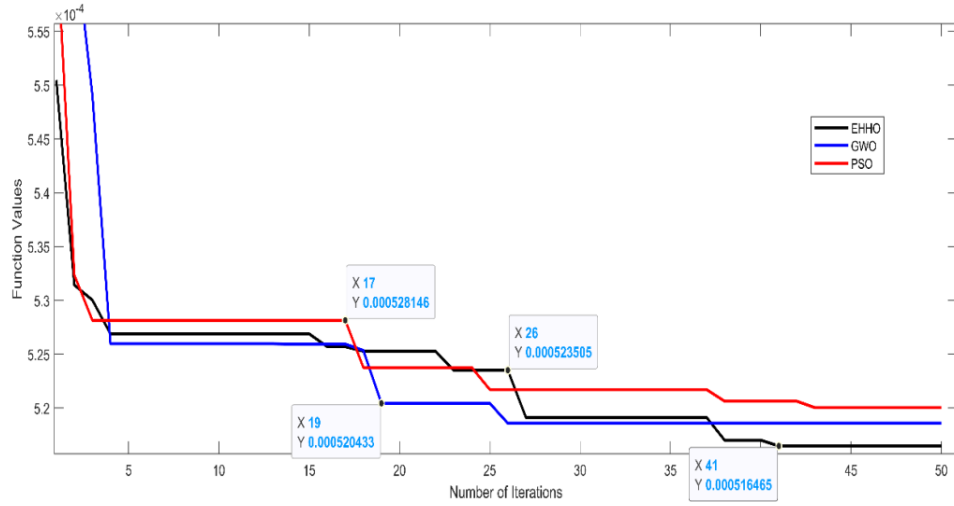
Figure 6.39 Comparison of convergence plot under PSO, GWO and EHHO optimization technique.

6.5. Implementation of proposed controllers

The study aims to improve the performance of the system and comprehension by introducing various controllers, including PID, 3DOF-FOPIDN, and 3DOF-TIDN, and optimizing their parameters through PSO algorithm. Additionally, the study conducts stability and robustness analyses.

6.5.1 3DOF-FOPIDN Control structure

The PID controller is widely recognized as the foundational and primitive control technique that the field of control has ever developed. However, it has been observed that this controller may not perform well when the system is exposed to parameter changes, uneven disturbances, or non-linearities. To address these complications, the

FO based-PID controller has been integrated with the concept of higher DOF. This integration provides additional features for tuning the controller and enhances its operating capabilities [225].

To incorporate extra inertia, damping control, and supplementary control, a fractional order controller (specifically, the dual-stage FOPID (1 + PI) controller) has been employed. The proportional derivative (PD) component of the controller provides the additional damping and inertia, while the integral (I) component offers supplementary control to the power system. As a result, the derivative portion of the controller enhances the transient performance and improves the system's steady-state response by reducing steady-state error [226].
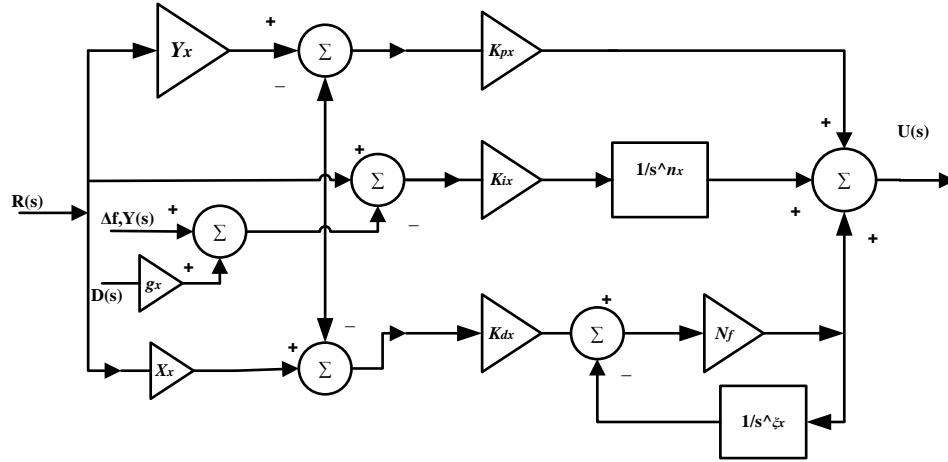
Figure 6.40 3DOF-FOPIDN Structure

A 3DOF (3 Degree of Freedom) controller consists of three independent feedback loops where three inputs, R(s), Y(s), and D(s), are obtained from each of the loops. The 3DOF structure is combined with a FOPIDN (Fractional Order Proportional Integral Derivative with Notch) controller to form a 3DOF-FOPIDN controller. This new controller has an extra independent loop, which helps in achieving a better response compared to a 2DOF-FOPIDN controller.

The fractional calculus involves using differentiation and integration with fractional-order or complex-order. Fractional derivatives have an advantage in that they can inherit the characteristics of the processes being modeled. The fractional-order PID controller (FO-PID) is a transfer function written as in Equation (6.28).

$$Controllerresponse.(y) = D_a \Delta F + KS^{-\lambda} \Delta F + M_a S^{\mu} \Delta F$$
$$(0 < \lambda \leq 1, 0 < \mu \leq 0)$$

(6.28)

with three gain constants, including a proportional part, D_a, an integral part, K, and a derivative part, Ma, with two fractional operators, λ and μ. The actuating signal of the 3DOF-FOPIDN controller is described by an equation, which takes into account the three inputs from the independent loops. the transfer functions of the FOPIDN controller is shown below.

$$U(s) = \left\{ y_x k_{px} + \frac{k_{ix}}{s^n} + x_x k_{dx} s^{\xi} \left(\frac{N_f}{N_f + s^{\xi}} \right) \right\} R(s) + \left\{ -k_{px} - \frac{k_{ix}}{s^n} - k_{dx} s^{\xi} \left(\frac{N_f}{N_f + S^{\xi}} \right) \right\} Y(s) +$$

$$\left\{ -g_x k_{px} - \frac{k_{ix}}{s^n} - g_x k_{dx} s^{\xi} \left(\frac{N_f}{N_f + S^{\xi}} \right) \right\} D(s)$$

(6.29)

Table 6.4 Gain/ Weights/FO of Controllers

Gain	PID Controller			3DOF-FOPIDN			3DOF-TIDN		
	Ctr:1	Ctr:2	Ctr:3	Ctr:1	Ctr:2	Ctr:3	Ctr:1	Ctr:2	Ctr:3
$K_{px/tx}$	1.8500	1.4910	2.4600	3.1842	3.0802	2.8092	3.1842	3.0802	2.8092
K_{ix}	1.8500	1.5430	2.2500	2.8241	1.7621	1.4614	2.8241	1.7621	1.4614
K_{dx}	1.8500	1.6820	1.7500	1.4632	2.4824	1.6324	1.4632	3.1284	1.4234
$y_{x/B}$				0.0468	0.0278	0.0628	0.0468	0.0486	0.0228
$x_{x/C}$				0.4328	0.3246	0.0426	0.4328	0.2446	0.0246
g_x				0.2495	0.4576	0.3458	0.2458	0.4876	0.6487
$N_{f/tf}$				45.6289	85.6189	36.1289	35.5489	102.4529	46.1379
η				0.0482	0.1842	0.4641	0.2482	0.4142	0.6241
ξ				0.6289	0.0684	0.8824	0.0094	0.0684	0.4524

6.5.2 3DOF-TIDN Control Structure

In control systems, the degree of freedom (DOF) refers to the number of independent adjustments that can be made to the closed-loop transfer functions. By utilizing a 3DOF controller, closed-loop stability and dynamic response of the system can be improved while minimizing the effect of disturbances. The structure of a proposed 3DOF-TIDN controller is illustrated in a diagram which includes input reference R(S), system disturbance D(s), 3DOF output Y(s), and system output U(S).

This controller is designed to enhance the dynamic response of the system by reducing the number of oscillations, minimizing deviation of frequency and tripping of power, and maintaining system stability. It is also intended to improve the damping ratio of the system in response to sudden loading changes [227]. The output of the controller in a closed-loop configuration is mathematically expressed in an equation.

$$Y(s) = \left[\frac{G_{CO}(s)G_P(s)}{1+G_{CO}(s)G_P(s)} \boldsymbol{G}_{RC}(s) \right] R(s) + \left[\frac{G_P(s) - G_{CO}(s)G_P(s)G_{FFC}(S)}{1+G_{CO}(s)G_P(s)} \right] D(s) \qquad (6.30)$$

The GCO(s) is designed to limit certain parameters in the control system, such as tilt, integral, derivative gain (K_{Ts}, K_{Is}, K_{Ds}), tilt parameter (Ns), and low-pass filter (N_{Tf}). The proportional (B) and derivative (C) set point weights for R(s) are also represented by the GCO(s), while the gain parameter of the GFFC Controller is represented by G_x. To determine the optimal gain values for the controllers and related parameters, an optimization algorithm is utilized, specifically the Enhanced Harris Hawks optimization algorithm, which minimizes the ITAE (Integral absolute error, Time, and Absolute Error), while adhering to certain constraints. These constraints include minimum and maximum bounds of 0 and 2 for the controller, 0 to 200 for the filters, and 2 to 3 for N.

$$\left. \begin{array}{l} K_{Ts}^{Min} \le K_{Ts} \le K_{Ts}^{Max}, K_{Is}^{Min} \le K_{Is} \le K_{Is}^{Max}, K_{Ds}^{Min} \le K_{Ds} \le K_{Ds}^{Max} \\ N_{Tf}^{Min} \le N_{Tf} \le N_{Tf}^{Max}, N_s^{Min} \le N_s \le N_s^{Max}, c^{min} \le c \le c^{Max}, \\ b^{min} \le b \le b^{Max}, G_{ff}^{min} \le G_{ff} \le G_{ff}^{Max} \end{array} \right\} \qquad (6.31)$$

When choosing between the 3DOF FOPIDN and 3DOF TIDN controllers for controlling three-degree-of-freedom mechanical systems, several differences should be considered. Firstly, the FOPIDN controller employs fractional calculus in its control approach, whereas the TIDN controller uses integer calculus. While the FOPIDN controller offers greater flexibility in adjusting control parameters, the TIDN controller may be simpler to implement. In terms of precision, the FOPIDN controller is generally regarded as more accurate than the TIDN controller due to its ability to utilize fractional calculus for control. Additionally, the FOPIDN controller is more robust, allowing it to effectively handle changes in the system or external disturbances.

However, its implementation may be more complex than the TIDN controller, which relies on integer calculus and does not use notch filters [228].
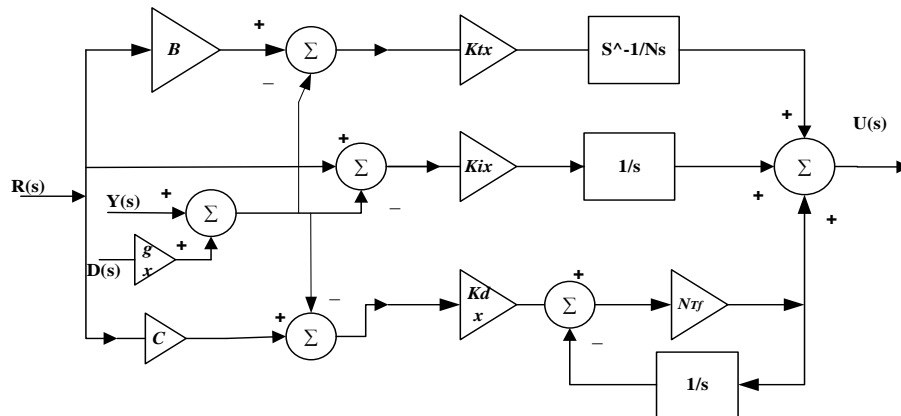
Figure 6.41 3DOF-TIDN Structure

Ultimately, the performance of each controller will depend on the specific application and the mechanical system being controlled. In some situations, the TIDN controller may be sufficient, while in others, the FOPIDN controller may be required for optimal performance. Therefore, the selection between the two controllers will depend on the specific requirements of the application and the mechanical system being controlled. Analysis of the controller in Area 1,2&3 are shown in the following figures
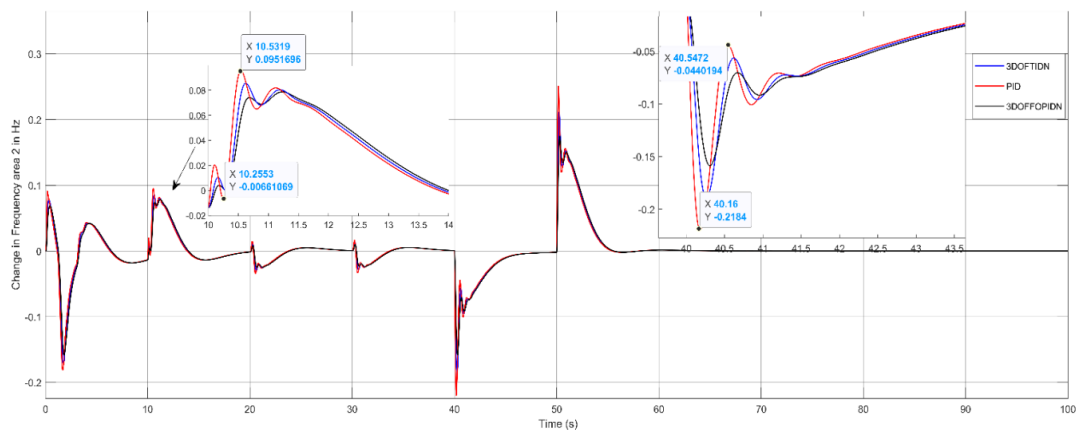
(a)
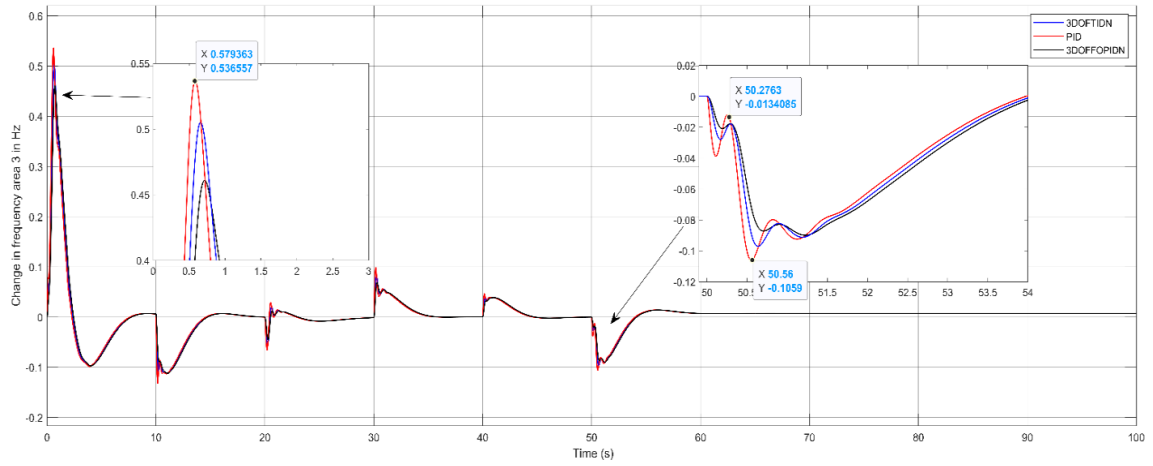
(b)
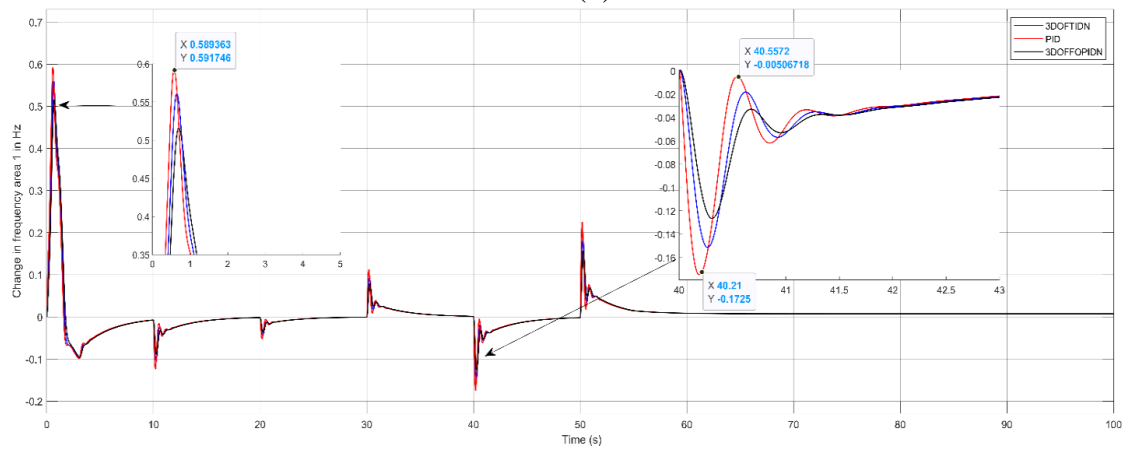
(c)

Figure 6.42 Tie line frequency deviation of (a) area 1&2 (b) area 2&3 and (c) area 1&3.
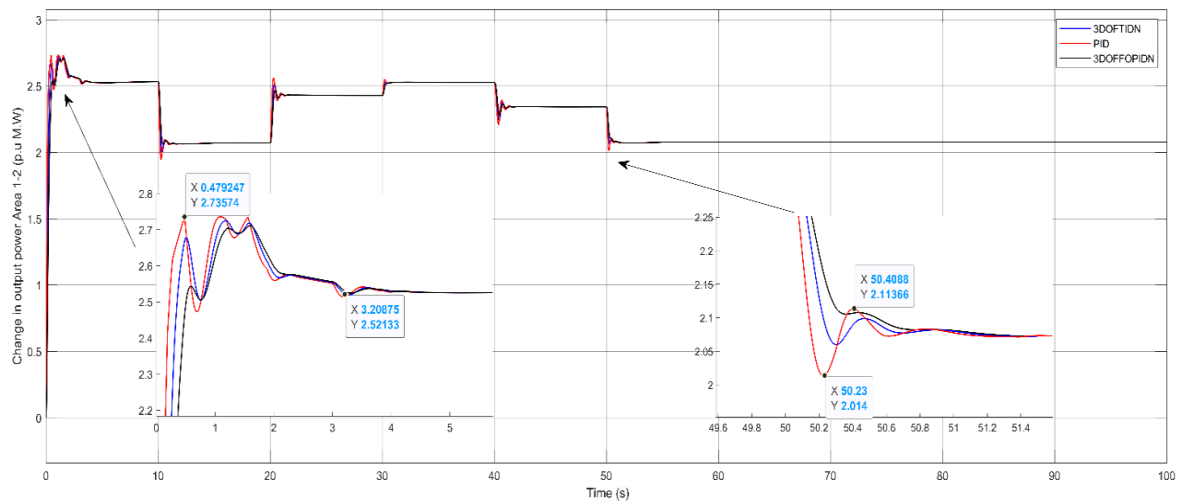
Figure 6.43 Change in power of area 2

Based on the analysis, the obtained results from Figure 6.42 and figure 6.43 demonstrate that the 3DOF-DOPIDN controller proposed in the study exhibits superior dynamic responses compared to other controllers. It effectively reduces oscillation and settling time in frequency and tie power deviation in each area. Additionally, the controller helps to maintain the generated incremental power in the area. As there is no additional load demand, the total generated power in both areas remains at 0.04 p.u.MW. Figure 6.42 provides further insight into the controller's performance by showing the power generation by various sources in area 2, which amounts to 2.5 p.u.MW peak in total.

6.6 Stability analysis and Robustness analysis

6.6.1 Stability analysis

To evaluate the stability of the system, an eigenvalue analysis is conducted with and without various secondary controllers while violating the contract. The eigenvalue plot is displayed in Figure 6.44 and listed in Table 6.5. The damping factor of the system is an indicator of how quickly the system is damped. The damping factors for the system are also provided in Table 6.5. The study examines several secondary controllers, including PID, 3DOF-TIDN, and 3DOF-FOPIDN.

Table 6.5 Eigen Values of different controllers

Condition	Eigen Values	Minimum Damping Ratio (ξ)
Without Controller	-0.42, -2.4833, -9.65, -0.451, -1.3243, -12.46, -0.81, -4.3573, 5.0101, 17.6, -10.194, $\pm16.2862i$, $\pm6.4872i$, -0.1027, -15.246, 4.876, ±1.6349, 0.0967, 3.0083, -2.4083, -46.8248, $\pm0.1465i$, -4.4645, -0.3754, $\pm6.489i$, -4.1342, 0.0046 ,-0.6042, -4.3647, -2.4242, 0.0092, 0.0644, -0.3273, -1.487, -0.4565	0.0031
PID	-0.62, -2.5633, -9.85, -0.461, -1.3424, -999.9999, -123.2457, -0.7315 , -0.4601, 2.0252, 0.5883, 0.018, -0.0025, 0.000017, -0.1, -3.3333-12.5, -12.5, -0.0005, -63.8067, -12.5, -0.0013, -0.0048, -0.0168, -0.2081, -0.7309, -2.5662, -9.0106, -31.11022, -39n 0.0464, -1111.111 -432.7409, $\pm999.9998i$, $\pm1111.1112i$, $\pm1111.110i$, -421.056, -201.0436, -119.9169, -35.1089, -39.2896, -34.1601, -25.0608, -10.6331, -7.0251, -8.8011, -9.8919, -9.3841, -2.02, -0.8967, 1.9435, -2.6039, -2.3997, -0.2908, -1.4883, -0.4845, 0.8993, -0.9093, -0.3768, -0.1862, -0.1547, -0.0599, -0.055, -0.025, -0.0171, -0.0052, -0.005 , -0.0015, -0.0014, -0.0017, -0.0024, -0.0003, -0.3333, -0.00002, -0.6666. -1 -0.5555	0.2802

3DOF-TIDN	-0.1007, -3.334, -999.9993, -0.0585, -111.086, ±999.9992i, ±123.245i , -0.7322, 0.4594, 2.216, 0.7791, -0.1424, -0.1629, -0.160417, -0.0604, -3.1729, -12.3396i, -12.3396, -0.1599, -63.6463, -12.3404, -0.1887, -0.1852, -0.1732, -0.0181, -0.5409, -2.3762, -8.8206, -30.920, ±389.8564i, ±1110.9211i, ±432.5509i, ±999.2098i, ±1110.32i, ±1110.3211i, -420.266, -200.2536, -119.1269, -34.3189, -38.5491, -33.4196, -24.3203, -9.9126, -7.7456, 8.0806, -10.6124, -10.1046, -2.7405, -1.6172, -1.262, -2.1127, -1.9085, -0.2004, -0.9971, 0.0067, 1.2715, -0.5371, -0.0046, -0.186, -0.2175, ±0.3123i, -0.5083, -0.5383, -0.6764, -0.6883, -0.6885, -0.692, -0.6921, -0.6918, -0.6499, -0.0087, -0.3243, -0.00898, -0.6666, -1, -0.5555	0.4025
3DOF-FOPIDN	-0.42, -2.4833, -9.65, -0.451, -1.3243, -12.46, -1000.0449, -123.2907, -0.6865, -0.5051, -2.0702, -0.6333, -0.0034, -0.0171, -0.014617, -0.0854, -3.3187, -12.4854, -12.4854, -0.0141, -63.7921, -12.4854, -0.0437, -0.0402, -0.0282, -0.1631, -0.6859, -2.5212, -8.9656, -31.06522, -390.0014, -1111.0661, ±432.6959i, ±999.9548i, ±1111.0662i, ±1111.0661i, -421.011, ±200.9986i, ±119.8719i, -35.0639, -39.2941, -34.1646, -25.0653, -10.6286, -7.0296, -8.7966, ±9.8964i, -9.3886, -2.0245, -0.9012, -1.978, -2.5694, -2.3652, -0.2563, -1.4538, -0.45, -0.8148, -0.9938, -0.4613, -0.2707, -0.2392, -0.1444, -0.1395, -0.1095, -0.0286, -0.0405, -0.0407, -0.0442, -0.0443, -0.044, -0.0021, -0.0042, -0.3288, -0.00448, -0.6666, -1, --0.5555	0.4824

Upon analyzing the obtained eigenvalues, it was observed that the uncontrolled system had some eigenvalues in the right half of the s-plane, indicating instability. For the PID controllers, some of the eigenvalues were zero along with negative real parts, indicating marginal stability. However, it was observed from Figure 6.44 that the PID controllers resulted in initial system oscillations, but the system reached its steady-state value after some time. On the other hand, for the 3DOF-TIDN and 3DOF-FOPIDN controllers, all eigenvalues had negative real parts, indicating system stability. The damping ratio of the 3DOF-TIDN controller was found to be higher than others, indicating that the system oscillation will sustain for less time with this controller. Based on this analysis, it can be concluded that the 3DOF-FOPIDN controller provides more stable performance compared to the other controllers considered in the study.
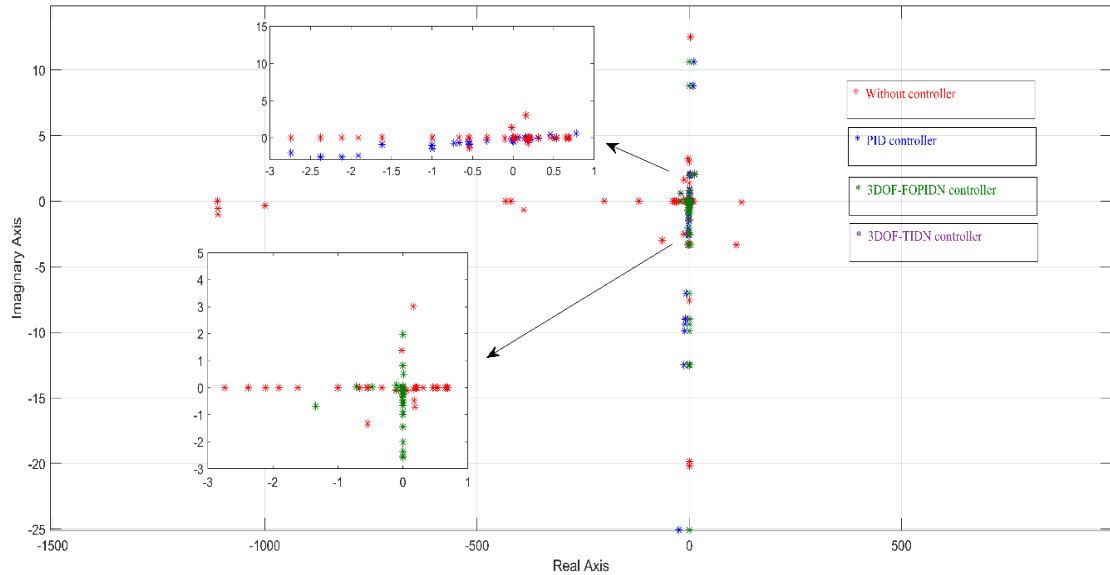
Figure 6.44. Comparison of Eigen value plot for proposed controllers

6.6.2 Robustness analysis

Robustness analysis is a method used to evaluate the ability of a system, process, or product to maintain its performance even in the presence of uncertainties or changes in its operating conditions or environment. This analysis involves subjecting the system to different scenarios or inputs and analyzing its response to assess its performance. The objective of robustness analysis is to determine the system's resilience and adaptability to various conditions and to identify the sources of variability and uncertainty that affect its performance.

The given passage describes a sensitivity analysis conducted to assess the robustness of a proposed 3DOF-FOPIDN controller by considering various scenarios and uncertainties. The analysis involves changing the values of different parameters within the system, such as varying the output of Wind, changing the system loading from the nominal scenario, and disconnecting one of the microgrid area. The results of the analysis are presented in Table 6.6, which shows the optimum gains and other parameters of the proposed controller under different uncertainties. The system dynamics are then compared by considering the gain values of the 3DOF-FOPIDN controller corresponding to different conditions and their responses under nominal conditions.

Table 6.6 Optimum values of 3DOF-FOPIDN controllers at different system conditions and system parameters.

Optimum	Variation in Wind	-25% System loading	+25% System loading	Disconnecting Solar in Area 1
K_{tx1}	1.6142	1.3254	3.1254	0.3216
K_{tx2}	0.4876	3.0802	2.8092	3.1842
K_{tx3}	0.3548	3.1245	2.3265	1.2874
K_{ix1}	1.1457	1.7621	1.4614	2.8241
K_{ix2}	0.3687	1.3548	1.3259	0.6542
K_{ix3}	0.1358	1.3258	0.1234	0.3246
K_{dx1}	0.1358	2.4824	1.6324	1.4632
K_{dx2}	1.3547	2.1546	2.3458	1.9753
K_{dx3}	1.1548	1.3254	2.3178	1.3246
$B1$	0.4248	0.0278	0.0628	0.0468
$B2$	0.3485	0.3254	0.0032	0.3256
$B3$	0.1466	0.3246	0.3648	0.0024
$C1$	1.0328	0.3246	0.0426	0.4328
$C2$	2.1789	1.2334	1.3249	3.2165
$C3$	1.8462	0.3289	2.1323	3.1247
g_x	2.4275	0.4576	0.3458	0.2458
N_{tf1}	145.6289	185.6189	136.1289	15.5263
N_{tf2}	102.0482	87.6142	186.6312	112.2382
N_{tf3}	164.6289	176.8064	184.8623	45.1094

Table 6.6 presents the optimum gains and other parameters for the 3DOF-FOPIDN controller based on the results of the sensitivity analysis. To compare the system dynamics, the gain values of the 3DOF-FOPIDN controller obtained under nominal conditions are used to generate responses for different scenarios. These responses are then compared to those obtained under changed conditions, as shown in Figures 6.50, and 6.51. Overall, the sensitivity analysis involves six dynamic responses to assess the robustness of the 3DOF-FOPIDN controller.

The system encountered a variation in its output, which increased from 0.006 p.u.MW to 0.012 p.u.MW. The gains and other parameters of the proposed 3DOF-FOPIDN controller, taking into account various uncertainties, are listed in Table 6.6.

To assess the controller's robustness, its performance under the changed conditions is compared to its response under nominal conditions, using the gain values obtained from both scenarios. The resulting dynamic responses are presented in the below Figures.

6.6.2.1 Varying load of the system

In this particular case, the system's loading was intentionally increased by 25% from its nominal value of 50% to examine the robustness of the controller's gain values obtained under nominal conditions. Table 6.6 lists the gains and other parameters of the proposed 3DOF-FOPIDN controller for different loading conditions. To assess the controller's robustness, its performance under the changed conditions is compared to its response under nominal conditions, using the gain values obtained from both scenarios. The resulting dynamic responses are presented Figure 6.47, 6.48 and 6.49.

6.6.2.2 Varying Wind in area -2

To evaluate the robustness of the proposed controller's gain values obtained at the nominal condition, the wind turbine in area-2 were disconnected, while considering the system loading and power generation in all areas. The gains and other parameters of the proposed 3DOF-FOPIDN controller in this scenario are shown in Table 6.6. To validate the controller's robustness, the system dynamics were compared using the gain values of the 3DOF-FOPIDN controller corresponding to changed conditions with the responses obtained under nominal conditions. The total power generation microgrid in area-2 is depicted in Figure 6.45 and 6.46.
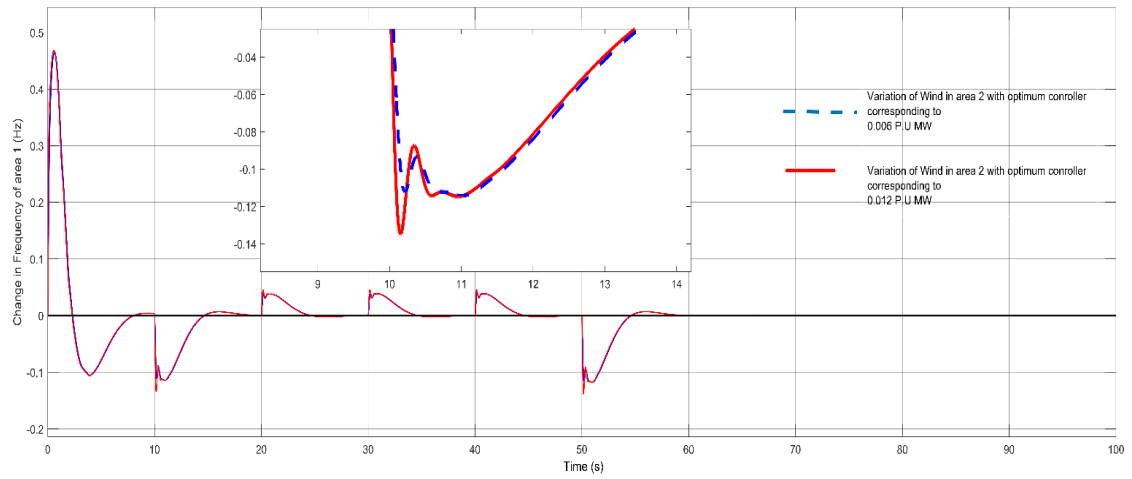
Figure 6.45. variation in wind turbine output considering frequency of area 1
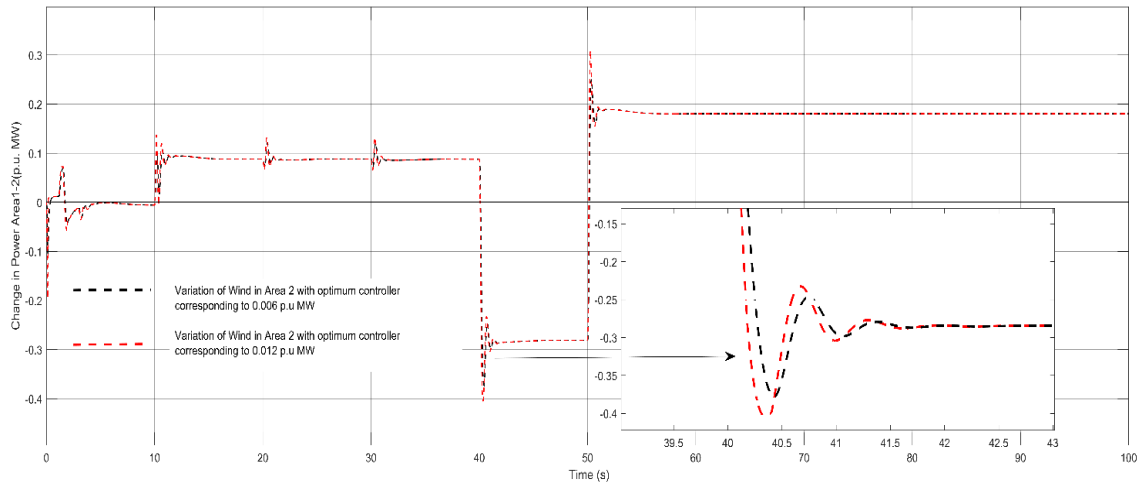
Figure 6.46. variation in wind output considering change in power of area 1&2
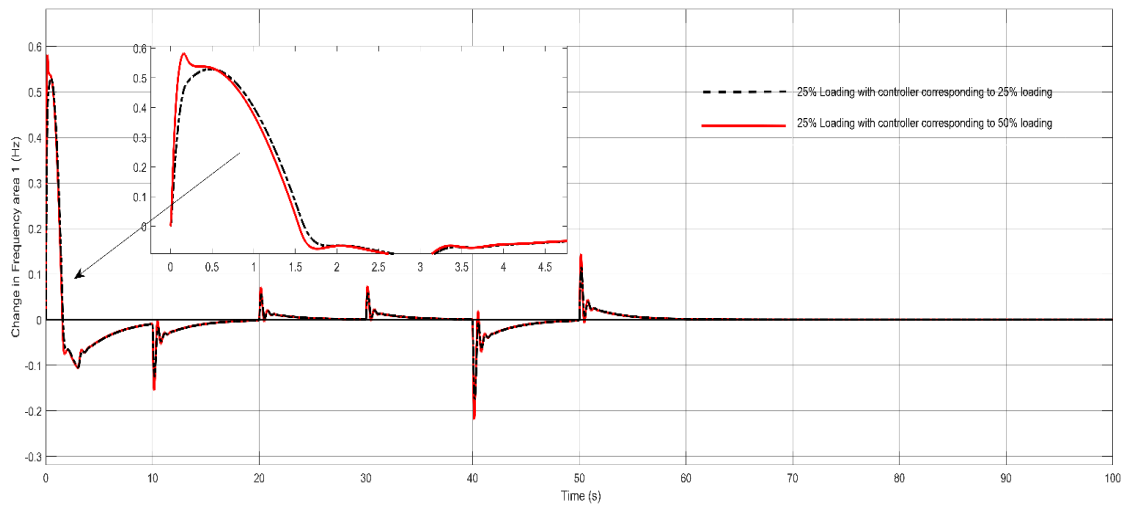
Figure 6.47 Robustness under different loading frequency area 1
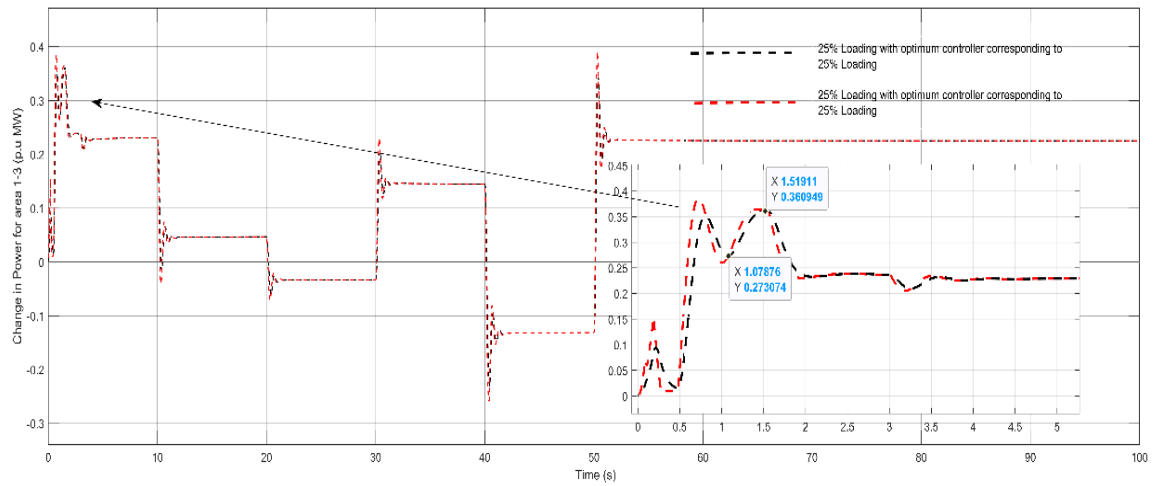
Figure 6.48 Robustness under different loading power area 1-3.
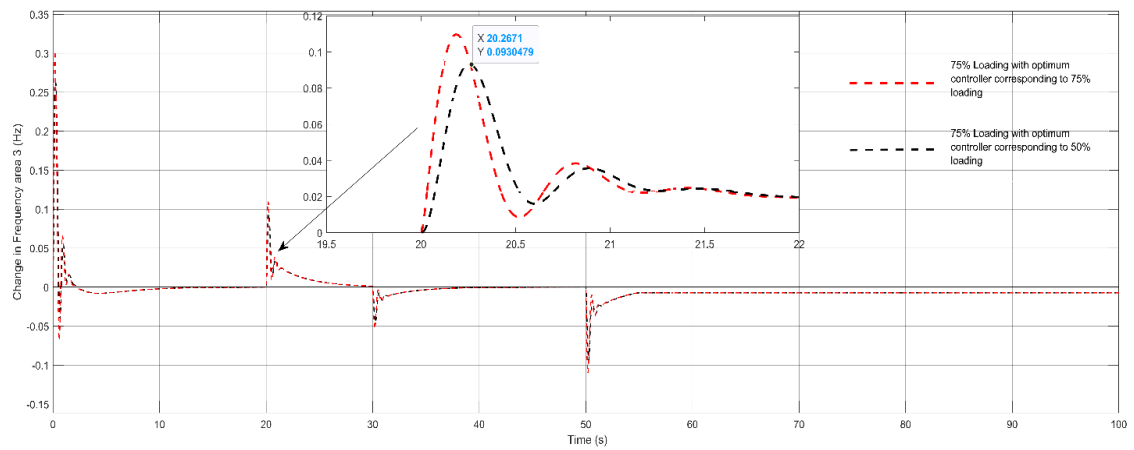
Figure 6.49 Robustness under different loading (75% and 50%)frequency area 3
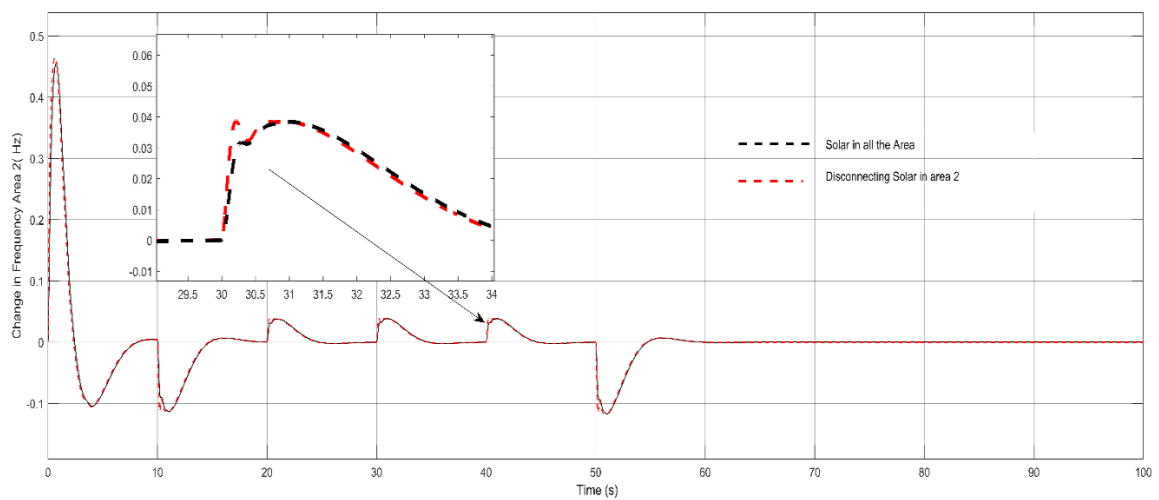
Figure 6.50 Robustness frequency without solar in area 2.
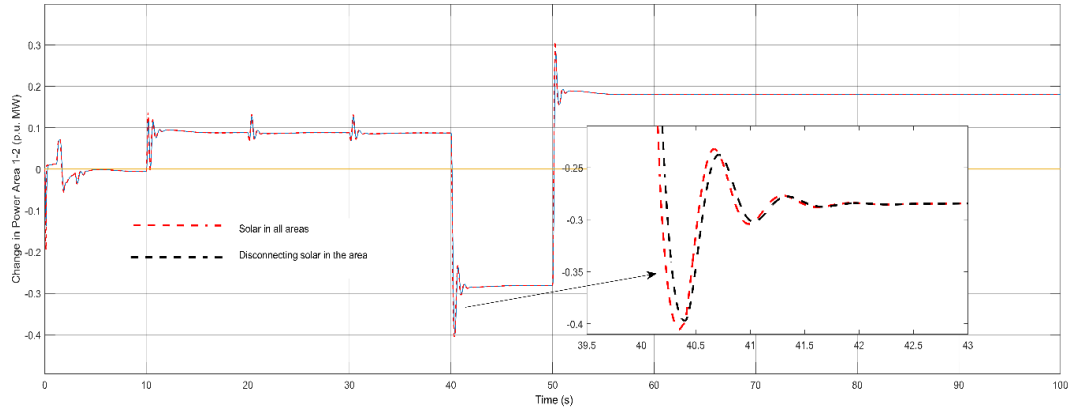
Figure 6.51 Robustness Power without solar in area 2

6.7. Conclusion

This chapter introduces a novel approach to controlling frequency deviation in a multi-microgrid system with RES and DEG, taking into consideration the power supply of a WTP with various pumping and power stations. The proposed system incorporates different energy sources such as DEG, SPV, WTG, and BESS as power sources for each area of the microgrid system. To enhance the performance of the PID controller, the tuning parameters are optimally selected using the EHHO method. The performance of the proposed controller is then compared to existing techniques, such as PSO and GWO, using MATLAB software. Load demand and frequency are used to analyze and evaluate the performance of the proposed controller. The results show that the proposed EHHO-based PID controller effectively regulates the load frequency deviation in a RES-based multi-microgrid system. In comparison to PSO and GWO, the proposed controller outperforms these existing techniques, demonstrating better performance for controlling load frequency deviation.

The study includes the design of an optimal control approach using a 3DOF-FOPIDN secondary controller based on PSO algorithm to improve system dynamic performance. The results indicate that the 3DOF-FOPIDN controller outperforms other secondary controllers viz. 3DOF-TIDN in reducing oscillations, settling time of frequency, and tie power deviation. Finally, the study shows that the 3DOF-FOPIDN controller is robust enough to handle uncertain parametric variations, such as the absence of Solar, variation of wind speed, and varying system inertia, without needing repeated resetting of controller parameters.

Chapter

7

Conclusion

7.1 Introduction

Existing literature and studies in the field of WTP have primarily focused on WWTPs and improvements related to water quality and quantity in the treatment process. However, there is a significant lack of research specifically addressing conventional WTPs, particularly those employing SCADA-based systems with a focus on self-energy sufficiency. Therefore, the concept of microgrid-based WTP has emerged as a potential game changer in the current scenario, with the potential for significant improvements in the efficiency and sustainability of water treatment processes. Studies have shown that SCADA systems can effectively enhance system efficiency, making research on their implementation in existing WTPs valuable in improving the quality and quantity of treatment parameters. Furthermore, the integration of renewable energy sources, such as solar, wind, and hydro, into existing WTPs to optimize power flow, improve efficiency, and minimize energy consumption costs requires a comprehensive feasibility study to accurately assess the cost constraints and technical barriers associated with their implementation.

Several analyses and studies have explored the potential of utilizing advanced control schemes, such as droop control and LFC, with state-of-the-art optimization techniques and AI-based systems to enhance the performance of WTPs. Conducting real-time tests of implementing droop control using AI, such as ANFIS, in the intake process of a WTP, can provide valuable insights into the performance of such advanced control schemes compared to conventional control approaches. Additionally, addressing the challenges of LFC in conventional systems, particularly

when considering existing plants that may require cascaded and higher degree controllers for effective control, is essential. Furthermore, exploring the potential of utilizing Enhanced Harris Hawks optimization techniques in the context of multi-area microgrid systems for LFC can provide new insights into the effectiveness of this technique compared to conventional optimization techniques.

Moreover, the study aims to improve the monitoring system in GAWSS P-I&II by implementing SCADA control and management while addressing its current limitations. Additionally, the study highlights the importance of a microgrid-based system to address the challenges faced in the WTP, such as high energy consumption, interrupted power supply, and operational issues due to old equipment and hilly terrain.

The current SCADA system in phase I&II only allows for monitoring, but the study proposes an integrated SCADA system with energy management capabilities. By collecting data from devices, the SCADA system can optimize pump and backwash scheduling, leading to a more efficient plant process. The study recognizes the absence of renewable energy sources and the high cost of diesel engine operation due to frequent power interruptions. Implementing SCADA systems into WTPs would significantly improve the efficiency of overall water supply management, leading to reduced energy consumption and bills. The data collected from the SCADA system would be stored in local servers, enabling better management of the plant process.

However, several challenges exist in the operation and maintenance of the system under study. The remote and hilly location of the study region, coupled with limited internet connectivity, can lead to data loss due to internet and optical fiber issues. The system also requires skilled engineers and technically capable personnel to handle technical issues that may arise during operation and maintenance. Mitigating these challenges requires deploying proficient field staff, implementing GSM/GPRS modems, and improving internet connectivity. Developing online web-based and mobile applications could provide a platform for remote monitoring, enabling smart solutions and swift responses to any issues. By addressing these challenges, the reliability, efficiency, and longevity of the equipment can be improved, further enhancing the water supply system.

An analysis of an existing WTP using ETAP software to perform load flow, short circuit analysis, and relay coordination is also presented in the study. The analysis report includes data from all power substations, loads, and transmission systems. The report shows that the system has the potential for improvement, especially in the absence of proper analysis and plan for renewable energy source installation. The relay coordination problem in a radial network is a challenging optimization issue, and the report's technique is based on industrial guidelines and IEEE publications. The use of static variable compensators and current limiting reactors improves the load flow and short circuit analysis results. The report also includes analysis with and without renewable energy sources such as solar, under consideration of the Microgrid concept.

The study aims to evaluate the ANFIS-based droop control technique in a microgrid system operating under different loading conditions, in comparison to the conventional droop control technique using GDC. The ANFIS technique is successfully trained for both P-F and Q-V droop cases and is employed to address issues related to transient behavior during switching and power sharing between the source and load in grid connected and islanded modes of operation. The battery system compensates for power sharing between the source and load as different loads change. The simulation results demonstrate successful ANFIS training and improved performance of the controller units for both P-F and Q-V droop.

The stability of frequency and voltage is essential in a microgrid system, and the proposed ANFIS-based droop controller shows promising results in regulating these aspects of the intake microgrid system. The batteries play a crucial role in balancing real and reactive power in case of frequency and voltage imbalances. The ANFIS-based droop control technique can have applications beyond the WTP-based intake microgrids and be used to address various issues faced by WTPs, such as high operational costs, power-related issues, and frequent maintenance. Moreover, this approach can be applied to other treatment plants, such as waste water treatment and sewage treatment.

A new approach to controlling frequency deviation in a multi-microgrid system with renewable energy sources (RES) and distributed energy generation was also presented and discussed. Where the system includes a WTP with multiple pumping

and power stations, and different energy sources such as DEG, SPV, WTG, and BESS are used to power each area of the microgrid. The proposed system uses the EHHO method to optimally select tuning parameters for a PID controller, which is then compared to existing techniques such as PSO and GWO using MATLAB software. Load demand and frequency are used to evaluate the performance of the proposed controller, and the results show that it effectively regulates load frequency deviation and outperforms PSO and GWO.

The study also includes the design of an optimal control approach using a 3DOF-FOPIDN secondary controller based on the PSO algorithm to improve system dynamic performance. The results demonstrate that the 3DOF-FOPIDN controller performs better than other secondary controllers such as 3DOF-TIDN in reducing oscillations, settling time of frequency, and tie power deviation. Additionally, the 3DOF-FOPIDN controller is robust enough to handle uncertain parametric variations, such as the absence of solar, variation of wind speed, and varying system inertia, without requiring repeated resetting of controller parameters.

7.2. Future scope

Investigating the integration of multiple microgrids with different energy sources and loads, and developing optimal control strategies to ensure efficient operation and stability of the overall system.

Further exploration of the economic and environmental benefits of microgrid systems, particularly in comparison to traditional grid systems. This could include evaluating the potential for microgrid systems to reduce greenhouse gas emissions and improve energy security.

Investigating the potential application of microgrid systems in other fields, such as wastewater treatment and sewage treatment, to address issues related to high operational costs, power-related issues, and frequent maintenance.

Integration of Artificial Intelligence (AI) and Machine Learning (ML) algorithms to enhance the control and management of the SCADA system. This could include using predictive analytics to anticipate system failures or optimize energy consumption.

Further investigation into the optimal sizing and placement of renewable energy sources in the microgrid system. This could involve exploring the use of advanced optimization techniques, such as genetic algorithms or particle swarm optimization.

Developing more sophisticated secondary control strategies, such as 3DOF-FOPIDN and latest techniques to further improve the dynamic performance of microgrid systems, especially in situations where there are parametric uncertainties

Investigation into the use of new energy storage technologies, such as solid-state batteries or flow batteries, to improve the performance and efficiency of the microgrid system.

Overall, future research in this area has the potential to contribute to the development of more efficient and reliable microgrid systems, which can help address various energy-related challenges and contribute to sustainable development

Appendices

APPENDIX -A (Chapter 2)

1. SCADA operational description at WTP in Phase III

Sl. No	Equipment Description	Live Valve	Remote Monitoring	Report	Interlock
			WTP		
1	LT Motors	-	Start	-	LT Motors Interlock with Level & Pressure Transmitter.
			Stop		
			ON		
			OFF		
			Trip		
2	Electrical Actuators	-	Start	-	Electrical Actuators Interlock with Loss of Head & Motors
			Stop		
			OPEN		
			CLOSE		
			Trip		
3	600KVA,415V DG SET	Current	Start	Fuel Consumption & Operating Hours will recorded in SCADA	LV DG Set Interlock with LT EB Incomming Power
		Voltage	Stop		
		KW	ON		
		KWH	OFF		
		PF	Trip		
		KVA			
		Battery Voltage			
		Lube Oil Temperature & Pressure			
		Engine RPM			
		Operating Hours			
4	500KVA LT Transformer	Winding Temperature	-	-	No Interlock. Monitoring Only
		Oil Temperature			
5	Centrifuge VFD Drive-A/B	Motor RPM	Start	-	Centrifuge Motors Interlock with Level Transmitter.
		Frequency	Stop		
			ON		
			OFF		
			Trip		
6	Inlet Open Chanel Flow Meter	Current Flow	-	Daily Cumulative flow will recorded in SCADA	No Interlock. Monitoring Only
		Total Flow			
7	Airblower Common Head Flow Meter	Current Flow	-	-	No Interlock. Monitoring Only
		Total Flow			
8	Wash Water Pump Flow Meter	Current Flow	-	Daily Cumulative flow will recorded in SCADA	No Interlock. Monitoring Only
		Total Flow			
9	Recycling Transfer Pump Flow Meter	Current Flow	-	Daily Cumulative flow will recorded in SCADA	No Interlock. Monitoring Only
		Total Flow			
10		Current Flow	-		

	Rate of Flow Meter at Filterbed	Total Flow		Daily Cumulative flow will recorded in SCADA	Rate of flow interlock with filterbed Actuators.
11	Raw Water pH Meter	Current pH	-	Daily pH Value will recorded in SCADA	No Interlock. Monitoring Only
12	Treated Water pH Meter	Current pH	-	Daily pH Value will recorded in SCADA	No Interlock. Monitoring Only
13	Raw Water Turbidity Meter	Current Turbidity Value	-	Daily Turbidity Value will recorded in SCADA	No Interlock. Monitoring Only
14	Treated Water Turbidity Meter	Current Turbidity Value	-	Daily Turbidity Value will recorded in SCADA	No Interlock. Monitoring Only
15	Treated Water Chlorine Analyzer Meter	Current Chlorine Value	-	Daily Chlorine Value will recorded in SCADA	Chlorine Analyser interlock with Dosing Pump
16	Sludge Disposal Pump Common Head Pressure Transmitter	Current Pressure Value	-	-	Pressure Transmitter Interlock with Motors
17	Wash Water Pump common Head Pressure Transmitter	Current Pressure Value	-	-	Pressure Transmitter Interlock with Motors
18	Recycling Transfer Pump common head Pressure Transmitter	Current Pressure Value	-	-	Pressure Transmitter Interlock with Motors
19	Over Head tank Level Transmitter	Current Level Value	-		Level Transmitter Interlock with Motors
20	BWWRS Level Transmitter	Current Level Value	-	-	Level Transmitter Interlock with Motors
21	Loss of Head Transmitter at Filter bed	Current Level Value	-	-	Loss of Head Transmitter interlock with filter bed Actuators
22	Dosing Tank Level Switch	-	Tank LOW	-	Dosing tank Level switch interlock with dosing pump & Agitators
			Tank HIGH		

2. SCADA operational description of Clear water pump house I

Sl. No	Equipment Description	Live Value	Remote Monitoring	Report	Interlock
		CLEAR WATER PUMP HOUSE-01			
1	Clear water Transfer Pump-A/B	Current	Start	Operating Hours will recorded in SCADA	CWPH-01 Interlock with CWPH-01 Tank level & Pressure Transmitter.
		Voltage	Stop		
		Frequency	ON		
		Bearing Temperature	OFF		
		Winding Temperature	Trip		
		Running Hours			
2	1475HP Diesel Engine-A/B	Current	Start	Fuel Consumption & Operating Hours will recorded in SCADA	Engine Drive Interlock with CWPH-01 Tank level & Pressure Transmitter& Motor Winding & Bearing Temperature.
		Voltage	Stop		
		KW	ON		
		KWH	OFF		
		PF	Trip		
		KVA			
		Battery Voltage			
		Lube Oil Temperature & Pressure			
		Engine RPM			
		Operating Hours			
3	LT Motors	-	Start	-	LT Motors Interlock with Level & Pressure Transmitter.
			Stop		
			ON		
			OFF		
			Trip		
4	Electrical Actuators	-	Start	-	Electrical Actuators Interlock with HT Motor & Engine
			Stop		
			OPEN		
			CLOSE		
			Trip		
6	HT Panel	Current	Start	-	HT Panel Interlock with Motor Bearing & Winding Temperature.
		Voltage	Stop		
		KW	ON		
		KWH	OFF		
		PF	Trip		
		KVA			
7	Level Transmitter	Current Level Height	-	-	Level Transmitter Interlock with Motor.
8	Flow Meter	Current Flow	-	Daily Cumulative flow will recorded in SCADA	No Interlock. Monitoring Only

3. GAWSS P-III SCADA Screen

WTP Screen	WTP filter bed Screen
CWPH-1 Screen	Electro chlorination system
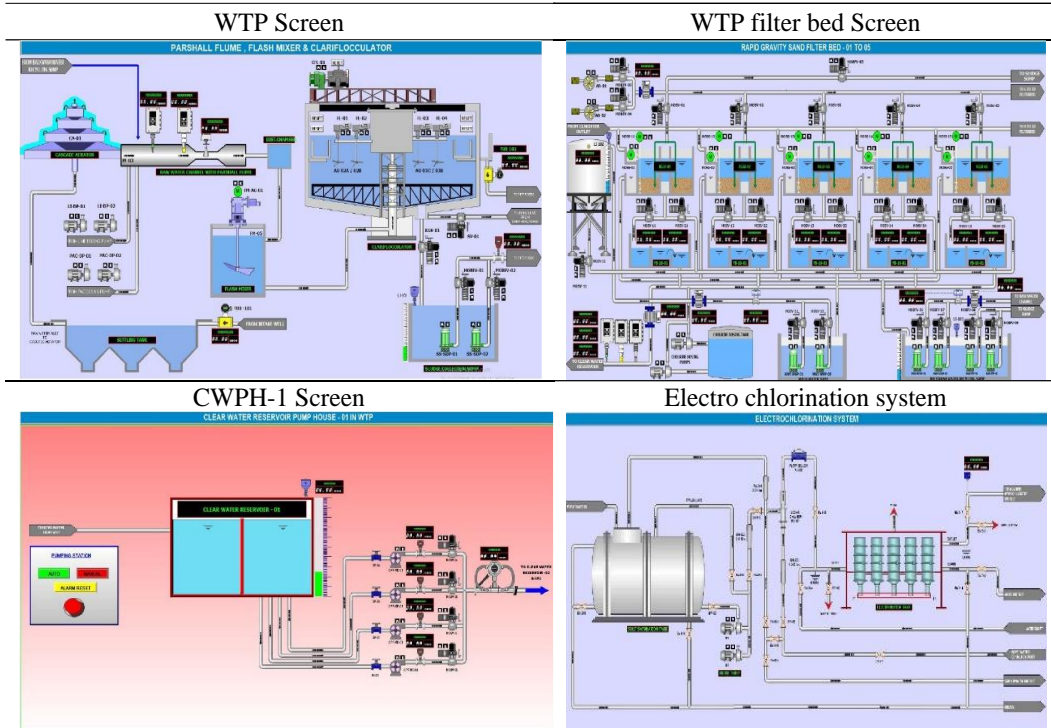
4. Field Equipment at GAWSS P-I&II

Digital energy meter	PLC, HMI and UPS system	Transmitter
Electromagnetic flow meter	Pressure Transmitter	Level meter
Pressure Transmitter at Phase II	Open channel flow meter at Filter house	

APPENDIX -B (Chapter 3)

1. pH sensor description

Sl. No.	Data of pH Sensor for Intake	Type/ Range
1	Measuring principle	Glass Electrode
2	Measuring range	0 to 14
3	Measuring Temperature	5 C to 80 C
4	Process Pressure	5 to 10 kg/cm2

2. Turbidity sensor description

Sl. No.	Data of Turbidity Sensor	Type/ Range
1	Measuring principle	Four beam alternating light
2	Design	40 mm sensor
3	Measuring range	1000 NTU
4	Measuring Temperature	5 C to 80 C
5	Process Pressure	0 to 20 kg/cm^2

3. Conductivity sensor description

Sl. No.	Data of conductivity Sensor	Type/ Range
1	Measuring principle	Graphite electrode
2	Design	Two electrode system
3	Measuring range	K=1:10 ms/cm to 80 ms/cm
4	Measuring Temperature	-20 C to 135 C
5	Process Pressure	246 i

4. Flow meter description

Sl. No.	Data of flow meter	Type/ Range
1	Measuring principle	Electromagnetic
2	Measured Variable	Volume flow, conductivity, mass flow
3	Nominal Flow Range (m^3/hr)	560 (5 n.o.); 500 (6 n.o.); 150 (1 n.o.); 130 (1 n.o.); 255 (6 n.o.) ; 280 (6 n.o.)
4	Protection	IP 68
5	Accuracy	+/- 0.025%
6	Process Pressure	1000 psi

5. Pressure transmitter description

Sl. No.	Data of pressure Transmitter	Type/ Range
1	Measuring principle	Diaphragm
2	Accuracy	+/- 0.075
3	Measuring range	8 kg/cm^2 to 90 kg/cm^2
4	Measuring Temperature	10 C to 50 C
5	Main welded part	SS 316 L

6. Level meter description

Sl. No.	Data of pressure Transmitter	Type/ Range
1	Measuring principle	Ultrasonic
2	Accuracy	+/- 0.025
3	Measuring range	0.5 m to 5 m
4	Measuring Temperature	-10 C to 80 C
5	Process pressure	Atmospheric
6	Output Ampere	4 to 20 mA

APPENDIX -C (Chapter 4)

1. **33 kV Substation layout of phase III power supply**
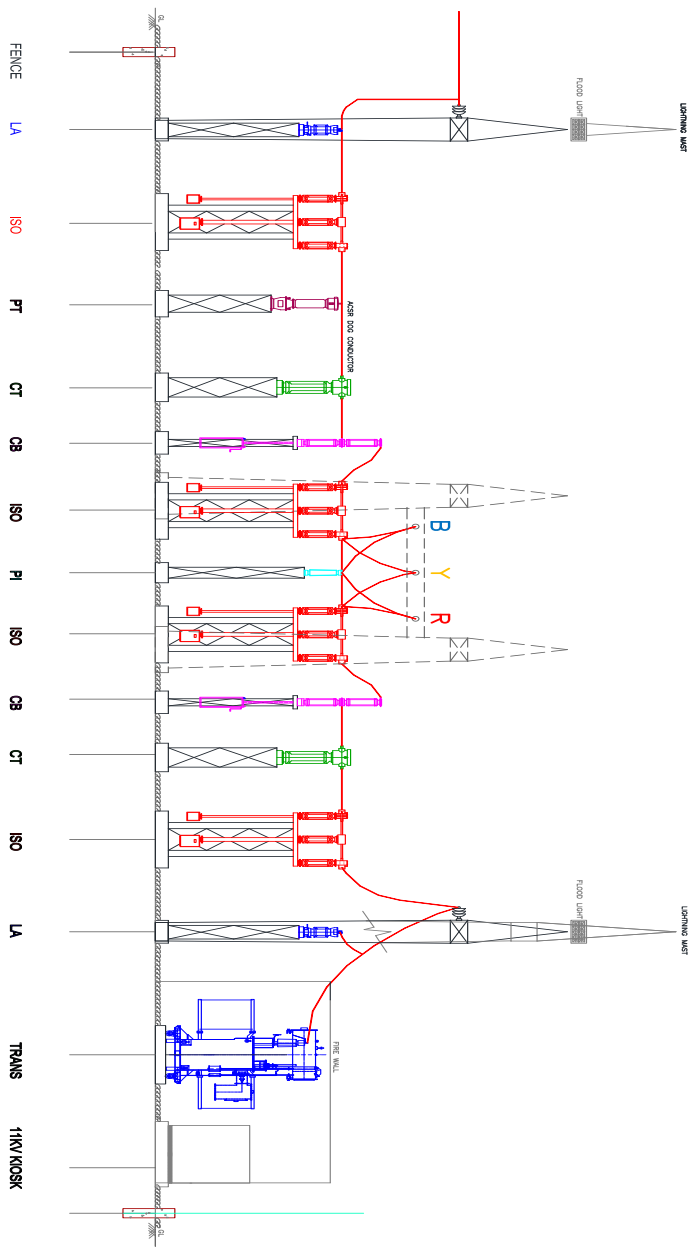
2. SLD of 33 kV Switchyard of Phase III power supply
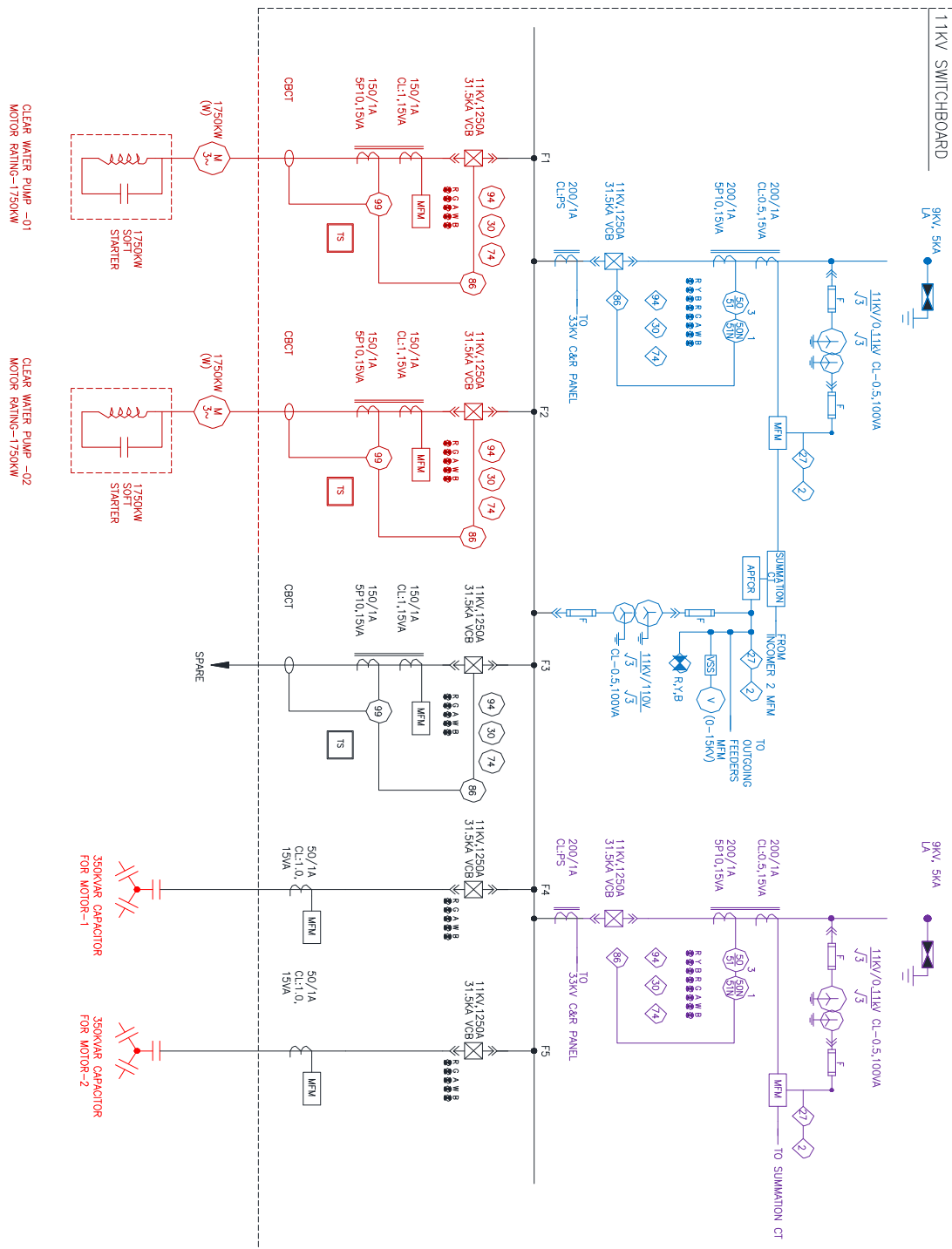
3. SLD of LT MPCC panel of phase III power supply
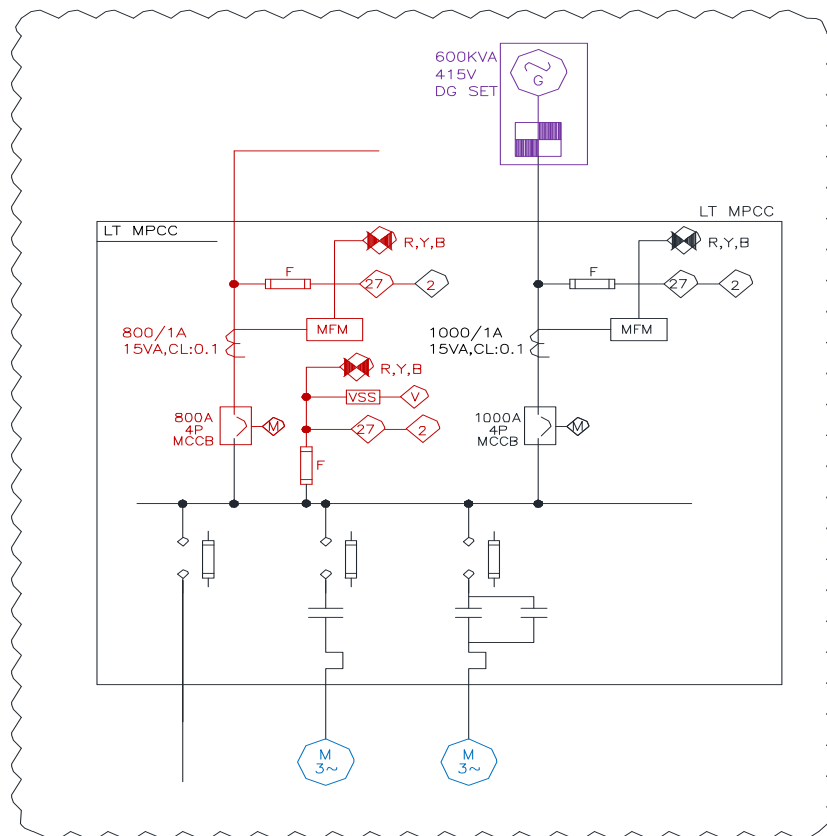
4. Load Flow Analysis case I table

Bus	Voltage			Generation		Load		Load Flow				
ID	kV	%Mag.	Ang.	MW	Mvar	MW	Mvar	ID	MW	Mvar	Amp	%PF
CM-VT-01-B1	11.0	99.170	-1.4	0.000	0.000	0.000	-0.14	RWITPH	0.000	0.148	7.8	0.0
CM-VT-02-B4	11.0	99.169	-1.4	0.000	0.000	0.000	-0.14	RWITPH	0.000	0.148	7.8	0.0
CM-VT-03-B7	11.0	99.169	-1.4	0.000	0.000	0.000	-0.14	RWITPH	0.000	0.148	7.8	0.0
CM1-B1	11.0	98.089	-2.2	0.000	0.000	0.000	-0.39	CWPH-2	0.000	0.399	21.4	0.0
CM1-B4	11.0	98.394	-2.0	0.000	0.000	0.000	-0.33	CWPH -1	0.000	0.339	18.1	0.0
CM2- B5	11.0	98.394	-2.0	0.000	0.000	0.000	-0.33	CWPH -1	0.000	0.339	18.1	0.0
CM2-B5	11.0	98.089	-2.2	0.000	0.000	0.000	-0.39	CWPH-2	0.000	0.399	21.4	0.0
CWP1- B1	11.0	98.391	-2.0	0.000	0.000	1.850	0.998	CWPH -1	-1.85	-0.99	112.1	88.0
CWP1-B1	11.0	98.085	-2.2	0.000	0.000	1.945	1.102	CWPH-2	-1.94	-1.10	119.7	87.0
CWP2-B1	11.0	98.391	-2.0	0.000	0.000	1.850	0.998	CWPH -1	-1.85	-0.99	112.1	88.0
CWP2-B2	11.0	98.085	-2.2	0.000	0.000	1.945	1.102	CWPH-2	-1.94	-1.10	119.7	87.0
CWPH -1	11.0	98.394	-2.0	0.000	0.000	0.000	0.000	CM1-B4	0.000	-0.33	18.1	0.0

							CM2- B5	0.000	-0.33	18.1	0.0
							CWP1- B1	1.850	0.998	112.1	88.0
							CWP2-B1	1.850	0.998	112.1	88.0
							CWPH I/C1-B	-3.70	-1.31	209.5	94.2
CWPH I/C1-B	11.0	98.416	-2.0	0.0	0.0	0.0	0.0	CWPH -1	3.701	1.315	209.4	94.2
								CWPH1-B2	-3.7	-1.31	209.4	94.2
CWPH-2	11.0	98.088	-2.2	0.0	0.0	0.0	0.0	CM1-B1	0.000	-0.40	21.4	0.0
							CM2-B5	0.000	-0.40	21.4	0.0
							CWP1-B1	1.945	1.102	119.6	87.0
							CWP2-B2	1.945	1.102	119.6	87.0
							CWPH2 I/C1- B	-3.89	-1.40	221.4	94.1
* CWPH-PV I/C- B1	0.415	100.0	0.0	0.0	0.0	0.0	0.0	CWPH-PV I/C- B2	0.000	0.000	0.0	0.0
CWPH-PV I/C- B2	0.415	100.0	0.0	0.0	0.0	0.0	0.0	CWPH-PV I/C- B1	0.000	0.000	0.0	0.0
* CWPH-PV I/C-B3	0.415	100.0	0.0	0.0	0.0	0.0	0.0	CWPH-PV I/C-B4	0.000	0.000	0.0	0.0
CWPH-PV I/C-B4	0.415	100.0	0.0	0.0	0.0	0.0	0.0	CWPH-PV I/C-B3	0.000	0.000	0.0	0.0
CWPH1-B2	33.0	99.9	0.0	0.0	0.0	0.0	0.0	WTP-1	-3.71	-1.46	69.8	93.0
							CWPH I/C1-B	3.711	1.467	69.8	93.0
CWPH2 I/C1- B	11.0	98.1	-2.2	0.000	0.000	0.000	0.0	CWPH-2	3.89	1.402	221.3	94.1
							IPSA T/F-1 IC-B1	-3.89	-1.40	221.3	94.1

CWPH2 I/C2- B	11.0	99.8	-0.1	0.0	0.0	0.0	0.0	IPSA T/F-2 IC-C1~	0.00	-0.05	0.3	0.0
							IPSA T/F-2 IC-B2	0.00	0.005	0.3	0.0
* I/C1- B	33.0	100.0	0.0	4.897	1.771	0.0	0.0	WTP-1	4.897	1.771	91.1	94.0
* I/C2-B	33.0	100.0	0.0	3.909	1.084	0.0	0.0	WTP-2	3.909	1.084	71.0	96.4
IPSA T/F-1 IC-B1	33.0	99.80	-0.1	0.0	0.0	0.0	0.0	IPSA.	-3.90	-1.57	73.8	92.8
							CWPH2 I/C1- B	3.904	1.571	73.8	92.8
IPSA T/F-2 IC-B2	33.0	99.87	-0.1	0.0	0.0	0.0	0.0	IPSA.	0.000	0.005	0.1	0.0
							CWPH2 I/C2- B	0.000	-0.05	0.1	0.0
IPSA.	33.0	99.80	-0.1	0.0	0.0	0.0	0.0	IPSA T/F-1 IC-B1	3.904	1.564	73.7	92.8
							IPSA T/F-2 IC-B2	0.000	-0.11	0.2	0.0
							WTP-2	-3.90	-1.53	73.6	92.9

Bus ID	kV	% Mag.	Ang.	Gen MW	Gen Mvar	Load MW	Load Mvar	Load Flow ID	MW	Mvar	Amp	%PF
RWITPH	11.0	99.18	-1.4	0.0	0.0	0.0	0.0	CM-VT-01-B1	0.000	-0.15	7.9	0.0
								CM-VT-02-B4	0.000	-0.14	7.8	0.0
								CM-VT-03-B7	0.000	-0.18	7.8	0.0
								RWP-VT1-B2	0.591	0.366	36.8	85.0
								RWP-VT2-B3	0.591	0.366	36.8	85.0
								RWP-VT3-B5	0.000	0.000	0.0	0.0
								RWPH-I/C1-B	-1.18	-0.28	64.4	97.2
RWP-VT1-B2	11.0	99.6	-1.4	0.0	0.0	0.591	0.367	RWITPH	-0.59	-0.37	36.8	85.0
RWP-VT2-B3	11.0	99.6	-1.4	0.0	0.0	0.591	0.367	RWITPH	-0.59	-0.37	36.8	85.0
RWP-VT3-B5	11.0	99.8	-1.4	0.0	0.0	0.0	0.0	RWITPH	0.000	0.000	0.0	0.0
RWPH-B1	33.0	99.9	0.0	0.0	0.0	0.0	0.0	WTP-1	-1.16	-0.16	21.5	96.6
								RWPH-I/C1-B	1.186	0.316	21.5	96.6
* RWPH-DG I/C- B	11.0	100.0	0.0	0.0	-0.001	0.000	0.0	RWPH-DG I/C- C~	0.000	-0.01	0.1	0.0
RWPH-I/C1-B	11.0	99.3	-1.4	0.0	0.0	0.000	0.0	RWITPH	1.183	0.285	64.4	97.2
								RWPH-B1	-1.18	-0.28	64.4	97.2
WTP-1	33.0	99.9	0.0	0.0	0.0	0.0	0.0	CWPH1-B2	3.711	1.460	69.8	93.1
								I/C1- B	-4.89	-1.77	91.1	94.0
								RWPH-B1	1.18	0.313	21.5	96.7
WTP-2	33.0	99.9	0.0	0.0	0.0	0.0	0.0	I/C2-B	-3.90	-1.086	71.0	96.4
								IPSA.	3.90	1.086	71.0	96.4
RWPH-DG I/C- C~	11.0	100.0	0.0	0.00	0.0	0.0	0.0	RWPH-DG I/C- B	0.000	0.000	0.0	0.0

5. Load Flow Analysis case 5

Bus		Voltage			Generation		Load		Load Flow				
ID		kV	% Mag.	Ang.	MW	Mvar	MW	Mvar	ID	MW	Mvar	Amp	%PF
CM-VT-01-B1		11.000	99.423	-1.4	0.000	0.000	0.000	-0.148	RWITPH	0.000	0.148	7.8	0.0
CM-VT-02-B4		11.000	99.422	-1.4	0.000	0.000	0.000	-0.148	RWITPH	0.000	0.148	7.8	0.0
CM-VT-03-B7		11.000	99.422	-1.4	0.000	0.000	0.000	-0.148	RWITPH	0.000	0.148	7.8	0.0

ID	kV	% Mag.	Ang.	MW	Mvar	MW	Mvar	ID	MW	Mvar	Amp	%PF
CM1-B1	11.000	98.089	-2.2	0.000	0.000	0.000	-0.399	CWPH-2	0.000	0.399	21.4	0.0
CM1-B4	11.000	98.430	-1.6	0.000	0.000	0.000	-0.339	CWPH -1	0.000	0.339	18.1	0.0
CM2- B5	11.000	98.430	-1.6	0.000	0.000	0.000	-0.339	CWPH -1	0.000	0.339	18.1	0.0
CM2-B5	11.000	98.089	-2.2	0.000	0.000	0.000	-0.399	CWPH-2	0.000	0.399	21.4	0.0
CWP1- B1	11.000	98.426	-1.6	0.000	0.000	1.850	0.998	CWPH -1	-1.850	-0.998	112.1	88.0
CWP1-B1	11.000	98.085	-2.2	0.000	0.000	1.945	1.102	CWPH-2	-1.945	-1.102	119.7	87.0
CWP2-B1	11.000	98.426	-1.6	0.000	0.000	1.850	0.998	CWPH -1	-1.850	-0.998	112.1	88.0
CWP2-B2	11.000	98.085	-2.2	0.000	0.000	1.945	1.102	CWPH-2	-1.945	-1.102	119.7	87.0
CWPH -1	11.000	98.429	-1.6	0.000	0.000	0.000	0.000	CM1-B4	0.000	-0.339	18.1	0.0
								CM2- B5	0.000	-0.339	18.1	0.0
								CWP1- B1	1.850	0.998	112.1	88.0
								CWP2-B1	1.850	0.998	112.1	88.0
								CWPH I/C1-B	-2.977	-1.359	174.5	91.0
								CWPH-PV I/C-	-0.723	0.041	38.6	-99.8
CWPH I/C1-B	11.000	98.448	-1.6	0.000	0.000	0.000	0.000	CWPH -1	2.978	1.356	174.4	91.0
								CWPH1- B2	-2.978	-1.356	174.4	91.0
CWPH-2	11.000	98.088	-2.2	0.000	0.000	0.000	0.000	CM1-B1	0.000	-0.400	21.4	0.0
								CM2-B5	0.000	-0.400	21.4	0.0
								CWP1-B1	1.945	1.102	119.6	87.0
								CWP2-B2	1.945	1.102	119.6	87.0
								CWPH2 I/C1-	-3.891	-1.405	221.4	94.1
* CWPH-PV I/C-	0.415	100.000	0.0	0.735	-0.022	0.000	0.000	CWPH-PV I/C-	0.735	-0.022	1023.1	-
CWPH-PV I/C- B2	0.415	98.472	-0.9	0.000	0.000	0.000	0.000	CWPH-PV I/C-	-0.723	0.033	1023.1	-99.9
								CWPH -1	0.723	-0.033	1023.1	-99.9
* CWPH-PV I/C-B3	0.415	100.000	0.0	0.000	0.000	0.000	0.000	CWPH-PV I/C-	0.000	0.000	0.0	0.0
CWPH-PV I/C-B4	0.415	100.000	0.0	0.000	0.000	0.000	0.000	CWPH-PV I/C-	0.000	0.000	0.0	0.0
CWPH1- B2	33.000	99.999	0.0	0.000	0.000	0.000	0.000	WTP-1	-2.985	-1.461	58.1	89.8
								CWPH I/C1-B	2.985	1.461	58.1	89.8

Bus		Voltage		Generation		Load		Load Flow				
ID	kV	% Mag.	Ang.	MW	Mvar	MW	Mvar	ID	MW	Mvar	Amp	%PF
CWPH2 I/C1- B	11.000	98.116	-2.2	0.000	0.000	0.000	0.000	CWPH-2	3.892	1.402	221.3	94.1
								IPSA T/F-1 IC-B1	-3.892	-1.402	221.3	94.1
CWPH2 I/C2- B	11.000	99.812	-0.1	0.000	0.000	0.000	0.000	IPSA T/F-2 IC-C1~	0.000	-0.005	0.3	0.0
								IPSA T/F-2 IC-B2	0.000	0.005	0.3	0.0
* I/C1- B	33.000	100.000	0.0	4.168	1.642	0.000	0.000	WTP-1	4.168	1.642	78.4	93.0
* I/C2-B	33.000	100.000	0.0	3.909	1.084	0.000	0.000	WTP-2	3.909	1.084	71.0	96.4
IPSA T/F-1 IC-B1	33.000	99.807	-0.1	0.000	0.000	0.000	0.000	IPSA.	-3.904	-1.571	73.8	92.8
								CWPH2 I/C1- B	3.904	1.571	73.8	92.8
IPSA T/F-2 IC-B2	33.000	99.807	-0.1	0.000	0.000	0.000	0.000	IPSA.	0.000	0.005	0.1	0.0
								CWPH2 I/C2- B	0.000	-0.005	0.1	0.0

IPSA.	33.000	99.807	-0.1	0.000	0.000	0.000	0.000	IPSA T/F-1 IC-B1	3.904	1.564	73.7	92.8
								IPSA T/F-2 IC-B2	0.000	-0.011	0.2	0.0
								WTP-2	-3.904	-1.553	73.6	92.9
RWITPH	11.000	99.421	-1.4	0.000	0.000	0.000	0.000	CM-VT-01-B1	0.000	-0.151	8.0	0.0
								CM-VT-02-B4	0.000	-0.149	7.9	0.0
								CM-VT-03-B7	0.000	-0.149	7.9	0.0
								RWP-VT1-B2	0.589	0.246	33.7	92.3
								RWP-VT2-B3	0.591	0.366	36.7	85.0
								RWP-VT3-B5	0.000	0.000	0.0	0.0
								RWPH-I/C1-B	-1.180	-0.164	62.9	99.1
RWP-VT1-B2	11.000	99.420	-1.4	0.000	0.000	0.589	0.247	RWITPH	-0.589	-0.247	33.7	92.2
RWP-VT2-B3	11.000	99.419	-1.4	0.000	0.000	0.591	0.367	RWITPH	-0.591	-0.367	36.7	85.0
RWP-VT3-B5	11.000	99.421	-1.4	0.000	0.000	0.000	0.000	RWITPH	0.000	0.000	0.0	0.0
RWPH-B1	33.000	99.999	0.0	0.000	0.000	0.000	0.000	WTP-1	-1.183	-0.192	21.0	98.7
								RWPH-I/C1-B	1.183	0.192	21.0	98.7
* RWPH-DG I/C- B	11.000	100.000	0.0	0.000	-0.001	0.000	0.000	RWPH-DG I/C- C~	0.000	-0.001	0.1	0.0
RWPH-I/C1-B	11.000	99.426	-1.4	0.000	0.000	0.000	0.000	RWITPH	1.180	0.163	62.9	99.1
								RWPH-B1	-1.180	-0.163	62.9	99.1
WTP-1	33.000	99.999	0.0	0.000	0.000	0.000	0.000	CWPH1- B2	2.985	1.454	58.1	89.9
								I/C1- B	-4.168	-1.643	78.4	93.0
								RWPH-B1	1.183	0.189	21.0	98.7
WTP-2	33.000	99.999	0.0	0.000	0.000	0.000	0.000	I/C2-B	-3.909	-1.086	71.0	96.4
								IPSA	3.909	1.086	71.0	96.4

6. Relay settings for RWPH -I
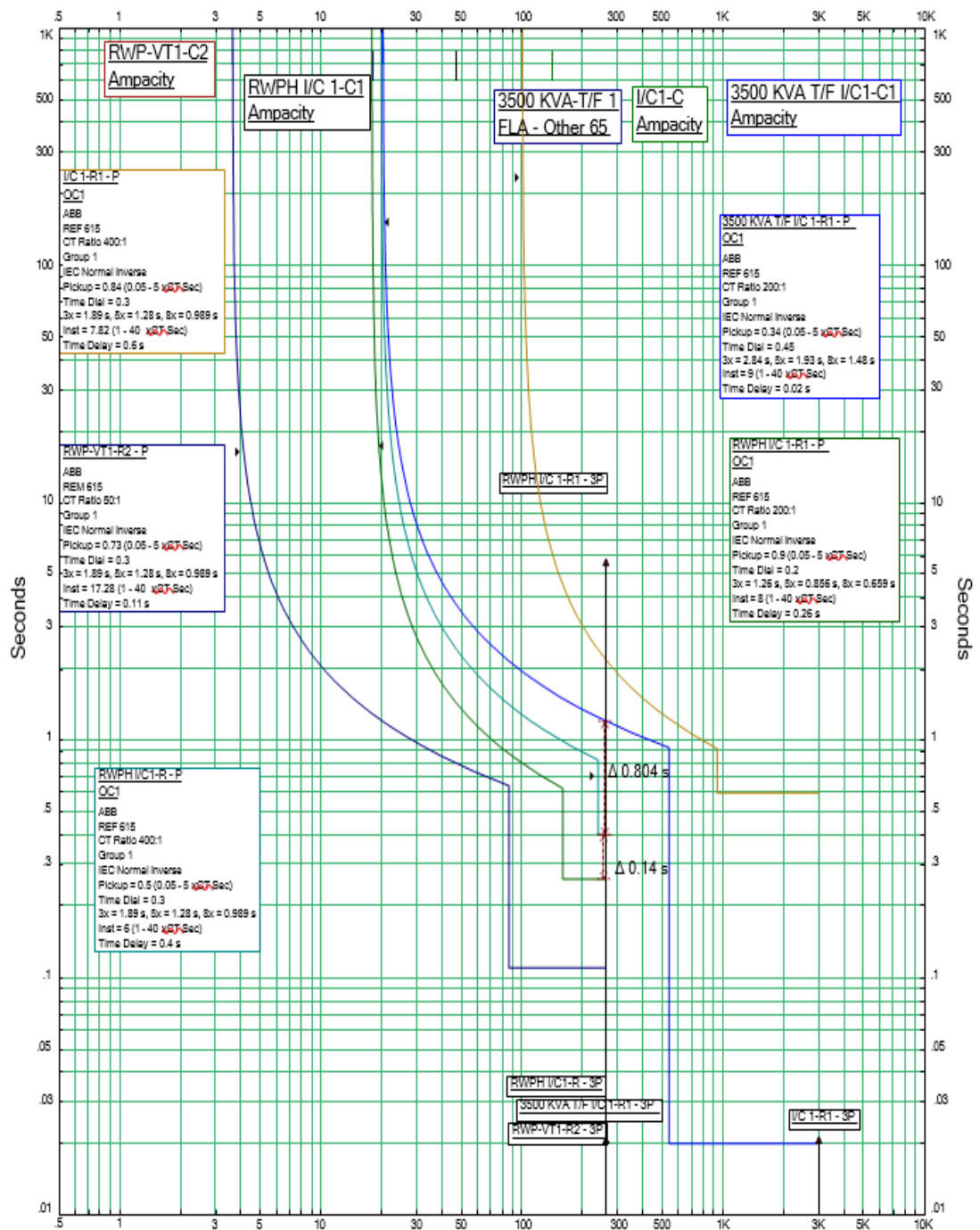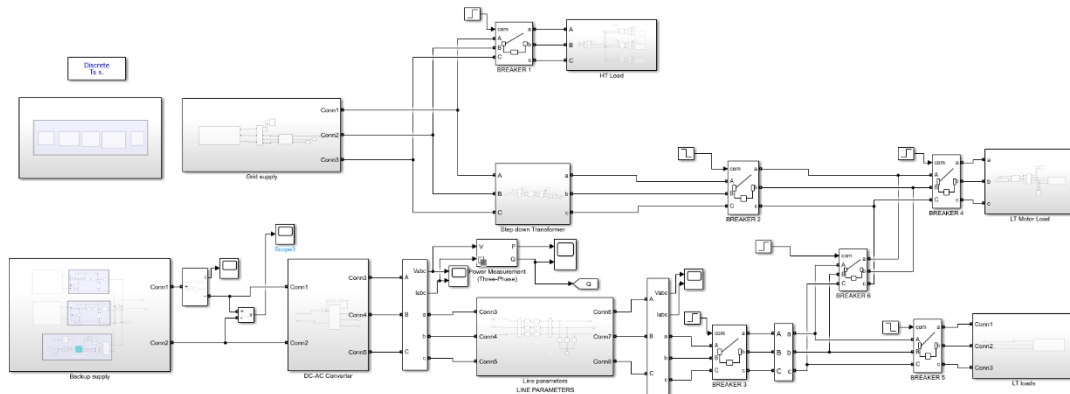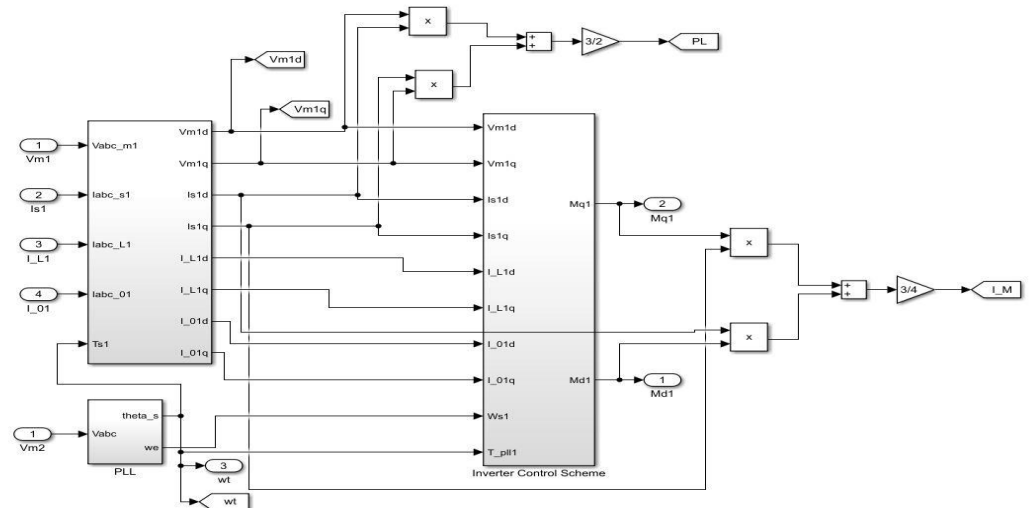
7. Relay settings for CWPH-I
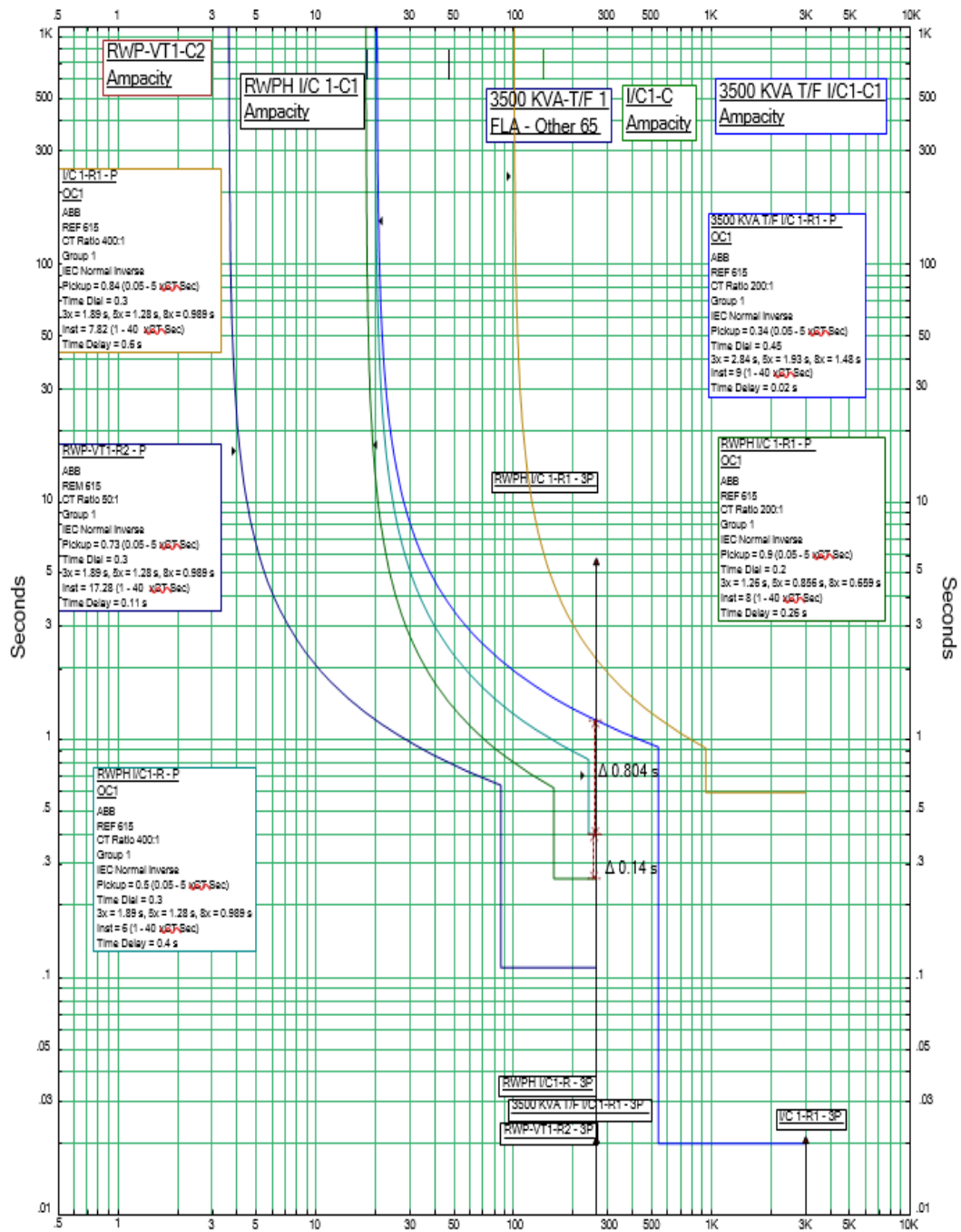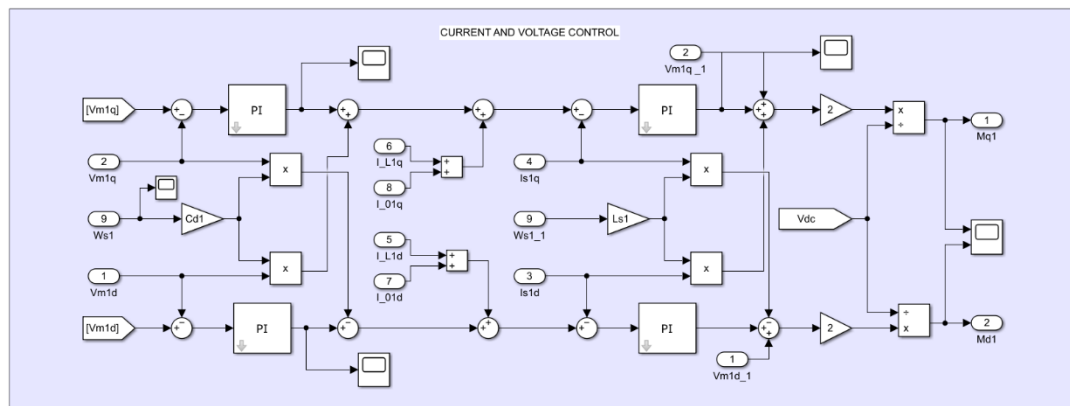
APPENDIX -D (Chapter 5)
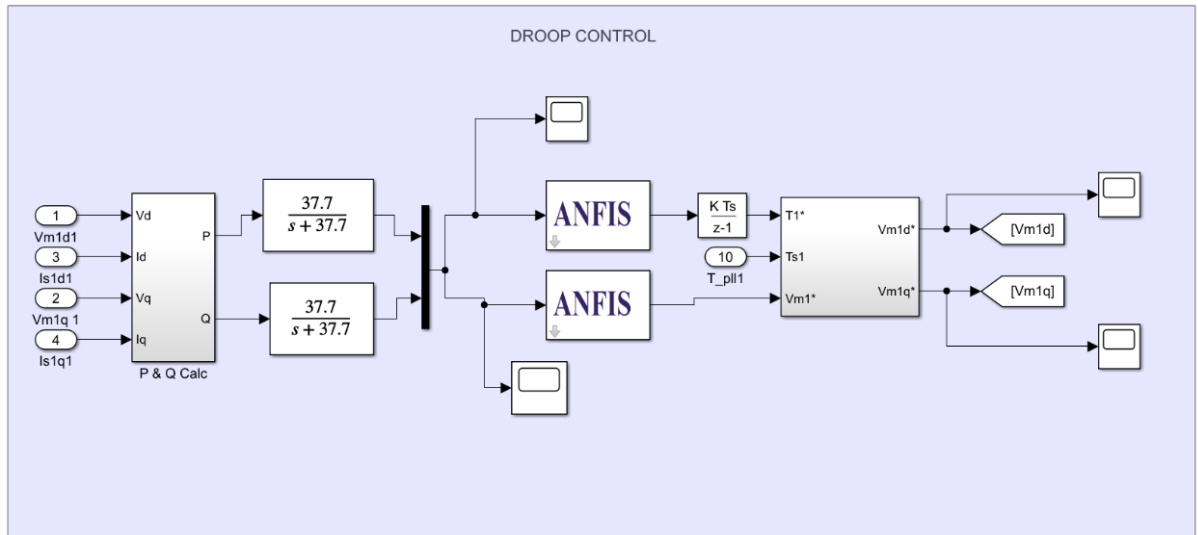
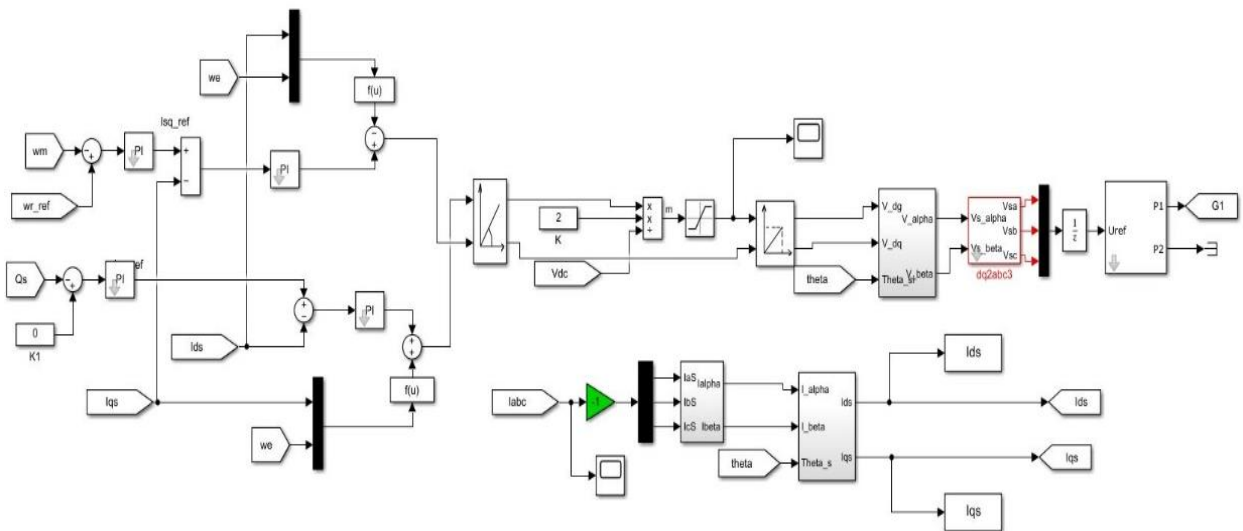1. MATLAB model of complete model

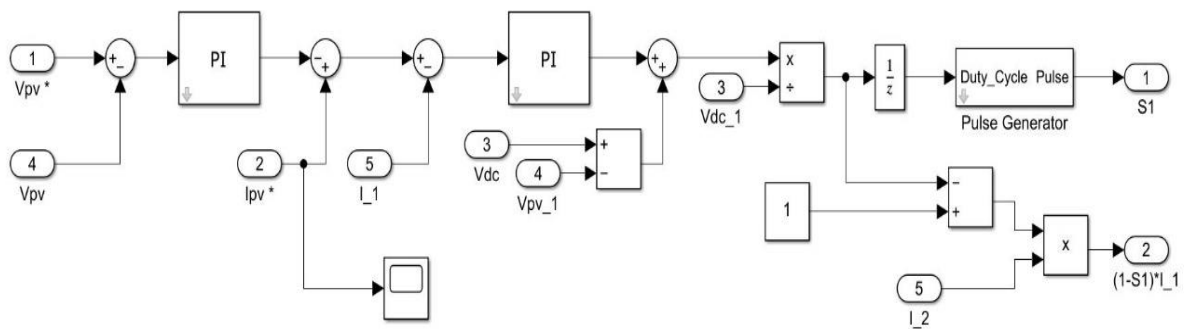2. Inverter control scheme

3. Current and Voltage control
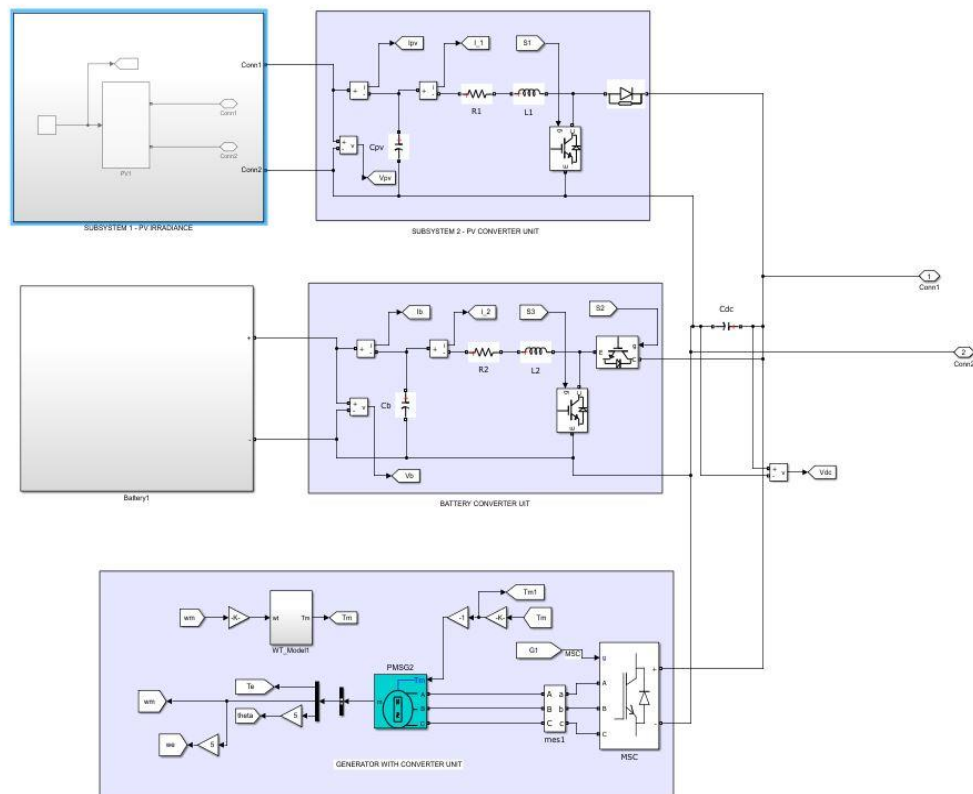
4. Droop control

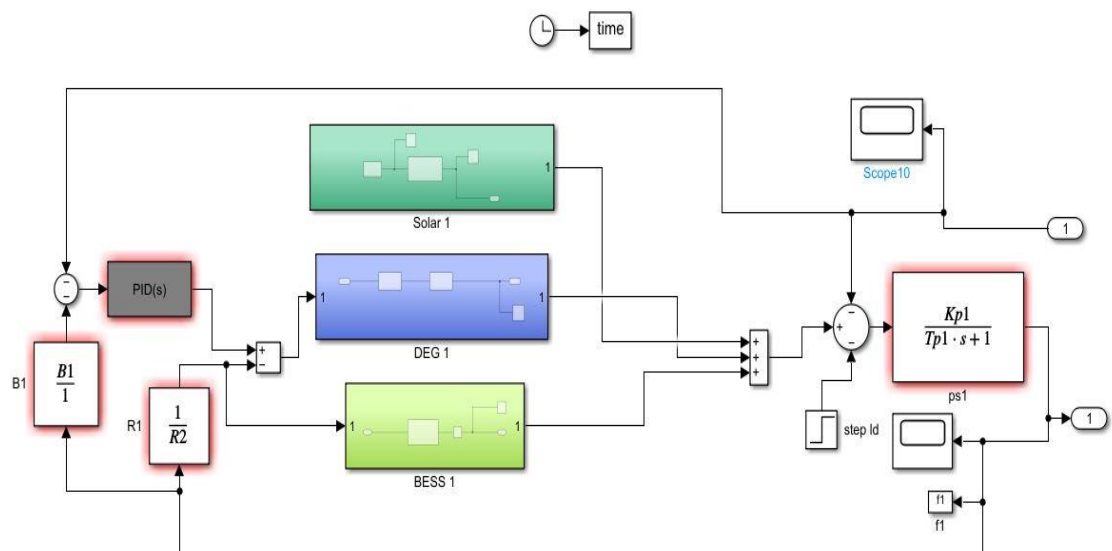5. Machine side control model

6. PV boost control scheme
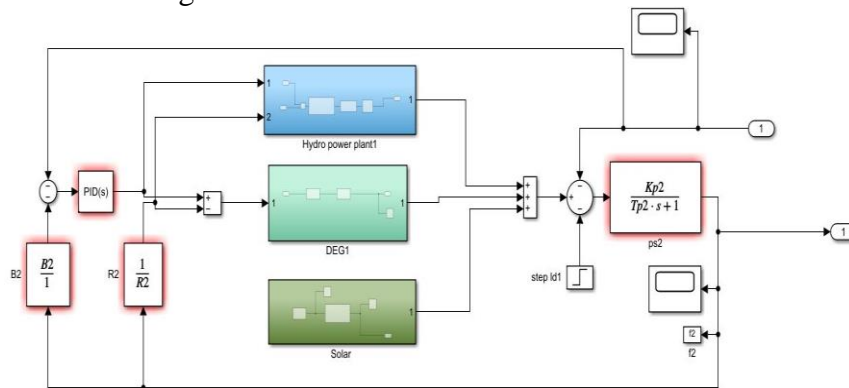
7. RES control scheme

APPENDIX -E (Chapter 6)

1. Microgrid area 1

2. Microgrid area 2

3. Microgrid area 3
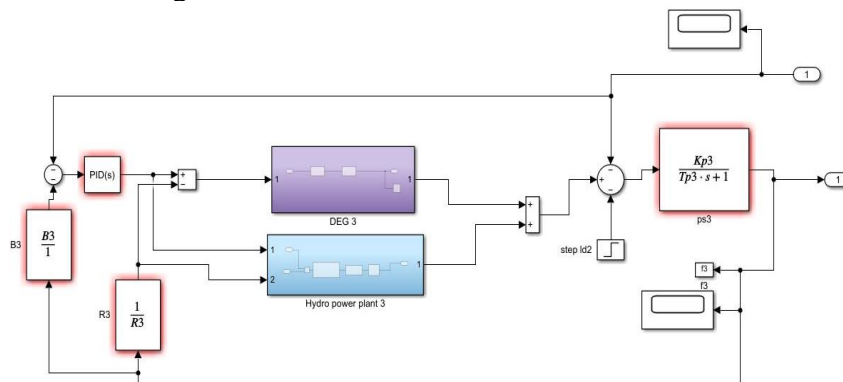
4. Microgrid Tie line
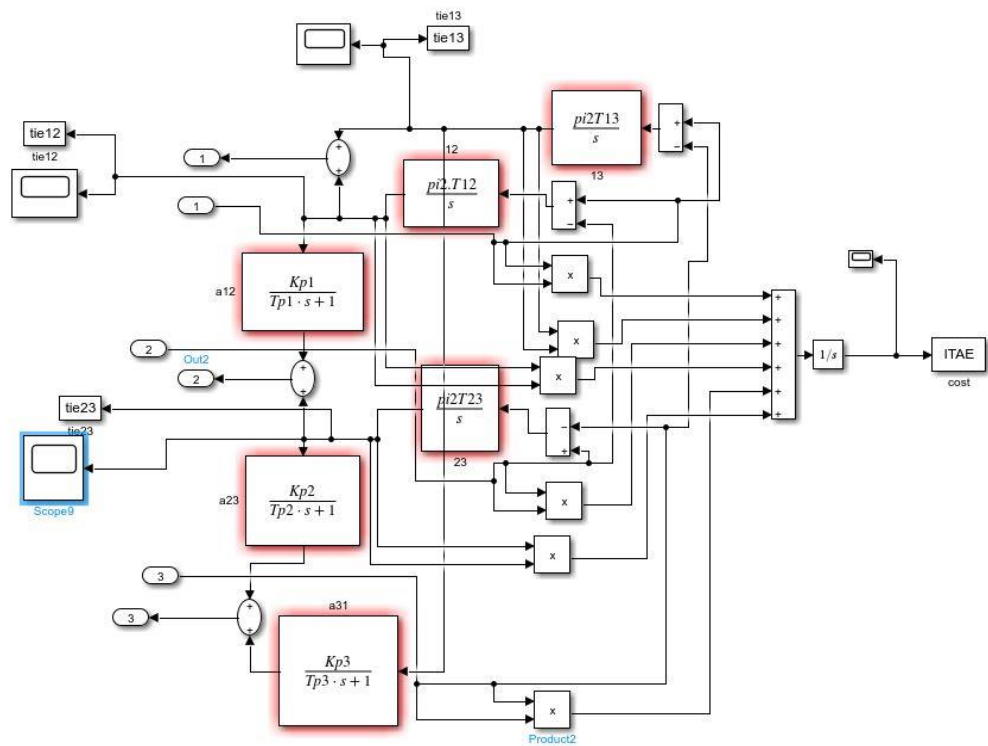
References

[1] CPHEEO, "Manual on Water Supply and Treatment," 3rd ed. Ministry of Urban. [Online]. Available: https://cpheeo.gov.in/upload/uploadfiles/files/1_0.pdf

[2] N. G. Pizzi, Water Treatment Operator Handbook. American Water Works Association, USA, 2011.

[3] A. O. Babatunde and Y. Q. Zhao, "Constructive Approaches Toward Water Treatment Works Sludge Management: An International Review of Beneficial Reuses," Crit. Rev. Environ. Sci. Technol., vol. 37, no. 2, pp. 129-164, 2007.

[4] National Water Supply and Drainage Board, "National Water Supply & Drainage Board - Annual Report," Sri Lanka, 2011.

[5] M. A. Eldib and M. A. A. Elbayoumy, "Evaluation of A Water Treatment Plant Performance–Case Study," in Seventh International Water Technology Conference (IWTC-7), Egypt, Apr. 1-3, 2003, pp. 471-478.

[6] J. C. Crittenden, R. R. Trussell, D. W. Hand, K. J. Howe and G. Tchobanoglous, MWH's Water Treatment: Principles and Design. John Wiley & Sons Inc., Hoboken, NJ, USA, 2012.

[7] L. Eis, "Load management on a municipal water treatment plant," Master's dissertation, Department of Mechanical Engineering, North-West University: Potchefstroom Campus, 2014.

[8] K. Anjithan, "Management practices of water treatment sludge in Sri Lanka," University of Moratuwa, 2015.

[9] N. G. Pizzi, Water Treatment Operator Handbook. American Water Works Association, USA, 2011.

[10] R. S. Dhaneshwar, V. P. Sharma, T. Raut, R. K. Gupta, P. S. Kelkar and R. Paramasivam, "Performance Evaluation of Five Urban Water Treatment Plants in Utter Pradesh," Indian Water Works Association Journal, Jan.-Mar. 1991, pp. 23-30.

[11] H. G. Solomon, "The Role of ICT in Water Resource Management," International Telecommunication Union, Geneva, SMW-O-0007, 2014.

[12] H. Dharmappa, A. Hasia, and P. Hagare, "Water Treatment Plant residuals management," Water Science and Technology, vol. 35, no. 8, pp. 45-56, 1997.

[13] N. M. Sahar Saghafi, G. Nabi Bid Hendy, and H. Amini Rad, "Energy efficiency in waste Water Treatment Plant emphasizing on COD removal; A case study of amol industrial zone, Iran," Can. J. Pure Appl. Sci., vol. 9, no. 2, pp. 3441-3448, 2015.

[14] S. Y. Alnouri, P. Linke, and M. El-Halwagi, "A synthesis approach for industrial city water reuse networks considering central and distributed treatment systems," Journal of Cleaner Production, vol. 89, pp. 231-250, 2015.

[15] S. K. Bhattacharya and R. K. Choudhary, "Performance of Engineering Parameter of a Water Treatment Plant A Case Study," presented at 28th WEDC conference on Sustainable Environment Sanitation and Water Services at Kolkata (Culcutta), India, 2002.

[16] G. Tchobanoglus, F. Burton, and H. D. Stensel, "Wastewater engineering: treatment and reuse," American Water Works Association Journal, vol. 95, no. 5, p. 201, 2003.

[17] M. Seiya, R. Chandran, M. Fujii, T. Fujita, Y. Shiraishi, S. Ashina, and N. Yabe, "Innovative information and communication technology (SCADA) system for energy management of public utilities in a post disaster region: case study of a waste Water Treatment Plant in Fukushima," J. Clean. Prod., vol. 233, pp. 1425-1436, 2019.

[18] J. C. Crittenden, R. R. Trussell, D. W. Hand, K. J. Howe, and G. Tchobanoglous, MWH's Water Treatment: Principles and Design. Hoboken, New Jersey: John Wiley & Sons Inc., 2012.

[19] G. Venkatesh and H. Brattebø, "Energy consumption, costs and environmental impacts for urban water cycle services: case study of Oslo (Norway)," Energy, vol. 36, no. 2, pp. 792-800, 2011.

[20] A. A. Khan, M. Naeem, M. Iqbal, S. Qaisar, and A. Anpalagan, "A compendium of optimization objectives, constraints, tools and algorithms for energy management in microgrids," Renewable and Sustainable Energy Reviews, vol. 58, pp. 1537-1552, May 2016.

[21] A.U.A. Arif, M.T. Sorour, and S.A. Aly, "Design and comparison of waste Water Treatment Plant types (activated sludge and membrane bioreactor), using GPSX

simulation program: case study of tikrit Waste Water Treatment Plant (Middle Iraq)," J. Environ. Protect., vol. 9, no. 6, pp. 636-651, 2018.

[22] J.T. Liao, Y.S. Chuang, H.T. Yang, and M.S. Tsai, "BESS-Sizing Optimization for Solar PV System Integration in Distribution Grid," IFAC-Papers Online, vol. 51, no. 28, pp. 85-90, 2018.

[23] N.M. Sahar Saghafi, Gholamreza Nabi Bid Hendy, and Hasan Amini Rad, "Energy efficiency in waste Water Treatment Plant emphasizing on COD removal; A case study of amol industrial zone, Iran," Can. J. Pure Appl. Sci., vol. 9, no. 2, pp. 3441-3448, 2015.

[24] L.I. Ruiz, H. Castro, and D. Romero, "Real-Time technology? Migration of traditional SCADA systems technology: Part2: Advantages of implementation," in 2017 IEEE 37th Central America and Panama Convention (CONCAPAN XXXVII), Managua, 2017, pp. 1-7.

[25] Eastern Research Group (ERG), Inc., "Opportunities for and Benefits of Combined Heat and Power at Wastewater Treatment Facilities," U.S. Environmental Protection Agency Combined Heat and Power Partnership, Dec. 2006.

[26] Schneider Electric SA, "Water and Wastewater Power Solution Handbook," Oct. 2008.

[27] J.A. Ruiz Carmona, J.C. Muñoz Benítez, and J.L.García-Gervacio, "SCADA system design: A proposal for optimizing a production line," in Proceedings of the International Conference on Electronics, Communications and Computers (CONIELECOMP), 2016.

[28] S.W. Ho, K.K. Cheung, and W.C. Fung, "Sustainable wastewater treatment – ways to achieve energy neutrality," HKIE Transactions, 2014.

[29] G. Venkatesh and H. Brattebø, "Energy consumption, costs and environmental impacts for urban water cycle services: case study of Oslo (Norway)," Energy, vol. 36, no. 2, pp. 792-800, 2011.

[30] E. Zaev, D. Babunski, A. Tuneski, et al., "SCADA System for Real-time Measuring and Evaluation of River Water Quality," in Proceedings of MECO 2016 conference, Bar, Montenegro, IEEE 2016, pp. 83-86.

[31] L. McCarty, J. Bae and J. Kim, "Domestic Wastewater Treatment as a Net Energy Producer Can This be Achieved?," Environ. Sci. Technol., vol. 45, pp. 7100-7106, 2011.

[32] N.G. Pizzi, "Water Treatment Operator Handbook," American Water Works Association, USA, 2011.

[33] M.P. Ward, "An architectural framework for describing supervisory control and data acquisition (SCADA) systems," Master Thesis, Naval Postgraduate School, Monterey, CA, 2004.

[34] Quickdraw SCADA IDS, [Online]. Available: http://www.digitalbond.com, 2012.

[35] H. Dharmappa, A. Hasia and P. Hagare, "Water Treatment Plant residuals management," Water Sci. Technol., vol. 35, no. 8, pp. 45-56, 1997.

[36] D.R. S., V.P. Sharma, T. Raut, R.K. Gupta, P.S. Kelkar and R. Paramasivam, "Performance Evaluation of Five Urban Water Treatment Plants in Utter Pradesh," Indian Water Works Association Journal, vol. Jan-March, pp. 23-30, 1991.

[37] A.D.L. Gray, I. Pisica, et al., "A Standardised Modular Approach for Site SCADA Applications within a Water Utility," IEEE Access, vol. PP, no. 99, 2017.

[38] E. Zaev, D. Babunski, et al., "Design of optimal SCADA program for automation of HPP," in Proc. 9th Int. Conf. on Advanced Materials and Operations (AMO 09), Kranevo, Bulgaria, 2009, pp. 227-231.

[39] S. Ralhan and S. Ray, "Optimal Coordination of Directional Overcurrent Relays using Interval Two Phase Simplex Linear Programming," Int. J. Adv. Comput. Res., vol. 3, no. 3, issue 11, pp. September, 2013.

[40] C.J. Soni, P.R. Gandhi and S.M. Takalkar, "Design and analysis of 11 KV Distribution System using ETAP Software," in Proc. Int. Conf. on Computation of Power, Energy Information and Communication (ICCPEIC), 2015, pp. 451-456.

[41] N. Nisar, M.B. Khan, S. Gondal and M. Naveed, "Analysis and Optimization of 132KV Grid Using ETAP," 2005.

[42] R. P., "Load Flow and Short Circuit Analysis of 400/220 kV Substation," Int. J. Creative Res. Thoughts, vol. 1, no. 4, pp. 1-4, Apr. 2013.

[43] B. Oza, N. Nair, R. Mehta and V. Makwana, "Power System Protection & Switchgear," Tata McGraw Hill Education Private Limited, New Delhi, 2010.

[44] N. Nisar et al., "Analysis and Optimization of 132KV Grid using ETAP," in Proc. Power Generation System and Renewable Energy Technologies (PGSRET), 2015, pp. 1-6.

[45] N. Li, Y. Xu, and Chen, "FACTS-Based Power flow control in interconnected power systems," IEEE Transactions on Power Systems, vol. 15, no. 1, pp. 257-262, 2000.

[46] A. Kamel, M. A. Alaam, A. M. Azmy, and A. Y. Abdelaziz, "Protection Coordination of Distribution Systems Equipped with Distributed Generation," Electrical and Electronics Engineering: An International Journal (ELELIJ), vol. 2, no. 2, pp. 1-13, May 2013.

[47] S. O. Edward, D. C. Idoniboyeobu, and C. O. Ahiakwo, "The Study and Improvement of Electricity Power Distribution in Opolo Bayelsa State," Global Scientific Journal, vol. 8, no. 4, pp. 12-19, 2020.

[48] N. Athamsiadis, "A new technique for a STATIC Var Compensator using EMTP modelling Environment," Electrical Engineering, vol. 84, no. 2, pp. 255-261, May 2002.

[49] H. Zhu, "The application of the ETAP Solftware in the Analysis and Simulation of Power System," in International Conference on Energy and Power Engineering, 2014, pp. 209-213.

[50] J. Francois and S. Datta, "SVC Protection and Control basics," Protective Relay Engineers, 2005, 58th Annual Conference, vol. , no. 5-7, pp. 86-95, April 2005.

[51] M. P. Selvan and K. S. Swarup, "Distribution System Load Flow using Object-Oriented Methodology," in 2004 Int. Conf. on Power System Technology-POWERCON 2004, Singapore, Nov. 21-24, 2004.

[52] C. S. Chang and J. S. Huang, "Optimal multi objective SVC planning for voltage stability enhancement," IEEE Proceedings- Generation, Transmission and Distribution, vol. 145, no. 2, pp. 203-209, March 1998.

[53] N. Athamsiadis, "A new technique for a STATIC Var Compensator using EMTP modelling Environment," Electrical Engineering, vol. 84, no. 2, pp. 255-261, May 2002.

[54] L. Chengyi, "Operation Technology. Inc. ETAP 16.2 user guide," 2016. [Online]. Available: http://www.etap.com/. [Accessed: Apr. 23, 2020].

[55] A. Rath, S. Roy, and G. T. Goyal, "Optimal Allocation of Distributed Generation (DGs) and Static VAR Compensator (SVC) in a Power System using Revamp Voltage Stability Indicator," Department of Electrical Engineering, KIIT University, Bhubaneswar, India, retrieved April, 23, 2020, from http://www.iitk.ac.in/npsc/Papers/NPSC2016/1570291015.pdf.

[56] V. N. Kiran and K. Naveen, "Short Circuit Analysis Of 220/132 kV Substation By Using ETAP," International Journal of Advanced Technology in Engineering and Science, vol. 4, no. 3, pp. 9-18, March 2016.

[57] M.N. Malik, A. Iftikhar Toor, M.A. Siddiqui, N. Husain, and Akif Nadeem, "Load flow analysis of an eht network using ETAP," Journal of Multidisciplinary Engineering Science and Technology (JMEST), vol. 3, no. 6, pp. 5855-5860, June 2016.

[58] A.R. Phadke, S.K. Bansal, and K.R. Niazi, "A Comparison of Voltage Stability Indices for Placing Shunt FACTS Controllers," in Proceedings of the First International Conference on Emerging Trends in Engineering & Technology (ICETET'08), vol. 1, July 16-18, 2008, pp. 939-944.

[59] Zaheeruddin and M. Manas, "Renewable energy management through microgrid central controller design: An approach to integrate solar, wind and biomass with battery," Energy Reports, vol. 1, pp. 156-163, 2015.

[60] D. Ibarra and J. Arnal, "Parallel programming techniques applied to water pump scheduling problems," Journal of Water Resources Planning and Management, vol. 140, no. 7, pp. 06014002, Jul. 2014.

[61] H.R. Baghaee, M. Mirsalim, G.B. Gharehpetian, and H.A. Talebi, "Three phase AC/DC power-flow for balanced/unbalanced microgrids including wind/solar, droop-controlled and electronically-coupled distributed energy resources using RBF neural

networks," IET Power Electronics, vol. 10, no. 3, pp. 313-328, Mar. 2017, DOI: 10.1049/iet-pel.2016.0010.

[62] Z. Zhang, A. Kusiak, and Y. Zeng, "Modeling and optimization of a wastewater pumping system with data-mining methods," Applied Energy, vol. 164, pp. 303-311, 2016.

[63] G.J. Dalton, D.A. Lockington, and T.E. Baldock, "Feasibility analysis of stand-alone renewable energy supply options for a large hotel," Renewable Energy, vol. 33, no. 7, pp. 1475-1490, Jul. 2008.

[64] P. Sreedharan, J. Farbes, E. Cutter, et al., "Microgrid and renewable generation integration," Appl. Energy, vol. 169, pp. 709-720, 2016.

[65] N. Pogaku, M. Prodanovic, and T.C. Green, "Modeling, analysis and testing of autonomous operation of an inverter-based microgrid," IEEE Transactions on Power Electronics, vol. 22, no. 2, pp. 613-625, Mar. 2007.

[66] H. Han, X. Hou, J. Yang, J. Wu, M. Su, and J.M. Guerrero, "Review of power sharing control strategies for islanding operation of AC microgrids," IEEE Trans. Smart Grid, vol. 7, no. 1, pp. 200-215, Jan. 2016.

[67] X. Yang, J. Su, Z. Lü, H. Liu, and R. Li, "Overview on microgrid technology," Proceedings of the CSEE, vol. 34, pp. 57-70, Jan. 2014

[68] A. Llaria, O. Curea, J. Jiménez, and H. Camblong, "Survey on microgrids: unplanned islanding and related inverter control techniques," Renewable energy, vol. 36, no. 8, pp. 2052-2061, 2011.

[69] Y. Sun, G. Shi, X. Li, W. Yuan, M. Su, H. Han, X. Hou, "An f-P/Q Droop Control in Cascaded-Type Microgrid," IEEE Transactions on Power Systems, vol. 33, no. 1, pp. 1136-1138, Sep. 2017.

[70] R. Rahmani and A. Fakharian, "New control method of islanded microgrid system: a GA & ICA based optimization approach," Modares Journal of Electrical Engineering, 2016, in press.

[71] J. He, Y. Li, B. Liang, and C. Wang, "Inverse power factor droop control for decentralized power sharing in series-connected micro-converters based islanding microgrids," IEEE Trans. Ind. Electron., vol. 64, no. 9, pp. 7444-7454, Sep. 2017.

[72] B. Bahrani, M. Saeedifard, A. Karimi, and A. Rufer, "A multivariable design methodology for voltage control of a single-dg-unit microgrid," IEEE Transactions on Industrial Informatics, vol. 9, no. 2, pp. 589-599, 2013.

[73] R. Rahmani and A. Fakharian, "A combination of 3-phase and dq techniques for controlling the islanded microgrid system: New schemes," in Electrical Engineering (ICEE), 2015 23rd Iranian Conference on, 2015, pp. 1457-1462.

[74] M. Babazadeh and H. Karimi, "A robust two-degree-of-freedom control strategy for an islanded microgrid," IEEE transactions on power delivery, vol. 28, no. 3, pp. 1339-1347, 2013.

[75] A. Denda, "Shimizu's microgrid research activities," Symposium on Microgrids, Montreal, June 2006.

[76] I. Wasiak, R. Pawełek, and P. Kelm, "Autonomous Operation of Low Voltage Microgrids," Acta Energetica, 2014.

[77] I. Wasiak, R. Pawełek, and R. Mienski, "Energy storage application in low voltage microgrids for energy management and power quality improvement," IET Generation, Transmission & Distribution, vol. 8, no. 3, pp. 463-472, 2014.

[78] C. Rehtanz, Autonomous Systems and Intelligent Agents in Power System Control and Operation, Springer, 2003.

[79] X. Zhu, F. Meng, Z. Xie, and Y. Yue, "An inertia and damping control method of dc-dc converter in dc microgrid," IEEE Transactions on Energy Conversion, 2019.

[80] X. Wang, Y. W. Li, F. Blaabjerg, and P. C. Loh, "VirtualImpedance-Based Control for Voltage-Source and Current-Source Converters," IEEE Transactions on Power Electronics, vol. 30, pp. 7019-7037, 2015.

[81] H.R. Baghaee, M. Mirsalim, G.B. Gharehpetian, H.A. Talebi, "Fuzzy unscented transform for uncertainty quantification of correlated wind/PV microgrids: possibilistic-probabilistic power flow based on RBFNNs," IET Renewable Power Generation, vol. 11, no. 6, pp. 867-877, Mar. 2017

[82] X. Yu, A.M. Khambadkone, H. Wang, and S.T.S. Terence, "Control of Parallel-Connected Power Converters for Low-Voltage Microgrid—Part I: A Hybrid Control Architecture," IEEE Transactions on Power Electronics, vol. 25, no. 12, pp. 2962–2970, 2010.

[83] H.H. Zeineldin, E.F. El-Saadany, and M.M.A. Salama, "Distributed generation micro-grid operation: control and protection," in Power Systems Conf.: Advanced Metering, Protection, Control, Communication, and Distributed Resources, Clemson, SC, USA, Mar. 2006, pp. 105-111.

[84] N.B.D. Nadai, A.C.Z. d. Souza, J.G.C. Costa, C.A.M. Pinheiro, and F.M. Portelinha, "A secondary control based on fuzzy logic to frequency and voltage adjustments in islanded microgrids scenarios," in 2017 IEEE Manchester PowerTech, 2017, pp. 1-6.

[85] D. Wu, J.M. Guerrero, J.C. Vasquez, T. Dragicevic, and F. Tang, "Coordinated power control strategy based on primary-frequency signaling for islanded microgrids," in Proc. IEEE ECCE'2013, pp.1033-1038, Sept. 15-19, 2013.

[86] C.T. Lee, C.C. Chu, and P.T. Cheng, "A new droop control method for the autonomous operation of distributed energy resource interface converters," in 2010 IEEE Energy Conversion Congress and Exposition, 2010, pp. 702-709.

[87] P.C. Loh, D. Li, Y.K. Chai, and F. Blaabjerg, "Autonomous Control of Interlinking Converter With Energy Storage in Hybrid AC–DC Microgrid," IEEE Transactions on Industry Applications, vol. 49, no. 3, pp. 1374-1382, 2013.

[88] J. Zeng, W. Qiao, and L. Qu, "An isolated three-port bidirectional DC-DC converter for photovoltaic systems with energy storage," in IEEE Industry Applications Society Annual Meeting, pp. 3493-3503, 2013.

[89] C. Yuen, A. Oudalov, and A. Timbus, "The Provision of Frequency Control Reserves From Multiple Microgrids," IEEE Transactions on Industrial Electronics, vol. 58, no. 1, pp. 173-183, Jan. 2011.

[90] Prajof Prabhakaran, Yogendra Goyal, and Vivek Agarwal, "Novel Nonlinear Droop Control Techniques to Overcome the Load Sharing and Voltage Regulation Issues in DC Microgrid," IEEE Transactions on Power Electronics, vol. 33, no. 5, pp. 4477-4487, May 2018.

[91] A. Bidram, "Distributed cooperative control of AC microgrids," Ph.D. dissertation, The University of Texas at Arlington, Ann Arbor, MI, USA, 2014.

[92] L. Che, X. Zhang, et al., "Optimal interconnection planning of community microgrids with renewable energy sources," IEEE Trans. Smart Grid, vol. 8, no. 3, pp. 1054-1063, May 2017.

[93] Y. Zhang, et al., "Interactive control of coupled microgrids for guaranteed system-wide small signal stability," IEEE Trans. Smart Grid, vol. 8, no. 2, pp. 713-722, Mar. 2017.

[94] P. P. Vergara et al., "A Generalized Model for the Optimal Operation of Microgrids in Grid-Connected and Islanded DroopBased Mode," IEEE Trans. Smart Grid, vol. 10, no. 5, pp. 5032-5045, Sep. 2019.

[95] L. Che, M. Shahidehpour, A. Alabdulwahab, and Y. Al-Turki, "Hierarchical coordination of a community microgrid with ac and dc microgrids," IEEE Trans. Smart Grid, vol. 6, no. 6, pp. 3042-3051, Nov. 2015.

[96] F. Shahnia, S. Bourbour, and A. Ghosh, "Coupling neighboring microgrids for overload management based on dynamic multicriteria decision-making," IEEE Trans. Smart Grid, vol. 8, no. 2, pp. 969-983, Mar. 2017.

[97] Z. Li, Q. Guo, H. Sun, and J. Wang, "Impact of Coupled Transmission-Distribution on Static Voltage Stability Assessment," IEEE Trans. Power Syst., vol. 32, no. 4, pp. 3311-3312, Jul. 2017.

[98] I. U. Nutkani, et al., "Distributed operation of interlinked ac microgrids with dynamic active and reactive power tuning," IEEE Trans. Industry Applications, vol. 49, no. 5, pp. 2188-2196, Sep./Oct. 2013.

[99] F. Shahnia, and A. Arefi, "Eigenanalysis-based small signal stability of the system of coupled sustainable microgrids," International Journal of Electrical Power & Energy Systems, vol. 91, pp. 42-60, Oct. 2017.

[100] M. Hemmati, S. Ghasemzadeh, et al., "Optimal scheduling of smart reconfigurable neighbour micro-grids," IET Gen. Trans. & Dist., vol. 12, no. 19, pp. 4439-4446, Sep. 2018.

[101] S. K. Akula and H. Salehfar, "Frequency control in microgrid communities using neural networks," in Proc. 2019 North American Power Symposium (NAPS), Wichita, KS, USA, Sep. 2019, pp. 1-6.

[102] R. K. Sahu, S. Panda, A. Biswal and G. T. Sekhar, "Design and analysis of tilt integral derivative controller with filter for load frequency control of multi-area interconnected power systems," ISA Transactions, vol. 61, pp. 251-264, Mar. 2016.

[103] M. S. Bisht and Sathans, "Fuzzy based intelligent frequency control strategy in standalone hybrid AC microgrid," 2014 IEEE Conference on Control Applications (CCA), Juan Les Antibes, 2014, pp. 873-878.

[104] A. A. Heidari, S. Mirjalili, H. Faris, et al., "Harris hawks optimization: Algorithm and applications," Future Generation Computer Systems, vol. 97, pp. 849-872, Aug. 2019.

[105] R. K. Sahu, S. Panda, U. K. Routa and D. K. Sahoo, "Teaching learning based optimization algorithm for automatic generation control of power system using 2-DOF PID controller," International Journal of Electrical Power & Energy Systems, vol. 77, pp. 287-301, May 2016.

[106] J. Shing and R. Jang, "ANFIS: Adaptive-Network-Based Fuzzy Inference System," IEEE Transactions on Systems, Man, and Cybernetics, vol. 23, no. 3, pp. 665-685, May 1993.

[107] M. Singh and A. Chandra, "ANFIS Based Speed & Position Sensorless Control of Grid Connected, PMSG coupled Wind Turbine with 3P4W Non-Linear Unbalance Load Compensation," IEEE Transactions on Power Electronics, vol. 26, no. 1, pp. 165-175, Jan. 2011.

[108] N. Ghadimi and B. Sobhani, "Adaptive neuro-fuzzy inference system (ANFIS) islanding detection based on wind turbine simulator," International Journal of Physical Sciences, vol. 8, no. 27, pp. 1424-1436, July 2013.

[109] H. R. Baghaee, M. Mirsalim, G. B. Gharehpetian and H. A. Talebi, "A decentralized power management and sliding mode control strategy for hybrid AC/DC microgrids including renewable energy resources," IEEE Transactions on Industrial Informatics, vol. PP, no. 99, pp. 1-10, March 2017.

[110] M. Singh and A. Chandra, "Real Time Implementation of ANFIS Control for Renewable Interfacing Inverter in 3P4W Distribution Network," IEEE Transactions on Industrial Electronics, vol. 60, no. 1, pp. 121-128, Jan. 2013.

[111] M. Singh and A. Chandra, "ANFIS Based Speed & Position Sensorless Control of Grid Connected, PMSG coupled Wind Turbine with 3P4W Non-Linear Unbalance Load Compensation," IEEE Transactions on Power Electronics, vol. 26, no. 1, pp. 165-175, Jan. 2011.

[112] X. Li, Y. J. Song and S. B. Han, "Frequency control in MicroGrid power system combined with electrolyzer system and fuzzy PI controller," Journal of Power Sources, vol. 180, no. 1, pp. 468-475, May 2008.

[113] Public Health Engineering Department Government of Mizoram, "Greater Aizawl Water Supply Scheme - Phase I," [Online]. Available: https://phed.mizoram.gov.in/page/greater-aizawl-water-supply-scheme-phase-i.

[114] Public Health Engineering Department Government of Mizoram, "Greater Aizawl Water Supply Scheme - Phase II," [Online]. Available: https://phed.mizoram.gov.in/page/greater-aizawl-water-supply-scheme-phase-ii.

[115] Central Electricity Authority, "17th Electric Power Survey Report," [Online]. Available: https://www.scribd.com/doc/57505120/17th-Electric-Power-Survey-Report.

[116] National Renewable Energy Laboratory, "National Solar Radiation Database," [Online]. Available: https://nsrdb.nrel.gov/.

[117] National Renewable Energy Laboratory, "Wind Data and Tools," [Online]. Available: https://www.nrel.gov/wind/data-tools.html.

[118] Government of Mizoram, "Solar Power Policy of Mizoram," [Online]. Available: https://zeda.mizoram.gov.in/.

[119] Mizoram Science, Technology & Innovation Council (MISTIC), [Online]. Available: https://mistic.mizoram.gov.in/.

[120] B. Sparn and R. Hunsberger, "Opportunities and challenges for water and wastewater industries to provide exchangeable services," National Renewable Energy Lab. (NREL), Golden, CO, USA, Tech. Rep. NREL/TP-5500-63931, Nov. 2015.

[121] J. C. Swanson, C. Mueller, and S. Barrett, "Analysis of Intake and Discharge Salinity Regimes for a Desalination Plant," in OCEANS, Boston, MA, USA, 2006, pp. 1-5.

[122] V. Georgescu, "Operations Management in Water and Waste Water Treatment Plants," in Trans. Tech. Publications Switzerland, Applied Mechanics and Materials, Dec. 2012, pp. 179-184.

[123] Y. Tang and S. Zhang, "A Model Predictive Control Approach to Operational Efficiency of Intake Pump Stations," in Proc. Int. Conf. on Elect. and Control Engg., Wuhan, China, 2010, pp. 92-95.

[124] A. Bradley, "SCADA System," Publication AG-UM008C-EN-P, 2005.

[125] R. Malisa, E. Schwella, and B. Batinge, "Augmenting Water Supplies Through Urban Wastewater Recycling (March 2019)," IEEE Systems Journal, vol. 14, no. 1, pp. 1523-1530, Mar. 2020.

[126] Endress+Hauser, "Water quality monitoring with SWAS, efficient and reliable," [Online]. Available: https://www.endress.com/en/industry-expertise/power-energy/quality-water-steam-circuit

[127] D. Babunski et al., "Optimization methods for water supply SCADA system," in Proc. Mediterranean Conf. on Embedded Computing, Budva, Montenegro, 2018, pp. 1-4.

[128] E. Zaev, D. Babunski, and A. Tuneski, "SCADA system for real-time measuring and evaluation of river water quality," in Proc. Mediterranean Conf. on Embedded Computing, Bar, Montenegro, 2016, pp. 83-86.

[129] K. Oikonomou and M. Parvania, "Deploying Water Treatment Energy Flexibility in Power Distribution Systems Operation," in Proc. Power & Energy Society Inno. Smart Grid Technologies Conf., Washington, DC, USA, 2020, pp. 1-5.

[130] S. Shu et al., "Power Saving in Water Supply System with Pump Operation Optimization," in Proc. Asia-Pacific Power and Energy Engg. Conf., Chengdu, China, 2010, pp. 1-4.

[131] Rajesh K, Arjunamuthu A, Karuppasamypandiyan M, Bhuvanesh A, "Power Flow Analysis of 230/110 kV Substation using ETAP," in Proc. International Conference on Emerging Trends in Science, Engineering, Business and Disaster Management, 2014.

[132] M.A. Pai, "Computer Techniques in Power System Analysis," 2nd ed. Tata McGraw Hill, 2005.

[133] H. Zhu, "The application of the ETAP Software in the Analysis and Simulation of Power System," in Proc. International Conference on Energy and Power Engineering, 2014, pp. 209-213.

[134] Electrical Transient Analyzer Program (ETAP), [Online]. Available: www.etap.com.

[135] Kriti Singhal, "Comparison between Load Flow Analysis Methods in Power System using MATLAB," International Journal of Scientific & Engineering Research, vol. 5, no. 5, pp. 212-217, 2014.

[136] R. S. Maciel, A. Padilha-Feltrin, and E. Righeto, "Substitution Newton Raphson Method for the Solution of Electric Network Equations," in Proc. Transmission & Distribution Conference and Exposition: Latin America, 2006, pp. 1-6.

[137] C. R. Fuerte-Esquivel, E. Acha, and H. Ambriz-Perez, "A comprehensive Newton-Raphson UPFC model for the quadratic power flow solution of practical power networks," IEEE Trans. Power Syst., vol. 15, no. 1, pp. 102–109, 2000.

[138] V.N. Kiran, K. Naveen, "Short Circuit Analysis Of 220/132 kV Substation By Using ETAP," International Journal of Advanced Technology in Engineering and Science, vol. 4, no. 3, pp. 276-282, 2016.

[139] E. Kang, S. Adepu, D. Jackson, and A. P. Mathur, "Model-based security analysis of a water treatment system," in Proc. 2nd SEsCPS, 2016.

[140] R. Palma-Behnke, L. S. Vargas, J. R. Perez, J. D. Nunez, and R. A. Torres, "OPF with SVC and UPFC modeling for longitudinal systems," IEEE Trans. Power Syst., vol. 19, no. 4, pp. 1742-1753, Nov. 2004.

[141] J. H. Chen, W. J. Lee, and M. S. Chen, "Using a Static Var Compensator to Balance a Distribution System," IEEE Trans. Ind. Appl., vol. 35, no. 2, pp. 298-304, Mar./Apr. 1999.

[142] T. Ghanbari and E. Farjah, "Unidirectional Fault Current Limiter: An Efficient Interface Between the Microgrid and Main Network," IEEE Trans. Power Syst., vol. 27, no. 4, pp. 1928-1937, Aug. 2012.

[143] C. S. Chang and J. S. Huang, "Optimal multi objective SVC planning for voltage stability enhancement," IEE Proc. Gener. Transm. Distrib., vol. 145, no. 2, pp. 203-209, Mar. 1998.

[144] M. R. D. Zadeh and Z. Zhang, "A New DFT-Based Current Phasor Estimation for Numerical Protective Relaying," IEEE Trans. Power Del., vol. 28, no. 4, pp. 2172-2179, Oct. 2013.

[145] M. A. Kamarposhti and M. Alinezhad, "Comparison of SVC & STATCOM in Static Voltage Stability Margin Enhancement," Proc. World Acad. Sci. Eng. Technol., vol. 38, pp. 635-638, Feb. 2009.

[146] B. Patil and S. Namekar, "Load Flow & Short Circuit Analysis of 132/33/11KV Substation using ETAP," Int. J. Appl. Eng. Res., vol. 13, no. 11, pp. 9943-9952, 2018.

[147] H. Wang, "A new method to eliminate DG's negative effect on existing distribution network protection," in Proc. 20th Int. Conf. Electricity Distribution, Prague, 2009.

[148] J. Arrillaga and N. R. Watson, Computer Modelling of Electrical Power Systems, 2nd ed. Chichester, U.K.: John Wiley and Sons, 2001.

[149] S. Devabhaktuni, H. S. Jain, and P. K. Kumar, "Current Limiting Reactor Support to Retain Short Circuit Ratings of Circuit Breakers and the Power Systems," in Proc. Switching Transients Conf. (SWITCHCON), pp. 164-168, 2016.

[150] Y. Jin, J. E. Fletcher, and J. O'Reilly, "Short-Circuit and Ground Fault Analyses and Location in VSC-Based DC Network Cables," IEEE Trans. Ind. Electron., vol. 59, no. 10, pp. 3827-3837, Oct. 2012.

[151] J. A. X. Prabhu, K. S. Nande, S. Shukla, and C. N. Ade, "Design of Electrical System Based on Short Circuit Study Using ETAP for IEC Projects," in Proc. IEEE Int. Conf. 6th Power Systems (ICPS), pp. 1-6, Oct. 2016.

[152] C. Jangun, P. Sungwon, K. Younghun, and Y. Heuiweon, "Thermal and coupled electromagnetic-mechanical analyses for the development of a dry type current limiting reactor," in Proc. ASME 2013 Int. Mech. Eng. Congress and Exhibition, pp. 1-6, 2013. DOI: 1115/IMECE2013-64277

[153] J. Yang, J. E. Fletcher, and J. O'Reilly, "Short-Circuit and Ground Fault Analyses and Location in VSC-Based DC Network Cables," IEEE Trans. Ind. Electron., vol. 59, no. 10, pp. 3827-3837, Oct. 2012.

[154] P. Pinceti, M. Vanti, C. Brocca, M. Carnesecchi, and G. P. Macera, "Design Criteria for a Power Management System for Microgrids with Renewable Sources," Electr. Power Syst. Res., vol. 122, pp. 168-179, May 2015.

[155] K. Mazlumi and H. A. Abyaneh, "Relay Coordination and Protection Failure Effects on Reliability Indices in an Interconnected Sub Transmission System," Electr. Power Syst. Res., vol. 79, no. 7, pp. 1011-1017, 2009.

[156] S. A. M. Javadian, M. R. Haghifam, and P. Barazandeh, "An Adaptive Overcurrent Protection Scheme for MV Distribution Networks Including DG," in Proc. IEEE Int. Symp. Ind. Electron., pp. 2084-2089, UK, 2008.

[157] M. J. Talarposhti, S. H. Fathi, and H. A. Abyaneh, "Impact of Critical Clearing Time on Over-current Relays Coordination in a Multi-Machine Power System in Presence of Resistive SFCL," in Proc. 11th Int. Conf. Protection & Automation in Power System, pp. 1-6, Iran University of Science & Technology, Tehran, Iran, 2017.

[158] S. Thangalakshmi, "Planning and Coordination of Relays in Distribution System," Indian J. Sci. Technol., ISSN (p): 0974-5645, August 2016.

[159] Y. Lee, A. K. Ramasamy, F. Hafiz, and A. Abidin, "Numerical Relay for Overcurrent Protection Using TMS320F2812," in Proc. 9th WSEAS Int. Conf. Circuits, Syst., Electron., Control & Signal Process. (CSECS '10), pp. 1-6, 2010.

[160] R. Muthu Kumar and Vahab P., "Overcurrent and Earth fault Relay Coordination for Microgrids with Modern Numerical Relay Features," Int. J. Eng. Res. Gen. Sci., vol. 4, no. 3, pp. 243-252, May-Jun. 2016.

[161] J. M. Guerrero, J. C. Vasquez, J. Matas, L. G. de Vicuña, and M. Castilla, "Hierarchical control of droop-controlled AC and DC microgrids—A general approach toward standardization," IEEE Trans. Ind. Electron., vol. 58, no. 1, pp. 158-172, Jan. 2011.

[162] R. Majumder, A. Ghosh, G. Ledwich, and F. Zare, "Power Management and Power Flow Control with Back-to-Back Converters in a Utility Connected Microgrid," IEEE Trans. Power Syst., vol. 25, no. 2, pp. 821-834, May 2010.

[163] J. F. Hu, J. G. Zhu, and G. Platt, "A droop control strategy of parallel-inverter-based microgrid," in Proc. 2011 Int. Conf. Appl. Supercond. Electromagn. Devices, Sydney, Australia, Dec. 2011, pp. 188-191.

[164] Q. C. Zhong, "Robust Droop Controller for Accurate Proportional Load Sharing Among Inverters Operated in Parallel," IEEE Trans. Ind. Electron., vol. 60, no. 3, pp. 1281-1290, Mar. 2013.

[165] A. Ali, W. Li, R. Hussain, X. He, B. W. Williams, and A. H. Memon, "Overview of current microgrid policies, incentives and barriers in the European union, united states and china," Sustainability, vol. 9, no. 7, pp. 1146, Jul. 2017.

[166] T. Vigneysh, N. Kumarappan, and R. Arulraj, "Operation and control of wind/fuel cell based hybrid microgrid in grid connected mode," in Proc. Int. Conf. Automation, Computing, Communication, Control and Compressed Sensing, 2013, pp. 754-758.

[167] Y. Li and Y. W. Li, "Power Management of Inverter Interfaced Autonomous Microgrid Based on Virtual Frequency-Voltage Frame," IEEE Trans. Smart Grid, vol. 2, no. 1, pp. 30-40, Mar. 2011.

[168] T. Vigneysh and N. Kumarappan, "Autonomous operation and control of photovoltaic/solid oxide fuel cell/battery energy storage based microgrid using fuzzy logic controller," Int. J. Hydrogen Energy, vol. 41, no. 3, pp. 1877-1891, Jan. 2016.

[169] J. Hu, Y. Shan, X. Yinliang, and J. M. Guerrero, "A coordinated control of hybrid ac/dc microgrids with PV-wind-battery under variable generation and load conditions," Int. J. Electr. Power Energy Syst., vol. 104, pp. 583-592, Feb. 2019.

[170] A. Tah and D. Das, "An Enhanced Droop Control Method for Accurate Load Sharing and Voltage Improvement of Isolated and Interconnected DC Microgrids," IEEE Trans. Sustain. Energy, vol. 7, pp. 1194-1204, 2016.

[171] L. Meng, F. Tang, M. Savaghebi, J.C. Vasquez, and J.M. Guerrero, "Tertiary Control of Voltage Unbalance Compensation for Optimal Power Quality in Islanded Microgrids," IEEE Trans. Energy Convers., vol. 29, pp. 802-815, 2014.

[172] C. Yoon, H. Bai, R.N. Beres, X. Wang, C.L. Bak, and F. Blaabjerg, "Harmonic stability assessment for multi-paralleled grid-connected inverters," in Proc. IEEE Int. Power Electron. Appl. Conf. Expo., Shanghai, China, 2014, pp. 1098-1103.

[173] A. Rosato, R. Altilio, R. Araneo, and M. Panella, "Prediction in photovoltaic power by neural networks," Energies, vol. 10, p. 1003, 2017.

[174] J.G. de Matos, F.S.F. de Silva, and L.A. de S Ribeiro, "Power control in ac isolated microgridss with renewable energy sources and energy storage systems," IEEE Trans. Ind. Electron., vol. 62, pp. 3490-3498, 2015.

[175] D.E. Olivares, C.A. Canizares, M. Kazerani, A. Mehrizi-Saini, A.H. Etemadi, R. Iravani, A.H. Hajimiragha, O. Gomis-Bellmunt, M. Saeedifard, R. Palma-Behnke, et al., "Trends in microgrid control," IEEE Trans. Smart Grid, vol. 5, pp. 1905-1919, 2014.

[176] L. Igualada, C. Corchero, M. Cruz-Zambrano, and F.J. Heredia, "Optimal energy management for a residential microgrid including a vehicle-to-grid system," IEEE Trans. Smart Grid, vol. 5, pp. 2163-2172, 2014.

[177] H. Bevrani and S. Shokoohi, "An Intelligent Droop Control for Simultaneous Voltage and Frequency Regulation in Islanded Microgrids," IEEE Trans. Smart Grid, vol. 4, pp. 1505-1513, 2013.

[178] M. Kermani, "Transient voltage and frequency stability of an isolated microgrid based on energy storage systems," in Proc. IEEE 16th Int. Conf. Environ. Electr. Eng. (EEEIC), Florence, Italy, 2016, pp. 1-5.

[179] Z. Zou, G. Buticchi, M. Liserre, A.M. Kettner, and P. Paolone, "Voltage stability analysis using a complete model of grid-connected voltage source converters," in Proc. IEEE Energy Convers. Congr. Expo. (ECCE), Milwaukee, WI, USA, 2016, pp. 1-8.

[180] G. G. Lage, R. A. S. Fernandes, G. R. M. da Costa, and J. Cao, "Optimal power flows with voltage stability constraint based on voltage stability indices and artificial neural networks," in Proceedings of the IEEE Power Tech, Eindhoven, The Netherlands, Jun. 29-Jul. 2, 2015.

[181] S. Leonori, E. De Santis, A. Rizzi, and F. M. Frattale Mascioli, "Multi objective optimization of a fuzzy logic controller for energy management in microgrids," in Proceedings of the 2016 IEEE Congress on Evolutionary Computation (CEC), Vancouver, BC, Canada, Jul. 24-29, 2016, pp. 319-326.

[182] V. G. Nguyen, X. Guo, C. Zhang, C. Chen, and N. T. Tran, "The analysis of electric power steering base on fuzzy-PI control," in Proceedings of the 2017 4th International Conference on Systems and Informatics (ICSAI), Hangzhou, China, Nov. 11-13, 2017, vol. 2018, pp. 121-126.

[183] Y. Liu, Y. Han, C. Lin, P. Yang, and C. Wang, "Design and Implementation of Droop Control Strategy for DC Microgrid Based on Multiple DC/DC Converters," in Proceedings of the 2019 IEEE Innovative Smart Grid Technologies-Asia (ISGT Asia), Chengdu, China, May 21-24, 2019, pp. 3896-3901.

[184] D. Magdefrau, T. Taufik, M. Poshtan, and M. Muscarella, "Analysis and review of DC microgrid implementations," in Proceedings of the 2016 International Seminar on Application for Technology of Information and Communication (ISemantic), Semarang, Indonesia, Aug. 5-6, 2016, pp. 241-246.

[185] S. Adhikari and F. Li, "Coordinated Vf and PQ control of solar photovoltaic generators with MPPT and battery storage in microgrids," IEEE Trans. Smart Grid, vol. 3, pp. 1270-1281, Sep. 2014.

[186] E. Planas, J. Andreu, J. I. Gárate, I. M. De Alegria, and E. Ibarra, "AC and DC technology in microgrids: A review," Renew. Sustain. Energy Rev., vol. 43, pp. 726-749, Jan. 2015.

[187] P. Molotov, A. Vaskov, and M. Tyagunov, "Modeling Processes in Microgrids with Renewable Energy Sources," in Proceedings of the IEEE Conference UralCon, Chelyabinsk, Russia, Oct. 4-6, 2018, pp. 203-208.

[188] Y. Wang, J. Meng, X. Zhang, and L. Xu, "Control of PMSG-based wind turbines for system inertial response and power oscillation damping," IEEE Trans. Sustain. Energy, vol. 6, pp. 565-574, Jan. 2015.

[189] P.S. Kumar, R.P.S. Chandrasena, V. Ramu, G.N. Srinivas, and K.V.S.M. Babu, "Energy Management System for Small Scale Hybrid Wind Solar Battery Based Microgrid," IEEE Access, vol. 8, pp. 8336-8345, 2020.

[190] M. Alramlawi and P. Li, "Design Optimization of a Residential PV-Battery Microgrid with a Detailed Battery Lifetime Estimation Model," IEEE Trans. Ind. Appl., vol. 56, no. 1, pp. 1-10, Jan.-Feb. 2020.

[191] C. Lebron, F. Andrade, E. O'Neill, and A. Irizarry, "An intelligent Battery management system for home Microgrids," in Proc. IEEE 2016 IEEE Power & Energy Society Innovative Smart Grid Technologies Conference (ISGT), Minneapolis, MN, USA, Sep. 6-9, 2016, pp. 1-5.

[192] H.K. Davijani, "Analysis and Control of a Microgrid with Converter Fed Distributed Energy Resources," Ph.D. Thesis, Tennessee Technological University, USA, 2012.

[193] S. Chandrakala Devi, B. Singh, and S. Devassy, "Modified generalised integrator-based control strategy for solar PV fed UPQC enabling power quality improvement," IET Gen. Trans. Distrib., vol. 14, no. 15, pp. 3127-3138, Dec. 2020.

[194] S.M. Ferdous, "Operation and Control Strategy of Coupled Microgrid Clusters," Murdoch University, Perth, Australia, 2021.

[195] H. Chen and N. David, "Analysis of permanent-magnet synchronous generator with Vienna rectifier for wind energy conversion system," IEEE Trans. Sustain. Energy, vol. 4, no. 1, pp. 154-163, Jan. 2013.

[196] S.M. Dehghan, M. Mohamadian, and A.Y. Varjani, "A new variable-speed wind energy conversion system using permanent-magnet synchronous generator and Z-source inverter," IEEE Trans. Energy Convers., vol. 24, no. 3, pp. 714-724, Sep. 2009.

[197] C. Chen, S. Duan, T. Cai, B. Liu, and G. Hu, "Smart energy management system for optimal microgrid economic operation," IET Renew. Power Gener., vol. 5, no. 3, pp. 258-267, May 2011.

[198] C.N. Bhende, S. Mishra, and S.G. Malla, "Permanent magnet synchronous generator based standalone wind energy supply system," IEEE Trans. Sustain. Energy, vol. 2, no. 4, pp. 361-373, Oct. 2011.

[199] A.M. Eltamaly and H.M. Farh, "Maximum power extraction from wind energy system based on fuzzy logic control," Electr. Power Syst. Res., vol. 97, pp. 144-150, Mar. 2013.

[200] D. Zhou, F. Blaabjerg, T. Franke, M. Tönnes, and M. Lau, "Comparison of wind power converter reliability with low-speed and medium-speed permanent-magnet synchronous generators," IEEE Trans. Ind. Electron., vol. 62, no. 10, pp. 6575-6584

[201] H. Polinder, J.A. Ferreira, B.B. Jensen, A.B. Abrahamsen, K. Atallah, and R.A. McMahon, "Trends in wind turbine generator systems," IEEE J. Emerg. Sel. Top. Power Electron., vol. 1, pp. 174-185, 2013.

[202] F. Blaabjerg and M. Ke, "Future on Power Electronics for Wind Turbine Systems," IEEE J. Emerg. Sel. Top. Power Electron., vol. 1, pp. 139-152, 2013.

[203] J. Liu, Y. Miura, H. Bevrani, and T. Ise, "Enhanced Virtual Synchronous Generator Control for Parallel Inverters in Micro grids Static Synchronous Generators for Distributed Generation and Renewable Energy," IEEE Trans. Smart Grid, vol. 99, pp. 2268-2277, 2016.

[204] J. Liu, Y. Miura, and T. Ise, "Comparison of Dynamic Characteristics Between Virtual Synchronous Generator and Droop Control in Inverter Based Distributed Generators," IEEE Trans. Power Electron., vol. 31, pp. 3600-3611, 2016.

[205] H. Bevrani, A. Ghosh, and G. Ledwich, "Renewable energy sources and frequency regulation: Survey and new perspectives," IET Renew. Power Gener., vol. 4, pp. 438-457, 2010.

[206] G.A. Diaz, C. Gonzalez-Moran, J. Gomez-Aleixandre, and A. Diez, "Scheduling of droop coefficients for frequency and voltage regulation in isolated microgrids," IEEE Trans. Power Syst., vol. 25, pp. 489-496, 2010.

[207] Y. Li, Z. Xu, L. Xiong, G. Song, J. Zhang, D. Qi, and H. Yang, "A cascading power sharing control for microgrid embedded with wind and solar generation," Renew. Energy, vol. 132, pp. 846-860, 2019.

[208] X. Meng, J. Liu, and Z. Liu, "A generalized droop control for grid supporting inverter based on comparison between traditional droop control and virtual synchronous generator control," IEEE Trans. Power Electron., vol. 34, pp. 5416-5438, 2018.

[209] Amandeep, "ANFIS based control strategy for frequency regulation in AC microgrid," in Proc. 2016 Fifth International Conference on Eco-Friendly Computing and Communication Systems (ICECCS), Bhopal, India, Dec. 8-9, 2016, pp. 38-42.

[210] S. Leonori, A. Martino, A. Rizzi, and F.M.F. Mascioli, "Anfis synthesis by clustering for microgrids ems design," in Proc. IJCCI 2017-9th International Joint Conference on Computational Intelligence, Funchal, Portugal, Nov. 1-3, 2017, pp. 328-337.

[211] F. Dubuisson, M. Rezkallah, A. Chandra, M. Saad, M. Tremblay, and H. Ibrahim, "Control of hybrid wind-diesel standalone microgrid for water treatment system application," IEEE Transactions on Industry Applications, vol. 55, no. 6, pp. 6499-6507, Nov./Dec. 2019.

[212] A. Jafari, T. Khalili, H. Ganjeh Ganjehlou, and A. Bidram, "Optimal integration of renewable energy sources, diesel generators, and demand response program from pollution, financial, and reliability viewpoints: A multi-objective approach," Journal of Cleaner Production, vol. 247, p. 119100, Jan. 2020.

[213] C. Yammani and S. Maheswarapu, "Load frequency control of multi-microgrid system considering renewable energy sources using grey wolf optimization," Smart Sci, vol. 7, no. 3, pp. 198-217, Jul./Sep. 2019.

[214] Y. Karimi, H. Oraee, and J. M. Guerrero, "Decentralized method for load sharing and power management in a hybrid single/three-phase-islanded microgrid consisting of hybrid source PV/battery units," IEEE Transactions on Power Electronics, vol. 32, no. 8, pp. 6135-6144, Aug. 2016.

[215] Z. A. Obaid, L. M. Cipcigan, L. Abrahim, and M. T. Muhssin, "Frequency control of future power systems: reviewing and evaluating challenges and new control methods," Journal of Modern Power Systems and Clean Energy, vol. 7, no. 1, pp. 9-25, Jan. 2019.

[216] C. Zhang, Y. Xu, Z. Y. Dong, and K. P. Wong, "Robust coordination of distributed generation and price-based demand response in microgrids," IEEE Transactions on Smart Grid, vol. 9, no. 5, pp. 4236-4247, Sep. 2017.

[217] T. Adefarati, R. C. Bansal, and J. J. Justo, "Techno-economic analysis of a PV-wind-battery-diesel standalone power system in a remote area," The Journal of Engineering, no. 13, pp. 740-744, Mar. 2017.

[218] M. A. Hossain, H. R. Pota, M. J. Hossain, and F. Blaabjerg, "Evolution of microgrids with converter-interfaced generations: Challenges and opportunities," International Journal of Electrical Power & Energy Systems, vol. 109, pp. 160-186, May 2019.

[219] S. Mishra, R. C. Prusty, and S. Panda, "Design and Analysis of 2dof-PID Controller for Frequency Regulation of Multi-Microgrid Using Hybrid Dragonfly and Pattern Search Algorithm," Journal of Control, Automation and Electrical Systems, pp. 1-15, Mar. 2020.

[220] T. John and S. P. Lam, "Voltage and frequency control during microgrid islanding in a multi-area multi-microgrid system," IET Generation, Transmission & Distribution, vol. 11, no. 6, pp. 1502-1512, Mar. 2017.

[221] D. O. Amoateng, M. Al Hosani, M. S. Elmoursi, K. Turitsyn, and J. L. Kirtley, "Adaptive voltage and frequency control of islanded multi-microgrids," IEEE Trans. Power Syst., vol. 33, no. 4, pp. 4454-4465, 2017.

[222] M. Gheisarnejad and M. H. Khooban, "Secondary load frequency control for multi-microgrids: HiL real-time simulation," Soft Comput., vol. 23, no. 14, pp. 5785-5798, 2019.

[223] N. Vafamand, M. H. Khooban, T. Dragičević, J. Boudjadar, and M. H. Asemani, "Time-delayed stabilizing secondary load frequency control of shipboard microgrids," IEEE Syst. J., vol. 13, no. 3, pp. 3233-3241, 2019.

[224] D. Yousri, T. S. Babu, and A. Fathy, "Recent methodology based Harris Hawks optimizer for designing load frequency control incorporated in multi-interconnected renewable energy plants," Sustain. Energy Grids Networks, vol. 22, pp. 100352, 2020.

[225] B. Khokhar, S. Dahiya, and K. P. S. Parmar, "A Novel Hybrid Fuzzy PD- TID Controller for Load Frequency Control of a Standalone Microgrid," Arab J. Sci. Eng., vol. 46, pp. 1053-1065, 2021.

[226] M. Ahmed, G. Magdy, M. Khamies, and S. Kamel, "Modified TID controller for load frequency control of a two-area interconnected diverse-unit power system," Int. J. Elect. Power Energy Syst., vol. 135, pp. 107528, 2022.

[227] D. Guha, P. K. Roy, and S. Banerjee, "Equilibrium optimizer-tuned cascade fractional-order 3DOF-PID controller in load frequency control of power system having renewable energy resource integrated," Int. Trans. Elect. Energy Syst., vol. e12702, pp. 1-25, 2020.

Name of the Scholar	C Rohmingtluanga
Contact No.	8729934708
Email Id	crotea.research@gmail.com
Permanent Address	H No. E-75, Zion Veng, Tanhril, Aizawl
	Mizoram -796009
Marital Status	Single

Educational Background

B.E/ B.Tech	Electrical and Electronics Engineering
M.E/ M.tech	Power Systems Engineering
Ph.D.	Microgrid

PUBLICATIONS ARISING FROM THIS THESIS

1. JOURNAL

Sl. No.	Paper Title	Authors	Name of Journal (SCI/ESCI/ Scopus/WoS)	ISSN	Impact factor
1	SCADA based Intake monitoring for improving energy management plan: Case study	C Rohmingtluanga, S. Datta, N. Sinha, T. S. Ustun	Energy Reports, Elsevier (SCIE/DOAJ/Ei Compendex /Scopus/INSPEC)	2352-4847 https://doi.org/10.1016/j.egyr.2022.11.037	4.937
2	ANFIS-Based Droop Control of an AC Microgrid System: Considering Intake of Water Treatment Plant	C Rohmingtluanga, S. Datta, N. Sinha, T. S. Ustun A. Kalam	Energies, MDPI (SCIE/Scopus etc.)	1996-1073, Published by MDPI https://doi.org/10.3390/en15197442	3.252
3	Load Flow analysis considering Microgrid system	C. Rohmingtluanga; Subir Datta; Nidul Sinha	UNDER REVIEW		
4	Load Frequency Control of multiarea multisource based microgrid system	C. Rohmingtluanga; Subir Datta; Nidul Sinha;	UNDER REVIEW		

2. CONFERENCE

Sl. No.	Paper Title	Authors	Conference Name	ISBN	Publisher	Dates of conference
1.	A Comprehensive Study on SCADA based Intake, Water Treatment Plant and Intermediate Pumping Station of Existing Water Supply System	C Rohmingtluanga, S. Datta, N. Sinha,	International Conference on Computational Intelligence & Sustainable Technologies (ICoCIST-2021)	ISBN: 978-981-16-6893-7	Springer	October 28th -30th, 2021
2.	Study of SCADA based Existing Water Treatment Plant- GAWSS P-I in Mizoram, India	C Rohmingtluanga, S. Datta, N. Sinha	2021 IEEE International Power and Renewable Energy Conference (IPRECON2021)	ISBN:978-1-6654-0137-1	IEEE	September 24th, 25th & 26th 2021
3	Performance Study of a Wind-Battery-Based Islanding System	S. Lalngaihawma, C. Rohmingtluanga, R. Roy, D. Hmingthanmawia, S. Datta & N. Sinha	SIS-2021 (International Conference on Smart and Intelligent Systems	Online ISBN 978-981-16-2109-3	Springer, Singapore	February 25-26, 2021.

Name of the Scholar   C Rohmingtluanga

Degree   Ph.D

Department   Electrical Engineering department,

Mizoram University

Title of Thesis   Investigation and control of WTP with

consideration of microgrid concept.

Date of Admission   10/08/2018

Approval of Research Proposal

    1. DRC   04/04/2019

    2. BOS   25/04/2019

    3. School Board   23/11/2022

MZU Registration No.   1800052

PhD Registration No   MZU/Ph.D/1299 of 10.08.2018

Extension if any   None

Dr. Subir Datta

Head

Dept.of Electrical Engineering

ABSTRACT

INVESTIGATION AND CONTROL OF WATER TREATMENT PLANT WITH CONSIDERATION OF MICRO-GRID CONCEPT

AN ABSTRACT SUBMITTED IN PARTIAL FULFILLMENT OF THE REQUIREMENT FOR THE DEGREE OF DOCTOR OF PHILOSOPHY

C ROHMINGTLUANGA
MZU REGN. NO. 1800052
Ph.D. Reg No. MZU/Ph.D./1299 of 10.08.2018

DEPARTMENT OF ELECTRICAL ENGINEERING

SCHOOL OF ENGINEERING AND TECHNOLOGY

MAY 2023

INVESTIGATION AND CONTROL OF WATER TREATMENT PLANT WITH CONSIDERATION OF MICROGRID CONCEPT

BY

C Rohmingtluanga

Department of Electrical Engineering

Name of Supervisor: Dr Subir Datta

Joint- Supervisor: Prof. Nidul Sinha

Submitted

In partial fulfillment of the requirement of the Degree of Doctor of Philosophy in Electrical Engineering of Mizoram university, Aizawl

ABSTRACT

Water is a vital resource that has a profound impact on various aspects of development and is closely associated with almost all of the Sustainable Development Goals (SDGs). It is essential for maintaining healthy ecosystems, promoting economic progress, and sustaining life itself. Access to safe water and sanitation is a fundamental human right, yet a significant number of people around the world still lack these basic necessities. This lack of access to water and sanitation presents significant challenges to economic growth, poverty reduction, and sustainable development. Existing literature and studies in the field of Water treatment Plant (WTP) has mainly focused on Waste Water Treatment Plants (WWTPs) and their effect on water quality and quantity, there is a significant lack of research on conventional WTPs. Specifically, there is a need for more research on SCADA-based systems that promote self-energy sufficiency, as well as power-related issues and power management in conventional WTPs.

Recent studies have demonstrated that implementing SCADA systems in WTPs can be an effective way to enhance system efficiency. Thus, further research is needed to explore their implementation in conventional WTPs and to evaluate their potential to improve treatment quality and quantity. In addition, the integration of renewable energy sources such as solar, wind, and hydro power into existing WTPs has the potential to reduce energy consumption costs while increasing efficiency. However, comprehensive feasibility studies are required to assess the technical and cost constraints associated with the implementation of such technologies in WTPs. To address these gaps, the concept of microgrid-based WTPs has emerged as a potentially transformative solution that can significantly improve the efficiency and sustainability of water treatment processes.

Based on the above concept, WTP of Aizawl, India has been selected as a suitable site for consideration of the study system. The research focuses on detailed investigation and analysis of the Greater Aizawl Water Supply systems considering improvement in the SCADA system, deploying various power analysis with and

without consideration of various RESs, such as 1) load flow analysis, 2) Short circuit analysis and 3) Relay coordination. In order to enhanced the system performance, Static var compensators and current limiting reactors were used in load flow and short circuit analysis. Moreover, with consideration of the microgrid concept, implementation of control mechanisms using the Simulink environment is also done focusing on single area and multi area microgrid system, that can address stability, control, and excessive generation issues. The aim is to improve voltage and frequency quality through droop control and various optimization methods, while also coordinating power-sharing among different Distributed Energy Resources (DERs) like solar, wind, small hydro, diesel engine generators, and local battery energy storage systems (BES).

These proposed techniques are designed to overcome the limitations of existing methods in the literature and offer a more generalizable solution. This makes it possible to consider self-sufficient WTP-based microgrid systems in the future. The findings of this research can have practical implications in improving the efficiency and sustainability of water treatment processes in Aizawl, India, and can also serve as a reference for other similar WTPs around the world.

This thesis also aims to evaluate the effectiveness of the ANFIS-based droop control technique in a microgrid system, specifically for the intake of WTP, under various loading conditions. The study compares the ANFIS technique to the conventional droop control technique using GDC. The ANFIS technique is trained successfully for both P-F and Q-V droop cases and is utilized to address issues related to transient behaviour during switching and power sharing between the source and load in grid connected and islanded modes of operation. The battery system compensates for power sharing between the source and load as different loads change. The simulation results demonstrate the successful ANFIS training and improved performance of the controller units for both P-F and Q-V droop.

Furthermore, the study presents a novel method to regulate frequency deviation in a multi-microgrid system that incorporates renewable energy sources (RES) and distributed energy generation. The system consists of a water treatment plant with

multiple pumping and power stations, and different energy sources, such as DEG, SPV, WTG, and BESS, are used to power different areas of the microgrid. The proposed method uses the EHHO technique to optimally select tuning parameters for a PID controller, which is then compared to existing methods, such as PSO and GWO, using MATLAB software. The proposed controller's performance is evaluated using load demand and frequency, and the results show that it effectively regulates load frequency deviation and outperforms PSO and GWO.

The study also presents an optimal control approach that employs a 3DOF-FOPIDN secondary controller designed using the PSO algorithm to improve system dynamic performance. The results demonstrate that the 3DOF-FOPIDN controller performs better than other secondary controllers, such as 3DOF-TIDN, in reducing oscillations, settling time of frequency, and tie power deviation. Additionally, the 3DOF-FOPIDN controller is robust enough to handle uncertain parametric variations, such as the absence of solar, variation of wind speed, and varying system inertia, without requiring repeated resetting of controller parameters.